UNIVERSITY OF CALIFORNIA

Los Angeles

Nanosphere Lithography for Intracellular Delivery

A dissertation submitted in partial satisfaction of the

requirements for the degree Doctor of Philosophy

in Chemistry

by

Natcha Wattanatorn

2019

ABSTRACT OF THE DISSERTATION

Nanosphere Lithography for Intracellular Delivery

by

Natcha Wattanatorn

Doctor of Philosophy in Chemistry

University of California, Los Angeles, 2019

Professor Paul S. Weiss, Chair

Nanosphere lithography (NSL) is a simple, high-throughput technique that can be used to form large-area, close-packed monolayer arrays of nanospheres. These arrays can be directly used as an etching or as a deposition mask, to generate silicon-based nanostructures. Typically, the nanostructures produced are created by single etches of the nanosphere array resulting in limitations in fabrication of novel patterns/nanostructures. Here, we report multiple patterning nanosphere lithography for fabrication of three-dimensional periodic silicon-based nanostructures, exploiting their degradable nature during selected and repeated etching of the polymer nanospheres. As a result, the masks can be shaped in parallel for each processing step enabling the fabrication of wafer-scale three-dimensional (3D) periodic silicon nanostructures. These nanotubes and hierarchical nanostructures can be tuned precisely with independent control in three dimensions including outer/inner diameters, heights/hole-depths, and pitches. We have demonstrated our technique to

construct solid/hollow nanotubes, multilevel solid/hollow nanotowers, and 3D concentric plasmonic nanodisk/nanorings with tunable optical properties on a variety of substrates.

In the second part of my dissertation, I used NSL to fabricate periodic arrays of conical nanoneedles for non-viral gene delivery for chimeric antigen receptor (CAR) T cell production. Gene delivery using non-viral methods has significant advantages in terms of safe delivery of cargo and cost. Especially, physical membrane disruption *via* nanoneedles has the capability to inject and deliver molecules of interest directly as well as the capability to create transient pores in the cell membrane, enabling biomolecule diffusion into the cells. However, the challenges for these systems include inconsistency of membrane penetration and slow processing throughputs. Here, we use a nanoneedle-integrated microfluidic system and gene-encapsulated supramolecular nanoparticle for production of CAR-T cells, in both model and primary T cells. Using NSL, we can achieve conical shaped silicon nanoneedles, where the height, base width, tip sharpness, and pitches are individually tunable, resulting in sturdy structures that can penetrate the cells. With this platform, we can efficiently load CAR plasmids inside nanoparticles, which are tethered to the substrate for direct injection, as well as co-flow an excess of CAR-encapsulated nanoparticles, for diffusion through transient pores that are created by the nanoneedles. This platform enables continuous and sequential intracellular delivery, which provides a path for sustainable CAR-T cell production.

This dissertation of Natcha Wattanatorn is approved.

Richard B. Kaner

Alexander Michael Spokoyny

Alireza Khademhosseini

Paul S. Weiss, Committee Chair

University of California, Los Angeles

2019

For my parents,

who have always supported me

through this journey far away from home.

Table of Contents

Chapter II

Multiple-Patterning Nanosphere Lithography for Fabricating Periodic Three-Dimensional Hierarchical Nanostructures Polymer-Pen Chemical Lift-Off Lithography

Chapter III

Intracellular Delivery *via* a Nanoneedle-Integrated Microfluidic System for Cellular Immunotherapies

Chapter IV

Conclusions and Prospects

Appendix A

Surface Dipole Control of Liquid Crystal Alignment

Appendix B

Photoinduced Charge Transfer in Single-Molecule *p*–*n* Junctions

List of Abbreviations and Symbols

Acronyms and Symbols

1O2	*o*-1,2-carboranedithiol
3D	three-dimensional
5CB	4-cyano-4′-pentylbiphenyl
9O12	*o*-9,12-carboranedithiol
α	molecular polarizability tensors
AC	time-varying
Ad	adamantane
Ad-PAMAM	adamantane-grafted polyamidoamine dendrimer
AF647	Alexa Fluor 647
AFM	atomic force microscopy
$\overrightarrow{\mathbf{Au}}$	gold evaporation direction
C11	1-undecanethiol
C12	1-dodecanethiol
C18	1-octadecanethiol
CAR	chimeric antigen receptor
CD	cyclodextrin
CD-PEI	cyclodextrin-grafted polyethylenimine
CRISPR	clustered regularly interspaced short palindromic repeats
CTLA-4	cytotoxic T lymphocyte antigen-4
δ	delta

$\Delta\varepsilon$	dielectric anisotropies
Δn	liquid crystal birefringence
d	wedge thickness
d_o	outer diameter
d_i	inner diameter
DAPI	4',6-diamidino-2-phenylindole
DC	constant, time independent
ddPCR	digital droplet polymerase chain reaction
DI	deionized
DNA	deoxyribonucleic acid
DRIE	deep reactive ion etching
γ	gamma
Γ	optical retardation
FBS	fetal bovine serum
FDA	Food and Drug Administration
FDTD	finite-difference time-domain
FIB	focused ion-beam
FSC	forward scatter
h_0	outer height
h_i	hole depth
hcp	hexagonal close-packed
HSC	hematopoietic stem cell
I	current

J WT	Jurkat wild type
K_{22}	twist elastic constant
λ	wavelength
LC	liquid crystal
μ	permanent molecular dipole moment
m	fringe order integer
M1	*m*-1-carboranethiol
M9	*m*-9-carboranethiol
MBBA	*N*-(4-methoxybenzylidene)-4-butylaniline
MP-NSL	multiple-patterning nanosphere lithography
mRNA	messenger ribonucleic acid
N	sample size
NMP	N-methyl-2-pyrolidone
NSL	nanosphere lithography
η_d	equilibrium director orientations
η_0	easy alignment axis
O1	*o*-1-carboranethiol
O9	*o*-9-carboranethiol
φ	angle at which the director deviates from the easy axes
Ψ	angular twist
p	pitches
$p_{\parallel}$	parallel dipole moment orientation
$p_{\perp}$	perpendicular dipole moment orientation

P	pressure
PBS	phosphate-buffered saline
PD-1	programmed cell death-1
PDMS	poly(dimethylsiloxane)
PEG	polyethylene glycol
PS	polystyrene spheres
RIE	reactive-ion etching
RNA	ribonucleic acid
RPMI	Roswell Park Memorial Institute
σ	uncertainty
SAM	self-assembled monolayer
SCID	severe combined immunodeficiency
SEM	scanning electron microscopy
Si	single-crystalline silicon
SMNP	supramolecular nanoparticles
SSC	side scatter
STM	scanning tunneling microscope
T	temperature
T cells	T lymphocytes
$\mathbf{T_{NI}}$	transition temperature
$\boldsymbol{w}$	sidewall thickness
$\boldsymbol{W_{az}}$	azimuthal anchoring energy

Units

Å	Ångströms
bp	base pairs
C	Celsius
cm	centimeters
D	Debye
eV	electron volts
h	hours
kb	kilobases
kHz	kilohertz
µJ	microjoules
µL	microliters
µm	micrometers
m	meters
mg	milligrams
min	minutes
mL	milliliters
mm	millimeters
mM	millimolar
mΩ·cm	milliohm-centimeters
ms	milliseconds
mTorr	millitorr
nm	nanometers

s	seconds
sccm	standard cubic centimeters per minute
V	volts
W	watts

Acknowledgments

I would like to start by thanking my parents, Supaporn and Vimol Wattanatorn, for teaching me to always have faith in myself and encourage me to do whatever I wish even it means I have to be far away from home. Thank you for your unconditional love and for raising me to become the person I am today. I want to thank my younger brother, Thanapol, who has always been there for me. I am eternally grateful to my aunt, Pranom, for your love and endless support. To both my grandfathers, who passed away during my academic pursuit in the United States, and to both my grandmothers, who are still living strong, your teaching and nurturing makes me feel like I am the luckiest girl to have you both as my grandparents.

I would like to express my sincere gratitude to my advisor, Professor Paul S. Weiss, for his mentorship and continuous supports throughout my graduate career. Paul has always encouraged me to never be afraid of new challenges and to be ready to explore when the opportunity comes. He has taught me not only valuable scientific skills, but also work ethics that have shaped me into the researcher I am today. I would also like to thank my committee members, Professors Richard B. Kaner, Alexander M. Spokoyny, and Ali Khademhosseini, for their guidance since my qualifying exam.

I would also like to thank my undergraduate research advisor, Professor Eunsuk Kim, for supporting, understanding me, as well as guiding me through a difficult time. Her passion for research continues to inspire me. As well, Dr. Mary Elizabeth Anderson has always been supportive of me. Her advice and friendship have been invaluable.

I am so grateful for my Liquid Crystals family, Dr. Jeffrey J. Schwartz and Dr. Alexandra M. Mendoza. Jeffrey has taught and inspired me a great deal. His excitement for science and

his creativities in solving problems will always be great examples for me. He continues to be a great mentor and friend even after his graduation. I am very fortunate and thankful to have the opportunity to work closely with Alex. She has always been there for me from my struggles through the candidacy exam, to learning together through many failed and successful experiments. I could not have asked for a better academic family.

I am also appreciative of the Weiss group members for their friendship and expertise. Dr. Yuxi Zhao introduced me to the photon STM world, the first project I learned in the Weiss group. Dr. Xiaobin Xu brought me to nanosphere lithography and nanofabrication field. Dr. Steve J. Jonas introduced the gene delivery field to me, making many projects and collaborations available for our group. Dr. Naihao Chiang has dedicated his time to help revise my writing and improve my countless drafts. I would like to thank my friends and labmates: Shenkai Wang, Kevin M. Cheung, Dr. Nako Nakatsuka, Dr. John M. Abendroth, Dr. Qing Yang, Kristopher K. Barr, Dominic P. Goronzy, Logan S. Stewart, Thomas D. Young, Chuanzhen Zhao, Jason Belling, and Lisa Kawakami, for their friendship and helpful scientific discussion.

I am grateful to have the opportunity to work with our collaborators. Professor Satiro N. De Olivera and Dr. Tzu-TIng Chiuo, who shared their expertise in molecular biology and gene delivery. Professor Hsian-Rong Tseng and his group shared and taught me their supramolecular nanoparticles and microfluidic platforms. Together, we were able to move the nanoneedle-integrated microfluidic project forward.

I also wish to acknowledge the facilities at UCLA and thank the staff of the Nano and Pico Characterization Lab, Electron Imaging Center, Integrated Systems Nanofabrication Cleanroom, NanoLab, Electron MicroProbe Laboratory and physical sciences student

machine shop, including Dr. Adam Stieg, Lorna Tokunaga, Krissy Do, Tony Wright, Ivo Atanasov, Tom Lee, Hoc Quang Ngo, Brian Matthews, Dr. Rosario Esposito, and Shylo Stiteler.

In addition, I would like to acknowledge the Royal Thai Government and National Science and Development Agency of Thailand (NSTDA) for their support throughout the pursuit of my higher education in the United States. I also thank the U.S. Department of Energy (DE-SC-0005025), the Keck Foundation, the National Science Foundation (CMMI-1636136), the Alex's Lemonade Stand Foundation for Childhood Cancer Research, the Hyundai Hope on Wheels Foundation, the St. Baldrick's Foundation, and the Tower Cancer Research Foundation.

I would like to thank all friends I made at UCLA, in particular, Sheba Plamthottam, Sayoni Ray, Chain Lee, Chia-Jung Yu, and Thanutra Zhang, for listening, caring, supporting, and sharing ups and downs. Finally, I want to thank Nics, for your friendship, understanding, and unconditional support. You are the most patient man I ever met. Without you, I would have already given up a million times over. I am very fortunate to have you in my life.

Vita

Natcha Wattanatorn received a Thai Government Scholarship from the National Science and Development Agency of Thailand (NSTDA) and came to the United States of America to pursue an undergraduate degree in chemistry at Brown University. She joined the research group of Professor Eunsuk Kim focusing on developing and characterizing novel dinitrosyl iron complexes and analyzing their reactivities with oxygen. She did a summer internship at the National Center for Genetic Engineering and Biotechnology in Thailand under the mentorship of Dr. Srung Smanmoo developing a colorimetric sensor for the detection of antimalarial drugs. In the Summer of 2011, she also organized an international science fair run by the Asia-Pacific Economic Cooperation (APEC). Natcha graduated with a Bachelor of Science degree in Chemistry in 2013.

Shortly thereafter, Natcha began her graduate studies at the University of California, Los Angeles under the mentorship of Professor Paul S. Weiss in the Department of Chemistry and Biochemistry. She independently designed and developed nanosubstrate-integrated microfluidic gene-delivery platform for manufacturing chimeric antigen receptor T cells. Outside of research, she was also involved with the nanoscience outreach program at the California NanoSystems Institute at UCLA to teach Los Angeles high school teachers ways to integrate nanoscience experiments into their curriculum in order to introduce and excite students to the field of nanoscience.

Publications

Wattanatorn, N.; Chiou, T.T.; Xu, X.; Mendoza, A.M.; De Oliveira, S.N.; Jonas, S.J.; Weiss, P.S. Nanosubstrate-Mediated Intracellular Delivery for High-Throughput Gene Modification. *In preparation* (2019).

Wang, S; **Wattanatorn, N.**; Chiang, N.; Zhao, Y.; Kim, M.; Ma, H.; Jen, A. K.-Y.; Weiss, P. S. Photo-Induced Charge Transfer in Single-Molecular *p-n* Junctions. *J. Phys. Chem. Lett.* **2019**, *10*, 2175-2181.

Wang, S; Goronzy, D. P.; Young, T. D.; **Wattanatorn, N.**; Stewart, L. L.; Baše, T; Weiss, P. S. Formation of Highly Ordered Terminal Alkyne Self-Assembled Monolayers on Au{111} Surface through Substitution of 1-Decaboranethiolate. *J. Phys. Chem. C*, **2019**, *123*, 1348-1353.

Xu, X.; Yang, Q.; **Wattanatorn, N.**; Zhao, C.; Jonas, S. J.; Weiss, P. S. Multiple-Patterning Nanosphere Lithography for Fabricating Periodic Three-Dimensional Hierarchical Nanostructures. *ACS Nano* **2017**, *11*, 10384-10391.

Xu, X.; Yang, Q.; Cheung, K. M.; Zhao, C.; **Wattanatorn, N.;** Belling, J. N.; Abendroth, J. M.; Slaughter, L. S.; Mirkin, C. A.; Andrews, A. M.; Weiss, P. S. Polymer-Pen Chemical Lift-Off Lithography. *Nano Letters* **2017**, *17*, 3302-3311.

Schwartz, J. J.; Mendoza, A. M.; **Wattanatorn, N.**; Zhao, Y.; Nguyen, V.; Spokoyny, A. M.; Mirkin, C. A.; Baše, T.; Weiss, P. S. Surface Dipole Control of Liquid Crystal Alignment. *JACS.* **2016**, *138*, 5957-5967.

Selected Conference Presentations

Wattanatorn, N.; Hou, S.; Chiou, T.-T., Xu, X.; Yang, Q.; De Oliveira, S.N.; Tseng, H.-R.; Jonas, S. J.; Weiss, P. Nanosubstrate-Mediated Intracellular Delivery for High-Throughput Gene Modification. 255th American Chemical Society Meeting, March 2018, oral presentation.

Wattanatorn, N.; Xu, X.; Yang, Q.; Zhao, C.; Jonas, S. J.; Weiss, P. S. Multiple-Patterning Nanosphere Lithography for Periodic Three-Dimensional Hierarchical Nanostructures, 254thFall American Chemical Society Meeting, August 2017, poster presentation.

Wattanatorn, N.; Xu, X.; Wang, F.; Yang, Q.; Zhao, C.; Tseng, H.-R.; Jonas, S. J.; Weiss, P. S. Multifaceted Silicon Nanostructures to Enable Targeted and Rapid Gene Modification. Cancer Nanotechnology Summer Symposium, August 2017, poster presentation.

CHAPTER I

Nanosphere Lithography for Intracellular Delivery

I.A Motivation and Background

Periodic micro- and nanostructures are gaining increasing attention due to their attractive properties (*i.e.*, adhesion, wetting, anti-reflection, surface plasmon resonances, etc.), which are distinct from their bulk material properties.[1–12] Thus, the development of fabrication methods to produce micro- and nanostructures with control is advantageous. Current fabrication methods, such as photolithography, electron beam lithography, and focused ion beam lithography, are capable of patterning nanostructures with precise control over size and shape spacing, but are low throughput and/or expensive to scale up.[13–18] Researchers have developed unconventional fabrication techniques, which include microcontact printing, nanoimprinting, and templating.[19–37] However, most techniques still require photolithography to make the initial master pattern. On the other hand, nanosphere lithography (NSL) exploits bottom-up self-assembly of polystyrene beads to form a mask, which serves as a template for top-down modification to create nanostructures.[32,33] Although NSL has enabled fabrication of wafer-scale nanostructures, it is inadequate to produce complex structures as the template only can be used once. During my doctoral work, I developed a method that utilizes the nanospheres multiple times. This new fabrication method, called multiple patterning nanosphere lithography, enables the fabrication of three-dimensional (3D) hierarchical nanostructures with precise control of structural dimensions, which is detailed in Chapter II.[38] In Chapter III, I optimized a NSL process to achieve wafer scale production of nanoneedle arrays for high-throughput chimeric antigen receptor (CAR) T-cell processing.

I.B Nanosphere Lithography

Nanosphere lithography (NSL) is an inexpensive, high-throughput nanofabrication technique that is capable of producing periodic arrangements of nanostructures with control over the sizes, shapes, and spacings of the features.[32,33] This method combines the advantages of both bottom-up, where small building blocks assemble into more complex structures, and top-down approaches, where subtractive and additive transfer of layers leads to different structures. Nanosphere lithography is also referred to as colloidal lithography or natural lithography because of its use of self-assembly.[39] In 1981, Fischer and Zingsheim pioneered the field when they showed that a small-area of particle monolayers formed an ordered array when a suspension of colloidal particles was drop-cast on a substrate and allowed to evaporate.[40] They used the hexagonally arranged spheres as a deposition mask for preparing platinum nanostructures. In 1982, Deckman and Dunsmuir developed a spin-coating technique that could produce mosaic arrays of particles over entire substrate; they also examined factors affecting monolayer formation.[39] Since this process is not uniform and relies on self-assembly, they observed defects, such as point defects, dislocations, and grain boundaries. In 1995, Van Duyne extended the work to double layers, leading to the fabrication of dot arrays.[32,41,42] They also studied plasmonic resonance properties of those structures for applications in optical biosensors. Since then, nanosphere lithography has gained increasing interest for manufacturing one-, two-, or three-dimensional nanostructures.[43–47]

A typical NSL process is divided into two steps: first monodisperse polystyrene (PS) or silica nanospheres are assembled into hexagonally closed-pack colloidal crystal mask by deposition techniques such as spin coating, drop casting, or deposition on an air/water

interface.[32] The ability to arrange themselves to seek favorable energy configurations upon drying allows the nanospheres to form a close-packed mask.[33] Then, this mask is used to pattern the substrate selectively, either as an etching or as a deposition mask. Subsequently, the colloidal crystal mask can be removed by sonication in solvent, leaving an array of ordered nanostructures on the substrate surface. Significant research has focused on trying to improve or to modify the NSL to expand fabrication capabilities for more variety and complexity of structures.[48–52] For example, shadow sphere lithography exploits sequential deposition from multiple angles to create two-dimensional arrays of multi-material optical metasurfaces.[53] Moiré nanosphere lithography can be used to fabricate a variety of complex nanostructures with moiré patterns by sequential stacking the nanosphere. The tunable multiband metasurfaces can be produced by controlling the size and the in-plane rotation angle between the two layers of the nanospheres.[54,55] Stretchable colloidal lithography can generate elliptical rings overcoming a circular geometry limitation of conventional colloidal lithography by harnessing the stretchable nature of poly(dimethylsiloxane) molds.[56] Still, new fabrication techniques that can easily and cost-effectively create control over 2D and 3D complex structures are critical to the field of nanotechnology and its practical application in electronics and biotechnology.

I.B.1 Mask Preparation and Modification

Mask preparation is a crucial first step in NSL as it determines how well ordered the final product will be.[57,58] Different strategies have been developed to improve the quality of the mask by performing the self-assembly process during solvent evaporation, dip coating, spin coating, or at air-liquid interfaces.[59–65] Self-assembly during solvent evaporation occurs by capillary forces and the quality of the lattice depends on the rate of solvent evaporation,

temperature, and humidity, all of which can affect reproducibility.[40,59,63] Dip coating involves withdrawing the substrate from a colloidal solution at a controlled pulling speed and evaporation rate.[66,67] However, the process wastes half the amount of colloidal suspension since the arrays also form on the back sides of the substrates. Spin coating shows potential for large-scale production, where the thickness and quality of the array can be optimized by fine-tuning the spin speed, colloidal concentration, wettability, and size of the nanospheres.[68–70] Self-assembly at the air-liquid interface utilizes deposition of the nanosphere monolayer on the liquid phase, which is subsequently transferred onto a substrate.[71–73] The key to transfer the close-packed monolayer successfully is to maintain constant pressure on the monolayer while withdrawing the substrate, which can be done in either a Langmuir-Blodgett setup or by forming the monolayer in a confined space, such as a Petri dish.[57,74–78] Surface modification of the nanospheres with negatively charged functional groups is typically performed to enhance their hydrophobicity, promoting close-packed assembly. [79–84]

I.B.2 Polystyrene Mask Modification

Another important aspect in NSL is modification of the PS mask. Oxygen plasma treatment can modify the shape of polystyrene beads, allowing even more possible structures to be created.[85,86] For instance, polystyrene spheres can be shrunk to create more space between neighboring spheres, or the residuals in the suspension, resulting in neck formation that can be intentionally used to create hexagonal structures.[83-85] Then, the mask annealing process is performed to ensure that the polystyrene mask stays in place during the subsequent steps.[57] This annealing can be done by simply placing the substrate with the

PS nanosphere mask on a hot plate, or by heating with an air heat gun, for a short period of time, then rapidly cooling to prevent too much annealing and melting of the PS beads.

I.B.3 Nanostructure Formation *via* Nanosphere Lithography and Current Limitations

Nanostructures can be created either by depositing materials into the spacing between the colloidal crystal mask to create two-dimensional structures (*i.e.,* dots, lines, rings, triangles) or by using the colloidal crystal mask as a silicon etching mask to create three-dimensional structures (*i.e.,* pillars, holes, needles).[57,75,90–93] Despite the success in wafer-scale fabrication of periodic nanostructures, there remain limitations for commercial use. First, achieving fine dimensional control in the sub-100 nm range relies greatly upon the reduction of defects, especially for smaller colloidal particles. More research should focus on defect-free formation of the nanosphere layer quality.[61,71,79] Second, fabrication of novel patterns/nanostructures remains inadequate, due to intrinsic limitations in colloidal self-assembly processes. Novel design strategies are needed to advance the field. In Chapter II, I demonstrated a multiple-patterning NSL technique that can fabricate fully tunable three-dimensional nanostructures.[38] The fabrication process exploits reuse of a nanosphere template for repeated etching, enabling the formation of complex structures, such as nanotubes, multilevel solid/hollow nanotowers, and 3D concentric plasmonic nanodisks/nanorings.

I.C Nanosubstrate-Mediated Intracellular Delivery of Biomolecular Cargo

I.C.1 Engineered T Cells for Cancer Immunotherapy

Cancer immunotherapy harnesses the cancer-specific immune cells to recognize and to eliminate cancer cells.[94–97] Compared to surgery, chemotherapy, and radiotherapy, cancer

immunotherapy enables a targeted therapeutic approach, resulting in higher response rates and better quality of life for patients. Among the immune cells, T cells have been demonstrated to treat a limited range of cancers successfully, such as melanoma and virus-induced lymphoma.[98] Yet, the majority of cancer cells can evolve to down-regulate immune activity, hindering T cells recognition of them.[99] One approach to enhance T cells' ability to fight cancer is to overcome these immune suppressive compounds (*i.e.,* cytotoxic T lymphocyte antigen-4 (CTLA-4) as well as programmed cell death-1 (PD-1) and its ligand PD-L1).[100,101] Another approach is to enable tumor specificity by genetically engineering T cells to insert surface receptors that can recognize tumor-associated antigens. The most well developed receptor, CD19-chimeric antigen receptor (CAR), has been used to treat patients with B cell malignancies.[95,102–108] To date, two autologous CAR-T cell therapies have been approved by the US Food and Drugs Administration (FDA) since 2017.

Generally, CAR-T cells are generated by isolating T cells from either the patient's blood, an autologous treatment, or from a healthy donor's blood, an allogenic treatment.[94] Then, the T cells are expanded, purified, and genetically modified *ex vivo* to express a CD19-CAR.[109,110] When infused back into patients, the CAR-T cells have an antigen-recognition domain that specifically binds to the tumor antigen and activates the immune system signaling, resulting in the elimination of the targeted tumor cells.[111] The CD19 CAR-T cell immunotherapy has achieved success in hematologic malignancies, but has not been as effective in treating solid tumors, partially due to low penetration ability as well as tumor microenvironments.[112] More research is needed to understand the nature of the tumor microenvironment in order to design CAR-T cell immunotherapies strategically that can achieve maximum potential for cancer treatment. [107]

I.C.2 Current Gene Delivery Strategies and their Limitations

Gene therapy is a promising approach to treat a disease at its genetic source by deleting or replacing a defective gene.[113,114] The first success in gene therapy was used in 1990 for severe combined immunodeficiency (SCID), which is caused by a single mutation in the DNA sequence coding for adenosine deaminase.[115] To date, several gene therapies have been shown to be safe and efficient ways to treat a wide-range of genetic diseases, including primary immunodeficiencies, hematological disorders, retinal dystrophy, and cancers.[116–122] Gene therapy can be done *ex vivo,* with haematopoietic stem cells (HSCs) or T lymphocytes (T cells), or *in vivo*, with hepatocytes in the liver or photoreceptors in the retina.[98,99,107,119-121] However, delivering gene-modifying materials to targets cells in a high-throughput, efficient, and safe manner remains a major challenge. There is a need to develop methods to overcome cell barriers to deliver genetic information without disrupting regulatory mechanisms. Moreover, the gene-editing cell quantity has to be large enough to be able to deliver sustainable genetic modification to treat the disease effectively.[126,127] Current standard techniques for intracellular delivery include viral vectors, electroporation, and lipofection.[124-126]

I.C.3 Viral Vectors

Viral vectors are inactivated viruses used to deliver genetic materials into cells by integrating their genetic sequence into the host.[128,131–133] Types of viral vectors include retrovirus, lentivirus, adenovirus, and hybrids.[123–125,134–142] Common challenges in using viral vectors include immunogenicity, high cost to scale up, and restricted size of the plasmid delivered(<5 kb in length).[143] Retroviruses can stably integrate into the host genome, but

have several drawbacks, including the need for cells to be actively dividing and insertional mutagenesis, where the vector inserts into nearby positions that results in off-target effects.[144–146] Lentiviruses can integrate into the genome of non-dividing cells, but do so at random positions, which is problematic as the function of the cell can be disturbed.[147,148] Adenoviruses show potential since they can be use with non-dividing cells and they do not permanently integrate into the genome.[140,149,150] However, they normally become inactive before they can reach the target cells since they are common in respiratory tract infections and most people have already developed antibodies to neutralize them.[151] Although viral vectors promise relatively high transfection efficiency, associated safety concerns hinder therapeutic applications. Ongoing research on viral vector development focuses on developing either new or hybrid vectors that will overcome the limitations of current viral vectors to increase safety and efficiency.[116,152–155]

I.C.4 Non-Viral Vectors

Even though the transfection efficiency of viral vectors is high, their use is limited due to the high cost of production, immunogenicity, and cytotoxicity.[156–158] Non-viral vectors have shown potential to overcome these concerns, but their efficiency is significantly lower. The application of non-viral vectors for gene transfer has to meet acceptable efficiency and risk before translation to clinical application.[157] In the past decades, many chemical and physical approaches have been intensely researched as alternatives. Chemical approaches focus on developing new materials to encapsulate biomolecules and modifying their surfaces not only to enhance intracellular uptake, but also to target specific cells; whereas physical methods involve creating platforms that achieve intracellular delivery of biomolecule by mechanically disrupting the cell membranes to enhance cell permeability.[159–166]

I.C.5 Chemical Carriers

Non-viral chemical systems have been studied as alternatives to overcome the biosafety concerns associated with viral systems. Research in this area has investigated creating new materials to mimic the properties of viral capsids to encapsulate and to protect biomolecules from degradation facilitating intracellular uptake.[159–161,164] A variety of systems has been commercialized such as cationic lipid (Lipofectamine), cationic polymer (ExpressFect), and hybrids of the two (Arrest-In).[130,167,168] Typically, the chemical carriers form complexes with the negatively charged phosphate group in the nucleic acids, encapsulating the plasmid. The positively charged complexes interact electrostatically with the negatively charged proteins on the cell membrane, facilitating intracellular uptake.[169] Current efforts explore how surface chemistry, molecular structures, and size affect the formation of biomolecule complexes to improve delivery efficiency.[84,159,170–172] Also, adding site-specific regions to the complex can enhance targeted delivery.[173–175]

The most common chemical carrier is based on cationic lipid, such as Lipofectamine, which is composed of cationic fatty acids that self-assemble into lipid bilayer membrane structure that encapsulates DNAs.[130,176] The interaction between the positive charge of the liposomes and negative charge of the cell membrane aids the intracellular delivery.[177,178] Liposomes have been shown to be safe alternatives to deliver genetic materials as they have low immunogenicity, are biodegradable and non-toxic, and their encapsulation protects the DNA from degrading.[179,180] However, the positive charge on their surface can lead to non-specific binding to extracellular matrix (*i.e.*, proteins, enzymes, etc.) when used *in vivo*, resulting in low transfection efficiency. [181,182]

Cationic polymer systems work similarly to the cationic lipid by forming complexes with DNA, but their surface chemistry is tunable and they are more shelf-stable compared to cationic lipids.[183,184] Typically, polymer-based systems usually consist of biodegradable polymers containing amine groups, such as polyethylenimine, chitosan, or poly(2-dimethylaminoethyl methacrylate).[84,159,160,171,185,186] The cationic polymer-DNA complexes can promote internalization of the DNA into the cells as well as protect DNA from degradation, similar to the lipid-DNA complexes.[161] However, they tend to aggregate and to precipitate in aqueous solution during synthesis, due to their positive charge.[185,187] There are efforts to increase the solubility of the complexes and cellular uptake by adding site-specific regions for targeting as well as understanding the dissociation of the complex in biological environments to develop these methods for clinical utility.[187,188]

I.C.6 Physical Delivery

Physical delivery methods utilize physical membrane disruption to deliver biomolecular cargos.[158,189,190] This strategy is an attractive option due to its potential be non-toxic and high throughput that can be universally deployed on any cell type without limitation to plasmid/cargo size.[191] Although applying or incubating naked DNA directly is a safe method, its transfection efficiency is limited, resulting in the need for development of delivery strategies.[192–194] Examples of physical methods include electroporation, hydrodynamic, ultrasound, magnetic field, or nanostructure penetration.[195–201]

Electroporation is one of the most widely used approaches to deliver a wide range of impermeable biomolecules (*i.e.,* drugs, DNA, nucleases, etc.) into target cells.[163,195,202,203] By applying electrical fields to the target cells, a potential is generated across the cell membrane.[129,204] This potential increases membrane permeability and creates transient

pores at the membrane, thereby allowing the molecules of interest to be internalized into the cytoplasm and later expressed.[157] Electroporation has been shown to be a reliable and efficient transfection method to both adherent and suspension cells.[207,209–211] However, optimization is highly critical and specific for each cell line and type of target plasmids. For example, if the parameters (*i.e.,* field strength and pulse duration) are incorrect, the cell membrane can be subjected to irreversible changes that can lead to no transfection or to cell death.[202,203,212,213]

Hydrodynamic delivery applies rapid controlled hydrodynamic pressure of DNA solutions to target tissues to enhance cell permeability.[162,196,214] The efficiency of the hydrodynamic system relies on the capillary structure, the hydrodynamic force, and the elasticity and structure of the tissues.[156,196] It has been a common method to deliver naked DNA into tissue *in vivo*.[162] However, delivering *in vivo* can trigger heart failure in patients since it creates too much excess liquid circulation in the system.[196,214] Hydrodynamic delivery has potential to be applied to suspension cells, especially CAR-T cell production, with the right apparatus and optimization.

Another interesting approach uses nanostructures to penetrate the cell membrane and to deliver cargo to cells directly.[201,215–218] Microinjection pioneered the field using physical penetration of glass micropipettes to deliver biomolecules effectively for *in vitro* fertilization applications.[219,220] Later, more researchers in this field adopted this idea and miniaturized the needles for efficient delivery and minimizing cell damage. Novel platforms for delivery include using biomolecules that dissociate from their supporting structures during penetration,[218,221] diffusion through transient holes after cells are punctured by needles,[222] or injection of the biomolecules through hollow nanostraws.[216,223] Using these

systems, siRNA, peptides, DNA, and proteins have successfully delivered biomolecular packages to hard-to-transfect cell types, such as neurons and immune cells.[217,218]

I.C.7 Nanostructure-Integrated Microfluidic System for CAR-T Cell Production

The current FDA-approved CAR-T cell therapies rely on lentiviral vectors, which are costly to produce at large scales.[224,225] The need to manufacture CAR-T cells efficiently and economically is critical for translation into clinical applications.[94] One approach is to design a system that combines the advantages from more than one intracellular delivery system to overcome the drawbacks of each system and for better overall efficiency.[226,227] Nanoparticles provide protection against DNA degradation, exhibit good storage capacity, and cause low cytotoxicity.[228,229] Nanostructures provide direct injection to deliver molecules of interest as well as the capability to create transient pores, enabling biomolecules diffusion.[218,221–223] In Chapter III, I demonstrate the use of a nanoneedle-integrated microfluidic system and DNA-encapsulated supramolecular nanoparticle for production of CAR-T cells, in both model and primary T cells. Using this platform, we can efficiently load DNA, which is tethered to the substrate, for direct injection, as well as co-flow an excess of DNA-encapsulated nanoparticles, for diffusion through transient pores that are created by the nanoneedles. This system enables continuous and sequential intracellular delivery, which provides a path for sustainable CAR-T cell production.

I.D Dissertation Overview

This dissertation is organized into four chapters and two appendices, which highlight the work I have done to develop a novel patterning technique based on nanosphere lithography and how we can use nanosphere lithography for applications fabricating devices

for gene-editing. Chapter I consists of an introduction of nanosphere lithography and background techniques used to deliver gene-editing materials. Chapter II introduces a scalable nanoscale patterning technique for fabrication of periodic 3D hierarchical nanostructures.[38] Chapter III shows how nanostructures, made from nanosphere lithography, can be utilized for intracellular delivery *via* physical membrane deformation. We demonstrate robust and high-throughput intracellular cargo delivery to suspension cells, including primary cells for CAR-T cell production. The future prospects for this work are summarized and discussed in Chapter IV. Prior to working with nanosphere lithography, my initial studies involved utilizing self-assembled monolayers as a tool to probe interactions at the molecular level. Appendix I elucidates the role of intermolecular dipole-dipole interactions of carboranethiol self-assembled monolayers on the alignment of liquid crystals.[230] Appendix II demonstrates the use of our custom-built laser-assisted scanning tunneling microscopy that enables the detection of the photoinduced charge transfer process within the molecular *p*-*n* junction of C_{60}-donor-C_{60} and its chromophore. [231]

Chapter 2 has been reformatted from the following manuscript with permission:

Xu, X.; Yang, Q.; **Wattanatorn, N.**; Zhao, C.; Jonas, S. J.; Weiss, P. S. Multiple-Patterning Nanosphere Lithography for Fabricating Periodic Three-Dimensional Hierarchical Nanostructures. *ACS Nano.* **2017**, *11*, 10384. DOI: 10.1021/acsnano.7b05472

Chapter 3 is based on a manuscript in preparation:

Wattanatorn, N.; Chiou, T.T.; Xu, X.; Mendoza, A.M.; De Oliveira, S.N.; Jonas, S.J.; Weiss, P.S. Nanosubstrate-Mediated Intracellular Delivery for High-Throughput Gene Modification. (in preparation).

Appendix A has been reformatted from the following manuscript with permission:

Schwartz; J. J.; Mendoza, A. M.; **Wattanatorn, N.**; Zhao, Y.; Nguyen, V.; Spokoyny, A. M.; Mirkin, C. A.; Baše, T.; Weiss, P. S. Surface Dipole Control of Liquid Crystal Alignment. *JACS.* **2016**, *138*, 5957. DOI: 10.1021/jacs.6b02026

Appendix B has been reformatted from the following manuscript with permission:

Wang, S; **Wattanatorn, N.**; Chiang, N.; Zhao, Y.; Kim, M.; Ma, H.; Jen, A. K.-Y.; Weiss, P. S. Photo-Induced Charge Transfer in Single-Molecular *p-n* Junctions. *J. Phys. Chem. Lett.*, **2019**, *10*, 2175. DOI: 10.1021/acs.jpclett.9b00855

References

(1) Kim, Y.-Y.; Kim, H.-J.; Jeong, J.-H.; Lee, J.; Choi, J.-H.; Jung, J.-Y.; Lee, J.-H.; Cheng, H.; Lee, K.-W.; Choi, D.-G. Facile Fabrication of Silicon Nanotube Arrays and Their Application in Lithium-Ion Batteries: Facile Fabrication of Silicon Nanotube Arrays *Adv. Eng. Mater.* **2016**, *18*, 1349–1353.

(2) Yoo, J.-K.; Kim, J.; Jung, Y. S.; Kang, K. Scalable Fabrication of Silicon Nanotubes and Their Application to Energy Storage. *Adv. Mater.* **2012**, *24*, 5452–5456.

(3) Park, M.-H.; Kim, M. G.; Joo, J.; Kim, K.; Kim, J.; Ahn, S.; Cui, Y.; Cho, J. Silicon Nanotube Battery Anodes. *Nano Lett.* **2009**, *9*, 3844–3847.

(4) Wu, H.; Chan, G.; Choi, J. W.; Ryu, I.; Yao, Y.; McDowell, M. T.; Lee, S. W.; Jackson, A.; Yang, Y.; Hu, L.; et al. Stable Cycling of Double-Walled Silicon Nanotube Battery Anodes through Solid–Electrolyte Interphase Control. *Nat. Nanotechnol.* **2012**, *7*, 310–315.

(5) Garnett, E.; Yang, P. Light Trapping in Silicon Nanowire Solar Cells. *Nano Lett.* **2010**, *10*, 1082–1087.

(6) Jeong, H.; Song, H.; Pak, Y.; Kwon, I. K.; Jo, K.; Lee, H.; Jung, G. Y. Enhanced Light Absorption of Silicon Nanotube Arrays for Organic/Inorganic Hybrid Solar Cells. *Adv. Mater.* **2014**, *26*, 3445–3450.

(7) Whitney, T. M.; Searson, P. C.; Jiang, J. S.; Chien, C. L. Fabrication and Magnetic Properties of Arrays of Metallic Nanowires. *Science* **1993**, *261*, 1316–1319.

(8) Martín, J. I.; Nogués, J.; Liu, K.; Vicent, J. L.; Schuller, I. K. Ordered Magnetic Nanostructures: Fabrication and Properties. *J. Magn. Magn. Mater.* **2003**, *256*, 449-501.

(9) Ross, M. B.; Mirkin, C. A.; Schatz, G. C. Optical Properties of One-, Two-, and Three-Dimensional Arrays of Plasmonic Nanostructures. *J. Phys. Chem. C* **2016**, *120*, 816-830.

(10) Luk'yanchuk, B.; Zheludev, N. I.; Maier, S. A.; Halas, N. J.; Nordlander, P.; Giessen, H.; Chong, C. T. The Fano Resonance in Plasmonic Nanostructures and Metamaterials. *Nat. Mater.* **2010**, *9*, 707–715.

(11) Srivastava, S. K.; Kumar, D.; Singh, P. K.; Kar, M.; Kumar, V.; Husain, M. Excellent Antireflection Properties of Vertical Silicon Nanowire Arrays. *Sol. Energy Mater. Sol. Cells* **2010**, *94*, 1506–1511.

(12) Evanoff, D. D.; Chumanov, G. Synthesis and Optical Properties of Silver Nanoparticles and Arrays. *ChemPhysChem* **2005**, *6*, 1221–1231.

(13) Wallraff, G. M.; Hinsberg, W. D. Lithographic Imaging Techniques for the Formation of Nanoscopic Features. *Chem. Rev.* **1999**, *99*, 1801–1822.

(14) Ito, T.; Okazaki, S. Pushing the Limits of Lithography. *Nature* **2000**, *406*, 1027–1031.

(15) Watt, F.; Bettiol, A. A.; Van Kan, J. A.; Teo, E. J.; Breese, M. B. H. Ion Beam Lithography And Nanofabrication: A Review. *Int. J. Nanosci.* **2005**, *04*, 269-286.

(16) Pfeiffer, H. C.; Stickel, W. PREVAIL - An e-Beam Stepper with Variable Axis Immersion Lenses. *Microelectron. Eng.* **1995**, *27*, 143–146.

(17) Berger, S. D. Projection Electron-Beam Lithography: A New Approach. *J. Vac. Sci. Technol. B Microelectron. Nanometer Struct.* **1991**, *9*, 2996.

(18) Nakayama, Y. Electron-Beam Cell Projection Lithography: A New High-Throughput Electron-Beam Direct-Writing Technology Using a Specially Tailored Si Aperture. *J. Vac. Sci. Technol. B Microelectron. Nanometer Struct.* **1990**, *8*, 1836.

(19) Xia, Y.; Whitesides, G. M. SOFT LITHOGRAPHY. *Annu. Rev. Mater. Sci.* **1998**, *28*, 153-184.

(20) Shestopalov, A. A.; Morris, C. J.; Vogen, B. N.; Hoertz, A.; Clark, R. L.; Toone, E. J. Soft-Lithographic Approach to Functionalization and Nanopatterning Oxide-Free Silicon. *Langmuir* **2011**, *27*, 6478–6485.

(21) Mullen, T. J.; Srinivasan, C.; Hohman, J. N.; Gillmor, S. D.; Shuster, M. J.; Horn, M. W.; Andrews, A. M.; Weiss, P. S. Microcontact Insertion Printing. *Appl. Phys. Lett.* **2007**, *90*, 063114.

(22) Vaish, A.; Shuster, M. J.; Cheunkar, S.; Weiss, P. S.; Andrews, A. M. Tuning Stamp Surface Energy for Soft Lithography of Polar Molecules to Fabricate Bioactive Small-Molecule Microarrays. *Small* **2011**, *7*, 1471–1479.

(23) Jackman, R.; Wilbur, J.; Whitesides, G. Fabrication of Submicrometer Features on Curved Substrates by Microcontact Printing. *Science* **1995**, *269*, 664–666.

(24) Alom Ruiz, S.; Chen, C. S. Microcontact Printing: A Tool to Pattern. *Soft Matter* **2007**, *3*, 168–177.

(25) Wilbur, J. L.; Kumar, A.; Kim, E.; Whitesides, G. M. Microfabrication by Microcontact Printing of Self-Assembled Monolayers. *Adv. Mater.* **1994**, *6*, 600–604.

(26) Love, J. C.; Estroff, L. A.; Kriebel, J. K.; Nuzzo, R. G.; Whitesides, G. M. Self-Assembled Monolayers of Thiolates on Metals as a Form of Nanotechnology. *Chem. Rev.* **2005**, *105*, 1103–1170.

(27) Liu, Y.; Goebl, J.; Yin, Y. Templated Synthesis of Nanostructured Materials. *Chem Soc Rev* **2013**, *42*, 2610–2653.

(28) Jones, M. R.; Osberg, K. D.; Macfarlane, R. J.; Langille, M. R.; Mirkin, C. A. Templated Techniques for the Synthesis and Assembly of Plasmonic Nanostructures. *Chem. Rev.* **2011**, *111*, 3736–3827.

(29) Zhang, Q.; Wang, W.; Goebl, J.; Yin, Y. Self-Templated Synthesis of Hollow Nanostructures. *Nano Today* **2009**, *4*, 494–507.

(30) Cheng, J. Y.; Mayes, A. M.; Ross, C. A. Nanostructure Engineering by Templated Self-Assembly of Block Copolymers. *Nat. Mater.* **2004**, *3*, 823–828.

(31) Shiu, J.-Y.; Kuo, C.-W.; Chen, P.; Mou, C.-Y. Fabrication of Tunable Superhydrophobic Surfaces by Nanosphere Lithography. *Chem. Mater.* **2004**, *16*, 561–564.

(32) Hulteen, J. C.; Van Duyne, R. P. Nanosphere Lithography: A Materials General Fabrication Process for Periodic Particle Array Surfaces. *J. Vac. Sci. Technol. Vac. Surf. Films* **1995**, *13*, 1553–1558.

(33) Haynes, C. L.; Van Duyne, R. P. Nanosphere Lithography: A Versatile Nanofabrication Tool for Studies of Size-Dependent Nanoparticle Optics. *J. Phys. Chem. B* **2001**, *105*, 5599–5611.

(34) Hulteen, J. C.; Treichel, D. A.; Smith, M. T.; Duval, M. L.; Jensen, T. R.; Van Duyne, R. P. Nanosphere Lithography: Size-Tunable Silver Nanoparticle and Surface Cluster Arrays. *J. Phys. Chem. B* **1999**, *103*, 3854–3863.

(35) Dameron, A. A.; Hampton, J. R.; Smith, R. K.; Mullen, T. J.; Gillmor, S. D.; Weiss, P. S. Microdisplacement Printing. *Nano Lett.* **2005**, *5*, 1834–1837.

(36) Liao, W.-S.; Cheunkar, S.; Cao, H. H.; Bednar, H. R.; Weiss, P. S.; Andrews, A. M. Subtractive Patterning via Chemical Lift-Off Lithography. *Science* **2012**, *337*, 1517-1521.

(37) Srinivasan, C.; Mullen, T. J.; Hohman, J. N.; Anderson, M. E.; Dameron, A. A.; Andrews, A. M.; Dickey, E. C.; Horn, M. W.; Weiss, P. S. Scanning Electron Microscopy of Nanoscale Chemical Patterns. *ACS Nano* **2007**, *1*, 191–201.

(38) Xu, X.; Yang, Q.; Wattanatorn, N.; Zhao, C.; Chiang, N.; Jonas, S. J.; Weiss, P. S. Multiple-Patterning Nanosphere Lithography for Fabricating Periodic Three-Dimensional Hierarchical Nanostructures. *ACS Nano* **2017**, *11*, 10384–10391.

(39) Deckman, H. W.; Dunsmuir, J. H. Natural Lithography. *Appl. Phys. Lett.* **1982**, *41*, 377-379.

(40) Fischer, U. Ch.; Zingsheim, H. P. Submicroscopic Pattern Replication with Visible Light. *J. Vac. Sci. Technol.* **1981**, *19*, 881–885.

(41) Jensen, T. R.; Malinsky, M. D.; Haynes, C. L.; Van Duyne, R. P. Nanosphere Lithography: Tunable Localized Surface Plasmon Resonance Spectra of Silver Nanoparticles. *J. Phys. Chem. B* **2000**, *104*, 10549–10556.

(42) Jensen, T. R.; Schatz, G. C.; Van Duyne, R. P. Nanosphere Lithography: Surface Plasmon Resonance Spectrum of a Periodic Array of Silver Nanoparticles by Ultraviolet−Visible Extinction Spectroscopy and Electrodynamic Modeling. *J. Phys. Chem. B* **1999**, *103*, 2394–2401.

(43) Li, L.; Zhai, T.; Zeng, H.; Fang, X.; Bando, Y.; Golberg, D. Polystyrene Sphere-Assisted One-Dimensional Nanostructure Arrays: Synthesis and Applications. *J Mater Chem* **2011**, *21*, 40–56.

(44) Li, Y.; Koshizaki, N.; Cai, W. Periodic One-Dimensional Nanostructured Arrays Based on Colloidal Templates, Applications, and Devices. *Coord. Chem. Rev.* **2011**, *255*, 357-373.

(45) Li, Y.; Cai, W.; Duan, G. Ordered Micro/Nanostructured Arrays Based on the Monolayer Colloidal Crystals †. *Chem. Mater.* **2008**, *20*, 615–624.

(46) Dewalque, J.; Cloots, R.; Dubreuil, O.; Krins, N.; Vertruyen, B.; Henrist, C. Microstructural Evolution of a TiO2 Mesoporous Single Layer Film under Calcination: Effect of Stabilization and Repeated Thermal Treatments on the Film Crystallization and Surface Area. *Thin Solid Films* **2012**, *520*, 5272–5276.

(47) Ye, X.; Qi, L. Two-Dimensionally Patterned Nanostructures Based on Monolayer Colloidal Crystals: Controllable Fabrication, Assembly, and Applications. *Nano Today* **2011**, *6*, 608–631.

(48) Lu, X.; Zhu, Y.; Cen, T.; Jiang, L. Centimeter-Scale Colloidal Crystal Belts via Robust Self-Assembly Strategy. *Langmuir* **2012**, *28*, 9341–9346.

(49) Im, H.; Bantz, K. C.; Lee, S. H.; Johnson, T. W.; Haynes, C. L.; Oh, S.-H. Self-Assembled Plasmonic Nanoring Cavity Arrays for SERS and LSPR Biosensing. *Adv. Mater.* **2013**, *25*, 2678–2685.

(50) Zhang, M.; Large, N.; Koh, A. L.; Cao, Y.; Manjavacas, A.; Sinclair, R.; Nordlander, P.; Wang, S. X. High-Density 2D Homo- and Hetero- Plasmonic Dimers with Universal Sub-10-Nm Gaps. *ACS Nano* **2015**, *9*, 9331–9339.

(51) Kim, J. J.; Li, Y.; Lee, E. J.; Cho, S. O. Fabrication of Size-Controllable Hexagonal Non-Close-Packed Colloidal Crystals and Binary Colloidal Crystals by Pyrolysis Combined with Plasma−Electron Coirradiation of Polystyrene Colloidal Monolayer. *Langmuir* **2011**, *27*, 2334–2339.

(52) Yan, W.-G.; Qi, J.-W.; Li, Z.-B.; Tian, J.-G. Fabrication and Optical Properties of Au-Coated Polystyrene Nanosphere Arrays with Controlled Gaps. *Plasmonics* **2014**, *9*, 565–571.

(53) Nemiroski, A.; Gonidec, M.; Fox, J. M.; Jean-Remy, P.; Turnage, E.; Whitesides, G. M. Engineering Shadows to Fabricate Optical Metasurfaces. *ACS Nano* **2014**, *8*, 11061-11070.

(54) Wu, Z.; Chen, K.; Menz, R.; Nagao, T.; Zheng, Y. Tunable Multiband Metasurfaces by Moiré Nanosphere Lithography. *Nanoscale* **2015**, *7*, 20391–20396.

(55) Chen, K.; Rajeeva, B. B.; Wu, Z.; Rukavina, M.; Dao, T. D.; Ishii, S.; Aono, M.; Nagao, T.; Zheng, Y. Moiré Nanosphere Lithography. *ACS Nano* **2015**, *9*, 6031–6040.

(56) Cai, Y.; Cao, Y.; Nordlander, P.; Cremer, P. S. Fabrication of Split-Rings via Stretchable Colloidal Lithography. *ACS Photonics* **2014**, *1*, 127–134.

(57) Kosiorek, A.; Kandulski, W.; Glaczynska, H.; Giersig, M. Fabrication of Nanoscale Rings, Dots, and Rods by Combining Shadow Nanosphere Lithography and Annealed Polystyrene Nanosphere Masks. *Small* **2005**, *1*, 439–444.

(58) Colson, P.; Henrist, C.; Cloots, R. Nanosphere Lithography: A Powerful Method for the Controlled Manufacturing of Nanomaterials. *J. Nanomater.* **2013**, *2013*, 1–19.

(59) Micheletto, R.; Fukuda, H.; Ohtsu, M. A Simple Method for the Production of a Two-Dimensional, Ordered Array of Small Latex Particles. *Langmuir* **1995**, *11*, 3333-3336.

(60) Kralchevsky, P. A.; Denkov, N. D. Capillary Forces and Structuring in Layers of Colloid Particles. *Curr. Opin. Colloid Interface Sci.* **2001**, *6*, 383–401.

(61) Ruan, W.; Lu, Z.; Ji, N.; Wang, C.; Zhao, B.; Zhang, J. Facile Fabrication of Large Area Polystyrene Colloidal Crystal Monolayer via Surfactant-Free Langmuir-Blodgett Technique. *Chem. Res. Chin. Univ.* **2007**, *23*, 712–714.

(62) Ge, M.; Lu, Y.; Ercius, P.; Rong, J.; Fang, X.; Mecklenburg, M.; Zhou, C. Large-Scale Fabrication, 3D Tomography, and Lithium-Ion Battery Application of Porous Silicon. *Nano Lett.* **2014**, *14*, 261–268.

(63) Denkov, N.; Velev, O.; Kralchevski, P.; Ivanov, I.; Yoshimura, H.; Nagayama, K. Mechanism of Formation of Two-Dimensional Crystals from Latex Particles on Substrates. *Langmuir* **1992**, *8*, 3183–3190.

(64) Rehg, T. J.; Higgins, G. Spin Coating of Colloidal Suspensions. *AIChE J.* **1992**, *38*, 489-501.

(65) Zhao, Y.; Marshall, J. S. Spin Coating of a Colloidal Suspension. *Phys. Fluids* **2008**, *20*, 043302.

(66) Dimitrov, A. S.; Nagayama, K. Continuous Convective Assembling of Fine Particles into Two-Dimensional Arrays on Solid Surfaces. *Langmuir* **1996**, *12*, 1303–1311.

(67) Rossi, R. C.; Tan, M. X.; Lewis, N. S. Size-Dependent Electrical Behavior of Spatially Inhomogeneous Barrier Height Regions on Silicon. *Appl. Phys. Lett.* **2000**, *77*, 2698-2700.

(68) Jiang, P.; Prasad, T.; McFarland, M. J.; Colvin, V. L. Two-Dimensional Nonclose-Packed Colloidal Crystals Formed by Spincoating. *Appl. Phys. Lett.* **2006**, *89*, 011908.

(69) Choi, J.-Y.; Alford, T. L.; Honsberg, C. B. Solvent-Controlled Spin-Coating Method for Large-Scale Area Deposition of Two-Dimensional Silica Nanosphere Assembled Layers. *Langmuir* **2014**, *30*, 5732–5738.

(70) Chen, J.; Dong, P.; Di, D.; Wang, C.; Wang, H.; Wang, J.; Wu, X. Controllable Fabrication of 2D Colloidal-Crystal Films with Polystyrene Nanospheres of Various Diameters by Spin-Coating. *Appl. Surf. Sci.* **2013**, *270*, 6–15.

(71) Retsch, M.; Zhou, Z.; Rivera, S.; Kappl, M.; Zhao, X. S.; Jonas, U.; Li, Q. Fabrication of Large-Area, Transferable Colloidal Monolayers Utilizing Self-Assembly at the Air/Water Interface. *Macromol. Chem. Phys.* **2009**, *210*, 230–241.

(72) Gao, P.; He, J.; Zhou, S.; Yang, X.; Li, S.; Sheng, J.; Wang, D.; Yu, T.; Ye, J.; Cui, Y. Large-Area Nanosphere Self-Assembly by a Micro-Propulsive Injection Method for High Throughput Periodic Surface Nanotexturing. *Nano Lett.* **2015**, *15*, 4591–4598.

(73) Yu, J.; Geng, C.; Zheng, L.; Ma, Z.; Tan, T.; Wang, X.; Yan, Q.; Shen, D. Preparation of High-Quality Colloidal Mask for Nanosphere Lithography by a Combination of Air/Water Interface Self-Assembly and Solvent Vapor Annealing. *Langmuir* **2012**, *28*, 12681–12689.

(74) Bardosova, M.; Pemble, M. E.; Povey, I. M.; Tredgold, R. H. The Langmuir-Blodgett Approach to Making Colloidal Photonic Crystals from Silica Spheres. *Adv. Mater.* **2010**, *22*, 3104–3124.

(75) Hsu, C.-M.; Connor, S. T.; Tang, M. X.; Cui, Y. Wafer-Scale Silicon Nanopillars and Nanocones by Langmuir–Blodgett Assembly and Etching. *Appl. Phys. Lett.* **2008**, *93*, 133109.

(76) Gwinner, M. C.; Koroknay, E.; Fu, L.; Patoka, P.; Kandulski, W.; Giersig, M.; Giessen, H. Periodic Large-Area Metallic Split-Ring Resonator Metamaterial Fabrication Based on Shadow Nanosphere Lithography. *Small* **2009**, *5*, 400–406.

(77) Yu, J.; Yan, Q.; Shen, D. Co-Self-Assembly of Binary Colloidal Crystals at the Air−Water Interface. *ACS Appl. Mater. Interfaces* **2010**, *2*, 1922–1926.

(78) Geng, C.; Zheng, L.; Yu, J.; Yan, Q.; Wei, T.; Wang, X.; Shen, D. Thermal Annealing of Colloidal Monolayer at the Air/Water Interface: A Facile Approach to Transferrable Colloidal Masks with Tunable Interstice Size for Nanosphere Lithography. *J. Mater. Chem.* **2012**, *22*, 22678.

(79) Burtsev, V.; Marchuk, V.; Kugaevskiy, A.; Guselnikova, O.; Elashnikov, R.; Miliutina, E.; Postnikov, P.; Svorcik, V.; Lyutakov, O. Hydrophilic/Hydrophobic Surface Modification Impact on Colloid Lithography: Schottky-like Defects, Dislocation, and Ideal Distribution. *Appl. Surf. Sci.* **2018**, *433*, 443–448.

(80) Ge, D.; Li, Y.; Yang, L.; Fan, Z.; Liu, C.; Zhang, X. Improved Self-Assembly through UV/Ozone Surface-Modification of Colloidal Spheres. *Thin Solid Films* **2011**, *519*, 5203–5207.

(81) Vlasov, Y. A.; Bo, X.-Z.; Sturm, J. C.; Norris, D. J. On-Chip Natural Assembly of Silicon Photonic Bandgap Crystals. *Nature* **2001**, *414*, 289–293.

(82) Schroden, R. C.; Al-Daous, M.; Blanford, C. F.; Stein, A. Optical Properties of Inverse Opal Photonic Crystals. *Chem. Mater.* **2002**, *14*, 3305–3315.

(83) Cai, Z.; Teng, J.; Yan, Q.; Zhao, X. S. Solvent Effect on the Self-Assembly of Colloidal Microspheres via a Horizontal Deposition Method. *Colloids Surf. Physicochem. Eng. Asp.* **2012**, *402*, 37–44.

(84) Kim, T.-H.; Jiang, H.-L.; Jere, D.; Park, I.-K.; Cho, M.-H.; Nah, J.-W.; Choi, Y.-J.; Akaike, T.; Cho, C.-S. Chemical Modification of Chitosan as a Gene Carrier in Vitro and in Vivo. *Prog. Polym. Sci.* **2007**, *32*, 726–753.

(85) Guruvenket, S.; Rao, G. M.; Komath, M.; Raichur, A. M. Plasma Surface Modification of Polystyrene and Polyethylene. *Appl. Surf. Sci.* **2004**, *236*, 278–284.

(86) Vesel, A. Modification of Polystyrene with a Highly Reactive Cold Oxygen Plasma. *Surf. Coat. Technol.* **2010**, *205*, 490–497.

(87) Yi, D. K.; Kim, D.-Y. Polymer Nanosphere Lithography: Fabrication of an Ordered Trigonal Polymeric NanostructureElectronic Supplementary Information (ESI) Available: Detailed Explanations of Fig. 2, AFM Image of Trigonal Shape after Etching and Scheme of Conventional Nanosphere Lithography. *Chem. Commun.* **2003**, No. 8, 982–983.

(88) Ellinas, K.; Smyrnakis, A.; Malainou, A.; Tserepi, A.; Gogolides, E. "Mesh-Assisted" Colloidal Lithography and Plasma Etching: A Route to Large-Area, Uniform, Ordered Nano-Pillar and Nanopost Fabrication on Versatile Substrates. *Microelectron. Eng.* **2011**, *88*, 2547–2551.

(89) Vogel, N.; Goerres, S.; Landfester, K.; Weiss, C. K. A Convenient Method to Produce Close- and Non-Close-Packed Monolayers Using Direct Assembly at the Air-Water Interface and Subsequent Plasma-Induced Size Reduction. *Macromol. Chem. Phys.* **2011**, *212*, 1719–1734.

(90) Whitney, A. V.; Myers, B. D.; Van Duyne, R. P. Sub-100 Nm Triangular Nanopores Fabricated with the Reactive Ion Etching Variant of Nanosphere Lithography and Angle-Resolved Nanosphere Lithography. *Nano Lett.* **2004**, *4*, 1507–1511.

(91) Cheung, C. L.; Nikolić, R. J.; Reinhardt, C. E.; Wang, T. F. Fabrication of Nanopillars by Nanosphere Lithography. *Nanotechnology* **2006**, *17*, 1339–1343.

(92) Wu, W.; Katsnelson, A.; Memis, O. G.; Mohseni, H. A Deep Sub-Wavelength Process for the Formation of Highly Uniform Arrays of Nanoholes and Nanopillars. *Nanotechnology* **2007**, *18*, 485302.

(93) Peng, K.; Zhang, M.; Lu, A.; Wong, N.-B.; Zhang, R.; Lee, S.-T. Ordered Silicon Nanowire Arrays via Nanosphere Lithography and Metal-Induced Etching. *Appl. Phys. Lett.* **2007**, *90*, 163123.

(94) June, C. H.; O'Connor, R. S.; Kawalekar, O. U.; Ghassemi, S.; Milone, M. C. CAR T Cell Immunotherapy for Human Cancer. *Science* **2018**, *359*, 1361–1365.

(95) Rosenberg, S. A.; Restifo, N. P. Adoptive Cell Transfer as Personalized Immunotherapy for Human Cancer. *Science* **2015**, *348*, 62–68.

(96) Rosenberg, S. A.; Yang, J. C.; Restifo, N. P. Cancer Immunotherapy: Moving beyond Current Vaccines. *Nat. Med.* **2004**, *10*, 909–915.

(97) Couzin-Frankel, J. Cancer Immunotherapy. *Science* **2013**, *342*, 1432–1433.

(98) Dudley, M. E.; Rosenberg, S. A. Adoptive-Cell-Transfer Therapy for the Treatment of Patients with Cancer. *Nat. Rev. Cancer* **2003**, *3*, 666–675.

(99) Restifo, N. P.; Marincola, F. M.; Kawakami, Y.; Taubenberger, J.; Yannelli, J. R.; Rosenberg, S. A. Loss of Functional Beta 2-Microglobulin in Metastatic Melanomas from Five Patients Receiving Immunotherapy. *J. Natl. Cancer Inst.* **1996**, *88*, 100–108.

(100) Callahan, M. K.; Wolchok, J. D.; Allison, J. P. Anti–CTLA-4 Antibody Therapy: Immune Monitoring During Clinical Development of a Novel Immunotherapy. *Semin. Oncol.* **2010**, *37*, 473–484.

(101) Zhu, Y.; Yao, S.; Chen, L. Cell Surface Signaling Molecules in the Control of Immune Responses: A Tide Model. *Immunity* **2011**, *34*, 466–478.

(102) Maude, S. L.; Frey, N.; Shaw, P. A.; Aplenc, R.; Barrett, D. M.; Bunin, N. J.; Chew, A.; Gonzalez, V. E.; Zheng, Z.; Lacey, S. F.; et al. Chimeric Antigen Receptor T Cells for Sustained Remissions in Leukemia. *N. Engl. J. Med.* **2014**, *371*, 1507–1517.

(103) Porter, D. L.; Levine, B. L.; Kalos, M.; Bagg, A.; June, C. H. Chimeric Antigen Receptor-Modified T Cells in Chronic Lymphoid Leukemia. *N. Engl. J. Med.* **2011**, *365*, 725–733.

(104) Grupp, S. A.; Kalos, M.; Barrett, D.; Aplenc, R.; Porter, D. L.; Rheingold, S. R.; Teachey, D. T.; Chew, A.; Hauck, B.; Wright, J. F.; et al. Chimeric Antigen Receptor–Modified T Cells for Acute Lymphoid Leukemia. *N. Engl. J. Med.* **2013**, *368*, 1509–1518.

(105) Davila, M. L.; Riviere, I.; Wang, X.; Bartido, S.; Park, J.; Curran, K.; Chung, S. S.; Stefanski, J.; Borquez-Ojeda, O.; Olszewska, M.; et al. Efficacy and Toxicity Management of 19-28z CAR T Cell Therapy in B Cell Acute Lymphoblastic Leukemia. *Sci. Transl. Med.* **2014**, *6*, 224ra25-224ra25.

(106) Rapoport, A. P.; Stadtmauer, E. A.; Binder-Scholl, G. K.; Goloubeva, O.; Vogl, D. T.; Lacey, S. F.; Badros, A. Z.; Garfall, A.; Weiss, B.; Finklestein, J.; et al. NY-ESO-1–Specific TCR–Engineered T Cells Mediate Sustained Antigen-Specific Antitumor Effects in Myeloma. *Nat. Med.* **2015**, *21*, 914–921.

(107) Klebanoff, C. A.; Rosenberg, S. A.; Restifo, N. P. Prospects for Gene-Engineered T Cell Immunotherapy for Solid Cancers. *Nat. Med.* **2016**, *22*, 26–36.

(108) Robbins, P. F.; Morgan, R. A.; Feldman, S. A.; Yang, J. C.; Sherry, R. M.; Dudley, M. E.; Wunderlich, J. R.; Nahvi, A. V.; Helman, L. J.; Mackall, C. L.; et al. Tumor Regression in Patients With Metastatic Synovial Cell Sarcoma and Melanoma Using Genetically Engineered Lymphocytes Reactive With NY-ESO-1. *J. Clin. Oncol.* **2011**, *29*, 917–924.

(109) Sadelain, M. CAR Therapy: The CD19 Paradigm. *J. Clin. Invest.* **2015**, *125*, 3392–3400.

(110) Kochenderfer, J. N.; Dudley, M. E.; Kassim, S. H.; Somerville, R. P. T.; Carpenter, R. O.; Stetler-Stevenson, M.; Yang, J. C.; Phan, G. Q.; Hughes, M. S.; Sherry, R. M.; et al. Chemotherapy-Refractory Diffuse Large B-Cell Lymphoma and Indolent B-Cell Malignancies Can Be Effectively Treated With Autologous T Cells Expressing an Anti-CD19 Chimeric Antigen Receptor. *J. Clin. Oncol.* **2015**, *33*, 540–549.

(111) Kochenderfer, J. N.; Rosenberg, S. A. Treating B-Cell Cancer with T Cells Expressing Anti-CD19 Chimeric Antigen Receptors. *Nat. Rev. Clin. Oncol.* **2013**, *10*, 267–276.

(112) Newick, K.; O'Brien, S.; Moon, E.; Albelda, S. M. CAR T Cell Therapy for Solid Tumors. *Annu. Rev. Med.* **2017**, *68*, 139–152.

(113) Mulligan, R. The Basic Science of Gene Therapy. *Science* **1993**, *260*, 926–932.

(114) Verma, I. M.; Naldini, L.; Kafri, T.; Miyoshi, H.; Takahashi, M.; Blömer, U.; Somia, N.; Wang, L.; Gage, F. H. Gene Therapy: Promises, Problems and Prospects. In *Genes and Resistance to Disease*; Boulyjenkov, V., Berg, K., Christen, Y., Eds.; Springer Berlin Heidelberg: Berlin, Heidelberg, 2000; pp 147–157.

(115) Blaese, R. M.; Culver, K. W.; Miller, A. D.; Carter, C. S.; Fleisher, T.; Clerici, M.; Shearer, G.; Chang, L.; Chiang, Y.; Tolstoshev, P.; et al. T Lymphocyte-Directed Gene Therapy for ADA- SCID: Initial Trial Results After 4 Years. *Science* **1995**, *270*, 475–480.

(116) Aiuti, A.; Cattaneo, F.; Galimberti, S.; Benninghoff, U.; Cassani, B.; Callegaro, L.; Scaramuzza, S.; Andolfi, G.; Mirolo, M.; Brigida, I.; et al. Gene Therapy for Immunodeficiency Due to Adenosine Deaminase Deficiency. *N. Engl. J. Med.* **2009**, *360*, 447–458.

(117) Nienhuis, A. W. Development of Gene Therapy for Blood Disorders. *Blood* **2008**, *111*, 4431–4444.

(118) Cavazzana-Calvo, M.; Fischer, A. Gene Therapy for Severe Combined Immunodeficiency: Are We There Yet? *J. Clin. Invest.* **2007**, *117*, 1456–1465.

(119) Cavazzana-Calvo, M.; Payen, E.; Negre, O.; Wang, G.; Hehir, K.; Fusil, F.; Down, J.; Denaro, M.; Brady, T.; Westerman, K.; et al. Transfusion Independence and HMGA2 Activation after Gene Therapy of Human β-Thalassaemia. *Nature* **2010**, *467*, 318-322.

(120) Al-Zaidy, S.; Rodino-Klapac, L.; Mendell, J. R. Gene Therapy for Muscular Dystrophy: Moving the Field Forward. *Pediatr. Neurol.* **2014**, *51*, 607–618.

(121) Hoffman, E. P.; Fischbeck, K. H.; Brown, R. H.; Johnson, M.; Medori, R.; Loire, J. D.; Harris, J. B.; Waterston, R.; Brooke, M.; Specht, L.; et al. Characterization of Dystrophin in Muscle-Biopsy Specimens from Patients with Duchenne's or Becker's Muscular Dystrophy. *N. Engl. J. Med.* **1988**, *318*, 1363–1368.

(122) Roth, J. A.; Cristiano, R. J. Gene Therapy for Cancer: What Have We Done and Where Are We Going? *JNCI J. Natl. Cancer Inst.* **1997**, *89*, 21–39.

(123) Cartier, N.; Hacein-Bey-Abina, S.; Bartholomae, C. C.; Veres, G.; Schmidt, M.; Kutschera, I.; Vidaud, M.; Abel, U.; Dal-Cortivo, L.; Caccavelli, L.; et al. Hematopoietic Stem Cell Gene Therapy with a Lentiviral Vector in X-Linked Adrenoleukodystrophy. *Science* **2009**, *326*, 818–823.

(124) Aiuti, A.; Biasco, L.; Scaramuzza, S.; Ferrua, F.; Cicalese, M. P.; Baricordi, C.; Dionisio, F.; Calabria, A.; Giannelli, S.; Castiello, M. C.; et al. Lentiviral Hematopoietic Stem Cell Gene Therapy in Patients with Wiskott-Aldrich Syndrome. *Science* **2013**, *341*, 1233151–1233151.

(125) Biffi, A.; Montini, E.; Lorioli, L.; Cesani, M.; Fumagalli, F.; Plati, T.; Baldoli, C.; Martino, S.; Calabria, A.; Canale, S.; et al. Lentiviral Hematopoietic Stem Cell Gene Therapy Benefits Metachromatic Leukodystrophy. *Science* **2013**, *341*, 1233158–1233158.

(126) Anderson, W. Prospects for Human Gene Therapy. *Science* **1984**, *226*, 401–409.

(127) Friedmann, T.; Roblin, R. Gene Therapy for Human Genetic Disease? *Science* **1972**, *175*, 949–955.

(128) Robbins, P. D.; Ghivizzani, S. C. Viral Vectors for Gene Therapy. *Pharmacol. Ther.* **1998**, *80*, 35–47.

(129) Rols, M.-P. Gene Delivery by Electroporation In Vitro: Mechanisms. In *Handbook of Electroporation*; Miklavčič, D., Ed.; Springer International Publishing: Cham, 2017; pp 387–401.

(130) Dalby, B. Advanced Transfection with Lipofectamine 2000 Reagent: Primary Neurons, SiRNA, and High-Throughput Applications. *Methods* **2004**, *33*, 95–103.

(131) Waehler, R.; Russell, S. J.; Curiel, D. T. Engineering Targeted Viral Vectors for Gene Therapy. *Nat. Rev. Genet.* **2007**, *8*, 573–587.

(132) Thomas, C. E.; Ehrhardt, A.; Kay, M. A. Progress and Problems with the Use of Viral Vectors for Gene Therapy. *Nat. Rev. Genet.* **2003**, *4*, 346–358.

(133) Walther, W.; Stein, U. Viral Vectors for Gene Transfer: A Review of Their Use in the Treatment of Human Diseases. *Drugs* **2000**, *60*, 249–271.

(134) Kotani, H.; Newton, P. B.; Zhang, S.; Chiang, Y. L.; Otto, E.; Weaver, L.; Blaese, R. M.; Anderson, W. F.; McGarrity, G. J. Improved Methods of Retroviral Vector Transduction and Production for Gene Therapy. *Hum. Gene Ther.* **1994**, *5*, 19–28.

(135) Hacein-Bey-Abina, S. LMO2-Associated Clonal T Cell Proliferation in Two Patients after Gene Therapy for SCID-X1. *Science* **2003**, *302*, 415–419.

(136) Huber, B. E.; Richards, C. A.; Krenitsky, T. A. Retroviral-Mediated Gene Therapy for the Treatment of Hepatocellular Carcinoma: An Innovative Approach for Cancer Therapy. *Proc. Natl. Acad. Sci.* **1991**, *88*, 8039–8043.

(137) Miller, A. D. Retrovirus Packaging Cells. *Hum. Gene Ther.* **1990**, *1*, 5–14.

(138) Yáñez-Muñoz, R. J.; Balaggan, K. S.; MacNeil, A.; Howe, S. J.; Schmidt, M.; Smith, A. J.; Buch, P.; MacLaren, R. E.; Anderson, P. N.; Barker, S. E.; et al. Effective Gene Therapy with Nonintegrating Lentiviral Vectors. *Nat. Med.* **2006**, *12*, 348–353.

(139) Marshall, E. CLINICAL TRIALS:Gene Therapy Death Prompts Review of Adenovirus Vector. *Science* **1999**, *286*, 2244–2245.

(140) Kozarsky, K. F.; Wilson, J. M. Gene Therapy: Adenovirus Vectors. *Curr. Opin. Genet. Dev.* **1993**, *3*, 499–503.

(141) Hildinger, M.; Auricchio, A.; Gao, G.; Wang, L.; Chirmule, N.; Wilson, J. M. Hybrid Vectors Based on Adeno-Associated Virus Serotypes 2 and 5 for Muscle-Directed Gene Transfer. *J. Virol.* **2001**, *75*, 6199–6203.

(142) Huang, S.; Kamihira, M. Development of Hybrid Viral Vectors for Gene Therapy. *Biotechnol. Adv.* **2013**, *31*, 208–223.

(143) Wu, Z.; Yang, H.; Colosi, P. Effect of Genome Size on AAV Vector Packaging. *Mol. Ther.* **2010**, *18*, 80–86.

(144) Devi, G. R. SiRNA-Based Approaches in Cancer Therapy. *Cancer Gene Ther.* **2006**, *13*, 819–829.

(145) Bupp, K.; Roth, M. J. Targeting a Retroviral Vector in the Absence of a Known Cell-Targeting Ligand. *Hum. Gene Ther.* **2003**, *14*, 1557–1564.

(146) Devroe, E.; Silver, P. A. Therapeutic Potential of Retroviral RNAi Vectors. *Expert Opin. Biol. Ther.* **2004**, *4*, 319–327.

(147) Naldini, L.; Blomer, U.; Gallay, P.; Ory, D.; Mulligan, R.; Gage, F. H.; Verma, I. M.; Trono, D. In Vivo Gene Delivery and Stable Transduction of Nondividing Cells by a Lentiviral Vector. *Science* **1996**, *272*, 263–267.

(148) Zufferey, R.; Nagy, D.; Mandel, R. J.; Naldini, L.; Trono, D. Multiply Attenuated Lentiviral Vector Achieves Efficient Gene Delivery in Vivo. *Nat. Biotechnol.* **1997**, *15*, 871–875.

(149) Wilson, J. M. Adenoviruses as Gene-Delivery Vehicles. *N. Engl. J. Med.* **1996**, *334*, 1185–1187.

(150) Zabner, J.; Couture, L. A.; Gregory, R. J.; Graham, S. M.; Smith, A. E.; Welsh, M. J. Adenovirus-Mediated Gene Transfer Transiently Corrects the Chloride Transport Defect in Nasal Epithelia of Patients with Cystic Fibrosis. *Cell* **1993**, *75*, 207–216.

(151) Yang, Y.; Li, Q.; Ertl, H. C.; Wilson, J. M. Cellular and Humoral Immune Responses to Viral Antigens Create Barriers to Lung-Directed Gene Therapy with Recombinant Adenoviruses. *J. Virol.* **1995**, *69*, 2004.

(152) Markowitz, D.; Goff, S.; Bank, A. A Safe Packaging Line for Gene Transfer: Separating Viral Genes on Two Different Plasmids. *J. Virol.* **1988**, *62*, 1120.

(153) Morsy, M. A.; Gu, M.; Motzel, S.; Zhao, J.; Lin, J.; Su, Q.; Allen, H.; Franlin, L.; Parks, R. J.; Graham, F. L.; et al. An Adenoviral Vector Deleted for All Viral Coding Sequences Results in Enhanced Safety and Extended Expression of a Leptin Transgene. *Proc. Natl. Acad. Sci.* **1998**, *95*, 7866–7871.

(154) Nathwani, A. C.; Reiss, U. M.; Tuddenham, E. G. D.; Rosales, C.; Chowdary, P.; McIntosh, J.; Della Peruta, M.; Lheriteau, E.; Patel, N.; Raj, D.; et al. Long-Term Safety and Efficacy of Factor IX Gene Therapy in Hemophilia B. *N. Engl. J. Med.* **2014**, *371*, 1994–2004.

(155) Kaplitt, M. G.; Feigin, A.; Tang, C.; Fitzsimons, H. L.; Mattis, P.; Lawlor, P. A.; Bland, R. J.; Young, D.; Strybing, K.; Eidelberg, D.; et al. Safety and Tolerability of Gene Therapy with an Adeno-Associated Virus (AAV) Borne GAD Gene for Parkinson's Disease: An Open Label, Phase I Trial. *The Lancet* **2007**, *369*, 2097–2105.

(156) Herweijer, H.; Wolff, J. A. Gene Therapy Progress and Prospects: Hydrodynamic Gene Delivery. *Gene Ther.* **2007**, *14*, 99–107.

(157) Davis, M. E. Non-Viral Gene Delivery Systems. *Curr. Opin. Biotechnol.* **2002**, *13*, 128-131.

(158) Mintzer, M. A.; Simanek, E. E. Nonviral Vectors for Gene Delivery. *Chem. Rev.* **2009**, *109*, 259–302.

(159) Lungwitz, U.; Breunig, M.; Blunk, T.; Göpferich, A. Polyethylenimine-Based Non-Viral Gene Delivery Systems. *Eur. J. Pharm. Biopharm.* **2005**, *60*, 247–266.

(160) Kean, T.; Roth, S.; Thanou, M. Trimethylated Chitosans as Non-Viral Gene Delivery Vectors: Cytotoxicity and Transfection Efficiency. *J. Controlled Release* **2005**, *103*, 643–653.

(161) Thomas, M.; Klibanov, A. M. Non-Viral Gene Therapy: Polycation-Mediated DNA Delivery. *Appl. Microbiol. Biotechnol.* **2003**, *62*, 27–34.

(162) Liu, F.; Song, Y. K.; Liu, D. Hydrodynamics-Based Transfection in Animals by Systemic Administration of Plasmid DNA. *Gene Ther.* **1999**, *6*, 1258–1266.

(163) Aihara, H.; Miyazaki, J. Gene Transfer into Muscle by Electroporation in Vivo. *Nat. Biotechnol.* **1998**, *16*, 867–870.

(164) Khalil, I. A. Uptake Pathways and Subsequent Intracellular Trafficking in Nonviral Gene Delivery. *Pharmacol. Rev.* **2006**, *58*, 32–45.

(165) Lai, S. K.; Wang, Y.-Y.; Hanes, J. Mucus-Penetrating Nanoparticles for Drug and Gene Delivery to Mucosal Tissues. *Adv. Drug Deliv. Rev.* **2009**, *61*, 158–171.

(166) Goldberg, M.; Langer, R.; Jia, X. Nanostructured Materials for Applications in Drug Delivery and Tissue Engineering. *J. Biomater. Sci. Polym. Ed.* **2007**, *18*, 241–268.

(167) Yamano, S.; Dai, J.; Moursi, A. M. Comparison of Transfection Efficiency of Nonviral Gene Transfer Reagents. *Mol. Biotechnol.* **2010**, *46*, 287–300.

(168) Liang, X.; Potter, J.; Kumar, S.; Zou, Y.; Quintanilla, R.; Sridharan, M.; Carte, J.; Chen, W.; Roark, N.; Ranganathan, S.; et al. Rapid and Highly Efficient Mammalian Cell Engineering via Cas9 Protein Transfection. *J. Biotechnol.* **2015**, *208*, 44–53.

(169) Jin, L.; Zeng, X.; Liu, M.; Deng, Y.; He, N. Current Progress in Gene Delivery Technology Based on Chemical Methods and Nano-Carriers. *Theranostics* **2014**, *4*, 240–255.

(170) Luten, J.; van Nostrum, C. F.; De Smedt, S. C.; Hennink, W. E. Biodegradable Polymers as Non-Viral Carriers for Plasmid DNA Delivery. *J. Controlled Release* **2008**, *126*, 97-110.

(171) Siu, Y. S.; Li, L.; Leung, M. F.; Lee, K. L. D.; Li, P. Polyethylenimine-Based Amphiphilic Core–Shell Nanoparticles: Study of Gene Delivery and Intracellular Trafficking. *Biointerphases* **2012**, *7*, 16.

(172) Iwashita, S.; Hiramatsu, Y.; Otani, T.; Amano, C.; Hirai, M.; Oie, K.; Yuba, E.; Kono, K.; Miyamoto, M.; Igarashi, K. Polyamidoamine Dendron-Bearing Lipid Assemblies: Their Morphologies and Gene Transfection Ability. *J. Biomater. Appl.* **2012**, *27*, 445-456.

(173) Huang, R.-Q.; Qu, Y.-H.; Ke, W.-L.; Zhu, J.-H.; Pei, Y.-Y.; Jiang, C. Efficient Gene Delivery Targeted to the Brain Using a Transferrin-Conjugated Polyethyleneglycol-Modified Polyamidoamine Dendrimer. *FASEB J.* **2007**, *21*, 1117–1125.

(174) Han, L.; Huang, R.; Li, J.; Liu, S.; Huang, S.; Jiang, C. Plasmid PORF-HTRAIL and Doxorubicin Co-Delivery Targeting to Tumor Using Peptide-Conjugated Polyamidoamine Dendrimer. *Biomaterials* **2011**, *32*, 1242–1252.

(175) Zhang, Q.; Chen, S.; Zhuo, R.-X.; Zhang, X.-Z.; Cheng, S.-X. Self-Assembled Terplexes for Targeted Gene Delivery with Improved Transfection. *Bioconjug. Chem.* **2010**, *21*, 2086–2092.

(176) Tabar, M. S.; Hesaraki, M.; Esfandiari, F.; Samani, F. S.; Vakilian, H.; Baharvand, H. Evaluating Electroporation and Lipofectamine Approaches for Transient and Stable Transgene Expressions in Human Fibroblasts and Embryonic Stem Cells. *Cell J Yakhteh* **2017**, No. 3.

(177) Liu, Y.; Mounkes, L. C.; Liggitt, H. D.; Brown, C. S.; Solodin, I.; Heath, T. D.; Debs, R. J. Factors Influencing the Efficiency of Cationic Liposome-Mediated Intravenous Gene Delivery. *Nat. Biotechnol.* **1997**, *15*, 167–173.

(178) Gao, X.; Huang, L. Potentiation of Cationic Liposome-Mediated Gene Delivery by Polycations †. *Biochemistry* **1996**, *35*, 1027–1036.

(179) Porteous, D.; Dorin, J.; McLachlan, G.; Davidson-Smith, H.; Davidson, H.; Stevenson, B.; Carothers, A.; Wallace, W.; Moralee, S.; Hoenes, C.; et al. Evidence for Safety and Efficacy of DOTAP Cationic Liposome Mediated CFTR Gene Transfer to the Nasal Epithelium of Patients with Cystic Fibrosis. *Gene Ther.* **1997**, *4*, 210–218.

(180) Song, Y. K.; Liu, F.; Chu, S.; Liu, D. Characterization of Cationic Liposome-Mediated Gene Transfer *In Vivo* by Intravenous Administration. *Hum. Gene Ther.* **1997**, *8*, 1585–1594.

(181) Karmali, P. P.; Chaudhuri, A. Cationic Liposomes as Non-Viral Carriers of Gene Medicines: Resolved Issues, Open Questions, and Future Promises. *Med. Res. Rev.* **2007**, *27*, 696–722.

(182) Wasungu, L.; Hoekstra, D. Cationic Lipids, Lipoplexes and Intracellular Delivery of Genes. *J. Controlled Release* **2006**, *116*, 255–264.

(183) De Smedt, S. C.; Demeester, J.; Hennink, W. E. Cationic Polymer Based Gene Delivery Systems. *Pharm. Res.* **2000**, *17*, 113–126.

(184) Liu, Z.; Zhang, Z.; Zhou, C.; Jiao, Y. Hydrophobic Modifications of Cationic Polymers for Gene Delivery. *Prog. Polym. Sci.* **2010**, *35*, 1144–1162.

(185) Kircheis, R.; Wightman, L.; Wagner, E. Design and Gene Delivery Activity of Modified Polyethylenimines. *Adv. Drug Deliv. Rev.* **2001**, *53*, 341–358.

(186) You, Y.-Z.; Manickam, D. S.; Zhou, Q.-H.; Oupický, D. Reducible Poly(2-Dimethylaminoethyl Methacrylate): Synthesis, Cytotoxicity, and Gene Delivery Activity. *J. Controlled Release* **2007**, *122*, 217–225.

(187) Park, T.; Jeong, J.; Kim, S. Current Status of Polymeric Gene Delivery Systems☆. *Adv. Drug Deliv. Rev.* **2006**, *58*, 467–486.

(188) Lv, H.; Zhang, S.; Wang, B.; Cui, S.; Yan, J. Toxicity of Cationic Lipids and Cationic Polymers in Gene Delivery. *J. Controlled Release* **2006**, *114*, 100–109.

(189) Mehierhumbert, S.; Guy, R. Physical Methods for Gene Transfer: Improving the Kinetics of Gene Delivery into Cells. *Adv. Drug Deliv. Rev.* **2005**, *57*, 733–753.

(190) Mellott, A. J.; Forrest, M. L.; Detamore, M. S. Physical Non-Viral Gene Delivery Methods for Tissue Engineering. *Ann. Biomed. Eng.* **2013**, *41*, 446–468.

(191) Nayerossadat, N.; Ali, P.; Maedeh, T. Viral and Nonviral Delivery Systems for Gene Delivery. *Adv. Biomed. Res.* **2012**, *1*, 27.

(192) Herweijer, H.; Wolff, J. A. Progress and Prospects: Naked DNA Gene Transfer and Therapy. *Gene Ther.* **2003**, *10*, 453–458.

(193) Luo, D.; Saltzman, W. M. Synthetic DNA Delivery Systems. *Nat. Biotechnol.* **2000**, *18*, 33–37.

(194) Wolff, J. A.; Budker, V. The Mechanism of Naked DNA Uptake and Expression. In *Advances in Genetics*; Elsevier, 2005; Vol. 54, pp 1–20.

(195) Yarmush, M. L.; Golberg, A.; Serša, G.; Kotnik, T.; Miklavčič, D. Electroporation-Based Technologies for Medicine: Principles, Applications, and Challenges. *Annu. Rev. Biomed. Eng.* **2014**, *16*, 295–320.

(196) Suda, T.; Liu, D. Hydrodynamic Gene Delivery: Its Principles and Applications. *Mol. Ther.* **2007**, *15*, 2063–2069.

(197) Ferrara, K.; Pollard, R.; Borden, M. Ultrasound Microbubble Contrast Agents: Fundamentals and Application to Gene and Drug Delivery. *Annu. Rev. Biomed. Eng.* **2007**, *9*, 415–447.

(198) Scherer, F.; Anton, M.; Schillinger, U.; Henke, J.; Bergemann, C.; Krüger, A.; Gänsbacher, B.; Plank, C. Magnetofection: Enhancing and Targeting Gene Delivery by Magnetic Force in Vitro and in Vivo. *Gene Ther.* **2002**, *9*, 102–109.

(199) Dobson, J. Gene Therapy Progress and Prospects: Magnetic Nanoparticle-Based Gene Delivery. *Gene Ther.* **2006**, *13*, 283–287.

(200) Chabri, F.; Bouris, K.; Jones, T.; Barrow, D.; Hann, A.; Allender, C.; Brain, K.; Birchall, J. Microfabricated Silicon Microneedles for Nonviral Cutaneous Gene Delivery. *Br. J. Dermatol.* **2004**, *150*, 869–877.

(201) Kim, W.; Ng, J. K.; Kunitake, M. E.; Conklin, B. R.; Yang, P. Interfacing Silicon Nanowires with Mammalian Cells. *JACS.* **2007**, *129*, 7228–7229.

(202) Meaking, W. S.; Edgerton, J.; Wharton, C. W.; Meldrum, R. A. Electroporation-Induced Damage in Mammalian Cell DNA. *Biochim. Biophys. Acta BBA - Gene Struct. Expr.* **1995**, *1264*, 357–362.

(203) Neumann, E. The Relaxation Hysteresis of Membrane Electroporation. In *Electroporation and Electrofusion in Cell Biology*; Neumann, E., Sowers, A. E., Jordan, C. A., Eds.; Springer US: Boston, MA, 1989; pp 61–82.

(204) Zaharoff, D. A.; Henshaw, J. W.; Mossop, B.; Yuan, F. Mechanistic Analysis of Electroporation-Induced Cellular Uptake of Macromolecules. *Exp. Biol. Med.* **2008**, *233*, 94–105.

(205) Golzio, M.; Teissie, J.; Rols, M.-P. Direct Visualization at the Single-Cell Level of Electrically Mediated Gene Delivery. *Proc. Natl. Acad. Sci.* **2002**, *99*, 1292–1297.

(206) Teissie, J.; Golzio, M.; Rols, M. P. Mechanisms of Cell Membrane Electropermeabilization: A Minireview of Our Present (Lack of ?) Knowledge. *Biochim. Biophys. Acta BBA - Gen. Subj.* **2005**, *1724*, 270–280.

(207) Boukany, P. E.; Morss, A.; Liao, W.; Henslee, B.; Jung, H.; Zhang, X.; Yu, B.; Wang, X.; Wu, Y.; Li, L.; et al. Nanochannel Electroporation Delivers Precise Amounts of Biomolecules into Living Cells. *Nat. Nanotechnol.* **2011**, *6*, 747–754.

(208) Kandušer, M.; Šentjurc, M.; Miklavčič, D. Cell Membrane Fluidity Related to Electroporation and Resealing. *Eur. Biophys. J.* **2006**, *35*, 196–204.

(209) Boukany, P. E.; Wu, Y.; Zhao, X.; Kwak, K. J.; Glazer, P. J.; Leong, K.; Lee, L. J. Nonendocytic Delivery of Lipoplex Nanoparticles into Living Cells Using Nanochannel Electroporation. *Adv. Healthc. Mater.* **2014**, *3*, 682–689.

(210) Zhao, Y.; Zheng, Z.; Cohen, C. J.; Gattinoni, L.; Palmer, D. C.; Restifo, N. P.; Rosenberg, S. A.; Morgan, R. A. High-Efficiency Transfection of Primary Human and Mouse T Lymphocytes Using RNA Electroporation. *Mol. Ther.* **2006**, *13*, 151–159.

(211) Jordan, E. T.; Collins, M.; Terefe, J.; Ugozzoli, L.; Rubio, T. Optimizing Electroporation Conditions in Primary and Other Difficult-to-Transfect Cells. *J. Biomol. Tech. JBT* **2008**, *19*, 328–334.

(212) Danfelter, M.; Engström, P.; Persson, B. R. R.; Salford, L. G. Effect of High Voltage Pulses on Survival of Chinese Hamster V79 Lung Fibroblast Cells. *Bioelectrochem. Bioenerg.* **1998**, *47*, 97–101.

(213) Hamilton, W.; Sale, A. Effects of High Electric Fields on MicroorganismsII. Mechanism of Action of the Lethal Effect. *Biochim. Biophys. Acta BBA - Gen. Subj.* **1967**, *148*, 789–800.

(214) Zhang, G.; Gao, X.; Song, Y. K.; Vollmer, R.; Stolz, D. B.; Gasiorowski, J. Z.; Dean, D. A.; Liu, D. Hydroporation as the Mechanism of Hydrodynamic Delivery. *Gene Ther.* **2004**, *11*, 675–682.

(215) Salem, A. K.; Searson, P. C.; Leong, K. W. Multifunctional Nanorods for Gene Delivery. *Nat. Mater.* **2003**, *2*, 668–671.

(216) Xie, X.; Xu, A. M.; Leal-Ortiz, S.; Cao, Y.; Garner, C. C.; Melosh, N. A. Nanostraw-Electroporation System for Highly Efficient Intracellular Delivery and Transfection. *ACS Nano* **2013**, *7*, 4351–4358.

(217) Shalek, A. K.; Gaublomme, J. T.; Wang, L.; Yosef, N.; Chevrier, N.; Andersen, M. S.; Robinson, J. T.; Pochet, N.; Neuberg, D.; Gertner, R. S.; et al. Nanowire-Mediated Delivery Enables Functional Interrogation of Primary Immune Cells: Application to the Analysis of Chronic Lymphocytic Leukemia. *Nano Lett.* **2012**, *12*, 6498–6504.

(218) Shalek, A. K.; Robinson, J. T.; Karp, E. S.; Lee, J. S.; Ahn, D.-R.; Yoon, M.-H.; Sutton, A.; Jorgolli, M.; Gertner, R. S.; Gujral, T. S.; et al. Vertical Silicon Nanowires as a Universal Platform for Delivering Biomolecules into Living Cells. *Proc. Natl. Acad. Sci.* **2010**, *107*, 1870–1875.

(219) Gordon, J. W.; Scangos, G. A.; Plotkin, D. J.; Barbosa, J. A.; Ruddle, F. H. Genetic Transformation of Mouse Embryos by Microinjection of Purified DNA. *Proc. Natl. Acad. Sci.* **1980**, *77*, 7380–7384.

(220) Chourrout, D.; Guyomard, R.; Houdebine, L.-M. High Efficiency Gene Transfer in Rainbow Trout (Salmo Gairdneri Rich.) by Microinjection into Egg Cytoplasm. *Aquaculture* **1986**, *51*, 143–150.

(221) McKnight, T. E.; Melechko, A. V.; Griffin, G. D.; Guillorn, M. A.; Merkulov, V. I.; Serna, F.; Hensley, D. K.; Doktycz, M. J.; Lowndes, D. H.; Simpson, M. L. Intracellular Integration of Synthetic Nanostructures with Viable Cells for Controlled Biochemical Manipulation. *Nanotechnology* **2003**, *14*, 551–556.

(222) Wang, Y.; Yang, Y.; Yan, L.; Kwok, S. Y.; Li, W.; Wang, Z.; Zhu, X.; Zhu, G.; Zhang, W.; Chen, X.; et al. Poking Cells for Efficient Vector-Free Intracellular Delivery. *Nat. Commun.* **2014**, *5*, 4466.

(223) VanDersarl, J. J.; Xu, A. M.; Melosh, N. A. Nanostraws for Direct Fluidic Intracellular Access. *Nano Lett.* **2012**, *12*, 3881–3886.

(224) Mullard, A. FDA Approves First CAR T Therapy. *Nat. Rev. Drug Discov.* **2017**, *16*, 669-669.

(225) Mullard, A. Second Anticancer CAR T Therapy Receives FDA Approval. *Nat. Rev. Drug Discov.* **2017**, *16*, 818–818.

(226) Yin, H.; Song, C.-Q.; Dorkin, J. R.; Zhu, L. J.; Li, Y.; Wu, Q.; Park, A.; Yang, J.; Suresh, S.; Bizhanova, A.; et al. Therapeutic Genome Editing by Combined Viral and Non-Viral Delivery of Crispr System Components in Vivo. *Nat. Biotechnol.* **2016**, *34*, 328–333.

(227) Gotwals, P.; Cameron, S.; Cipolletta, D.; Cremasco, V.; Crystal, A.; Hewes, B.; Mueller, B.; Quaratino, S.; Sabatos-Peyton, C.; Petruzzelli, L.; et al. Prospects for Combining Targeted and Conventional Cancer Therapy with Immunotherapy. *Nat. Rev. Cancer* **2017**, *17*, 286–301.

(228) Suk, J. S.; Xu, Q.; Kim, N.; Hanes, J.; Ensign, L. M. PEGylation as a Strategy for Improving Nanoparticle-Based Drug and Gene Delivery. *Adv. Drug Deliv. Rev.* **2016**, *99*, 28–51.

(229) Blanco, E.; Shen, H.; Ferrari, M. Principles of Nanoparticle Design for Overcoming Biological Barriers to Drug Delivery. *Nat. Biotechnol.* **2015**, *33*, 941–951.

(230) Schwartz, J. J.; Mendoza, A. M.; Wattanatorn, N.; Zhao, Y.; Nguyen, V. T.; Spokoyny, A. M.; Mirkin, C. A.; Baše, T.; Weiss, P. S. Surface Dipole Control of Liquid Crystal Alignment. *JACS.* **2016**, *138*, 5957–5967.

(231) Wang, S.; Wattanatorn, N.; Chiang, N.; Zhao, Y.; Kim, M.; Ma, H.; Jen, A. K.-Y.; Weiss, P. S. Photoinduced Charge Transfer in Single-Molecule *p*–*n* Junctions. *J. Phys. Chem. Lett.* **2019**, *10*, 2175–2181.

CHAPTER II

Multiple-Patterning Nanosphere Lithography for Fabricating Periodic Three-Dimensional Hierarchical Nanostructures Polymer-Pen Chemical Lift-Off Lithography

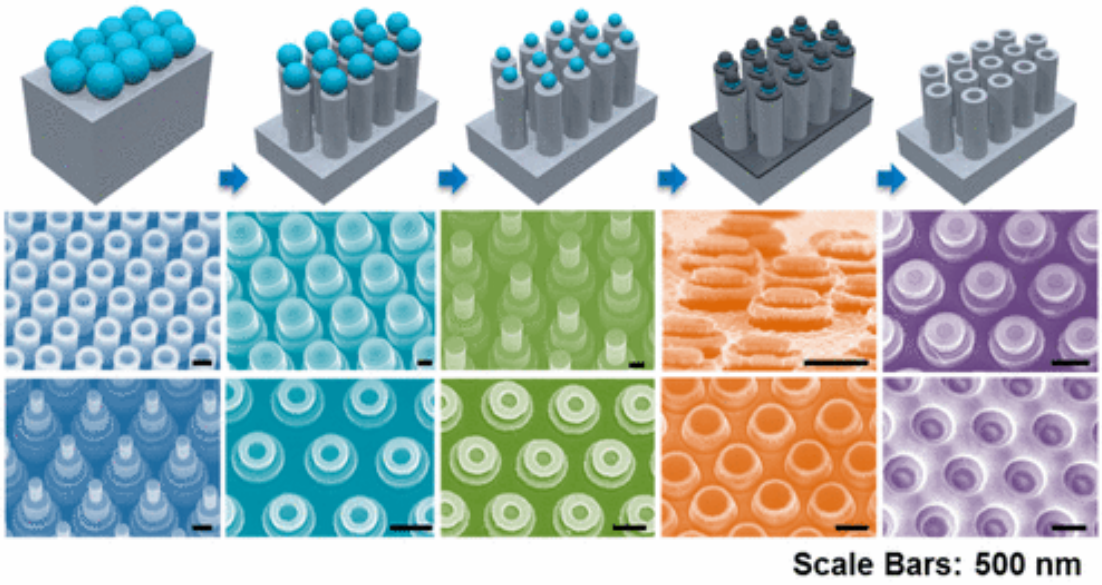

The information in this chapter was published in
ACS Nano. **2017**, *11*, 10384-10391
and is reproduced here.[1]

Authors: Xiaobin Xu, Qing Yang, Natcha Wattanatorn, Chuanzhen Zhao, Naihao Chiang, Steven J. Jonas, and Paul S. Weiss

II.A. Introduction

Periodic semiconductor nanostructures, such as pyramids, holes, wires, pillars, tubes, and cones are increasingly applied in the design of solar cells, biosensors, biomaterials, and drug delivery systems due to their superior optical/electrical properties, biocompatibility, and mechanical properties.[2–11] In particular, periodic single-crystalline silicon (Si) nanotubes[12] assembled via electron-beam lithography and nanoimprint lithography demonstrate better light conversion efficiency than other structures in hybrid solar cells, while their biocompatibility[13] and tubular structures also suggest their tantalizing potential as tools to enable improved studies of cellular mechanics,[14–16] circulating tumor cell capture/release,[17] and intracellular biochemical delivery.[18,19] However, despite this interest and their broad applicability, the deployment of periodic Si-nanotube-based devices with controlled dimensions has been limited by the lack of simple and scalable fabrication approaches for these structures.

Current strategies for the fabrication of periodic Si nanostructures, including nanopillars, nanocones, and nanoholes, involve nanosphere lithography,[20–26] because of its low cost, simplicity, and high throughput compared to conventional nanolithographic methods including electron-beam lithography and focused ion-beam milling. Nanosphere lithography employs periodic arrays of self-assembled close-packed mono/bilayer nanospheres (e.g., polystyrene, SiO_2, and others) as masks to pattern underlying substrate materials,[20] However, the fabrication of periodic Si nanotubes with precise dimensional control over large areas remains challenging due primarily to the nanosphere template being used only once during processing. This “one-time use” approach restricts traditional nanosphere lithography techniques in that only the outer diameter of Si nanotubes can be

defined fully. For example, previous attempts to generate nanoring-like masks for Si nanotube fabrication lacked suitable control over dimensions (such as tube thickness), quality, and reproducibility.

In this work, we propose and demonstrate a nanosphere lithography strategy named multiple-patterning nanosphere lithography (MP-NSL), which circumvents the limitations of traditional one-time use methods by adopting a multiple use template concept. The MP-NSL method achieves wafer-scale fabrication of periodic Si nanotubes while enabling independent control over all structural dimensions during fabrication including inner/outer tube diameters, heights, hole-depths, and pitches. To our knowledge, this degree of versatility and precision has not previously been reported for structures prepared via nanosphere lithography. Moreover, our MP-NSL technique represents a powerful three-dimensional (3D) nanolithographic tool for high-throughput fabrication of periodic hierarchical nanoarchitectures, enabling the assembly of multilevel solid/hollow Si nanotowers and 3D concentric plasmonic nanodisk/nanorings.

II.B. Results and Discussion

The process for fabricating periodic Si nanotubes by MP-NSL is illustrated schematically in **Figure II.1A** with associated scanning electron microscopy (SEM) images of the products from key steps shown in **Figure II.1B-G**. We fabricated a variety of Si nanotube arrays with different parameters: pitches (400 nm to 2 μm), outer heights (100 nm to 6 μm), inner heights (100 nm to 2 μm), outer diameters (220 nm to 1.3 μm), inner diameters (130 to 1050 nm), and tube thicknesses (sub-50 to 500 nm). Representative SEM images of a selection of Si nanotubes are depicted in **Figure II.2**. In addition, SEM images of

large area, well-ordered nanosphere templates and Si nanotube arrays with the corresponding Fourier transform patterns are shown in **Figure II.S1,S2**.

The template for MP-NSL consists of a monolayer of polystyrene nanospheres, which is assembled by slowly distributing an aqueous dispersion of the nanospheres drop cast onto a tilted glass slide, as reported elsewhere.[21] The monolayer is then transferred to a 2 cm × 2 cm Si substrate underneath the water/air interface by gently removing the liquid. Note that the pitch of the final Si nanotube arrays is determined by the original diameters of the polystyrene nanosphere template, which can be tailored from several hundred nanometers to several microns depending on their original size. Here, we specifically chose polystyrene nanospheres with diameters of 400 nm, 600 nm, 900 nm, 1 μm, and 2 μm as examples. The assembly of the nanosphere template is highly scalable such that one can easily reach the wafer scale manually and can conceivably reach the wafer scale manually and can conceivably reach the square meter scale using automated nanosphere dispensing systems.[27]

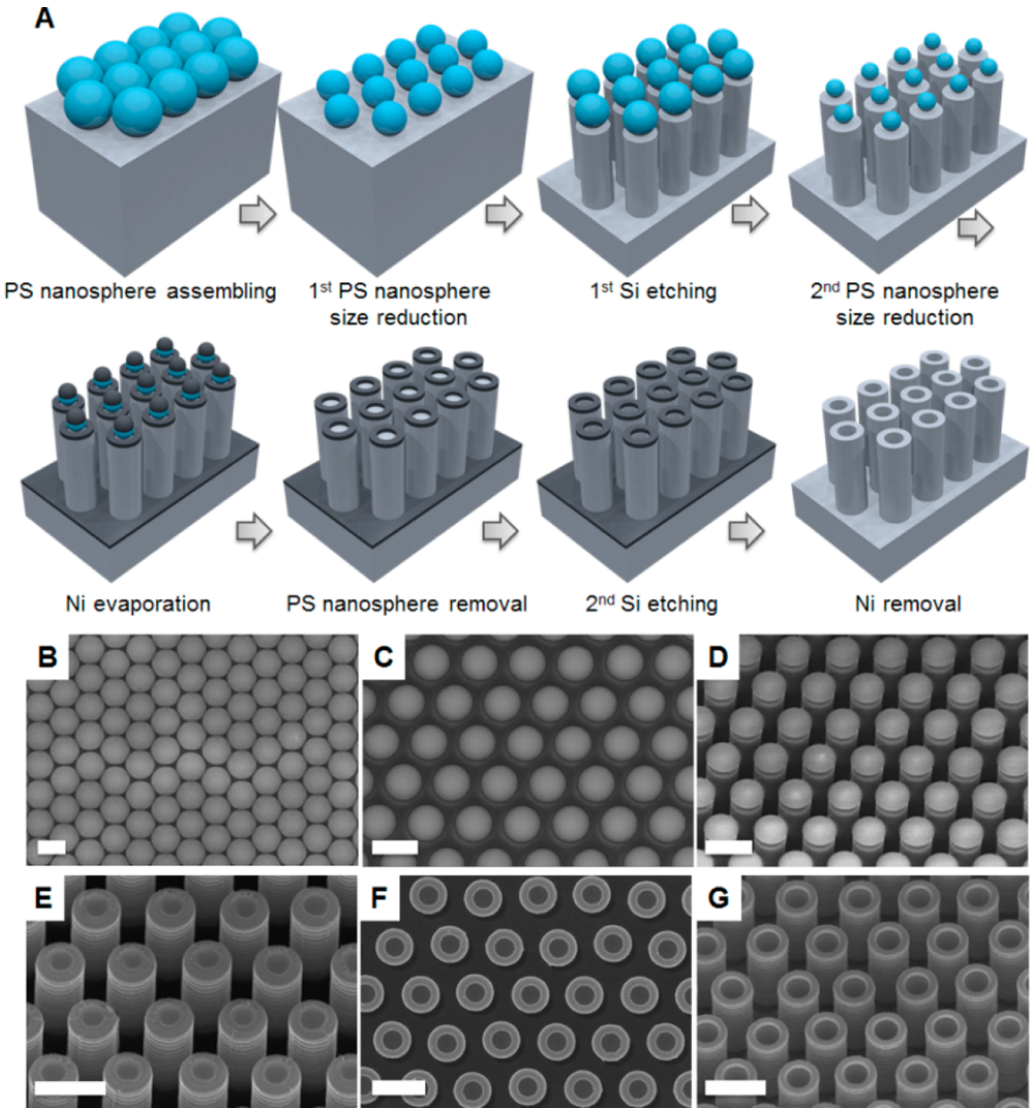

Figure II.1. Self-aligned multiple-patterning nanosphere lithography (MP-NSL) for Si nanotube arrays. (A) A schematic illustration of the process. Step 1: A monolayer of close-packed polystyrene (PS) nanospheres is formed at a water/air interface, then transferred onto a Si wafer. The size of the nanospheres defines the ultimate pitches (p) of the Si nanotubes. Step 2: Oxygen plasma RIE reduces the sphere size and defines the outer diameters (do) of Si nanotubes. Step 3: Deep reactive ion etching (DRIE) etches Si into nanopillars by using the nanospheres as masks. The outer heights (h_o) of Si nanotubes are controlled by the etch time. Step 4: A second oxygen plasma RIE further reduces the sizes of polymer nanoparticles and defines the inner diameters (d_i) of Si nanotubes. Step 5: Ni is deposited to form Ni nanorings on the Si nanopillars, and it functions as a DRIE mask. Step 6: Polystyrene nanoparticles are removed by 10 min oxygen plasma etching to expose the center part of the Si nanopillars. Step 7: DRIE is performed again to etch holes and to define the hole depth (h_i). Step 8: Ni is removed by HCl, and pristine Si nanotube arrays are obtained. Scanning electron microscope (SEM) images of key intermediates: (B) monolayer of closed-packed polystyrene nanospheres (diameter: 1 μm) formed on a Si wafer;

(C) polystyrene nanoparticles on Si wafer after first size reduction; (D) polystyrene nanoparticles on top of periodic Si nanopillar arrays; (E) second size reduction of polystyrene nanoparticles by oxygen plasma (step 4); and (F) Ni nanorings on top of Si nanopillars. The region displayed as dark is Si and the region displayed as bright is Ni. (G) Etching of the inner regions by DRIE to form Si nanotubes (step 7). Images (D, E, G) were taken at a tilt of 30°. Scale bars: 1 μm.

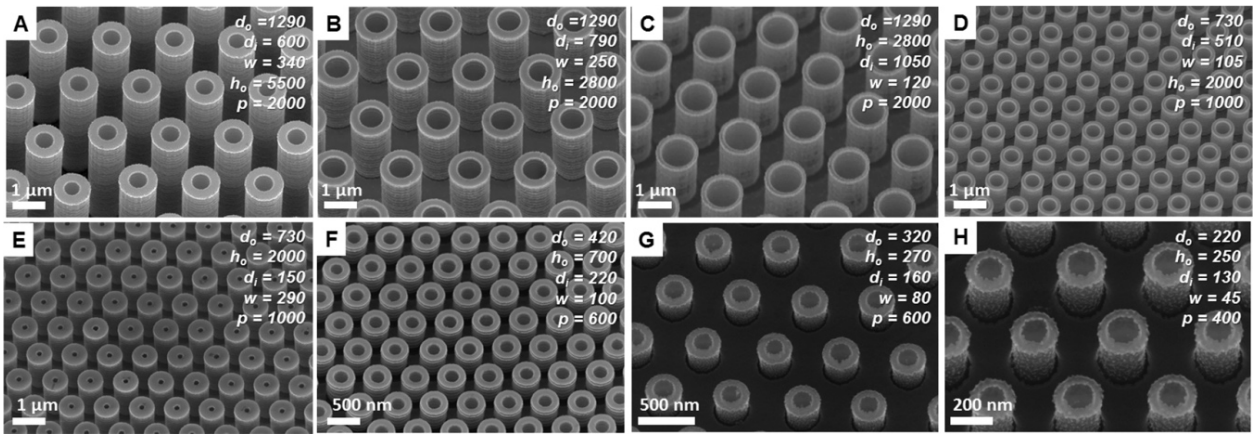

Figure II.2. (A–H) Scanning electron micrographs of representative periodic Si nanotube arrays with different parameters in nm: pitch (p), outer diameter (d_o), inner diameter (d_i), sidewall thickness ($w = (d_o - d_i)/2$), and outer height (h_o). Images were recorded at a tilt of 30°. (Units: nm).

Next, the diameters of the polystyrene nanospheres are configured via oxygen plasma reactive ion etching (RIE) to define the outer diameter (d_o) of the Si nanotubes. By controlling the oxygen plasma RIE time, one can tailor the nanosphere diameter precisely, without changing the pitch. For instance, a 4 min oxygen plasma RIE can uniformly and precisely etch close-packed polystyrene spheres of 1 μm diameter into ~820 nm diameter nanospheres with identical spacings of ~180 nm, **Figure II.1C**. As illustrated in **Figure II.2D** and **Table II.1**, the oxygen plasma RIE time and the diameters of polystyrene nanospheres correlate closely, and the results are highly reproducible. The diameters of the nanospheres notably decrease faster with increasing oxygen plasma RIE time due to the polymer nanoparticles becoming flatter with a more oblate ellipsoid shape (**Figure II.S4**).[28]

pitch = 1 μm		pitch = 2 μm	
etch time	d_0	etch time	d_0
2.5 min	910 ± 4 nm	4 min	1860 ± 9 nm
3 min	900 ± 4 nm	7 min	1630 ± 8 nm
3.5 min	860 ± 6 nm	10 min	1350 ± 10 nm
4 min	820 ± 5 nm	13 min	1160 ± 9 nm
5 min	760 ± 7 nm	15 min	800 ± 10 nm
6 min	610 ± 7 nm	16 min	740 ± 8 nm
7 min	480 ± 5 nm		
8 min	330 ± 6 nm		

Table II.1. Controlling Size Reduction of Polystyrene Nanospheres by Oxygen Plasma RIE

Note that enhancing the adhesion between the polystyrene nanospheres and the underlying Si substrate before dry etching helps to prevent random tilting of the etched polymer nanoparticles, which could lead to asymmetries in the final pillar/nanotube arrays (**Figure II.S5**). The nanospheres were coupled to the Si substrate after the initial oxygen RIE step by heating briefly to 120 °C for ~30 s. This treatment does not result in noticeable lateral deformation, but appears to fix the etched polymer nanoparticles to prevent moving or tilting during the subsequent processes.

Methods for etching Si involve either wet-etching strategies such as metal-assisted chemical etching[29] or dry-etching approaches such as RIE.[10] Here, we chose a dry etching technique, specifically deep reactive ion etching (DRIE), due to its capability for anisotropic etching, high reproducibility, and nontoxicity. The outer heights (h_o) and inner hole-depths (h_i) of the Si nanotubes are controlled by the DRIE time. Specifically, DRIE via the Bosch process, which consists of multiple cycles of passivation and etching, was applied to achieve high-aspect-ratio nanopillars. The alternating cycles of passivation and etching in the Bosch

process protect the sidewalls of nanostructures from being etched laterally over large depths. **Figure II.1D** illustrates a typical array of high-aspect-ratio Si nanopillars produced via MP-NSL with polystyrene nanoparticles sitting on their tops ($h_o = 2000$ nm). The Bosch process typically results in periodic "ripples" on the sidewalls as shown in **Figure II.2**, which is called the "scalloping effect". As shown in the high-resolution SEM image in **Figure II.S6**, the thickness of the "ripple" is typically ~25 nm. Note that the top surfaces of the silicon nanopillars remain smooth, as they were protected by the PS bead template during etching. However, the "scalloping effect" can be minimized and/or eliminated in MP-NSL by using an optimized Bosch process[30] or cryogenic-DRIE[31] to generate Si nanostructures with smooth sidewalls. In the present study, low-aspect-ratio Si nanostructures with smooth sidewalls were achieved straightforwardly via single-step DRIE, which uses C_4F_8 and SF_6 simultaneously as the etching and passivation gases (**Figures II.2G,H** and **II.S7**).

After the fabrication of Si nanopillars, a second oxygen plasma RIE was applied to reduce the size of the polystyrene nanoparticles sitting on top of the pillars (**Figure II.1D**). The smaller nanospheres remain centered on the pillars and serve as templates for subsequent etching treatments to obtain nanotubes. Next, a thin layer of nickel (Ni) was deposited via electron-beam evaporation along the exposed Si at the tops of the nanopillars to avoid undesired etching. Nickel was selected as the masking material as it is highly resistant to Si dry etching processes. The thin Ni layer, typically 20 nm, forms Ni nanorings at the top of the nanopillars and also covers the bottom surface of the Si substrate, **Figure II.1E**. The polymer nanoparticles are subsequently removed with tape to expose the centers of the Si pillars for etching **Figure II.1F**. The inner diameters of the Ni nanorings define the inner diameter (d_i) and sidewall thickness ($w = d_o - d_i$) of nanotubes generated

after a second round of DRIE. The Ni is then removed via a chemical etch treatment (5% HCl) to obtain the final Si nanotube arrays (**Figure II.1G**).

As illustrated in **Figure II.3A**, altering the time of the second oxygen plasma RIE step enables the inner diameter d_i and thus the sidewall thickness w of the Si nanotubes to be tuned precisely. As a proof of concept, we fabricated a series of Si nanotubes by using 1 and 2 μm polystyrene spheres as masks for MP-NSL. We first fabricated Si nanopillars with diameters of 730±7 nm and 1340±12 nm using the 1 and 2 μm polystyrene spheres masks, respectively. Then, we varied the second oxygen plasma RIE time to control the diameter of the polystyrene nanoparticles on top of the Si nanopillars and applied a second DRIE treatment as described above to generate ordered Si nanotubes with different sidewall thicknesses. As shown in the **Tables II.1** and **II.2**: For Si nanopillars with $d_o = 720$ nm, a second oxygen plasma RIE time of 3, 3.25, 3.5, 4, and 4.5 min, resulted in sidewall thicknesses of 105 ± 5, 120 ± 4, 150 ± 5, 200 ± 5, and 290 ± 7 nm, respectively, while for 1340 ± 12 nm diameter Si nanopillars, oxygen plasma RIE times of 3−7 min resulted sidewall thicknesses ranging from 120 ± 12 to 420 ± 8 nm. Even smaller sidewall thickness, such as 45±2, 80±2, 100±3nm, can be achieved by further decreasing the RIE time difference, see **Figure II.2F−H**. Such high accuracy control over the nanosphere size is comparable to many electron- or ion-beam-based nanolithographies.

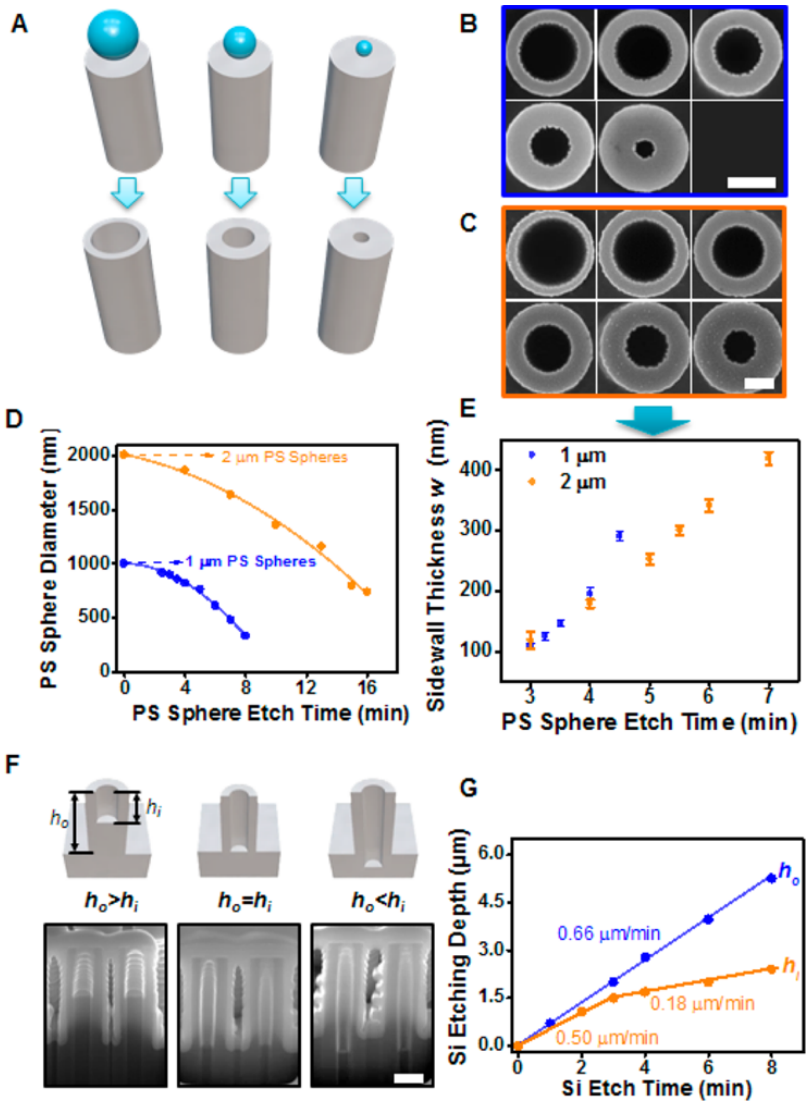

Figure II.3. (A) Schematic illustration of tuning the outer and inner diameters (d_o and d_i, respectively) of Si nanotubes. (B) Top-view Scanning electron micrographs of Si nanotubes fabricated from 1 μm polystyrene nanospheres with d_o = 730 ± 7 nm, and sidewall width ($w = (d_o - d_i)/2$) from 105 ± 5 nm to 290 ± 7 nm (scale bar: 400 nm). (C) Top-view SEM images of Si nanotubes fabricated from 2 μm polystyrene (PS) nanospheres with d_o = 1340 ± 12 nm, and w from 120 ± 12 nm to 420 ± 8 nm (scale bar: 400 nm). (D) Oxygen plasma reactive ion etching (RIE) time-dependent size reduction of polystyrene nanoparticles. (E) Oxygen plasma RIE time dependent w corresponding to (B,C) with d_o = 1340 ± 12 nm. (F) Schematic illustrations of independent control of ho and hi. From left to right, $h_o > h_i$, $h_o = h_i$, and $h_o < h_i$. Bottom: SEM images of corresponding Si nanotube cross sections prepared by focused ion-beam milling with Pt (white part) as protection layer (scale bar: 500 nm). (G) Plot of DRIE time dependence of h_o and h_i. Si etch rates were 0.66 μm/min for h_o and 0.50 μm/min (0–3 min); 0.18 μm/min (3–8 min) for h_i, respectively.

pitch = 1 μm		pitch = 2 μm	
etch time	w	etch time	w
3 min	105 ± 5 nm	3 min	120 ± 12 nm
3.25 min	120 ± 5 nm	4 min	180 ± 7 nm
3.5 min	150 ± 5 nm	5 min	250 ± 8 nm
4 min	200 ± 9 nm	5.5 min	300 ± 8 nm
4.5 min	290 ± 7 nm	6 min	340 ± 9 nm
		7 min	420 ± 8 nm

Table II.2. Controlling Sidewall Thicknesses (w) of Si Nanotubes by Varying the Etch Time Difference between Two Oxygen Plasma RIE

etch time	h_o	etch time	h_i
1 min	700 ± 25 nm	2 min	1100 ± 20 nm
3 min	2000 ± 28 nm	3 min	1500 ± 25 nm
4 min	2800 ± 32 nm	4 min	1700 ± 30 nm
6 min	4000 ± 38 nm	6 min	2000 ± 20 nm
8 min	5200 ± 50 nm	8 min	2410 ± 28 nm

Table II.3. Tuning the Outer/Inner Heights (h_o/h_i) of Si Nanotubes by Controlling the Duration of Deep Reactive Ion Etching

The outer height (h_o) and inner hole-depth (h_i) of the Si nanotubes can be controlled independently by varying their respective DRIE times. The SEM cross-sectional images shown in **Figure II.3F** illustrate three representative Si nanotube arrays with different h_o/h_i ratios, where from left to the right, $h_o > h_i$, $h_o = h_i$ (center), and $h_o < h_i$. The DRIE etching rates used for each h_o and h_i are shown in **Figure II.3G** and **Table II.3.** Specifically, an etch rate of 0.66 μm/min was used for h_o, while rates of 0.50 μm/min (0–3 min) and 0.18 μm/min (3–8 min) were used for hi. A slower etch rate is observed for h_i, which is known as "RIE lag", that is, the etching rate is related to the feature size, and the smaller the feature size, the lower the etching rate.[32]

The robust and rapid fabrication of periodic 3D hierarchical nanostructures is highly desirable for applications in nanophotonics, metamaterials, and biotechnology.[33] Direct writing fabrication strategies based on two-photon,[34] focused ion-beam, or electron-beam[35] techniques have been developed to assemble 3D hierarchical micro/nanostructures serially, but their widespread use within these areas has been precluded by low fabrication throughputs and a limited selection of compatible materials.

We find that MP-NSL can serve as a high-throughput 3D nanolithographic tool to fabricate a variety of periodic 3D hierarchical nanostructures. For example, as shown in **Figure II.4A**, multilevel Si nanopillars or "nanotowers" with two, three, and four levels were fabricated by reducing the polystyrene nanosphere size twice, three, and four times, respectively, with Si etching applied after each size reduction. A high-resolution SEM image (**Figure II.S6**) of multilevel silicon nanotowers shows all the levels have smooth surfaces. The smallest diameters at the apex of the Si nanotowers achieved so far are ~100 nm when using 900 nm nanospheres templates. The sidewall thickness (w) and height (h) of each level were controlled individually and precisely by varying the oxygen plasma RIE and DRIE times during processing (**Figure II.4A**). In principle, there is no limitation to the complexity of the nanostructures generated via MP-NSL. Potential applications for these multilevel nanotowers include nanobarcodes[36] and antireflective coatings.[37] It is also possible to fabricate hollow Si nanotowers by integrating the etching processes used to generate Si nanotubes above. Moreover, we have applied MP- NSL to pattern similar nanotowers with a wide range of materials, including SiO_2, and have used the nanostructures as a mold for soft materials, such as polydimethylsiloxane (PDMS) (**Figure II.4A**).[38–40]

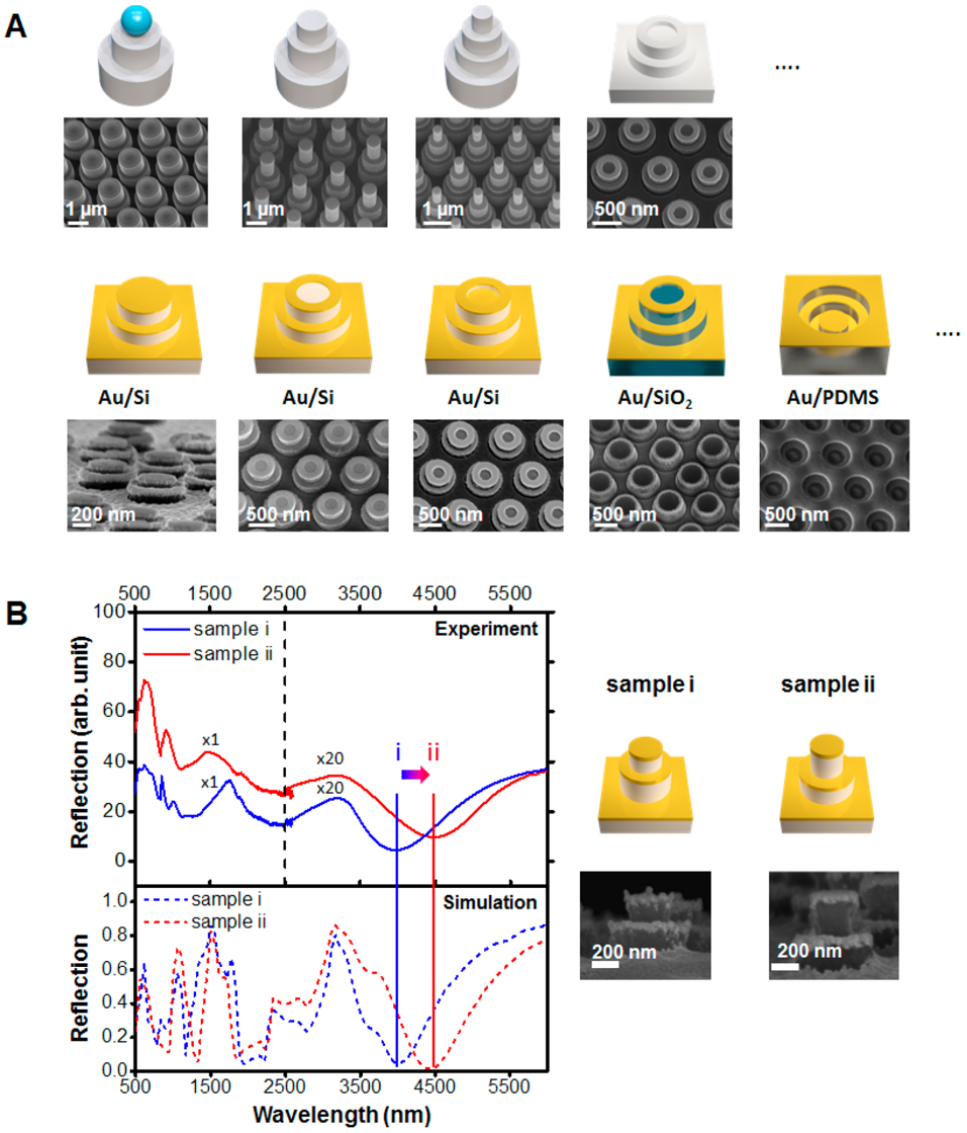

Figure II.4. (A) By using multiple-patterning nanosphere lithography, a variety of periodic hierarchical nanostructures have been designed and fabricated: Si nanotowers with two levels, three levels, and four levels with tunable heights (including negative heights for selected levels) and diameters for each level; configurable concentric plasmonic Au nanorings/nanodisk on Si substrates (solid/hollow two-level nanotowers), SiO_2 nanostructures (two-level nanotowers), and flexible polydimethylsiloxane (PDMS) substrates (negatively replicated hollow nanotowers). (B) Reflection visible-infrared spectra of Au/Si nanotowers with different dimensions. Solid lines are the experiment results, and dotted lines are corresponding simulation results. (Sample sizes in nm, sample i: $p = 900$, $d_1 = 530$, $h_1 = 300$, $d_2 = 320$, $h_2 = 230$, and $t_{Au} = 50$; Sample ii: $= 900$, $d_1 = 570$, $h_1 = 230$, $d_2 = 320$, $h_2 = 230$, and $t_{Au} = 50$). Note that the spectra (500 to 6000 nm) were collected using two different spectrometers with different ranges (500–2500 nm and 2500–6000 nm, respectively) and stitched together at 2500 nm for comparison to simulations (see detailed description in the Supporting Information).

Plasmonic nanostructures have attracted broad interest, including for potential applications ranging from biosensing and surface-enhanced spectroscopy to optical trapping.[41–47] So far, most plasmonic nanostructures fabricated by nanolithography have been largely two-dimensional. Our 3D nanostructures can further serve as templates for achieving periodic 3D hierarchical plasmonic nanostructures, important for engineering nanophotonics in 3D.[48–50] Simply by evaporating a layer of a plasmonic metal (e.g., gold, silver, aluminum), onto an array of periodic Si/SiO_2/PDMS nanotowers, we obtained periodic 3D plasmonic nanostructures (**Figure II.4A**). After Au evaporation, high-resolution SEM imaging reveals that each layer of the nanotower structures is smooth (**Figure II.S8**). The dimensions of these Au nanorings and Au nanodisks as well as the relative vertical distances between them are fully tunable with sub-20 nm-scale resolution, which presents the tantalizing possibility to design and to manipulate the optical properties of these periodic 3D plasmonic nanostructures. For example, we evaporated 50 nm of Au on two slightly different two-level Si nanotowers as shown in **Figure II.4B**, and fully tunable 3D ring/ disk plasmonic nanocavities were thereby fabricated. As shown in the reflection spectra of these vertically stacked plasmonic nanostructures, multiple resonant peaks ranged from visible to mid-IR were observed. The reflection spectra agree well with finite-difference-time-domain (FDTD) simulations. The simulation results indicate that multiple peaks and dips result from multimodal plasmonic resonances through hybridization between different plasmonic multipole modes of ring and disk cavities vertically (FDTD simulations of the electric-field and charge distributions are provided in **Figure II.S9**). Slight, intentional geometry differences between the two plasmonic nanostructures (sample i *vs* sample ii) result in shifts

in the reflection spectra due to changes of the resonance (**Figure II.4B**). Thus, MP-NSL is a tool to design and to fabricate optically tunable 3D plasmonic nanostructures.

II.C. Conclusions and Prospects

Our results suggest that MP-NSL is a promising 3D nanolithographic tool to achieve a variety of periodic 3D hierarchical nanostructures that can be configured to enable applications in nanophotonics, optoelectronics, electronics, metamaterials, and biotechnology. This strategy is compatible with and could be integrated into micro/nanoscale device manufacturing to add components with functions enabled by rationally designed 3D nanostructures. Additionally, by using beads with different physicochemical properties and/or geometries, even greater control can be achieved.

II.D. Materials and Methods

II.D.1. Materials

Prime quality 4 in. Si (100) wafers (*p*-type/B-doped, 1-10 Ω×cm) were purchased from University Wafer Inc. (Boston, MA, USA). All polystyrene spheres (1% solids, 400 nm to 2 μm) were purchased from Thermo Fisher Scientific Inc. (Fremont, CA, USA). Sodium dodecyl sulfate (SDS, 98%) was purchased from Sigma-Aldrich (St. Louis, MO, USA). Hydrochloric acid (36.5 to 38.0% w/w) was purchased from Fisher Scientific Inc. (Fair Lawn, NJ, USA). Evaporation materials including gold (99.99%) and nickel (99.995%) were purchased from K. J. Lesker Company (Jefferson Hills, PA, USA).

II.D.2. Morphology Characterization

The scanning electron micro- graphs were taken by a Zeiss Supra 40VP scanning electron microscope. Focused ion-beam samples were made and imaged using the Nova 600 SEM/FIB system.

II.D.3. Polystyrene Sphere Monolayer Formation on Si Substrates

The polystyrene nanospheres (1% solids) stock dispersion were centrifuged and redispersed in water/ethanol mixture (1:1 ratio) with 2–4% solids. A 2 cm × 2 cm Si substrate and a 22 mm × 22 mm glass coverslip were treated in an oxygen plasma (Harrick Plasma, Ithaca, NY) for 1 min to generate hydrophilic surfaces. Next, the Si substrate was put in a 2 in. Petri dish, ~4 mL water was added to immerse the Si substrate fully, and then ~50 μL 1 wt % SDS was added. The polystyrene nanosphere dispersion in water/ethanol was slowly added to the water/air interface through a tilted glass coverslip that was placed against the edge of the Petri dish to form close-packed monolayers. Then, the water was removed to transfer the polystyrene nanosphere monolayers to the surface of Si substrate. Finally, the Si substrate was dried in a vacuum desiccator.

II.D.4. Oxygen Plasma RIE of Polystyrene Nanospheres

An Oxford 80 Plus system was used to tailor the size of polystyrene nanospheres. A time-controlled etching process of the polystyrene nanospheres was carried out under a gas mixture of O_2 (35 sccm) and Ar (10 sccm) at a pressure of 60 mTorr and radio frequency power of 60 W. The polystyrene-nanosphere-coated Si substrate was heated at 120 °C for ~30 s to fix nanospheres on the Si substrate.

II.D.5. Deep Reactive Ion Etching of Silicon

(1) Bosch process: An inductively coupled plasma reactive ion etcher (ICP-RIE, Plasma Therm SLR700) was used. It involved alternate cycles of passivation and etching steps. During the passivation step, a flow of 24 sccm C_4F_8 and 12 sccm Ar was used at power of 825 W. During the etching step, a flow of 30 sccm SF_6 and 12 sccm Ar was used at a power of 825 W. (2) Single-step dry etching: The single-step RIE of silicon was completed in a simultaneous flow of 24 sccm C_4F_8, 21 sccm SF_6, and 5 sccm Ar at a pressure of 12 mTorr with ICP power of 650 W and platen power of 9 W (STS Advanced Oxide Etcher) to achieve silicon pillars/tubes with smooth sidewalls. For both processes, the etching depth of Si was controlled by the etching time.

II.D.6. Fabrication of SiO_2 Hierarchical Nanostructures

SiO_2/Si (500-nm-thick SiO_2) substrates with polystyrene nanoparticles as the masks were etched by an Oxford 80 Plus using a gas mixture of CHF_3 (25 sccm) and Ar (25 sccm) at 35 mTorr to generate the SiO_2 hierarchical nanostructures.

II.D.7. Pattern Replication to PDMS Substrates

A 10:1 mass ratio of Sylgard 184 elastomer silicone elastomer base and curing agent were thoroughly mixed and then degassed in a vacuum desiccator. This mixture was poured onto the Si mold with hierarchical nanostructures and cured overnight at 65 °C. After curing, PDMS stamps were carefully removed from the Si mold.

II.D.8. Metal Coating

Desirable substrates were loaded into the vacuum chamber of an electron-beam metal evaporator (Kurt J. Lesker Company, Jefferson Hills, PA) and held at a base pressure of

1×10^{-7} Torr. Ni film was deposited at rate of ~1 Å/s, and Au film was deposited at rate of ~0.5 Å/s.

II.E. Supporting Information

II.E.1. Characterization of Reflection Spectra

In the characterization of the reflection spectra of the plasmonic hierarchical nanostructures, we set the incident light and reflected light to be near normal to the substrate, as illustrated on the left. Note that we also used these settings for the finite-difference time-domain (FDTD) optical simulations.

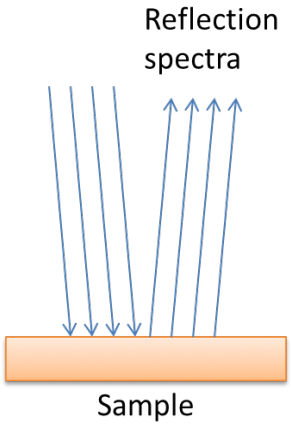

In order to obtain the reflection spectra across the wavelength range from 500 to 6000 nm, two spectrophotometers were used. One spectrophotometer measured the reflection spectra from 500 to 2500 nm and other measured the reflection spectra from 2500 to 6000 nm.

An UV-3101PC UV-VIS-NIR Spectrophotometer (Shimadzu Co., Japan) with an integrating sphere attachment (ISR-3100) was used to collect the reflection spectra of the plasmonic hierarchical nanostructures within the wavelength range (500 to 2500 nm). The scan rate was set at 1 nm/s.

A customized polarization modulation-infrared reflection-adsorption spectroscopy (PM-IRRAS) instrument was used to collect the reflection spectra of the plasmonic hierarchical nanostructures in the range of 2500 to 6000 nm. The scan step size was set at 2 nm with medium scan rate.

Due to the differences in sensitivities of the two spectrometers, for comparisons to the simulations, the two segments of the reflection spectra were stitched together as follows: **Sample i)** No changes were made to the reflection spectra from 500 to 2500 nm, and the intensity of reflection spectra from 2500 to 6000 nm was multiplied by 20× in order to combine the spectra. **Sample ii)** The overall intensity of the reflection spectra obtained from 500 to 2500 nm was increased by 20 (arbitrary units), while the intensity of the reflection spectra from 2500 to 6000 nm was multiplied by 20×. See **Figure II.S9A**

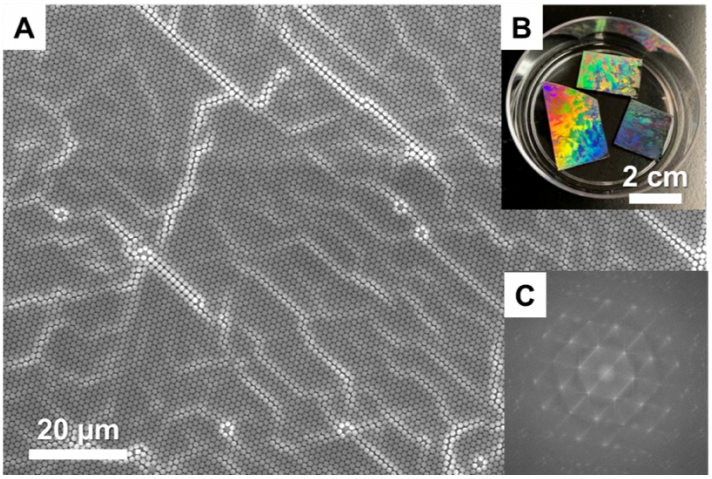

Figure II.S1. (A) A typical scanning electron microscope (SEM) image of close-packed 1 μm polystyrene spheres in micro-scale. (B) A photograph of Si wafers fully covered by close-packed 1 μm polystyrene spheres. The reflected colors indicate the well-ordered configuration of the polystyrene microspheres. (C) The corresponding fast Fourier transform (FFT) of the SEM image.

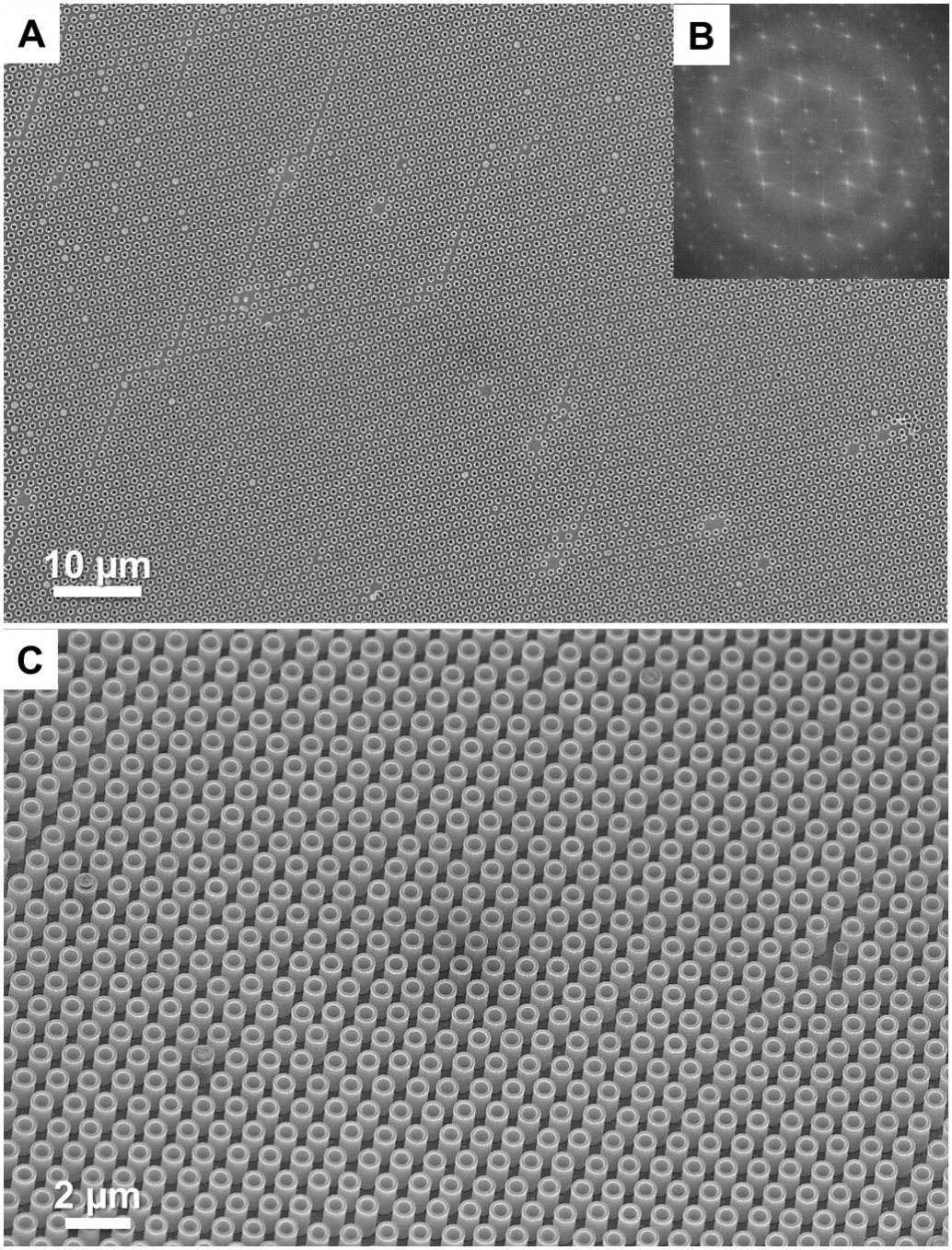

Figure II.S2. (A) A typical scanning electron microscope (SEM) image of a large area of the silicon nanotube arrays. (B) The corresponding fast Fourier transform (FFT) of the image. (C) A typical SEM image of large-area silicon nanotube arrays recorded at a tilt of 30°.

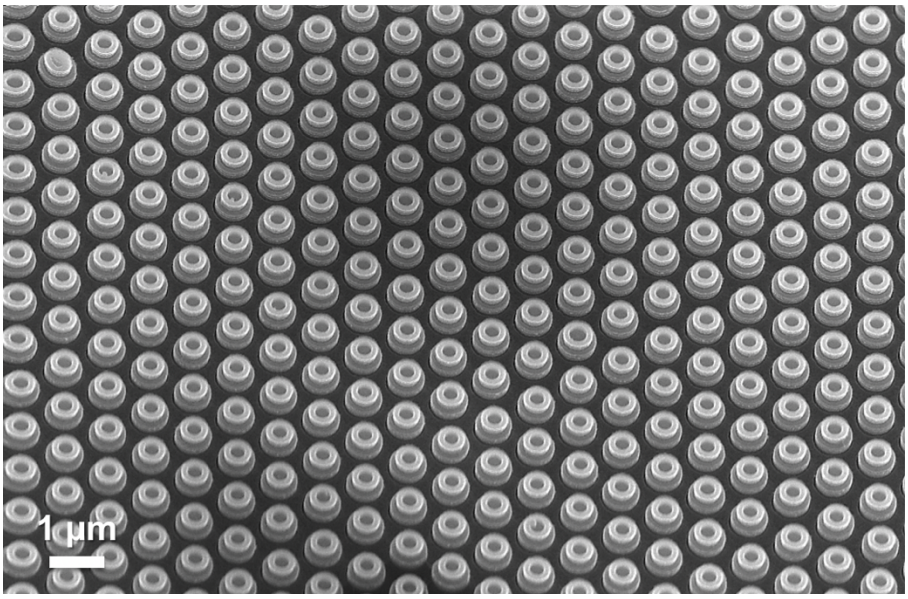

Figure II.S3. A typical scanning electron microscope (SEM) image of a large area of silicon nanostructures recorded at a tilt of 30°.

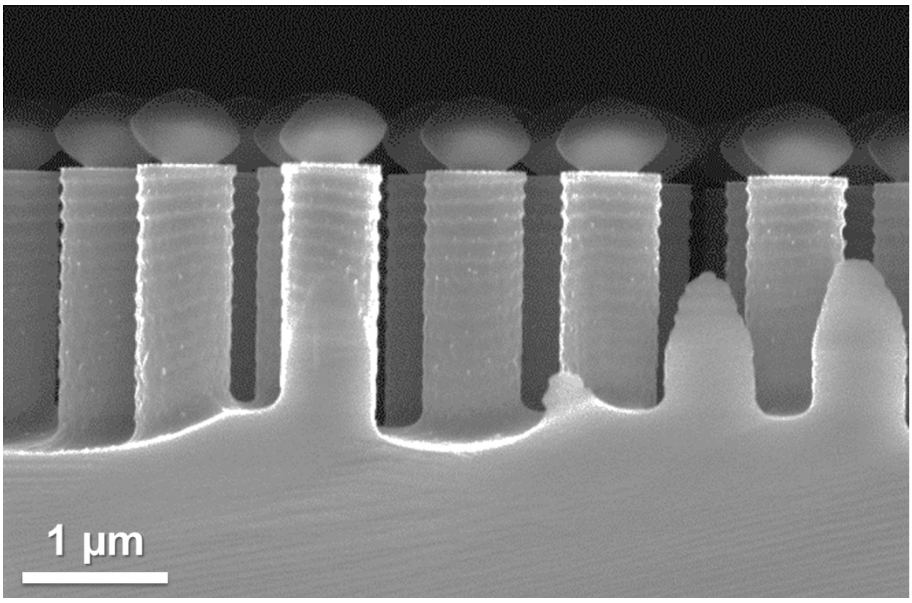

Figure II.S4. A typical scanning electron microscope image of polystyrene nanospheres with oblate ellipsoid shapes after oxygen plasma reactive ion etching.

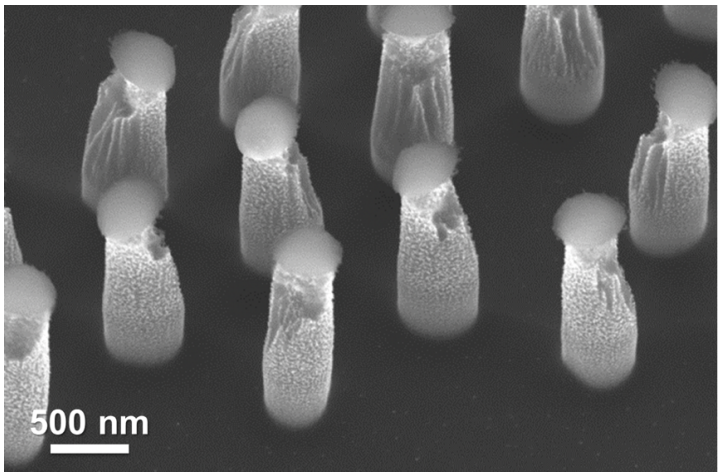

Figure II.S5. Enhancing the adhesion between the polystyrene nanospheres and the underlying silicon substrate before dry etching helps to prevent tilting of the etched polymer nanoparticles, which could lead to asymmetries in the final pillar/nanotube arrays without heating.

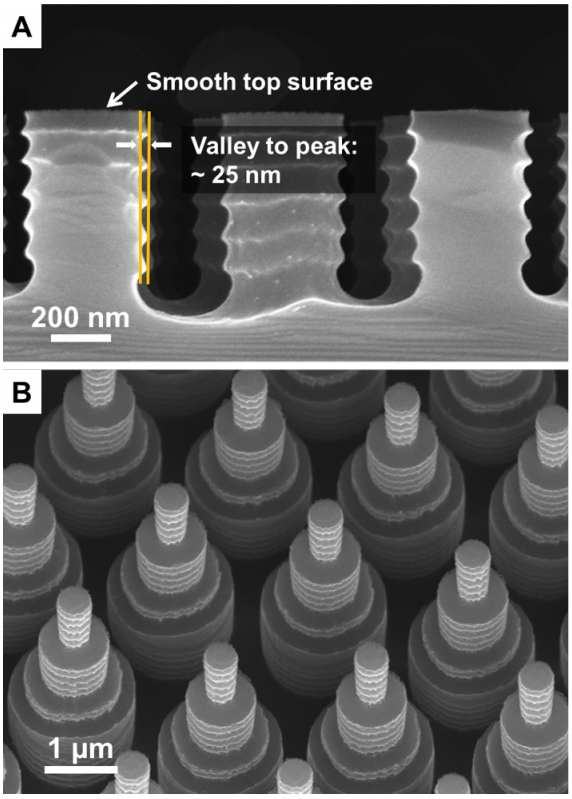

Figure II.S6. (A) A high-resolution scanning electron microscope (SEM) image of silicon nanopillars made via the Bosch process. The top surfaces of the silicon nanopillars are smooth. The average distance between valleys and peaks on the sidewall of a silicon nanopillar is ~25 nm. (B) A high-resolution SEM image of four-level silicon nanotowers shows the smooth surfaces on the four levels.

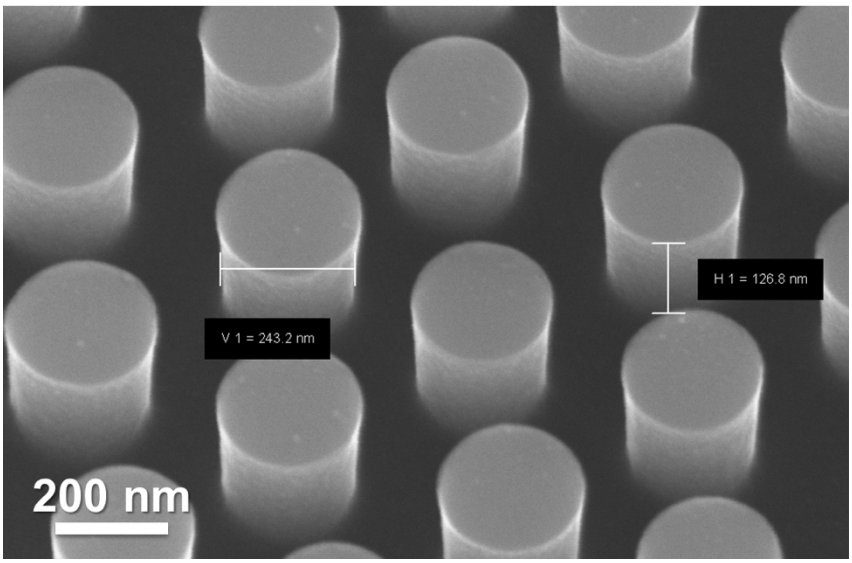

Figure II.S7. A scanning electron microscope (SEM) image of periodic silicon nanopillars with smooth sidewalls fabricated by single-step deep reactive ion etching.

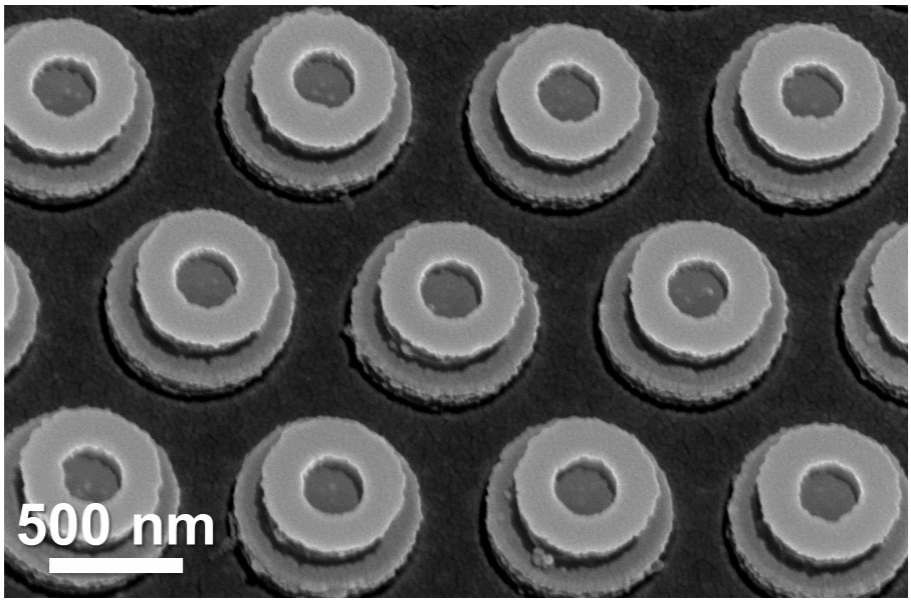

Figure II.S8. A high-resolution scanning electron microscope (SEM) image of 50 nm Au evaporated silicon nanostructures.

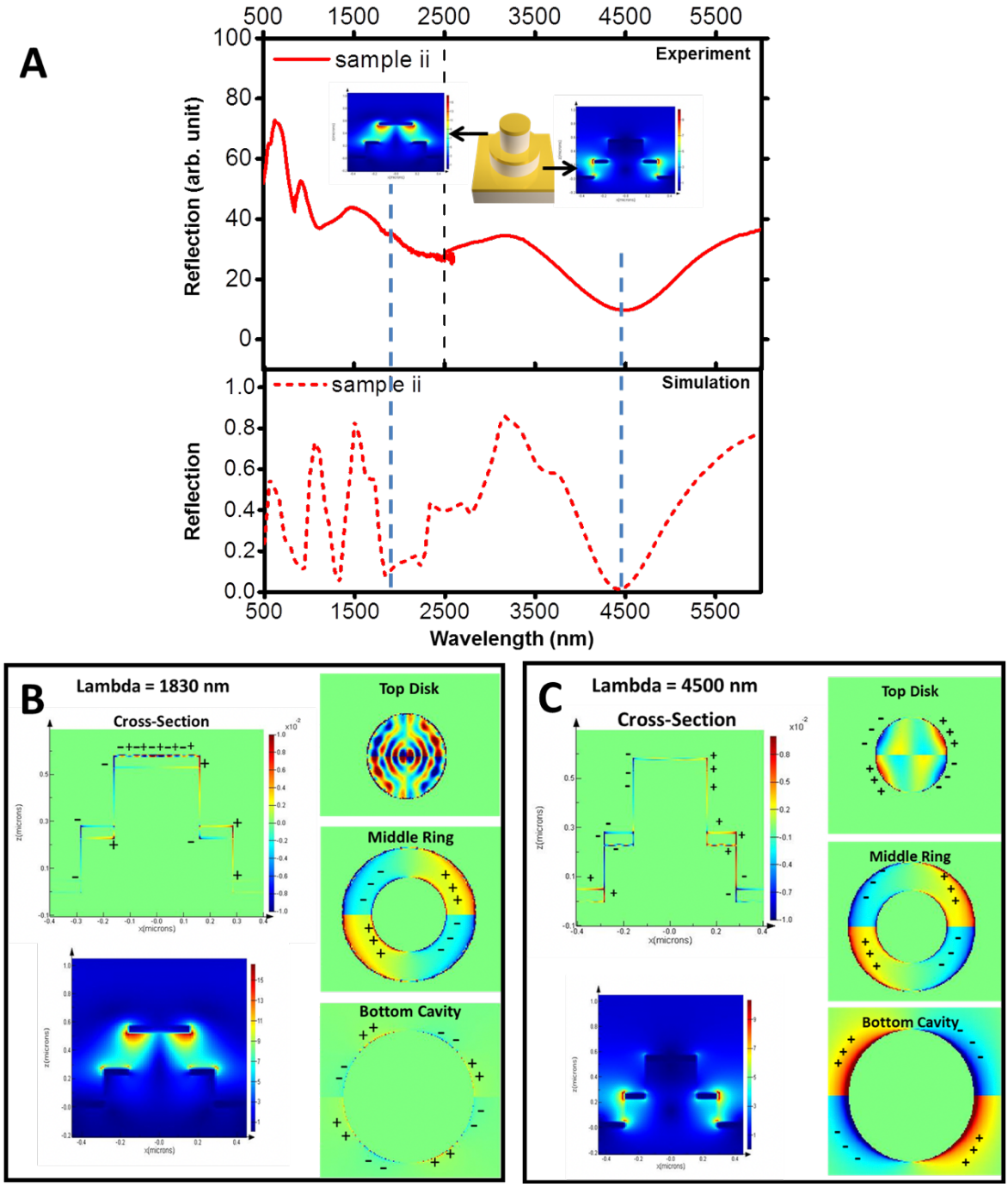

Figure II.S9. (A) The visible-infrared reflectance spectra of sample ii. Insets: simulation results of the electric-field distribution of sample ii under photoexcitation (cross section). (B-C) Simulation of charge distributions on the Au surfaces on different layers of the sample ii at the two major dips (1830 nm and 4500 nm), from which we can see the 1830 nm mode is a combination of different multipole modes from the three layers; while the 4500 nm mode corresponds to the quadrupole modes of all three layers.

II.F. References

(1) Xu, X.; Yang, Q.; Wattanatorn, N.; Zhao, C.; Chiang, N.; Jonas, S. J.; Weiss, P. S. Multiple-Patterning Nanosphere Lithography for Fabricating Periodic Three-Dimensional Hierarchical Nanostructures. *ACS Nano* **2017**, *11*, 10384–10391.

(2) Kim, Y.-Y.; Kim, H.-J.; Jeong, J.-H.; Lee, J.; Choi, J.-H.; Jung, J.-Y.; Lee, J.-H.; Cheng, H.; Lee, K.-W.; Choi, D.-G. Facile Fabrication of Silicon Nanotube Arrays and Their Application in Lithium-Ion Batteries. *Adv. Eng. Mater.* **2016**, *18*, 1349–1353.

(3) Yoo, J.-K.; Kim, J.; Jung, Y. S.; Kang, K. Scalable Fabrication of Silicon Nanotubes and Their Application to Energy Storage. *Adv. Mater.* **2012**, *24*, 5452–5456.

(4) Park, M.-H.; Kim, M. G.; Joo, J.; Kim, K.; Kim, J.; Ahn, S.; Cui, Y.; Cho, J. Silicon Nanotube Battery Anodes. *Nano Lett.* **2009**, *9*, 3844–3847.

(5) Wu, H.; Chan, G.; Choi, J. W.; Ryu, I.; Yao, Y.; McDowell, M. T.; Lee, S. W.; Jackson, A.; Yang, Y.; Hu, L.; et al. Stable Cycling of Double-Walled Silicon Nanotube Battery Anodes through Solid-Electrolyte Interphase Control. *Nat. Nanotechnol.* **2012**, *7*, 309–314.

(6) Xie, C.; Nie, B.; Zeng, L.; Liang, F.-X.; Wang, M.-Z.; Luo, L.; Feng, M.; Yu, Y.; Wu, C.-Y.; Wu, Y.; et al. Core-Shell Heterojunction of Silicon Nanowire Arrays and Carbon Quantum Dots for Photovoltaic Devices and Self-Driven Photodetectors. *Acs Nano* **2014**, *8*, 4015–4022.

(7) Wei, W.-R.; Tsai, M.-L.; Ho, S.-T.; Tai, S.-H.; Ho, C.-R.; Tsai, S.-H.; Liu, C.-W.; Chung, R.-J.; He, J.-H. Above-11%-Efficiency Organic-Inorganic Hybrid Solar Cells with Omnidirectional Harvesting Characteristics by Employing Hierarchical Photon-Trapping Structures. *Nano Lett.* **2013**, *13*, 3658–3663.

(8) Ali, M.; Zhou, F.; Chen, K.; Kotzur, C.; Xiao, C.; Bourgeois, L.; Zhang, X.; MacFarlane, D. R. Nanostructured Photoelectrochemical Solar Cell for Nitrogen Reduction Using Plasmon-Enhanced Black Silicon. *Nat. Commun.* **2016**, *7*, 11335.

(9) Kelzenberg, M. D.; Boettcher, S. W.; Petykiewicz, J. A.; Turner-Evans, D. B.; Putnam, M. C.; Warren, E. L.; Spurgeon, J. M.; Briggs, R. M.; Lewis, N. S.; Atwater, H. A. Enhanced Absorption and Carrier Collection in Si Wire Arrays for Photovoltaic Applications. *Nat. Mater.* **2010**, *9*, 239–244.

(10) Garnett, E.; Yang, P. Light Trapping in Silicon Nanowire Solar Cells. *Nano Lett.* **2010**, *10*, 1082–1087.

(11) Xu, X.; Liu, C.; Kim, K.; Fan, D. L. Electric-Driven Rotation of Silicon Nanowires and Silicon Nanowire Motors. *Adv. Funct. Mater.* **2014**, *24*, 4843–4850.

(12) Jeong, H.; Song, H.; Pak, Y.; Kwon, I. K.; Jo, K.; Lee, H.; Jung, G. Y. Enhanced Light Absorption of Silicon Nanotube Arrays for Organic/Inorganic Hybrid Solar Cells. *Adv. Mater.* **2014**, *26*, 3445–3450.

(13) Chiappini, C.; De Rosa, E.; Martinez, J. O.; Liu, X.; Steele, J.; Stevens, M. M.; Tasciotti, E. Biodegradable Silicon Nanoneedles Delivering Nucleic Acids Intracellularly Induce Localized in Vivo Neovascularization. *Nat. Mater.* **2015**, *14*, 532–539.

(14) Bucaro, M. A.; Vasquez, Y.; Hatton, B. D.; Aizenberg, J. Fine-Tuning the Degree of Stem Cell Polarization and Alignment on Ordered Arrays of High-Aspect-Ratio Nanopillars. *Acs Nano* **2012**, *6*, 6222–6230.

(15) Polacheck, W. J.; Chen, C. S. Measuring Cell-Generated Forces: A Guide to the Available Tools. *Nat. Methods* **2016**, *13*, 415–423.

(16) Weng, S.; Shao, Y.; Chen, W.; Fu, J. Mechanosensitive Subcellular Rheostasis Drives Emergent Single-Cell Mechanical Homeostasis. *Nat. Mater.* **2016**, *15*, 961–967.

(17) Green, B. J.; Safaei, T. S.; Mepham, A.; Labib, M.; Mohamadi, R. M.; Kelley, S. O. Beyond the Capture of Circulating Tumor Cells: Next-Generation Devices and Materials. *Angew. Chem.-Int. Ed.* **2016**, *55*, 1252–1265.

(18) Fox, C. B.; Cao, Y.; Nemeth, C. L.; Chirra, H. D.; Chevalier, R. W.; Xu, A. M.; Melosh, N. A.; Desai, T. A. Fabrication of Sealed Nanostraw Microdevices for Oral Drug Delivery. *Acs Nano* **2016**, *10*, 5873–5881.

(19) Wu, Y.-C.; Wu, T.-H.; Clemens, D. L.; Lee, B.-Y.; Wen, X.; Horwitz, M. A.; Teitell, M. A.; Chiou, P.-Y. Massively Parallel Delivery of Large Cargo into Mammalian Cells with Light Pulses. *Nat. Methods* **2015**, *12*, 439-+.

(20) Hulteen, J. C.; Van Duyne, R. P. Nanosphere Lithography: A Materials General Fabrication Process for Periodic Particle Array Surfaces. *J. Vac. Sci. Technol. Vac. Surf. Films* **1995**, *13*, 1553–1558.

(21) Chen, K.; Rajeeva, B. B.; Wu, Z.; Rukavina, M.; Dao, T. D.; Ishii, S.; Aono, M.; Nagao, T.; Zheng, Y. Moire Nanosphere Lithography. *Acs Nano* **2015**, *9*, 6031–6040.

(22) Kosiorek, A.; Kandulski, W.; Glaczynska, H.; Giersig, M. Fabrication of Nanoscale Rings, Dots, and Rods by Combining Shadow Nanosphere Lithography and Annealed Polystyrene Nanosphere Masks. *Small* **2005**, *1*, 439–444.

(23) Haynes, C. L.; Van Duyne, R. P. Nanosphere Lithography: A Versatile Nanofabrication Tool for Studies of Size-Dependent Nanoparticle Optics. *J. Phys. Chem. B* **2001**, *105*, 5599–5611.

(24) Huang, Z.; Fang, H.; Zhu, J. Fabrication of Silicon Nanowire Arrays with Controlled Diameter, Length, and Density. *Adv. Mater.* **2007**, *19*, 744.

(25) Jeong, S.; McGehee, M. D.; Cui, Y. All-Back-Contact Ultra-Thin Silicon Nanocone Solar Cells with 13.7% Power Conversion Efficiency. *Nat. Commun.* **2013**, *4*, 2950.

(26) Jeong, S.; Garnett, E. C.; Wang, S.; Yu, Z.; Fan, S.; Brongersma, M. L.; McGehee, M. D.; Cui, Y. Hybrid Silicon Nanocone-Polymer Solar Cells. *Nano Lett.* **2012**, *12*, 2971–2976.

(27) Gao, P.; He, J.; Zhou, S.; Yang, X.; Li, S.; Sheng, J.; Wang, D.; Yu, T.; Ye, J.; Cui, Y. Large-Area Nanosphere Self-Assembly by a Micro-Propulsive Injection Method for High Throughput Periodic Surface Nanotexturing. *Nano Lett.* **2015**, *15*, 4591–4598.

(28) Zhang, J.; Li, Y.; Zhang, X.; Yang, B. Colloidal Self-Assembly Meets Nanofabrication: From Two-Dimensional Colloidal Crystals to Nanostructure Arrays. *Adv. Mater.* **2010**, *22*, 4249–4269.

(29) Ge, M.; Rong, J.; Fang, X.; Zhou, C. Porous Doped Silicon Nanowires for Lithium Ion Battery Anode with Long Cycle Life. *Nano Lett.* **2012**, *12*, 2318–2323.

(30) Morton, K. J.; Nieberg, G.; Bai, S.; Chou, S. Y. Wafer-Scale Patterning of Sub-40 Nm Diameter and High Aspect Ratio (> 50 : 1) Silicon Pillar Arrays by Nanoimprint and Etching. *Nanotechnology* **2008**, *19*, 345301.

(31) Li, Z.; Chen, Y.; Zhu, X.; Zheng, M.; Dong, F.; Chen, P.; Xu, L.; Chu, W.; Duan, H. Fabrication of Single-Crystal Silicon Nanotubes with Sub-10 Nm Walls Using Cryogenic Inductively Coupled Plasma Reactive Ion Etching. *Nanotechnology* **2016**, *27*, 365302.

(32) Chung, C. K. Geometrical Pattern Effect on Silicon Deep Etching by an Inductively Coupled Plasma System. *J. Micromechanics Microengineering* **2004**, *14*, 656–662.

(33) Fan, Z.; Razavi, H.; Do, J.; Moriwaki, A.; Ergen, O.; Chueh, Y.-L.; Leu, P. W.; Ho, J. C.; Takahashi, T.; Reichertz, L. A.; et al. Three-Dimensional Nanopillar-Array Photovoltaics on Low-Cost and Flexible Substrates. *Nat. Mater.* **2009**, *8*, 648–653.

(34) Cumpston, B. H.; Ananthavel, S. P.; Barlow, S.; Dyer, D. L.; Ehrlich, J. E.; Erskine, L. L.; Heikal, A. A.; Kuebler, S. M.; Lee, I. Y. S.; McCord-Maughon, D.; et al. Two-Photon Polymerization Initiators for Three-Dimensional Optical Data Storage and Microfabrication. *Nature* **1999**, *398*, 51–54.

(35) Yamazaki, K.; Yamaguchi, H. Flexible Nanofabrication in Three-Dimensional Electron-Beam Lithography Enhanced by Suppression of Proximity Effect. *Appl. Phys. Express* **2008**, *1*, 097001.

(36) Qin, L.; Banholzer, M. J.; Millstone, J. E.; Mirkin, C. A. Nanodisk Codes. *Nano Lett.* **2007**, *7*, 3849–3853.

(37) Raut, H. K.; Ganesh, V. A.; Nair, A. S.; Ramakrishna, S. Anti-Reflective Coatings: A Critical, in-Depth Review. *Energy Environ. Sci.* **2011**, *4*, 3779–3804.

(38) Cao, H. H.; Nakatsuka, N.; Liao, W.-S.; Serino, A. C.; Cheunkar, S.; Yang, H.; Weiss, P. S.; Andrews, A. M. Advancing Biocapture Substrates via Chemical Lift-Off Lithography. *Chem. Mater.* **2017**, *29*, 6829–6839.

(39) Xu, X.; Yang, Q.; Cheung, K. M.; Zhao, C.; Wattanatorn, N.; Belling, J. N.; Abendroth, J. M.; Slaughter, L. S.; Mirkin, C. A.; Andrews, A. M.; et al. Polymer-Pen Chemical Lift-Off Lithography. *Nano Lett.* **2017**, *17*, 3302–3311.

(40) Liao, W.-S.; Cheunkar, S.; Cao, H. H.; Bednar, H. R.; Weiss, P. S.; Andrews, A. M. Subtractive Patterning via Chemical Lift-Off Lithography. *Science* **2012**, *337*, 1517-1521.

(41) Brolo, A. G. Plasmonics for Future Biosensors. *Nat. Photonics* **2012**, *6*, 709–713.

(42) Juan, M. L.; Righini, M.; Quidant, R. Plasmon Nano-Optical Tweezers. *Nat. Photonics* **2011**, *5*, 349–356.

(43) Lu, Y.-J.; Kim, J.; Chen, H.-Y.; Wu, C.; Dabidian, N.; Sanders, C. E.; Wang, C.-Y.; Lu, M.-Y.; Li, B.-H.; Qiu, X.; et al. Plasmonic Nanolaser Using Epitaxially Grown Silver Film. *Science* **2012**, *337*, 450–453.

(44) Nie, S. M.; Emery, S. R. Probing Single Molecules and Single Nanoparticles by Surface-Enhanced Raman Scattering. *Science* **1997**, *275*, 1102–1106.

(45) Rodrigo, D.; Limaj, O.; Janner, D.; Etezadi, D.; Javier Garcia de Abajo, F.; Pruneri, V.; Altug, H. Mid-Infrared Plasmonic Biosensing with Graphene. *Science* **2015**, *349*, 165-168.

(46) Xu, X.; Li, H.; Hasan, D.; Ruoff, R. S.; Wang, A. X.; Fan, D. L. Near-Field Enhanced Plasmonic-Magnetic Bifunctional Nanotubes for Single Cell Bioanalysis. *Adv. Funct. Mater.* **2013**, *23*, 4332–4338.

(47) Zheng, Y. B.; Payton, J. L.; Chung, C.-H.; Liu, R.; Cheunkar, S.; Pathem, B. K.; Yang, Y.; Jensen, L.; Weiss, P. S. Surface-Enhanced Raman Spectroscopy to Probe Reversibly Photoswitchable Azobenzene in Controlled Nanoscale Environments. *Nano Lett.* **2011**, *11*, 3447–3452.

(48) Kuzyk, A.; Schreiber, R.; Zhang, H.; Govorov, A. O.; Liedl, T.; Liu, N. Reconfigurable 3D Plasmonic Metamolecules. *Nat. Mater.* **2014**, *13*, 862–866.

(49) Frank, B.; Yin, X.; Schaeferling, M.; Zhao, J.; Hein, S. M.; Braun, P. V.; Giessen, H. Large-Area 3D Chiral Plasmonic Structures. *Acs Nano* **2013**, *7*, 6321–6329.

(50) De Angelis, F.; Malerba, M.; Patrini, M.; Miele, E.; Das, G.; Toma, A.; Zaccaria, R. P.; Di Fabrizio, E. 3D Hollow Nanostructures as Building Blocks for Multifunctional Plasmonics. *Nano Lett.* **2013**, *13*, 3553–3558.

CHAPTER III

Intracellular Delivery *via* a Nanoneedle-Integrated Microfluidic System for Cellular Immunotherapies

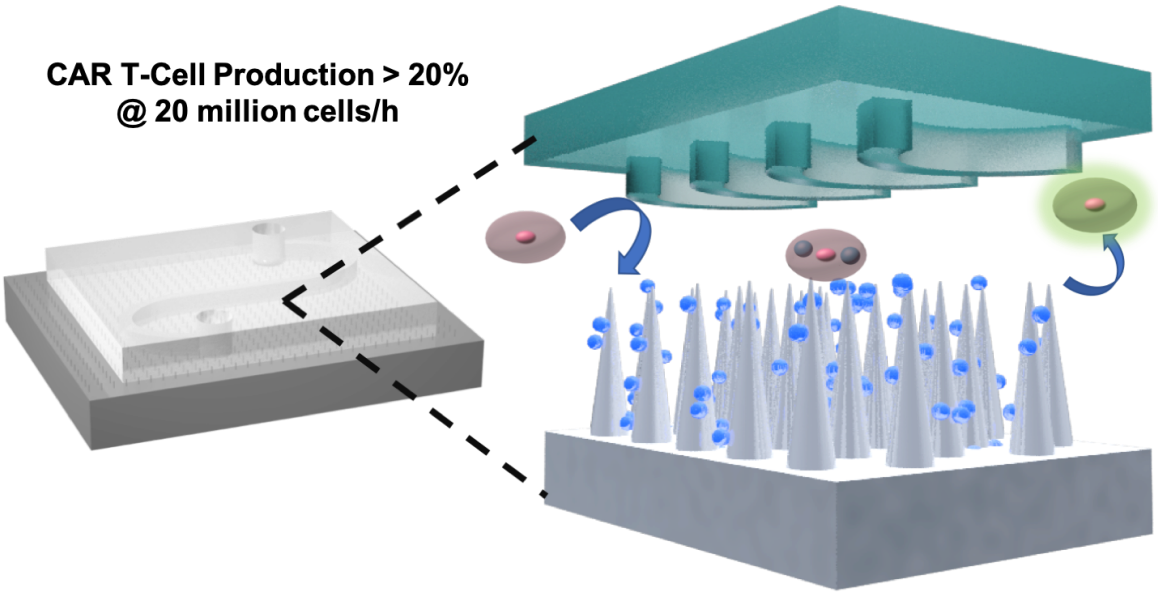

The information in this chapter is in preparation for publication.

Authors: Natcha Wattanatorn, Tzu-Ting Chiou, Xiaobin Xu, Alexandra M. Mendoza, Hsian-Rong Tseng, Satiro N. De Oliveira, Steve J. Jonas, Paul S. Weiss

III.A. Introduction

Cancer immunotherapy has received interest as a promising cancer treatment that works by enhancing immune system activity to target and to eliminate cancer. In particular, engineered chimeric antigen receptor T (CAR-T) cell treatments, relying on genetic modification of T cells, have been approved by the Food and Drug Administration (FDA) and show tremendous promise, as they promote cancer remissions in patients with chemotherapy-resistant malignancies. [1–5] For these therapies to be effective, there needs to be a safe, inexpensive, high-throughput, and sustainable way to produce CAR-T cells. However, state-of-the-art techniques used to genetically modify immune cells are lacking.[6-10] Typically, CAR-T cells are manufactured by viral vector-based transduction strategies, which provide suitable transfection efficiency, but have significant issues due to off-target effects as the viral sequence will permanently integrate into the genome and can randomly insert into active chromatin positions.6 Moreover, viral vector-based methods are limited in the size of cargo/plasmid that they can deliver, cannot be universally deployed, and can cause immunogenicity.[11–13] Also, non-viral commercial techniques, such as electroporation and lipofection, can circumvent issues with off-target effects but have limitations in terms of transfection efficiency, cytotoxicity, and throughput.[14]

In particular, non-viral physical DNA delivery methods based on membrane disruption (e.g., electroporation, cell squeezing, or sharp nanostructures) are attractive alternatives due to their simple mechanism, biosafety, low cost, and ability to deliver larger molecules and assembles.[15–20] Electroporation is efficient, but suffers immensely in terms of throughput and cell viability.[21] Mechanical cell-squeezing techniques using constricted channels or hydrodynamics are examples of strategies that create transient pores in the cell

membrane, enabling delivery via diffusion of target biomolecules.[22–24] Nanoparticle delivery strategies overcome challenges in DNA degradation and delivering large DNA payloads, but are inefficient due to intracellular trafficking and reliance on endocytosis for delivery.[25,26] Sharp nanostructure-based delivery systems have the ability both to disrupt the cell membrane mechanically, creating transient pores, and to inject biomolecules directly into target cells. However, nanoneedle-based platforms reported thus far are primarily focused on delivering biomolecules to adherent cells resting on nanostructures, resulting in limited throughput, low viability, and difficulties in recovering the processed cells, hindering clinical applications of these techniques.[27]

Herein, we report intracellular delivery of genetic materials to suspension cells using a nanoneedle-based microfluidic device that combines the advantages of large-cargo loading from nanoparticle encapsulation, direct injection, and enhanced permeability from the nanoneedle structures, as well as high-throughput microfluidic processing. Our platform is comprised of arrays of Si nanoneedles with controlled sharpness, size, and periodicity that are integrated with microfluidics. The high density of ordered nanoneedles provides a "bed-of-nails" effect, where the impact force is evenly distributed across the surface of the "nails".[27–31] Thus, the mechanical damage of the cells is reduced while facilitating plasmid delivery to target cells. Using siloxane chemistry, we functionalized the nanoneedle surface with DNA-encapsulated supramolecular nanoparticles (SMNP) prior to intracellular delivery. We examined the capacity of these nanoneedle-microfluidic devices to transfect Jurkat and human donor-derived suspension T cells to express anti-CD19 CAR. Using this method, we have achieved ~25% transfection with a throughput of 20 million cells/h, improving upon existing alternative ex vivo gene therapy methods.

III.B. Results and Discussion

The Si nanoneedle arrays were fabricated by combining nanosphere lithography with reactive-ion etching (RIE) of Si based on a previously published procedure.[32] In brief, **Figure III.1A-C** summarize the steps involved in this process. First, a hexagonal close-packed layer of 1 μm polystyrene spheres (PS) was self-assembled at an air/water interface. Upon the removal of solution, a large area of close-packed monolayer of spheres was transferred onto a hydrophilic Si substrate. The PS monolayer was then exposed to oxygen plasma to reduce the size of the spheres to ~700 nm and the resulting layer was used as an etch mask for subsequent single-step deep RIE of Si. Single-step deep RIE of Si was used as both the PS and Si can be etched simultaneously. By tuning the silicon etching gas ratio (SF_4 and C_4F_8), we achieve conical shaped Si nanoneedles, where the height, base width, tip sharpness, and pitches are individually tunable.

For intracellular delivery, the cone shape was imperative for the microfluidic platform since the base of the nanoneedles needed to be relatively large to withstand the colliding force of the cells coming from the microfluidic flow, but the tip needed to be small enough to penetrate the cell membrane and deliver biomolecular cargos.[33] Shalek et. al., 2012 have shown that cylindrical nanowire structures with >3 μm height, <150 nm diameter, and a density of 0.3-1 per μm^2 have minimal impact to the viability of human T cells.[33] Therefore, we decided to use 1μm PS beads to achieve the 1 per μm^2 density and 3 μm height. However, the aspect ratio of the nanoneedles is extremely critical, since where we found that nanoneedles with diameters <400 nm will result in broken structures upon cell collisions (**Figure III.S1**). Therefore, we used Si nanoneedle arrays with a 1 μm pitch, ~450 nm base, ~3 μm height, and sub-20-nm tip after removing the masking spheres.

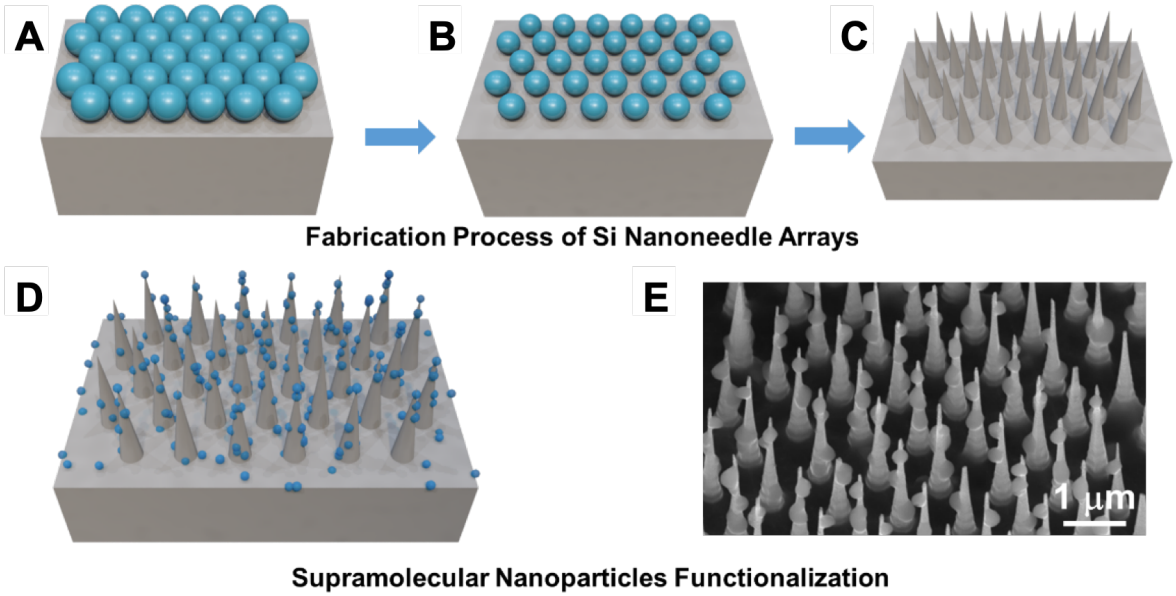

Figure III.1. Schematic of fabrication process of Si nanoneedle arrays via nanosphere lithography. (A) Step 1: Polystyrene spheres (PS) were self-assembled on Si substrate. (B) Step 2: The sizes of PS were reduced by oxygen plasma etching. (C) Step 3: Reactive ion etching to achieve Si nanoneedles. (D) Si nanoneedles were modified chemically to tether supramolecular nanoparticles. (E) A typical scanning electron micrograph (SEM) of Si nanoneedles functionalized with supramolecular nanoparticles (False Color).

Subsequently, the Si nanoneedle substrates were chemically modified to present adamantane (Ad) groups at their surfaces to enable tethering of the DNA-encapsulated SMNP. Anti-CD19-expressing CAR plasmid-encapsulated SMNPs (CAR⊂SMNPs) were prepared by mixing the CAR plasmid with SMNP building blocks. Here, the cyclodextrin-grafted polyethylenimine (CD-PEI) and adamantane-grafted polyamidoamine dendrimer (Ad-PAMAM) form positively charged hydrogel networks *via* the Ad and CD recognition that encapsulates the negatively charged DNA plasmids (**Figure III.S2**). The Ad-polyethylene glycol (PEG) acts as a capping reagent to stop the growth of the hydrogel network, yielding a controllable size of 150-200 nm for CAR⊂SMNPs (**Figure III.S3**).[34,35]

Molecular recognition between the Ad-functionalized Si nanoneedles and the CD moieties on the SMNP enables deposition of the payloads (**Figure III.1D, E**).

Our nanoneedle substrates were pre-loaded with CAR⊂SMNPs 30 min prior to the transfection experiments. Then, the substrates were rinsed thoroughly with phosphate-buffered saline (PBS) to remove any excess SMNPs. **Figure III.2A** illustrates working principles of the nanoneedle-microfluidic device. A chaotic mixing effect is achieved by implementing the herringbone structures on top of the polydimethylsiloxane (PDMS) microchannels. As a result, multiple effective cell-to-substrate contacts were established at an optimized flow rate of 0.5 mL/h,[36] which facilitated intracellular delivery of CAR⊂SMNPs. Once the target cells traveled through the microfluidic device, the transient pores in the membrane, caused by penetration of the nanoneedles, repairs within minutes.[37–41] The processed cells were subsequently collected to culture in the incubator (37 ^{o}C, 5% CO_2) for further characterization.

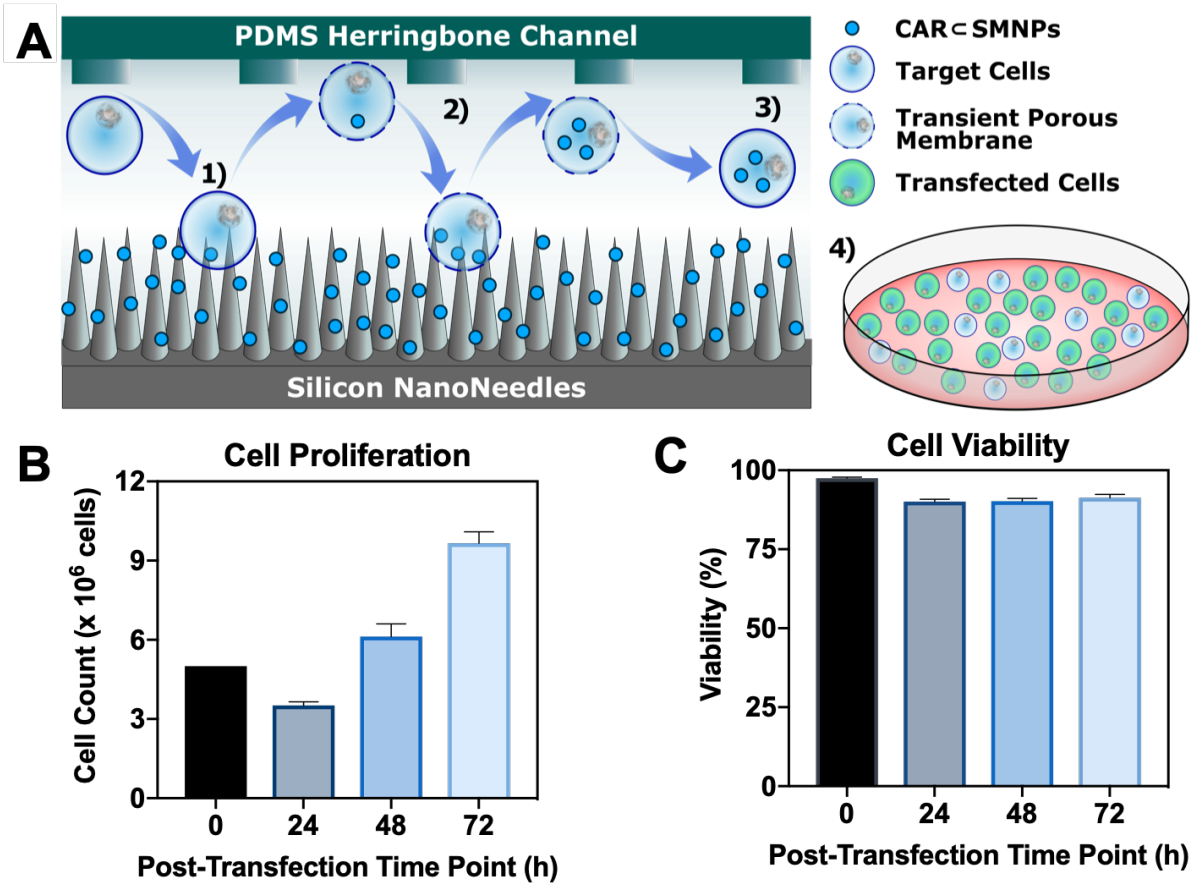

Figure III.2. (A) Schematic of the delivery of Anti-CD19-expression CAR plasmid encapsulated supramolecular nanoparticles (CAR⊂SMNPs) to target cells via the physical interaction between nanoneedles and target cells as they travel through a nanoneedle-microfluidic device. 1) Nanoparticle pickup by target cells through interaction with nanoneedles; 2) Polydimethylsiloxane (PDMS) microchannels with the herringbone structures induce chaotic mixing resulting in multiple interactions with nanoneedles creating transient porous membrane allowing extra nanoparticles to diffuse in; 3) Cell collecting and membrane repairing; 4) Cell culture in incubator. Cell (B) proliferation and (C) viability of Jurkat cells after being processed with the nanoneedle-microfluidic devices. Cells collected from the microfluidic devices maintain their proliferative capacity with above 90% viability after transfection. Errors represent standard errors of the means with N=10.

In general, we recovered more than 70% of the cells after transfection. The dense and ordered arrays of cone-shape Si nanoneedles (~1 nanoneedle/μm^2) distributed the incidental force uniformly throughout the membrane surface of the cells, thus reducing the

mechanical damage while allowing the cells to be easily released, which can be observed from the cell count and cell viability after the process. Cell contact with the nanoneedles enabled the direct delivery of pre-functionalized CAR⊂SMNPs into the cells, which has been previous reported.[36,42–46] Since the SMNPs are electrostatically tethered to the substrate, the cells uptake these nanoparticles upon contact with the nanoneedles. Moreover, we co-flow excess DNA-encapsulated nanoparticles with the cells, enabling SMNP replenishment and sustainable delivery. Since the CAR⊂SMNPs are formed *via* host-guest chemistry, the dynamic nature facilitates the dissociation of encapsulated DNA plasmids once they are inside the cells, improving transfection performance.[36,47,48]

The delivery of CAR⊂SMNPs to Jurkat cells, a model T cell line, was demonstrated using this nanoneedle-microfluidic device. After delivery, cell viability was measured by an automated cell counter using trypan blue to assess the number of viable cells at different time points post-transfection. As shown in **Figure III.2B**,**C**, the viability was higher than 90% after processing and their proliferation capacity was maintained. There was no significant statistical difference between the cell viability of the transfected cells at 0, 24, 48, and 72 h after transfection compared to the viability from the non-transfected control cells (**Figure III.S4**).

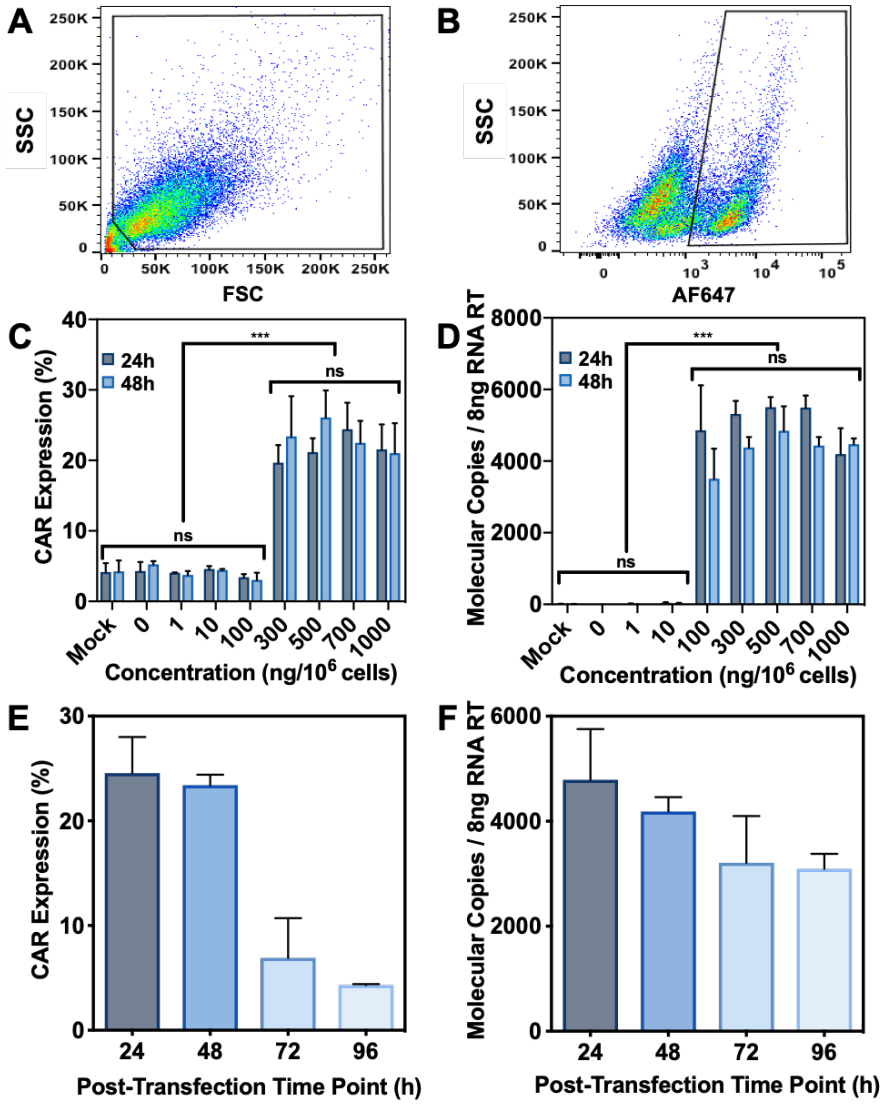

Figure III.3. Representative flow cytometry on CAR-modified Jurkat cells stained with anti-human IgG Fc gamma F(ab'). (A) Forward scatter (FSC) versus side scatter (SSC) density plot; (B) Alexa Fluor 647 (AF647)/SSC density plot. Concentration optimization for Jurkat cell CAR-transfection. (C) Flow cytometry analysis of Jurkat cells 24 and 48 h after delivery of anti-CD19 targeting chimeric antigen receptor (CD19CAR) expression plasmids. (D) Digital droplet polymerase chain reaction (ddPCR) at 24 and 48 h after anti-CD19 CAR delivery. Errors represent standard errors of the means with *N*=7 for each concentration. Significance is determined using a one-way ANOVA and a Tukey means comparison test (*** P <.001; ns is not significant). Transfection time course. Jurkat cells were transfected with 500 ng/ 1 x 10^6 cells via nanoneedle platform. Cells were collected and analyzed by (E) flow cytometry and (F) ddPCR at 24, 48, 72, and 96 h after transfection. Errors represent standard errors of the means with *N*=3.

To optimize transfection efficiency, different concentrations of CAR plasmids were tested. Post-transfection, the cells were fixed and analyzed by flow cytometry and digital droplet polymerase chain reaction (ddPCR). The collected cells were stained with Alexa Flour 647-conjugated anti-human IgG Fc gamma $F(ab')^2$ antibodies, which specifically stain CAR positive cells upon successful transfection. **Figure III.3A** shows a typical forward scatter (FSC) versus side scatter (SSC) density plot of the Jurkat cells after the transfection. The P1 population was gated to exclude debris and dead cells from the analysis. The gated population was then analyzed on an Alexa Fluor 647 (AF647)/SSC density plot (**Figure III.3B**). Plain Jurkat cells (Mock) were used as negative controls and demonstrated little fluorescence, forming a single AF647-negative population. Stably transduced anti-CD19 CAR-transduced Jurkat cells (positive control) exhibited fluorescence, forming AF647-positive population. Using these controls, thresholds were set to distinguish Jurkat cells that had been transfected with the CAR plasmid DNA clearly, allowing determination of intracellular delivery and expression efficiency.

Figure III.3C illustrates the transfection efficiency dependence on different DNA concentrations at 24 h and 48 h post-transfection expression of the anti-CD19 CAR. From flow cytometry results, we observed ~20-25% CAR expression when payloads of 300, 500, 700, and 1000 ng/million cells were delivered to Jurkat cells. Negative controls, in which the cells passed through the device without any DNA (Mock) or with empty nanoparticles (0 ng), had a ~5% background signal (**Figure III.3c**). When delivering payloads less than 300 ng (1, 10, and 100 ng) per million cells, we observed signals comparable to the background, indicating little to no transfection. Digital droplet PCR (ddPCR) was used as a secondary test of successful plasmid delivery and a quantitative measurement of the messenger RNA levels.

At 24 and 48 h, less than 10 copies/μL of CAR were detected from Mock and delivery payloads of 0, 1, and 10 ng/million cells; while payloads of 300-1000 ng/million cells exhibited ~4,000-6,000 copies/μL of CAR, complementing the flow cytometry results (**Figure III.3D**). These ddPCR results confirmed successful delivery and suggested that different payloads resulted in similar copy numbers. This result is consistent with the flow cytometry data, where substantial changes in the CAR expression level were not observed with increasing payloads, signifying a threshold in cell uptake capacity. Increasing DNA concentration from 300 to 1000 ng/million cells showed no significant increase in percentage of CAR expression or mRNA level. However, ddPCR detected 3000-4000 copies/μL from the samples where 100 ng/million cells of plasmid were delivered. This result suggests successful delivery of the plasmid to the cells, but the concentration is perhaps too low for the protein expression to be detected *via* flow cytometry.

To examine the dynamics of delivered plasmid DNA, Jurkat cells were transfected with the CAR plasmid at a concentration of 500 ng/million cells. Both flow cytometry and ddPCR data were taken at four time points during the 96-h incubation period. **Figure III.3E** shows that the CAR expression was ~25% at 24 h post-transfection, which was maintained at about the same level at 48 h. By 72 h, the expression decreased to about 8% and finally reached the background level (<~5%) at 96 h. A similar trend was observed in the corresponding ddPCR results (**Figure III.3F**). This trend indicates that our nanoneedle-microfluidic delivery enables transient transfection, which is expected as the expressed gene is lost through cell division during the culture.[49]

To validate the protein expression of the delivered plasmid to Jurkat cells further, we analyzed the transfected cells with fluorescence microscopy (**Figure III.S5**). Cells were stained with the Alexa Flour 647-conjugated anti-human IgG Fc gamma $F(ab')^2$ antibody as described above for flow cytometry analysis. We collected the cells at 24 h after transfection and compared them with a negative control, wild-type (WT) Jurkat cells, as well as a positive control, anti-CD19CAR-transduced Jurkat cells. The WT Jurkat cells showed no observable fluorescence signal, whereas the transfected cells and the anti-CD19CAR-induced Jurkat cells showed fluorescence signal on the cell membrane, indicating CAR protein expression on the surface and successful intracellular delivery.

To extend our method to hard-to-transfect primary cell lines, we tested our CAR delivery strategy with human T cells. Human T cells were isolated and enriched from whole blood samples collected from anonymous donors by the UCLA Virology core. The enriched T cell samples were characterized by automated cell counting for viability and by multicolor flow cytometry for expression of T cell markers (CD3, CD4, CD8, and CD45) prior to the nanoneedle-microfluidic transfection experiments (**Figure III.S6**). The enriched T cells were transfected with CAR plasmid at a concentration of 500 ng/million cells and a rate of 20 million cells per hour. Then, the cells were analyzed at three time points during the 72-h incubation period.

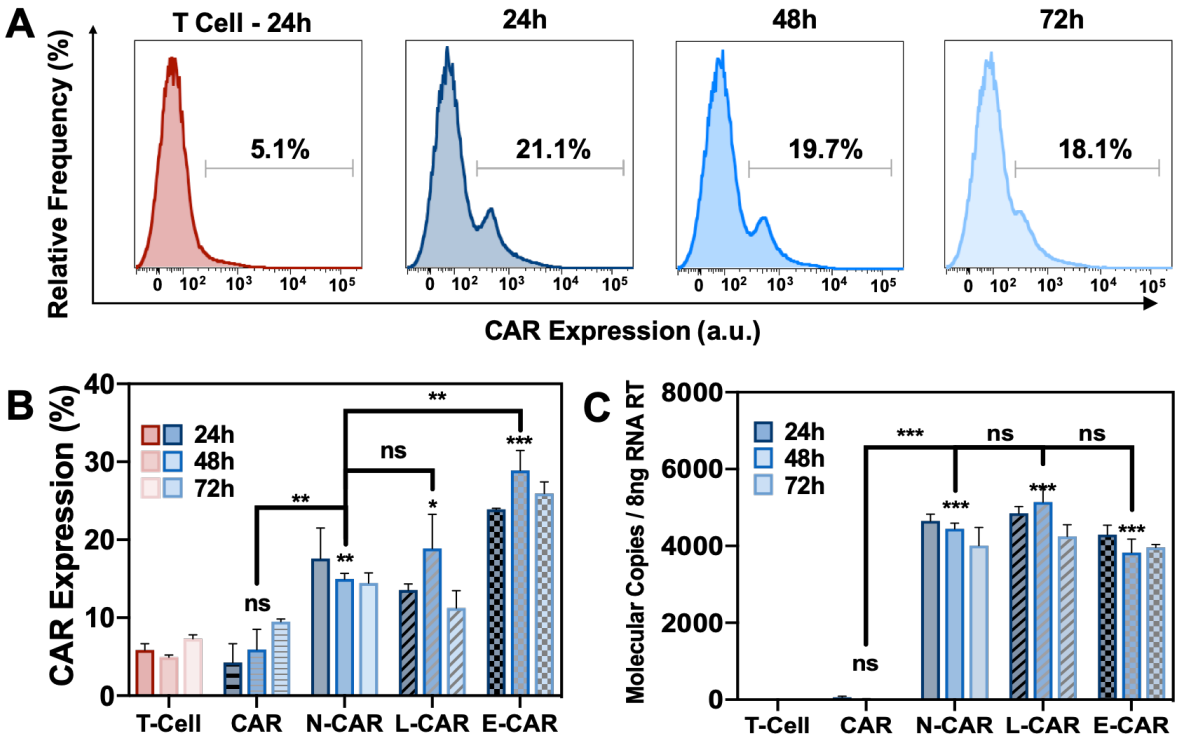

Figure III.4. (A) Representative flow cytometry histograms of nanoneedle-modified CAR-T cells stained with anti-human IgG Fc gamma F(ab'). (B) Flow cytometry analysis of T cells, T cells incubated with anti-CD19 CAR expression plasmids (CAR), T cells transfected with microfluidic nanoneedle (N-CAR), T cells transfected with Lipofectamine (L-CAR), and T cells transfected with electroporation (E-CAR). (C) Digital droplet polymerase chain reaction (ddPCR) of corresponding experiments. Errors represent standard errors of the means with *N*=5 for N-CAR, *N*=3 for T cell, CAR, L-CAR, and E-CAR. Significance is determined using a one-way ANOVA and a Tukey means comparison test (*P<.05, ** P <.01, *** P <.001, on top of bars for each group versus T-Cell expression; ** P <.01, *** P <.001, on top of bracket for each group versus N-CAR expression; ns is not significant).

Figure III.4A shows a representative flow cytometry histogram of CAR T cells processed by the nanoneedle-microfluidic device with approximately 21.1% CAR expression at 24 h (in comparison to 5.1% in the T-cell controls), which decreased by 72 h, consistent with the results from Jurkat cells. In **Figs. III.4B,C**, we compared the transfection efficiency of our nanoneedle-microfluidic method (N-CAR) with current benchmark techniques, such as electroporation (E-CAR) and lipofection (L-CAR), as well as negative controls of T cells

(T-Cell) and free CAR plasmid incubation (CAR). In **Figure III.4B**, the flow cytometry results showed that E-CAR exhibited slightly higher CAR expression (25-30%), while our method, N-CAR, resulted in 15-20%, comparable to L-CAR. Additionally, ddPCR showed that the copy number from N-CAR exhibited about 4,000-4,500 copies/μL, which was comparable to that of L-CAR and E-CAR (**Figure III.4C**). Overall, our method showed significantly higher CAR expression than the negative controls (T-Cell and CAR), indicating successful delivery to primary T cells. While the efficiency of our method is comparable to commercial standards, the viability of our method (N-CAR) is above 90% and the cell proliferation capacity was maintained and similar to the negative controls (T-Cell and CAR). This is a significant improvement relative to L-CAR and E-CAR, where their viabilities dropped to ~60-70% and in the case of E-CAR, the proliferation capacity of the transfected cells were hindered (**Figure III.S7**). The higher viability and cell proliferation of the transfected cells outweighs the slight CAR expression advantage of electroporation, lowering the barrier to clinical translation.

III.C. Conclusions and Prospects

In summary, we have demonstrated a high-throughput intracellular delivery approach using a rationally designed and fabricated nanoneedle-integrated microfluidic system. The ordered arrays of Si nanoneedles directly injects the biomolecular cargo to the targeted suspension cells by creating transient pores that enable cargo diffusion into the cells. Molecular recognition between the substrate and the nanoparticles enable continuous replenishing of the cargo, and thus sustainable delivery. Here, we showed this nanoneedle-microfluidic system to be a high-throughput, simple, and safe non-viral gene-delivery platform that can process >20 million cells/hour while maintaining above

90% cell viability and cell proliferative capacity. We demonstrated transient expression of CAR in a Jurkat model cell line with ~25% efficiency. We successfully transfected human donor-derived T cells at a level compared to current benchmark techniques, while preserving cell viability. This nanoneedle-microfluidic platform has potential for rapid production of CAR-T cells, illuminating a path to overcome the cell-processing requirements that is required by clinical oncologic treatment with CAR T-cell therapies.

III.D. Materials and Methods

III.D.1. Materials

Prime quality 4 in. Si (100) wafers (*p*-type/B-doped, 1-10 Ω×cm) were purchased from University Wafer Inc. (Boston, MA, USA). Polystyrene spheres were purchased from Thermo Fisher Scientific Inc. (Waltham, MA). Dimethyl sulfoxide, sodium dodecyl sulfate (398.5%), (3-aminopropyl)triethoxysilane (99%), and 1-adamantane isocyanate (97%) were purchased from Sigma-Aldrich (St. Louis, MO, USA). Lipofectamine® 3000 kits were purchased from Thermo Fisher Scientific Inc. (Waltham, MA). Cyclodextrin-grafted polyethyleneimine (CD-PEI), adamantane-grafted polyamidoamine dendrimer (Ad-PAMAM), adamantane-grafted poly(ethylene glycol) (Ad-PEG) were prepared and purified as reported previously.[34,50]

III.D.2. Preparation of Patterned Silicon Nanoneedle Substrates

Arrays of Si nanoneedles were prepared *via* multiple patterning nanosphere lithography.[32] Briefly, a close-packed monolayer of polystyrene spheres was transferred onto Si substrates. Stock dispersions of polystyrene spheres (1% solids) were assembled into close-packed monolayers at an air/water interface and transferred to silicon substrates.

Oxygen plasma (Oxford Plasmalab 80 Plus, Oxford Instruments, Abingdon, UK) was then applied to reduce the size of the spheres. The etching conditions were 35 sccm of O_2 and 10 sccm of Ar at a radio frequency (RF) power of 60 W and a pressure of 60 mTorr. Single-step deep reactive ion etching (STS Advanced Oxide Etcher) was performed with 21 sccm of C_4F_8, 27 sccm of SF_6, and 5 sccm of Ar at inductively coupled plasma power of 650 W, platen power of 9 W, and pressure of 12 mTorr to achieve a conical structure. Sub-20 nm tips were achieved when the polystyrene was completely etched and the height and base diameters were independently controlled by adjusting the etch time. Patterned Si nanoneedle substrates were sonicated in N-methyl-2-pyrolidone (NMP) for 1 min to remove the photoresist pattern, then were sonicated in isopropanol at room temperature for 1 min to remove the polymer residue.

III.D.3. Surface Functionalization of Silicon Nanoneedles

The substrate was then soaked in a piranha solution (3:1 (v/v) H_2SO_4/H_2O_2) for 1 h, rinsed with deionized water (DI), and dried under a stream of nitrogen. The silicon nanoneedle substrates were placed in a desiccator for vacuum deposition of (3-aminopropyl)triethoxysilane. Then, the substrates were immersed into 1-adamantane isocyanate in DMSO solution (1.0 mM) overnight. Afterward, the modified silicon substrates were washed three times with DMSO to remove excess 1-adamantane isocyanate. After, the substrates were rinsed with ethanol three times and stored at 4 ºC prior to integration with the microfluidics device and transfection studies with target cells.

III.D.4. Cell Culture and Isolation of Primary Human Cells

Jurkat cells (ATCC, Manassas, VA, USA) were cultured in Roswell Park Memorial Institute (RPMI) 1640 medium (Invitrogen, Damstadt, Germany) containing 10% FBS (R10 medium) and 100 IU/ml penicillin/streptomycin (Thermo Fisher Scientific, Waltham, MA) in 5% CO_2 at 37 °C. Human T cells were isolated from anonymous donor blood samples processed by the UCLA Center for AIDS Research (CFAR) Virology Core Laboratory. The RosetteSep Human T Cell Enrichment Cocktail (Stem Cell Technologies, Vancouver, BC) was used to isolate T cells from the peripheral blood mononuclear cells (PBMCs) populations. The isolated T cells were characterized by an automated cell counter for viability and by flow cytometry for expression of CD3, CD4, CD8, and CD45.

III.D.5. Vectors

The vector constructs for huEGFRt combined with an anti-CD19 second-generation chimeric antigen receptor (CAR) with the CD28 costimulatory molecule and CD3ζ chain was developed as described[51,52] and generously provided by Stephen Forman (City of Hope, Duarte, CA). The CD-19 CAR DNA plasmid was isolated from *Escherichia coli* using PureLink™ HiPure Plasmid MaxiPrep kits (Invitrogen, Darmstadt, Germany) according to the manufacture's guidelines.

III.D.6. Preparation of Gene-Encapsulated Supramolecular Nanoparticles

Gene-encapsulated supramolecular nanoparticles (SMNPs) were prepared *via* a host-guest chemistry-based method, as reported previously.[34,50] Briefly, the molecular building blocks Ad-PAMAM (3.96 μg), Ad-PEG (10.56 μg), CD-PEI (9.0 μg), and DNA plasmid

were combined under vigorous stirring in a 200 μL PBS solution. The mixture was kept at room temperature for 30 min, yielding the nanoparticles with a size of ~150 nm.

III.D.7. Microfluidic Nanostubstrate-Mediated Gene Delivery

In a typical gene-delivery experiment, 50 μL of the prepared gene-encapsulated supramolecular nanoparticle solution was aliquoted to incubate with the nanoneedle substrate in the microfluidic device 30 min prior to cell treatment. A total of $5x10^6$ Jurkat cells in 300 μL of RPMI medium and 150 μL of the prepared gene-encapsulated supramolecular nanoparticle solution were gently mixed and then introduced to the device at a rate of 0.5 mL/h. The cells were collected in a 1.5 mL Eppendorf tube with 500 mL of R10 medium, which was redistributed into two 6-well plates (Corning, Corning, NY) with a cell density of ~$2x10^6$ cells/well in 2 mL of R10 medium to culture at 37 ^oC, 5% CO_2. Collect cells were analyzed with flow cytometry and Quantitative reverse transcription-polymerase chain reaction (RT-qPCR) at 24 h and 48 h post-transfection.

III.D.8. Substrate Characterization

Scanning electron micrographs were recorded using a Zeiss Supra 40VP scanning electron microscope. Dynamic light scattering measurements were performed using a Zetasizer Nano instrument (Malvern Instruments Ltd., United Kingdom) equipped with a 10 mW helium-neon laser (λ = 632.8 nm) and a thermoelectric temperature controller.

III.D.9. Electroporation

For electroporation transfection controls, a cell pellet was re-suspended in 4D-Nucleofector™ Solution (Lonza, Switzerland) at a concentration of 5×10^5 cells per 20 µL. Then, the 20 µL cell suspension was transferred to a new tube and combined with 0.25 µg of plasmid DNA per reaction, composing up to 5% of the reaction mixture volume (1 µL of 250 ng/µL DNA per 20 µL cell suspension). The DNA/cell mixture was then transferred to the 20 µL reaction strip. Electroporation was carried out using the Lonza 4D-Nucleofector X-unit system, and the cells were allowed to sit at room temperature for 10 min following the reaction. Cells were resuspended with pre-warmed medium by gently pipetting up and down two to three times. The cells were equally distributed into 6-well cell culture plate with a cell density of 2×10^6 cells/well in 2 mL of media. Cells were collected for flow cytometry and Q-RT-ddPCR analysis at 24 h and 48h post-transfection.

III.D.10. Lipofection

DNA-lipid complexes were prepared according to the manufacturer's instructions. Briefly, complexes were prepared in Opti-MEM (Invitrogen, Carlsbad, CA) by mixing 0.5 µg of plasmid with 6 µL of lipofectamine LTX and 0.5 µL of PLUS reagents (Thermo Fisher Scientific, Waltham, MA) for each well in a 6-well plate. Before complexation, the DNA, PLUS reagent, and lipofectamine LTX were diluted with 149 µL and 144 µL of Opti-MEM. Complexes were left for 15-30 min at room temperature (RT) and then 250 µl of the DNA-lipid complex were added to the cells. Cells were analyzed by flow cytometry and Q-RT-ddPCR at 24, 48, and 72 h post-transfection.

III.D.11. Flow Cytometry

All flow cytometry measurements were made on a Fortessa cytometer (BD Biosciences, San Jose, CA) and data analyses were performed using BD FACS Diva Software 6.1 (BD Biosciences, San Jose, CA). The presence of the CAR was detected through flow cytometry using Alexa Fluor® 647-conjugated affiniPure $F(ab')_2$ fragment goat anti-human IgG, Fcγ fragment specific (Jackson ImmunoResearch Laboratories, West Grove, PA), which binds to the IgG1 Fcγ hinge region of the CAR construct.[1,53] The CD19 CAR expression was assessed by staining with the fluorescent-labeled murine monoclonal antibodies for 20 min in the dark at 4 °C, followed by washing in PBS with 2.5% FBS and fixation using BD stabilizing fixative (BD Biosciences, San Jose, CA) as described previously.[1] All experiments with determinations of geometric MFI were performed using the same protocol, fluorochrome voltages, and cytometer.

III.D.12. RNA Extraction and Reverse Transcription

Total RNA was extracted from collecting cells with spin-columns (RNeasy Plus Mini Kit, QIAGEN, Hilden, Germany) using the manufacturer's protocol. The RNA quality was determined using a nanodrop spectrophotometer (Thermo Fisher Scientific, Waltham, MA). All of the RNA samples used for the study were pure (A260/A280 ≥ 1.9; A260/A230 ≥ 2). Once purified, 200 ng RNA was subjected for reverse transcription in 50 µL of reaction using M-MLV reverse transcriptase (Thermo Fisher Scientific, Waltham, MA) and random hexamers (Thermo Fisher Scientific, Waltham, MA). The reactions were carried on at 37 °C for 50 min and deactivated by incubating at 70 °C for 15 min.

III.D.13. Droplet Digital PCR

Droplet digital PCR was performed with a QX200 Droplet Digital PCR System (Bio-Rad, Hercules, CA), according to the manufacturer's protocol.[54] Briefly, each of the 20 μL reactions contained 1× EvaGreen ddPCR Supermix (Bio-Rad, Hercules, CA), 250 nM gene-specific primers, and 2 μL of the cDNA sample. The following primers for CD19RCD28MZ were designed with Vector NIT software: forward: 5'- CCTGGTGAAGGGCTTCTACC -3' and reverse: 5'-CGGAGCAGCTAAAGACGTTG -3' (179 bp amplicon). Each reaction was mixed with 70 μL of Droplet Generation Oil (Bio-Rad, Hercules, CA), partitioned into 14,000-17,000 droplets in the QX200 Droplet Generator (Bio-Rad, Hercules, CA), which was transferred to 96-well plates (Bio-Rad, Hercules, CA) and heat sealed with foil by a PX™ PCR Plate Sealer (Bio-Rad, Hercules, CA). The PCR reactions were performed in a T100™ Thermal Cycler (Bio-Rad, Hercules, CA) with the following cycling conditions: 1× (95 °C for 5 min), 40× (95 °C for 30 s, 60 °C for 1 min), 1× (4 °C for 5 min, 90 °C for 5 min) with 2 °C/s ramp rate, hold at 4 °C. Immediately following end-point amplification, the fluorescence intensity of individual droplets was measured with the QX200 Droplet Reader (Bio-Rad, Hercules, CA). After data acquisition, the data analysis was performed with QuantaSoft droplet reader software (Bio-Rad, Hercules, CA) with manual thresholding. The absolute transcript levels reported were copies/μL of the final 1x ddPCR reaction.

III.D.14. Fluorescence Microscopy Imaging

Cells were pelleted and resuspended in PBS with 2.5% FBS and fixation using BD stabilizing fixative (BD Biosciences, San Jose, CA). The fixed cells were mixed in a 3:1 ratio with ProLong™ Diamond Antifade Mountant with DAPI (Invitrogen, Darmstadt, Germany)

onto clean microscope glass slides (VWR International, Radnor, PA) and sealed with a coverslip (Fisher Scientific, Hampton, NH, USA). Images were taken at 20x with the Zeiss M2 Imager with Apotome 2 and Zen Blue software (Zeiss, Oberkochen, Germany) with the DAPI fluorescent channel (exposure time = 300 ms) and the Cy5 fluorescent channel (exposure time = 2 s). All post-analysis and image processing were done with Fiji (ImageJ).

III.D.15. Statistical Analysis

Statistical analyses were performed using Graph Pad Prism 6.01 (GraphPad Software, CA, USA). All data were expressed as mean ± standard errors of the means (SEM). Analysis of variance (ANOVA) was used for multiple comparison. $P < 0.05$ was considered statistically significant.

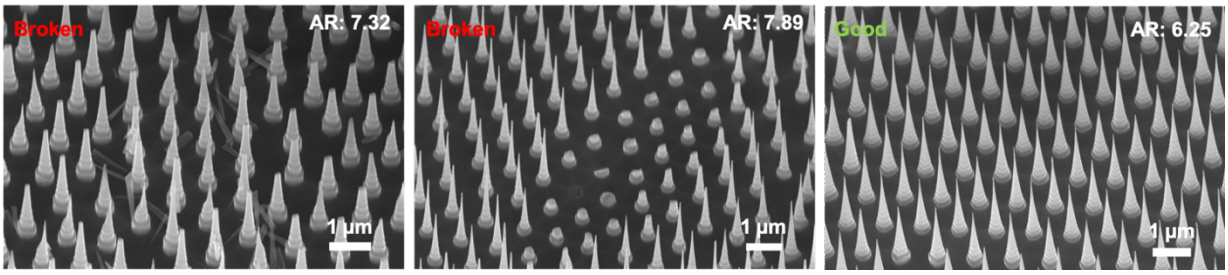

Figure III.S1. Scanning electron micrographs of nanoneedle structures after transfection experiment. Higher aspect ratio results in broken nanoneedles. Images were recorded at a tilt of 30°

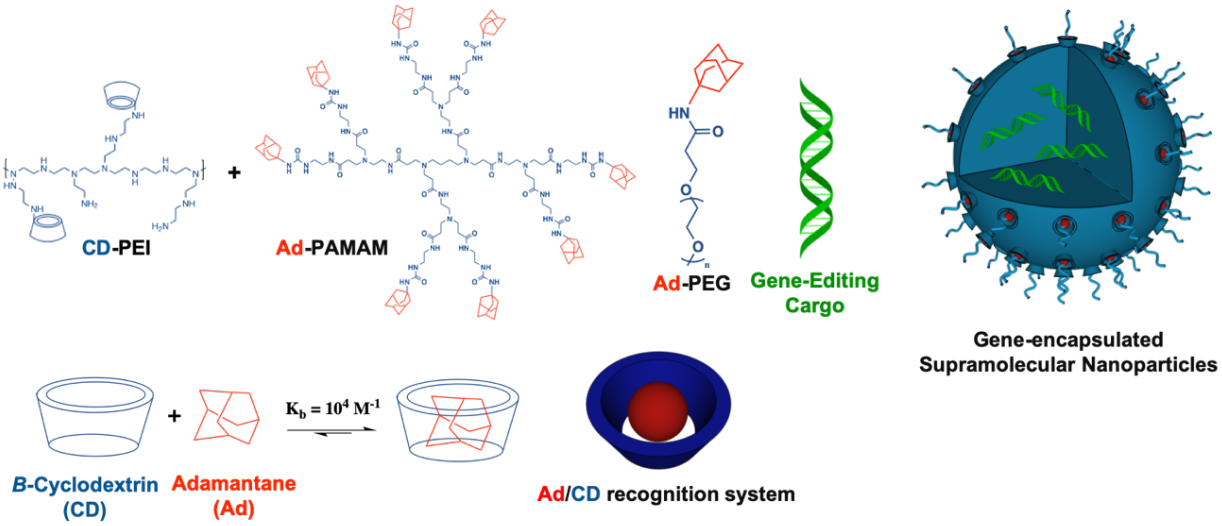

Figure III.S2. Scheme illustrating gene-encapsulated supramolecular nanoparticle (SMNP) formation. The molecular recognition between adamantane (Ad) and ß-cyclodextrin (ß-CD) motifs present on the molecular building blocks cyclodextrin-grafted polyethyleneimine (CD-PEI) and adamantane-grafted polyamidoamine dendrimer (Ad-PAMAM) enables the self-assembly of supramolecular nanoparticle (SMNP) that serve as carriers for biomolecular cargos (e.g., nucleic acids, proteins). The CD-PEI and Ad-PAMAM complex form cationic hydrogel networks that encapsulate negatively charged payloads, while the adamantane-grafted poly(ethylene glycol) (Ad-PEG) constrains nanoparticle growth.

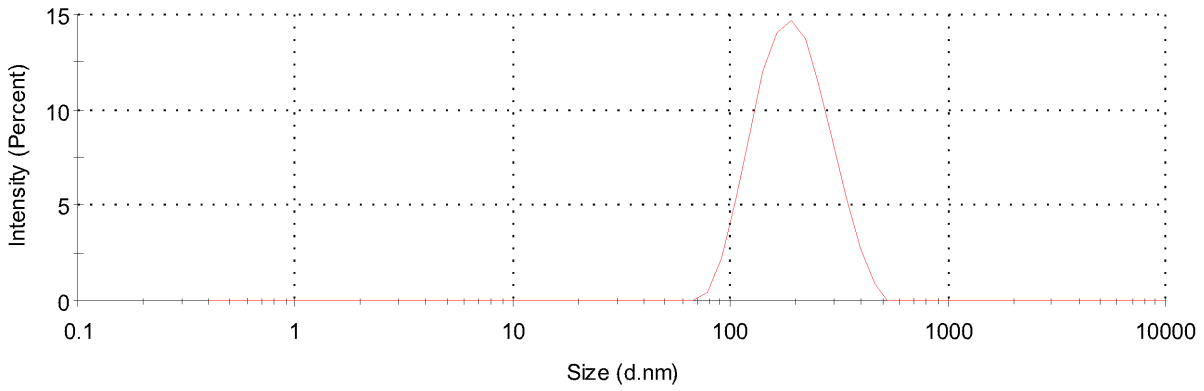

Figure III.S3. Representative Dynamic Light Scatter (DLS) measurement of the gene-encapsulated supramolecular nanoparticle (SMNP)

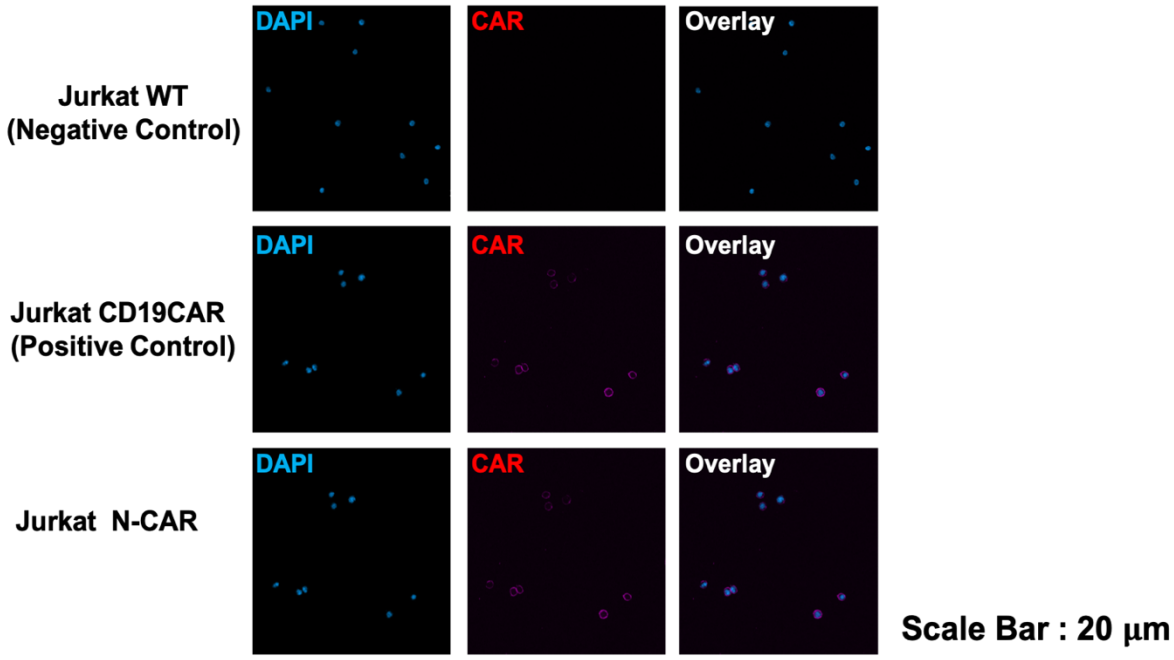

Figure III.S4. Fluorescence microscope images of Jurkat WT cells (negative control), anti-CD19 CAR-transduced Jurkat cells (positive control), Jurkat cells transfected with the microfluidic nanoneedle platform (N-CAR). The cells were stained with anti-human IgG Fc gamma F(ab') and fixed at 24 h after transfection. The nucleuses were stained with DAPI.

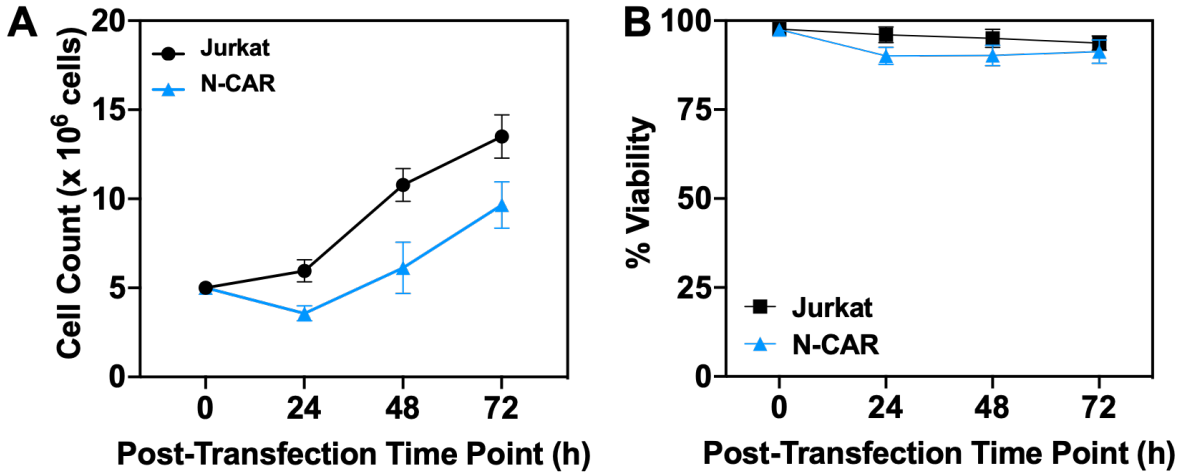

Figure III.S5. (A) Cell proliferation and (B) cell viability data of negative control (Jurkat cells) and Jurkat cells transfected with microfluidic nanoneedle (N-CAR).

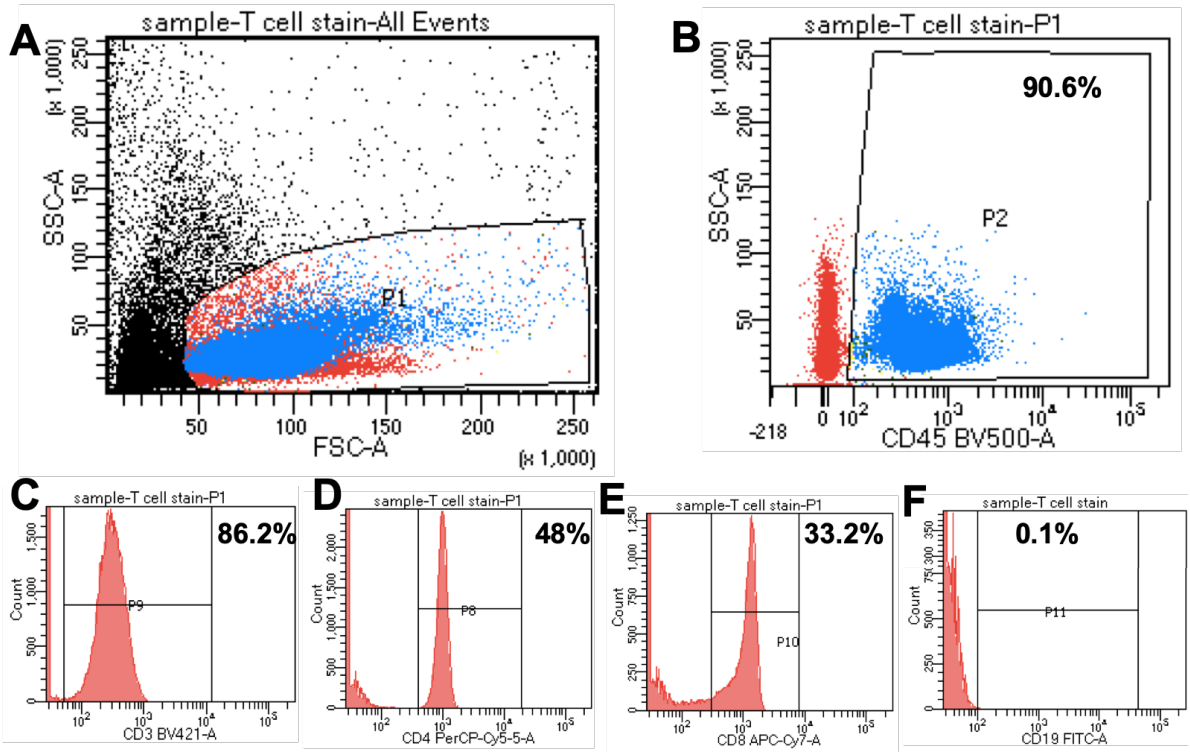

Figure III.S6. Isolated T cell characterization by flow cytometer prior to the nanoneedle-microfluidic transfection experiments (A) Representative flow cytometry FSC-SSC plot (B) CD45 positive cells (C) CD3 positive cells (D) CD4 positive cells (E) CD8 positive cells (F) CD19 positive cells

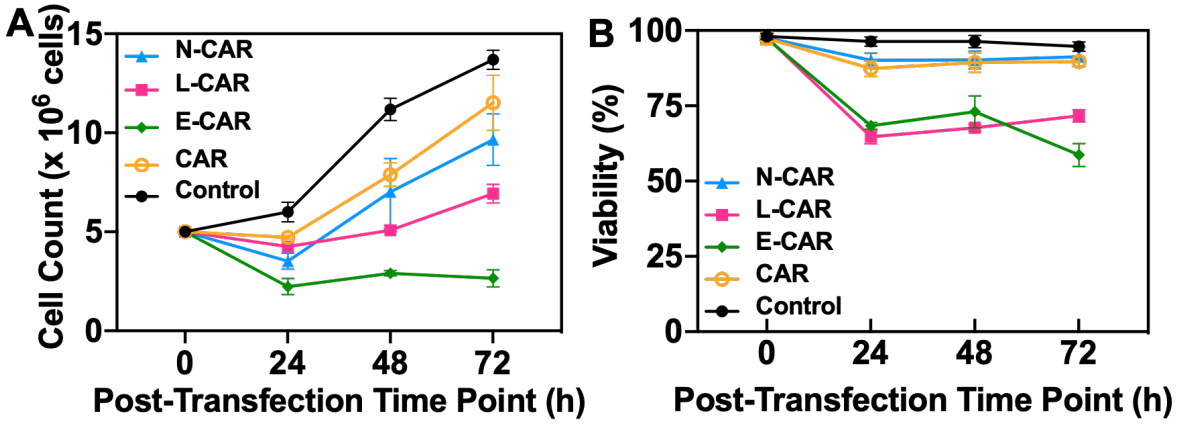

Figure III.S7. (A) Cell proliferation and (B) cell viability data of T cells transfected with microfluidic nanoneedle (N-CAR), T cells transfected with Lipofectamine (L-CAR), T cells transfected with electroporation (E-CAR), and T cells incubated with anti-CD19 CAR expression plasmids (CAR).

III.E. References

(1) De Oliveira, S. N.; Wang, J.; Ryan, C.; Morrison, S. L.; Kohn, D. B.; Hollis, R. P. A CD19/Fc Fusion Protein for Detection of Anti-CD19 Chimeric Antigen Receptors. *J. Transl. Med.* **2013**, *11*.

(2) Dzhandzhugazyan, K. N.; Guldberg, P.; Kirkin, A. F. Adoptive T Cell Cancer Therapy. *Nat. Mater.* **2018**, *17*, 475–477.

(3) Brentjens, R. J.; Davila, M. L.; Riviere, I.; Park, J.; Wang, X.; Cowell, L. G.; Bartido, S.; Stefanski, J.; Taylor, C.; Olszewska, M.; et al. CD19-Targeted T Cells Rapidly Induce Molecular Remissions in Adults with Chemotherapy-Refractory Acute Lymphoblastic Leukemia. *Sci. Transl. Med.* **2013**, *5*, 177ra38-177ra38.

(4) Grupp, S. A.; Kalos, M.; Barrett, D.; Aplenc, R.; Porter, D. L.; Rheingold, S. R.; Teachey, D. T.; Chew, A.; Hauck, B.; Wright, J. F.; et al. Chimeric Antigen Receptor–Modified T Cells for Acute Lymphoid Leukemia. *N. Engl. J. Med.* **2013**, *368*, 1509–1518.

(5) Lee, D. W.; Kochenderfer, J. N.; Stetler-Stevenson, M.; Cui, Y. K.; Delbrook, C.; Feldman, S. A.; Fry, T. J.; Orentas, R.; Sabatino, M.; Shah, N. N.; et al. T Cells Expressing CD19 Chimeric Antigen Receptors for Acute Lymphoblastic Leukaemia in Children and Young Adults: A Phase 1 Dose-Escalation Trial. *The Lancet* **2015**, *385*, 517–528.

(6) Thomas, C. E.; Ehrhardt, A.; Kay, M. A. Progress and Problems with the Use of Viral Vectors for Gene Therapy. *Nat. Rev. Genet.* **2003**, *4*, 346–358.

(7) Gresch, O.; Altrogge, L. Transfection of Difficult-to-Transfect Primary Mammalian Cells. In *Protein Expression in Mammalian Cells*; Hartley, J. L., Ed.; Humana Press: Totowa, NJ, 2012; Vol. 801, pp 65–74.

(8) Hamm, A.; Krott, N.; Breibach, I.; Blindt, R.; Bosserhoff, A. K. Efficient Transfection Method for Primary Cells. *Tissue Eng.* **2002**, *8*, 235–245.

(9) Van Tendeloo, V. F. I. Highly Efficient Gene Delivery by MRNA Electroporation in Human Hematopoietic Cells: Superiority to Lipofection and Passive Pulsing of MRNA and to Electroporation of Plasmid CDNA for Tumor Antigen Loading of Dendritic Cells. *Blood* **2001**, *98*, 49–56.

(10) Gresch, O. New Non-Viral Method for Gene Transfer into Primary Cells. *Methods* **2004**, *33*, 151–163.

(11) Robbins, P. D.; Ghivizzani, S. C. Viral Vectors for Gene Therapy. *Pharmacol. Ther.* **1998**, *80*, 35–47.

(12) Wu, Z.; Yang, H.; Colosi, P. Effect of Genome Size on AAV Vector Packaging. *Mol. Ther.* **2010**, *18*, 80–86.

(13) Kotterman, M. A.; Schaffer, D. V. Engineering Adeno-Associated Viruses for Clinical Gene Therapy. *Nat. Rev. Genet.* **2014**, *15*, 445–451.

(14) Nguyen, L. T.; Atobe, K.; Barichello, J. M.; Ishida, T.; Kiwada, H. Complex Formation with Plasmid DNA Increases the Cytotoxicity of Cationic Liposomes. *Biol. Pharm. Bull.* **2007**, *30*, 751–757.

(15) Stewart, M. P.; Sharei, A.; Ding, X.; Sahay, G.; Langer, R.; Jensen, K. F. In Vitro and Ex Vivo Strategies for Intracellular Delivery. *Nature* **2016**, *538*, 183–192.

(16) Stewart, M. P.; Langer, R.; Jensen, K. F. Intracellular Delivery by Membrane Disruption: Mechanisms, Strategies, and Concepts. *Chem. Rev.* **2018**, *118*, 7409–7531.

(17) Li, S.-D.; Huang, L. Gene Therapy Progress and Prospects: Non-Viral Gene Therapy by Systemic Delivery. *Gene Ther.* **2006**, *13*, 1313–1319.

(18) Davis, M. E. Non-Viral Gene Delivery Systems. *Curr. Opin. Biotechnol.* **2002**, *13*, 128-131.

(19) Mintzer, M. A.; Simanek, E. E. Nonviral Vectors for Gene Delivery. *Chem. Rev.* **2009**, *109*, 259–302.

(20) Lungwitz, U.; Breunig, M.; Blunk, T.; Göpferich, A. Polyethylenimine-Based Non-Viral Gene Delivery Systems. *Eur. J. Pharm. Biopharm.* **2005**, *60*, 247–266.

(21) Tabar, M. S.; Hesaraki, M.; Esfandiari, F.; Samani, F. S.; Vakilian, H.; Baharvand, H. Evaluating Electroporation and Lipofectamine Approaches for Transient and Stable Transgene Expressions in Human Fibroblasts and Embryonic Stem Cells. *Cell J Yakhteh* **2017**, No. 3.

(22) Sharei, A.; Zoldan, J.; Adamo, A.; Sim, W. Y.; Cho, N.; Jackson, E.; Mao, S.; Schneider, S.; Han, M.-J.; Lytton-Jean, A.; Basto, P. A.; Jhunjhunwala, S.; Lee, J.; Heller, D. A.; Kang, J. W.; Hartoularos, G. C.; Kim, K.-S.; Anderson, D. G.; Langer, R.; Jensen, K. F. A Vector-Free Microfluidic Platform for Intracellular Delivery. *Proc. Natl. Acad. Sci.* **2013**, *110*, 2082-2087.

(23) Han, X.; Liu, Z.; Jo, M. chan; Zhang, K.; Li, Y.; Zeng, Z.; Li, N.; Zu, Y.; Qin, L. CRISPR-Cas9 Delivery to Hard-to-Transfect Cells via Membrane Deformation. *Sci. Adv.* **2015**, *1*, e1500454.

(24) Deng, Y.; Kizer, M.; Rada, M.; Sage, J.; Wang, X.; Cheon, D.-J.; Chung, A. J. Intracellular Delivery of Nanomaterials via an Inertial Microfluidic Cell Hydroporator. *Nano Lett.* **2018**, *18*, 2705–2710.

(25) Chen, J.; Guo, Z.; Tian, H.; Chen, X. Production and Clinical Development of Nanoparticles for Gene Delivery. *Mol. Ther. - Methods Clin. Dev.* **2016**, *3*, 16023.

(26) Tian, H.; Chen, J.; Chen, X. Nanoparticles for Gene Delivery. *Small* **2013**, *9*, 2034–2044.

(27) Bonde, S.; Buch-Månson, N.; Rostgaard, K. R.; Andersen, T. K.; Berthing, T.; Martinez, K. L. Exploring Arrays of Vertical One-Dimensional Nanostructures for Cellular Investigations. *Nanotechnology* **2014**, *25*, 362001.

(28) Shalek, A. K.; Robinson, J. T.; Karp, E. S.; Lee, J. S.; Ahn, D.-R.; Yoon, M.-H.; Sutton, A.; Jorgolli, M.; Gertner, R. S.; Gujral, T. S.; MacBeath, G.; Yang, E. G.; Park, H. Vertical Silicon Nanowires as a Universal Platform for Delivering Biomolecules into Living Cells. *Proc. Natl. Acad. Sci.* **2010**, *107*, 1870–1875.

(29) Elnathan, R.; Kwiat, M.; Patolsky, F.; Voelcker, N. H. Engineering Vertically Aligned Semiconductor Nanowire Arrays for Applications in the Life Sciences. *Nano Today* **2014**, *9*, 172–196.

(30) Prinz, C. N. Interactions between Semiconductor Nanowires and Living Cells. *J. Phys. Condens. Matter* **2015**, *27*, 233103.

(31) Elnathan, R.; Delalat, B.; Brodoceanu, D.; Alhmoud, H.; Harding, F. J.; Buehler, K.; Nelson, A.; Isa, L.; Kraus, T.; Voelcker, N. H. Maximizing Transfection Efficiency of Vertically Aligned Silicon Nanowire Arrays. *Adv. Funct. Mater.* **2015**, *25*, 7215–7225.

(32) Xu, X.; Yang, Q.; Wattanatorn, N.; Zhao, C.; Chiang, N.; Jonas, S. J.; Weiss, P. S. Multiple-Patterning Nanosphere Lithography for Fabricating Periodic Three-Dimensional Hierarchical Nanostructures. *ACS Nano* **2017**, *11*, 10384–10391.

(33) Shalek, A. K.; Gaublomme, J. T.; Wang, L.; Yosef, N.; Chevrier, N.; Andersen, M. S.; Robinson, J. T.; Pochet, N.; Neuberg, D.; Gertner, R. S.; et al. Nanowire-Mediated Delivery Enables Functional Interrogation of Primary Immune Cells: Application to the Analysis of Chronic Lymphocytic Leukemia. *Nano Lett.* **2012**, *12*, 6498–6504.

(34) Wang, H.; Wang, S.; Su, H.; Chen, K.-J.; Armijo, A. L.; Lin, W.-Y.; Wang, Y.; Sun, J.; Kamei, K.; Czernin, J.; et al. A Supramolecular Approach for Preparation of Size-Controlled Nanoparticles. *Angew. Chem. Int. Ed.* **2009**, *48*, 4344–4348.

(35) Wang, H.; Liu, K.; Chen, K.-J.; Lu, Y.; Wang, S.; Lin, W.-Y.; Guo, F.; Kamei, K.; Chen, Y.-C.; Ohashi, M.; et al. A Rapid Pathway Toward a Superb Gene Delivery System: Programming Structural and Functional Diversity into a Supramolecular Nanoparticle Library. *ACS Nano* **2010**, *4*, 6235–6243.

(36) Peng, J.; Garcia, M. A.; Choi, J.; Zhao, L.; Chen, K.-J.; Bernstein, J. R.; Peyda, P.; Hsiao, Y.-S.; Liu, K. W.; Lin, W.-Y.; et al. Molecular Recognition Enables Nanosubstrate-Mediated Delivery of Gene-Encapsulated Nanoparticles with High Efficiency. *ACS Nano* **2014**, *8*, 4621–4629.

(37) Chang, D. C.; Reese, T. S. Changes in Membrane Structure Induced by Electroporation as Revealed by Rapid-Freezing Electron Microscopy. *Biophys. J.* **1990**, *58*, 1–12.

(38) Murakami, M.; Kano, F.; Murata, M. LLO-Mediated Cell Resealing System for Analyzing Intracellular Activity of Membrane-Impermeable Biopharmaceuticals of Mid-Sized Molecular Weight. *Sci. Rep.* **2018**, *8*.

(39) Idone, V.; Tam, C.; Goss, J. W.; Toomre, D.; Pypaert, M.; Andrews, N. W. Repair of Injured Plasma Membrane by Rapid Ca $^{2+}$ -Dependent Endocytosis. *J. Cell Biol.* **2008**, *180*, 905-914.

(40) Tang, S. K. Y.; Marshall, W. F. Self-Repairing Cells: How Single Cells Heal Membrane Ruptures and Restore Lost Structures. *Science* **2017**, *356*, 1022–1025.

(41) McNeil, P. L.; Miyake, K.; Vogel, S. S. The Endomembrane Requirement for Cell Surface Repair. *Proc. Natl. Acad. Sci.* **2003**, *100*, 4592–4597.

(42) Xie, X.; Xu, A. M.; Angle, M. R.; Tayebi, N.; Verma, P.; Melosh, N. A. Mechanical Model of Vertical Nanowire Cell Penetration. *Nano Lett.* **2013**, *13*, 6002–6008.

(43) Chiappini, C.; De Rosa, E.; Martinez, J. O.; Liu, X.; Steele, J.; Stevens, M. M.; Tasciotti, E. Biodegradable Silicon Nanoneedles Delivering Nucleic Acids Intracellularly Induce Localized in Vivo Neovascularization. *Nat. Mater.* **2015**, *14*, 532–539.

(44) Nair, B. G.; Hagiwara, K.; Ueda, M.; Yu, H.; Tseng, H.-R.; Ito, Y. High Density of Aligned Nanowire Treated with Polydopamine for Efficient Gene Silencing by SiRNA According to Cell Membrane Perturbation. *ACS Appl. Mater. Interfaces* **2016**, *8*, 18693–18700.

(45) Kim, W.; Ng, J. K.; Kunitake, M. E.; Conklin, B. R.; Yang, P. Interfacing Silicon Nanowires with Mammalian Cells. *JACS.* **2007**, *129*, 7228–7229.

(46) Chiappini, C.; De Rosa, E.; Martinez, J. O.; Liu, X.; Steele, J.; Stevens, M. M.; Tasciotti, E. Biodegradable Silicon Nanoneedles Delivering Nucleic Acids Intracellularly Induce Localized in Vivo Neovascularization. *Nat. Mater.* **2015**, *14*, 532–539.

(47) Wang, H.; Wang, S.; Su, H.; Chen, K.-J.; Armijo, A. L.; Lin, W.-Y.; Wang, Y.; Sun, J.; Kamei, K.-I.; Czernin, J.; Radu, C. G.; Tseng, H.-R. A Supramolecular Approach for Preparation of Size-Controlled Nanoparticles. *Angew. Chem. Int. Ed.* **2009**, *48*, 4344–4348.

(48) Hou, S.; Choi, J.-S.; Chen, K.-J.; Zhang, Y.; Peng, J.; Garcia, M. A.; Yu, J.-H.; Thakore-Shah, K.; Ro, T.; Chen, J.-F.;Peyda, P.; Fan, G.; Pyle, A. D.; Wang, H.; Tseng, H.-R. Supramolecular Nanosubstrate-Mediated Delivery for Reprogramming and Transdifferentiation of Mammalian Cells. *Small* **2015**, *11*, 2499–2504.

(49) Kim, T. K.; Eberwine, J. H. Mammalian Cell Transfection: The Present and the Future. *Anal. Bioanal. Chem.* **2010**, *397*, 3173–3178.

(50) Hou, S.; Choi, J.; Chen, K.-J.; Zhang, Y.; Peng, J.; Garcia, M. A.; Yu, J.-H.; Thakore-Shah, K.; Ro, T.; Chen, J.-F.; et al. Supramolecular Nanosubstrate-Mediated Delivery for Reprogramming and Transdifferentiation of Mammalian Cells. *Small* **2015**, *11*, 2499-2504.

(51) Wang, X.; Chang, W.-C.; Wong, C. W.; Colcher, D.; Sherman, M.; Ostberg, J. R.; Forman, S. J.; Riddell, S. R.; Jensen, M. C. A Transgene-Encoded Cell Surface Polypeptide for Selection, in Vivo Tracking, and Ablation of Engineered Cells. *Blood* **2011**, *118*, 1255-1263.

(52) Jonnalagadda, M.; Mardiros, A.; Urak, R.; Wang, X.; Hoffman, L. J.; Bernanke, A.; Chang, W.-C.; Bretzlaff, W.; Starr, R.; Priceman, S.; et al. Chimeric Antigen Receptors with Mutated IgG4 Fc Spacer Avoid Fc Receptor Binding and Improve T Cell Persistence and Antitumor Efficacy. *Mol. Ther.* **2015**, *23*, 757–768.

(53) Kowolik, C. M.; Topp, M. S.; Gonzalez, S.; Pfeiffer, T.; Olivares, S.; Gonzalez, N.; Smith, D. D.; Forman, S. J.; Jensen, M. C.; Cooper, L. J. N. CD28 Costimulation Provided through a CD19-Specific Chimeric Antigen Receptor Enhances In Vivo Persistence and Antitumor Efficacy of Adoptively Transferred T Cells. *Cancer Res.* **2006**, *66*, 10995–11004.

(54) McDermott, G. P.; Do, D.; Litterst, C. M.; Maar, D.; Hindson, C. M.; Steenblock, E. R.; Legler, T. C.; Jouvenot, Y.; Marrs, S. H.; Bemis, A.; et al. Multiplexed Target Detection Using DNA-Binding Dye Chemistry in Droplet Digital PCR. *Anal. Chem.* **2013**, *85*, 11619–11627.

CHAPTER IV

Conclusions and Prospects

IV.A. Summary

In this dissertation, I described how we have developed a novel and scalable nanopatterning technique, adapted from nanosphere lithography (NSL), for fabrication of periodic three-dimensional hierarchical nanostructures with tunable optical and plasmonic properties (Chapter II).[1] In addition, I optimized NSL to fabricate nanostructures and integrated them into microfluidic device for intracellular delivery *via* physical membrane deformation. In this work, I showed the platform to be a safe and efficient method for sustainable CAR-T cell production.

IV.B. Multiple-Patterning Nanosphere Lithography for Fabricating Periodic Three-Dimensional Hierarchical Nanostructures

Three-dimensional periodic silicon-based nanostructures have proven to be useful optical, electrical, and mechanical properties; however, these types of structures remain difficult to fabricate in a facile manner. Nanosphere lithography is a simple, high-throughput technique that can be used to form large-area, close-packed monolayer arrays of nanospheres. These arrays can be directly used as etch masks to generate silicon-based nanostructures. Typically, the nanostructures produced are created by single etches of the nanosphere array mask. Here, we reported multiple patterning nanosphere lithography, which enables size tuning of the nanostructures in three dimensions utilizing the nanospheres for multilayer masking throughout multiple rounds of etching. By exploiting the degradable nature of polystyrene during reactive ion etching, we have fabricated large-area three-dimensional periodic silicon nanostructures such as multilevel solid/hollow nanotowers. These hierarchical nanostructures can be precisely tailored to be tiered with independent tunability in height and diameter at each level. By combining metal

deposition with subsequent reactive ion etching, we can fabricate 3D concentric plasmonic nanodisk/nanorings with tunable optical properties on a variety of substrates. These results were described in detail in Chapter II and published in *ACS Nano*.[1]

IV.C. Nanosubstrate-Mediated Intracellular Delivery for High-Throughput Gene Modification.

Non-viral gene delivery methods have significant advantages in terms of biosafety, cargo size, and cost.[2] Physical techniques to produce membrane disruption *via* nanoneedles have the capability to penetrate cell membranes and to deliver genetic cargos.[3,4] However, the challenges for these systems include inconsistency of membrane penetration and slow processing throughputs, which lead to low transfection efficiency and poor viability of cell products. Here, we used an ordered array silicon nanoneedles fabricated by combining nanosphere lithography with isotropic dry etching of silicon. Gene-encapsulated supramolecular nanoparticles were then tethered on the nanoneedle surfaces *via* supramolecular recognition.[5,6] By integrating the nanoneedles with microfluidic devices, we demonstrated the system to be a high-throughput, simple, and safe non-viral gene-delivery platform that can process >20 million cells in an hour while maintaining over 90% cell viability and cell proliferative capacity. We also showed transient expression of chimeric antigen receptor plasmid in Jurkat model cell line with ~25% efficiency. Moreover, we successfully transfected patient-derived T cells at a level compared to current benchmark techniques, while preserving cell viability.[7] The versatile and scalable nanostructured platform proposed here represents a promissing system for the genetic engineering of a variety of cell types that will empower research focused on gene therapies and enable translation of these cellular therapy approaches.

IV.D. References

(1) Xu, X.; Yang, Q.; Wattanatorn, N.; Zhao, C.; Chiang, N.; Jonas, S. J.; Weiss, P. S. Multiple-Patterning Nanosphere Lithography for Fabricating Periodic Three-Dimensional Hierarchical Nanostructures. *ACS Nano* **2017**, *11*, 10384–10391.

(2) Davis, M. E. Non-Viral Gene Delivery Systems. *Curr. Opin. Biotechnol.* **2002**, *13*, 128-131.

(3) Elnathan, R.; Delalat, B.; Brodoceanu, D.; Alhmoud, H.; Harding, F. J.; Buehler, K.; Nelson, A.; Isa, L.; Kraus, T.; Voelcker, N. H. Maximizing Transfection Efficiency of Vertically Aligned Silicon Nanowire Arrays. *Adv. Funct. Mater.* **2015**, *25*, 7215–7225.

(4) Elnathan, R.; Kwiat, M.; Patolsky, F.; Voelcker, N. H. Engineering Vertically Aligned Semiconductor Nanowire Arrays for Applications in the Life Sciences. *Nano Today* **2014**, *9*, 172–196.

(5) Peng, J.; Garcia, M. A.; Choi, J.; Zhao, L.; Chen, K.-J.; Bernstein, J. R.; Peyda, P.; Hsiao, Y.-S.; Liu, K. W.; Lin, W.-Y.; et al. Molecular Recognition Enables Nanosubstrate-Mediated Delivery of Gene-Encapsulated Nanoparticles with High Efficiency. *ACS Nano* **2014**, *8*, 4621–4629.

(6) Hou, S.; Choi, J.-S.; Chen, K.-J.; Zhang, Y.; Peng, J.; Garcia, M. A.; Yu, J.-H.; Thakore-Shah, K.; Ro, T.; Chen, J.-F.;Peyda, P.; Fan, G.; Pyle, A. D.; Wang, H.; Tseng, H.-R. Supramolecular Nanosubstrate-Mediated Delivery for Reprogramming and Transdifferentiation of Mammalian Cells. *Small* **2015**, *11*, 2499–2504.

(7) Wang, X.; Rivière, I. Clinical Manufacturing of CAR T Cells: Foundation of a Promising Therapy. *Mol. Ther. Oncolytics* **2016**, *3*, 16015.

Appendix A

Surface Dipole Control of Liquid Crystal Alignment

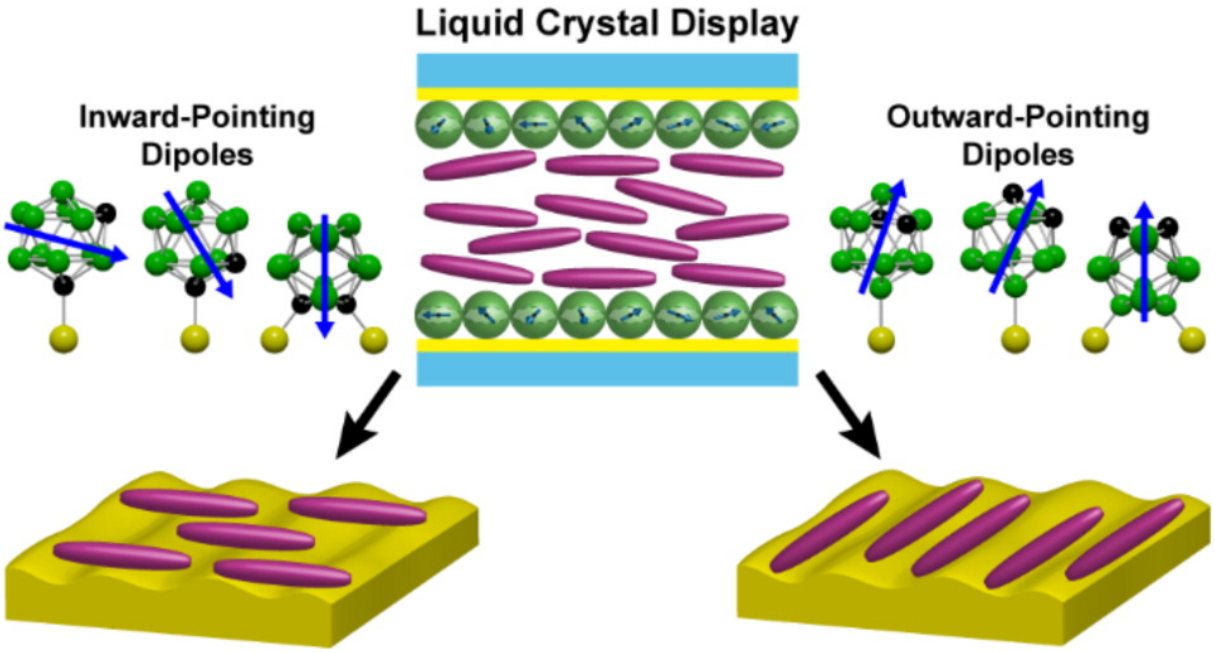

The information in this chapter was published in
JACS. **2016**, *138*, 5957-5967
and has been reproduced here with permission.[1]

Authors: Jeffrey J. Schwarz, Alexandra M. Mendoza, Natcha Wattanatorn, Yuxi Zhao, Vinh T. Nguyen, Alexander M. Spokoyny, Chad A. Mirkin, Tomáš Baše, and Paul S. Weiss

A.A. Introduction

Self-assembly plays critical roles in the development of materials with customized chemical and physical properties from the bottom up, and provides insights into molecular-scale phenomena.[2–5] Non-covalent interactions, including dipolar and dispersion forces, mediate molecular assembly and influence the properties and functions of pure and composite materials.[6–10] Understanding and controlling the types and strengths of these interactions, particularly at interfaces, enables engineering precisely tailored structures at the nanoscale.[11–16] Self-assembled monolayers (SAMs) not only exemplify these structures, but also serve as a powerful and versatile means of tuning the interactions of a surface with its surroundings and other molecular adsorbates.[17–20] A great deal of work has been done using SAMs to control the adsorption, position, orientation, and nucleation of crystalline and molecular assemblies.[21–27] Despite recent progress, however, predictive understanding of complex, extended assemblies across textured surfaces remains challenging.[28,29]

Liquid crystals (LCs) assemble with long-range orientational order due to anisotropic intermolecular interactions with their surroundings and are particularly sensitive to surface textures and coatings.[30–32] Industrially, LC alignment is controlled by unidirectional rubbing[33,34] or other techniques that break the rotational symmetry of the alignment surfaces.[35–37] One such alternative utilizes the dune-like surface texture of obliquely deposited, semi-transparent gold films[38,39] to direct LC alignment.[35,38,40–43] In this case, mesogens adopt in-plane orientations with their long axes perpendicular to the oblique deposition direction, minimizing elastic strain within the LC assembly.

Abbott and others have shown that SAMs also influence the alignment of LCs,[44–49] with the ability to control both azimuthal and polar orientations, which have found use in sensors.[50] However, a convolution of steric effects, surface topography, and intermolecular forces complicates our understanding of the mechanisms responsible for alignment.[47,48,51–53] Molecular adsorbates, in the form of either well-organized SAMs or adventitious surface contamination, can alter LC arrangement by changing the preferred in-plane alignment axis or inducing homeotropic alignment, normal to the surface.[44,46,54] In the case of alignment layers treated with SAMs, different LC orientations have been observed using polar and nonpolar adsorbate molecules.[39,45,52] Additionally, chiral and "odd–even"[55] effects have been observed, showing that LC alignment is sensitive to variations in the symmetry[56–58] and orientation[47,48] of the exposed moieties of the terminal functionality of the SAM. Self-assembled adsorbates used in previous studies typically varied in two or more of these factors simultaneously (*e.g.*, comparing structural analogues with different exposed moieties: $-CH_3$, −OH, and −COOH). As such, the independent effects of molecular geometry, orientation, and dipole moment on LC alignment are difficult to determine.

We used positional isomers of carboranethiol and -dithiol molecules[59] to deconvolve the effects of SAM dipole magnitude and orientation on the alignment of LCs. The isomers chemisorb onto gold surfaces through the formation of Au–S bonds, thereby assembling into monolayers with exposed carborane moieties. Each isomer possesses an identical molecular geometry and assembles "upright" with negligible tilt and a characteristic lattice spacing (7.2 and 7.6 Å for monothiol and dithiol species, respectively).[15,60–65] The primary attribute that distinguishes SAMs of each isomer is their different constituent dipole moments. Intermolecular forces between carboranethiol monolayers and mesogens resulted in

uniaxial planar alignment of LCs along one of two distinct directions relative to the underlying anisotropic substrate: parallel or perpendicular to the oblique gold deposition direction ($\overrightarrow{Au}$). The effects of these short-range, nanoscale forces[15,66] were transduced and amplified by the LCs to a macroscopic scale, enabling optical readout *via* transmitted light. Azimuthal anchoring energies of LCs on carboranethiol and -dithiol monolayers were measured to quantify SAM-LC coupling. This work targets and elucidates the roles of surface dipoles, in the form of adsorbed molecular dipoles, on the alignment and orientation of subsequent adsorbates (LCs), which has applications in sensing, catalysis, photovoltaics, and templated growth of nanostructures.[67–70] Self-assembled carboranethiols are well suited to this purpose as they enable direct comparison of the effects of different isomers' molecular dipoles, while holding constant other factors influencing LC alignment that have confounded previous studies.

A.B. Results and Discussion

Figure A.1 illustrates the molecules used in these studies. Caboranethiol isomers *m*-9-carboranethiol (M9), *m*-1-carboranethiol (M1), *o*-9-carboranethiol (O9), *o*-1-carboranethiol (O1), and -dithiol isomers *o*-9,12-carboranedithiol (9O12) and *o*-1,2-carboranedithiol (1O2) possess dipole moments with various strengths and orientations.[71] The dipole moments of these six carboranethiols were calculated using density functional theory.[15,61,72,73] Although the molecular dipoles will be altered upon chemisorption to a gold surface,[74] we use these values to make qualitative comparisons of their relative strengths, their orientations, and the degree to which they modify the surface energy of a substrate through their dipolar fields.[61,73] We use two LCs, 4-cyano-4′-pentylbiphenyl (5CB) and N-(4-methoxybenzylidene)-4-butylaniline (MBBA),

possessing oppositely signed dielectric anisotropies (Δε), to probe these fields. Mesogens with positive Δε (5CB) align parallel to an applied electric field, whereas the long axes of mesogens with negative Δε (MBBA) align perpendicular to an applied field. Comparison of the alignment of 5CB and MBBA on carboranethiol monolayers enables us to infer the role of the dipolar field on LC alignment.[44]

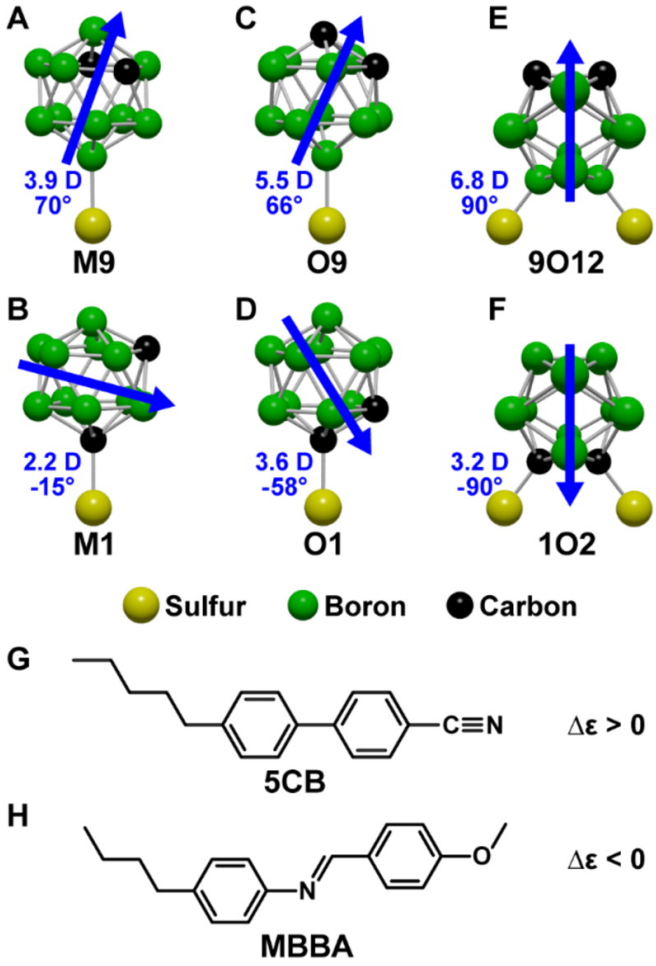

Figure A.1. Molecular structures of carboranethiol and -dithiol isomers: (A) *m*-9-carboranethiol (M9), (B) *m*-1-carboranethiol (M1), (C) *o*-9-carboranethiol (O9), (D) *o*-1-carboranethiol (O1), (E) *o*-9,12-carboranedithiol (9O12), and (F) *o*-1,2-carboranedithiol (1O2). Dipole moment magnitudes and orientations, calculated for isolated molecules, are indicated in blue. Positive (negative) angles estimate dipole orientations above (below) the plane of the substrate when assembled onto gold surfaces. Mesogen molecular structures of (G) 4-cyano-4′-pentylbiphenyl (5CB) and (H) N-(4-methoxybenzylidene)-4-butylaniline (MBBA) with corresponding dielectric anisotropy (Δε) signs noted. Hydrogen atoms are omitted from all structures for clarity.

To monitor SAM-regulated mesogen alignment, LC cells were constructed as shown in **Figure A.2A.** The outgoing polarization of light transmitted through a cell depends on the angle between the polarization of the incoming light and the orientation of the nematic director, which represents the average alignment direction of mesogens in a LC. If the mesogens align homeotropically, this angle is independent of cell rotations about axes normal to the alignment layers and the cells appear "dark" (0% transmittance) when viewed between crossed polarizers. Variations in the intensity of transmitted light with rotations of the cell, however, indicate planar alignment of the nematic director. **Figure A.3** shows the modulation in the intensity of the light transmitted through 5CB cells as they were rotated between crossed polarizers (**Figure A.2B**); corresponding MBBA data are provided in the Supporting Information. Alignment layers treated with M9, M1, O9, O1, 9O12, and 1O2 SAMs all induced uniaxial planar alignment in both 5CB and MBBA cells, as indicated by the four-fold symmetry of their transmittance spectra. Cells constructed without a twist in their nematic directors vary from nearly extinguishing all transmitted light to transmitting ~50%. By contrast, cells that possess a 90° twist in their directors have transmittances varying from ~50% to nearly 100%, due to the rotation of the transmitted light's polarization as it traverses the cell.[75]

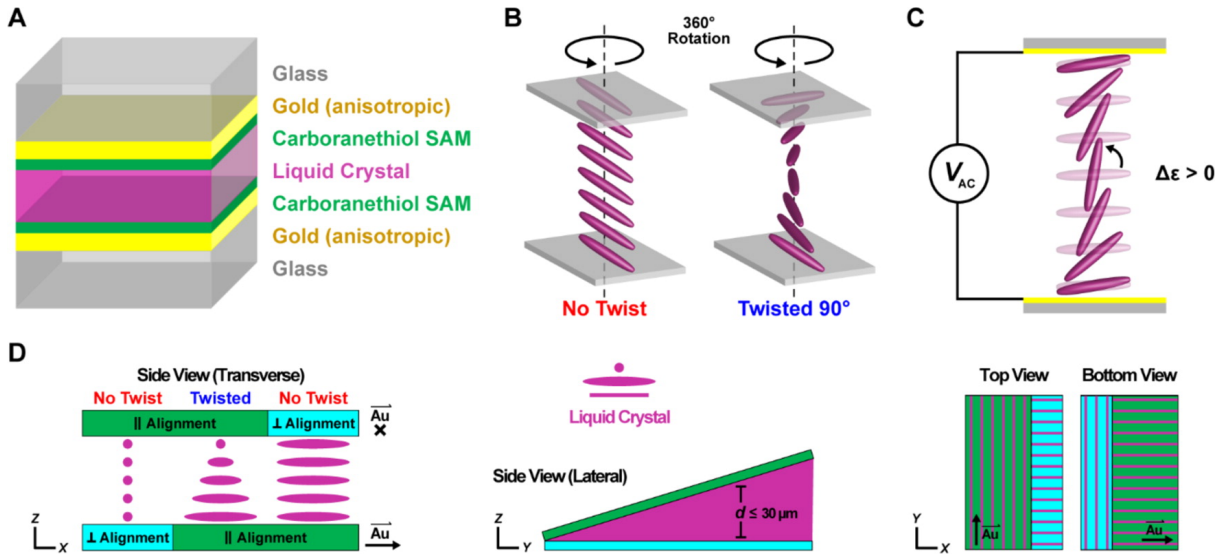

Figure A.2. (A) Schematic of liquid crystal (LC) cells used in rotation and electrically modulated optical transmittance measurements ("transmittance cells"). Carboranethiol and -dithiol self-assembled monolayers (SAMs) adsorbed on semitransparent, anisotropic gold films induced uniaxial planar alignment of a LC at the interface. Schematics illustrating the rotation of LC cells 360° about axes normal to their alignment planes (B) and a Fréedericksz transition (C) in a LC with positive dielectric anisotropy ($\Delta\varepsilon > 0$) upon application of an alternating electric potential (V_{AC}). (D) Wedge cell geometry used to measure azimuthal anchoring energies, as viewed from multiple perspectives ("anchoring energy cells"). Each alignment layer was divided into two distinct sections defined by SAMs composed of complementary molecules. Here, a carboranethiol or -dithiol isomer SAM (green) is shown to induce LC alignment parallel to the gold deposition direction ($\overrightarrow{Au}$), although other isomers may instead promote planar alignment perpendicular to $\overrightarrow{Au}$. Alkanethiol SAMs (blue) were used to induce planar LC alignment orthogonal to that induced by the carboranethiol or -dithiol isomer. Once assembled, the cell was comprised of three nematic regions, one possessing a ~90° twist in the azimuthal director orientation, while the other two exhibited untwisted LC alignment (90° apart) through the bulk of the cell. The thickness (d) of the gap between the alignment layers varied due to the presence of a spacer (not shown) at only one end of the cell.

Applying a potential difference between the alignment layers generates an electric field that can distort the planar alignment of LCs with $\Delta\varepsilon > 0$, inducing them to adopt an orientation parallel to the field (normal to the surface), as illustrated in **Figure A.2C**.[76] This reorientation of the mesogens alters the transmittances of LC cells viewed between crossed polarizers, as shown in **Figure A.4**. Transmittances of twisted nematic cells containing **5CB**

($\Delta\varepsilon > 0$) decrease to near 0% with increasing field strengths. By contrast, twisted nematic cells made using MBBA do not exhibit a change in their transmittance due to their $\Delta\varepsilon < 0$, maintaining planar alignments that are reinforced by the applied field (see Supporting Information). The applied potentials produce no lasting changes to the carboranethiol monolayers, as evidenced by the reproducibility of the voltage- modulated transmittance curves through repeated sweeping of the potential's amplitude between 0 and 7 V. The observed optical responses of the cells to applied electric fields is further indication of the planar alignment adopted by both 5CB and MBBA LCs on carboranethiol and -dithiol SAMs.

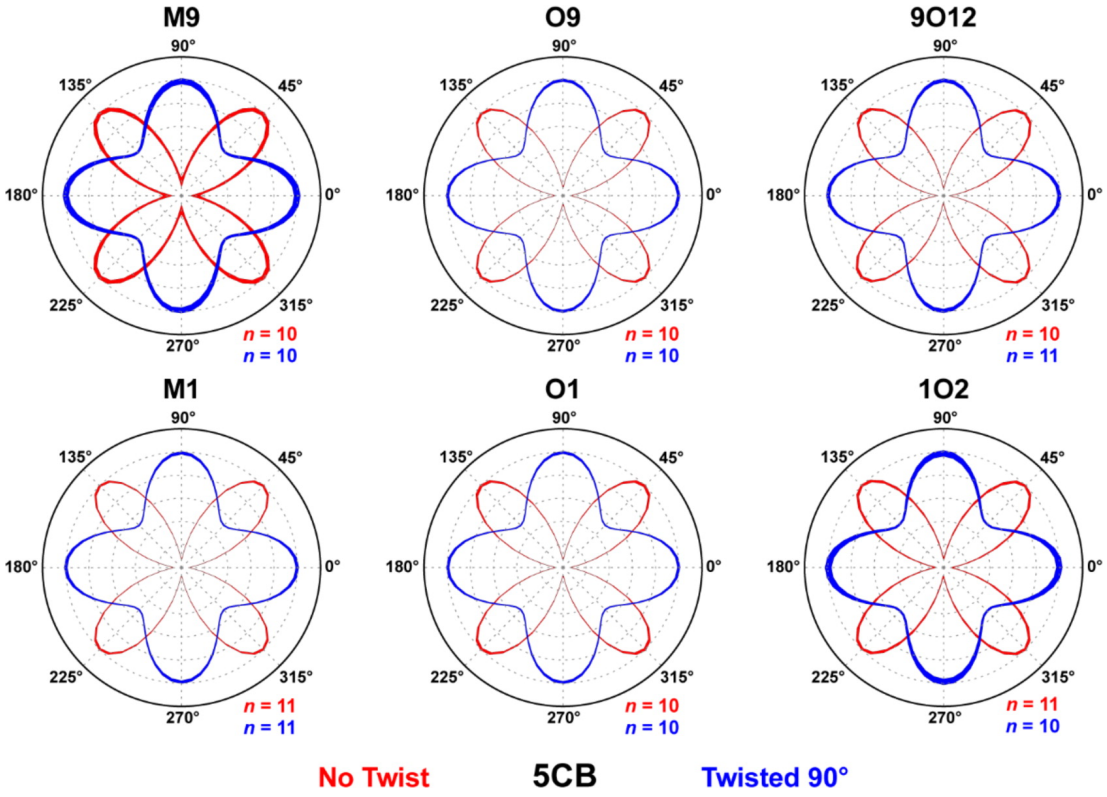

Figure A.3. Optical transmittances (indicated by the radial distance from the origin, in arbitrary units) of liquid crystal (LC) cells rotated between crossed polarizers. Alignment layers were prepared with matching self-assembled monolayers of *m*-9-carboranethiol (M9), *m*-1-carboranethiol (M1), *o*-9-carboranethiol (O9), *o*-1-carboranethiol (O1), *o*-9,12-carboranedithiol (9O12), and *o*-1,2-carboranedithiol (1O2), as indicated. At these surfaces, uniaxial, planar alignment was manifest in 4-cyano-4′-pentylbiphenyl (5BC) LCs, as evidenced by the variations in optical transmittance possessing four-fold rotational

symmetry. Cells were constructed with angles of either 0° or 90° between the alignment layers' gold deposition axes, inducing untwisted (red) or twisted (blue) nematic structures, respectively. Initially, one or both of a cell's gold deposition axes were aligned with the polarizer axis, defined to be at 0°. Rotation angles were measured with respect to this reference orientation, incremented in 5° steps. Reported spectra are averages of analyses performed on *n* separate LC cells, each consisting of three measured regions, where the radial line widths indicate the data's standard deviations. Spectra are scaled such that their respective transmittance maxima are equal; in actuality, the maximum transmittance of an untwisted nematic cell nearly equals the minimum transmittance of a cell with a 90° twist in its director.

The rotation- and field-induced variations in transmittance described above were observed uniformly over the entire area (~1 cm^2) of each cell measured. These results indicate uniaxial planar alignment of 5CB and MBBA on anisotropic gold surfaces treated with each of the six carboranethiols considered here. However, these observations, alone, do not uniquely determine the nematic director orientation on a surface. Transmittance minima of untwisted nematics are expected when the director aligns along either of the crossed polarizers' axes, while maxima are expected at these orientations for cells constructed with 90° twists in their directors. These expectations are realized in Figure A.3; transmittance extrema coincide with cell rotations that align $\overrightarrow{\text{Au}}$ parallel to, and 45° from, the polarizers' axes. Two possible in-plane director orientations can produce this effect: director alignment parallel or perpendicular to $\overrightarrow{\text{Au}}$.

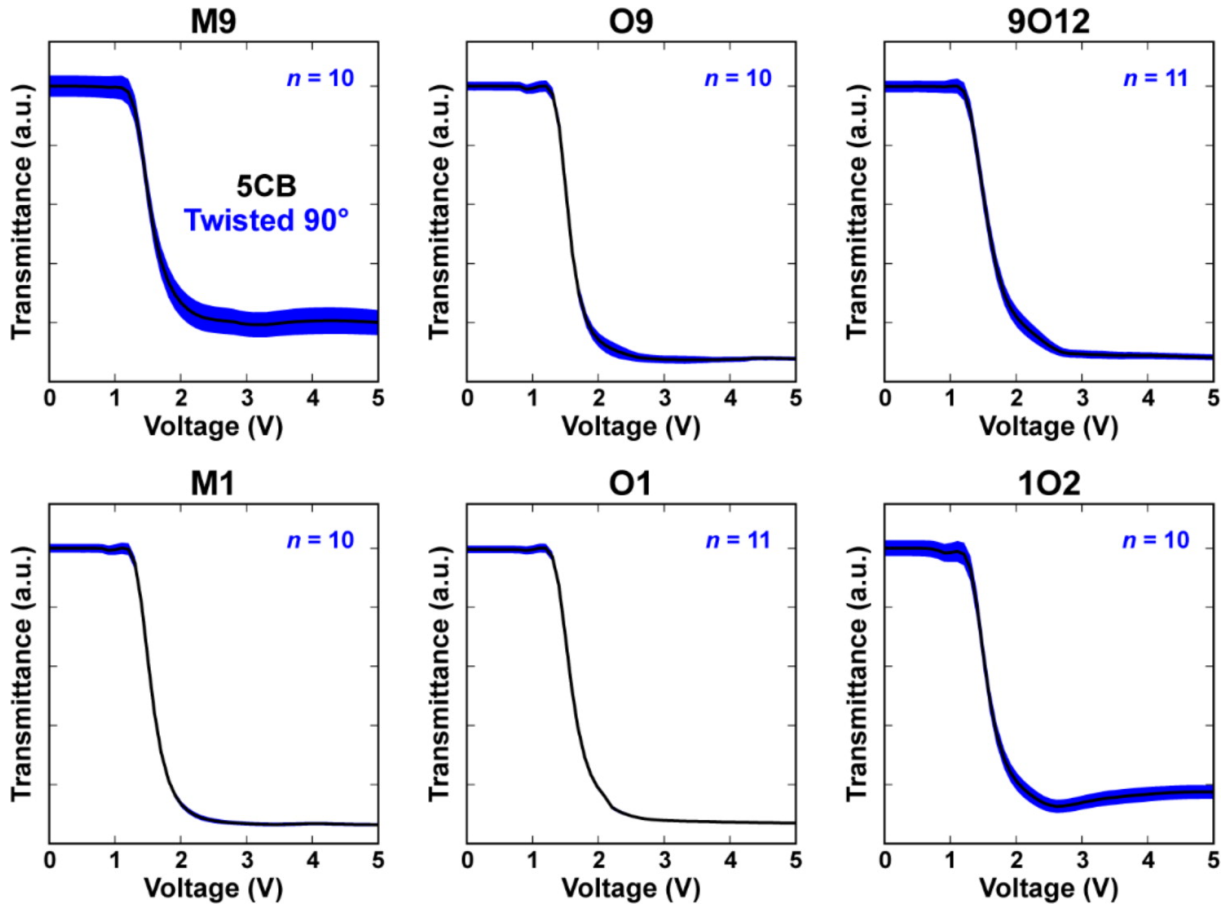

Figure A.4. Normalized optical transmittances of electrically modulated liquid crystal (LC) cells viewed between crossed polarizers. Alignment layers were prepared with matching self-assembled monolayers of *m*-9-carboranethiol (M9), *m*-1-carboranethiol (M1), *o*-9-carboranethiol (O9), *o*-1-carboranethiol (O1), *o*-9,12-carboranedithiol (9O12), and *o*-1,2-carboranedithiol (1O2), as indicated. These surfaces induced uniaxial planar alignment in 4-cyano-4′-pentylbiphenyl (5CB) LCs. Cells were constructed with perpendicular gold deposition axes, producing twisted nematic structures, and were positioned between crossed polarizers such that their zero-voltage optical transmittance was maximized. Subsequently, a sinusoidally varying (1 kHz) voltage was applied between the alignment layers in order to distort the LC director away from the surface. Root-mean-square voltages, varied in 0.1 V steps, are indicated along the horizontal axes. Reported spectra are averages (black lines) of analyses performed on *n* separate LC cells, where the vertical widths of the surrounding blue outlines indicate the data's standard deviations.

In order to determine, unambiguously, the LC orientation relative to the gold deposition axis (parallel or perpendicular), a wedge cell geometry was used, as illustrated in **Figure A.5**. Illuminating a LC wedge with monochromatic light, polarized 45° from its optical

axis, produced a series of bright and dark fringes visible within the cell when observed between crossed polarizers. These fringes result from changes in the transmitted light's polarization as it traverses the birefringent cell. The optical retardation (Γ) between ordinary and extraordinary waves causes transmitted light to vary continuously between linear and elliptical polarization states, dependent on the wedge thickness (d). In the two extremes, light exits the wedge linearly polarized parallel or perpendicular to its incoming polarization, producing transmittance minima and maxima, respectively. The conditions on the optical retardation (wedge thickness) required for a transmittance extreme are given by

$$\Gamma = \Delta n \cdot d = \begin{cases} (m + ½) \cdot \lambda, & \text{maxima} \\ m \cdot \lambda, & \text{minima} \end{cases} \qquad m = 0, 1, 2, 3, \ldots$$

where λ is the wavelength of light, Δn is the LC's birefringence, and m is an integer enumerating the fringe order. Wave plates, inserted in series with a wedge cell between crossed polarizers, modify the total retardation by fixed amounts and cause the apparent positions of the fringes to shift. When the optical axes of a wave plate and untwisted nematic align, the total retardation of the transmitted light increases, whereas when their optical axes are crossed, the retardation decreases. Increased (decreased) optical retardation results in shifts in the fringe position toward (away from) the vertex of the wedge, toward the thinner (thicker) end of the cell. In this way, one can infer the orientation of the nematic director from the known orientation of a wave plate's slow axis and the direction of the observed shift in fringe positions.

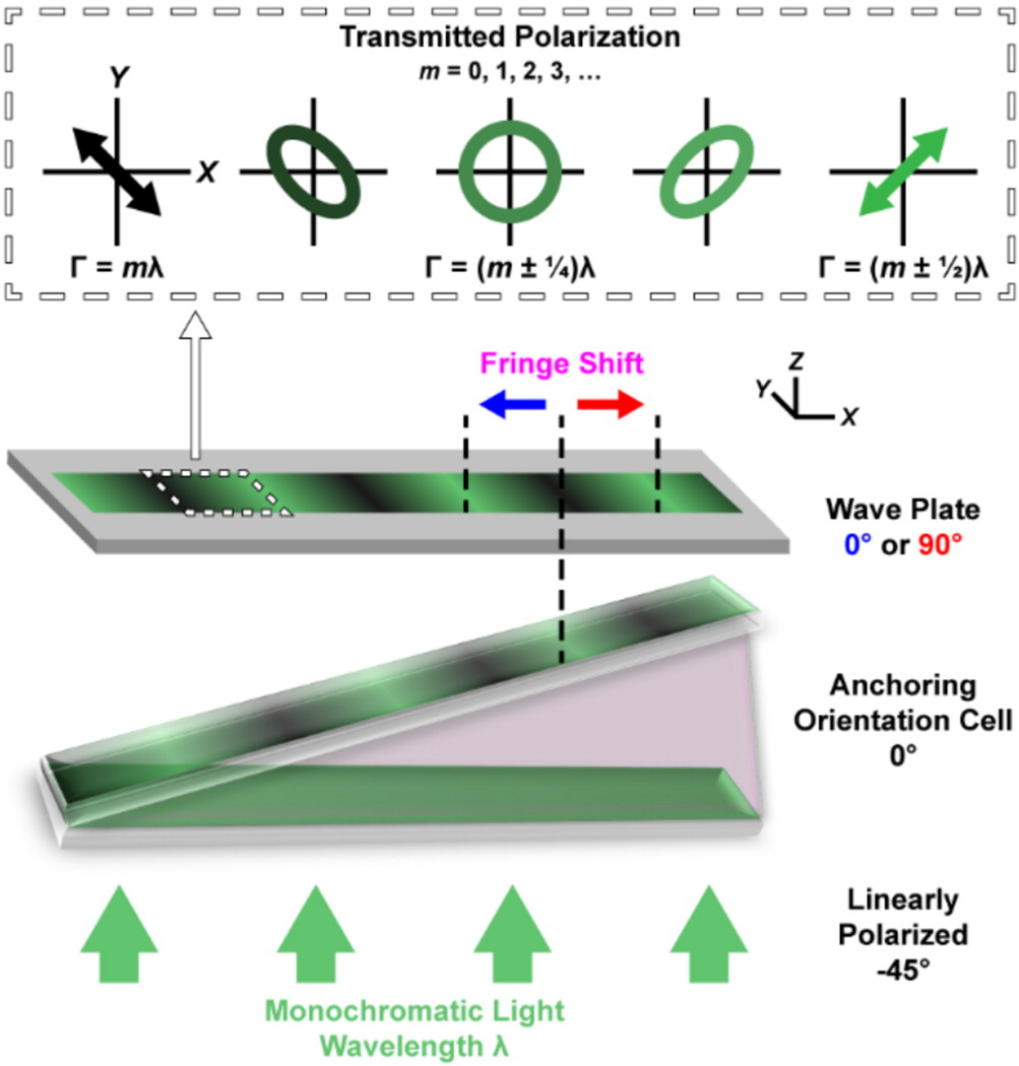

Figure A.5. Wedge cell scheme used to determine the in-plane liquid crystal director orientation with respect to the alignment layers' gold deposition axes ("anchoring orientation cells"). Linearly polarized, monochromatic light (λ = 531 nm) traversing the cell accumulates an optical retardation (Γ) dependent on the wedge thickness. As a result, the transmitted light varies between linear and elliptical polarization states, as indicated along the top of the figure. This retardation is modified by placing wave plates in series with the cell. When the optical axes of the cell and wave plate align, the overall retardation increases, whereas when the optical axis of the wave plate is perpendicular to that of the nematic, the total retardation is reduced. When viewed through an analyzer (not shown), oriented 90° from the incoming light's polarization, a series of bright and dark fringes are visible within the cell due to extinction of light polarized along the initial direction. As shown, the wave plate modifies the optical retardation of the transmitted light by $\lambda/2$, thereby causing the transmittance maxima to become minima, and vice versa. All angles indicate orientations in the *xy*-plane with respect to the *+x*-axis.

As shown in **Figure A.6**, the fringes observed in cells made using M1, O1, and 1O2 SAMs shift toward the thinner ends of the cells with increased optical retardation along $\overrightarrow{\text{Au}}$. This result indicates that the 5CB director is aligned parallel to $\overrightarrow{\text{Au}}$ in these cells. By contrast, cells prepared with M9, O9, and 9O12 SAMs induced planar alignment of the 5CB director perpendicular to $\overrightarrow{\text{Au}}$, as the fringes were observed to move toward the thicker ends of the cells. We note that self-assembled carboranethiol and -dithiol isomers with dipole moments directed toward the gold surface induced 5CB alignment parallel to $\overrightarrow{\text{Au}}$, whereas isomers with dipoles directed away from the substrate induced planar alignment perpendicular to $\overrightarrow{\text{Au}}$. A similar tendency was also observed in the case of MBBA LCs (see Appendix), with the exceptions of M9 and 1O2 SAMs, *vide infra*. Comparing the in-plane alignment orientations of 5CB and MBBA directors enables us to examine and to constrain the coupling mechanism between the mesogens and carboranethiol SAMs. If a dipolar electric field due to the SAM dominates the interaction, then orthogonal director orientations of the two LCs (with oppositely signed values of $\Delta\varepsilon$) are expected. However, this behavior is not observed, which is understandable due to the inversion symmetry of the nematic director (η and $-\eta$ represent equivalent director orientations).[77] Therefore, the molecular dipole moments in the SAM must influence mesogen alignment by other means.

Anchoring energy measures the work (per unit area) required to reorient a LC director perpendicular to its preferred, "easy axis" orientation on a surface. We compare azimuthal anchoring energies of 5CB aligned by M1, O9, O1, and 9O12 monolayers as a means of quantifying SAM-LC interactions. In doing so, we test for differences in anchoring strengths between isomers that align LCs in the same, and perpendicular, directions on

anisotropic gold surfaces. A torque-balance measurement scheme[78,79] was adopted to estimate anchoring energies on patterned, hybrid, alignment layers assembled in a wedge configuration, as illustrated in **Figure A.2D**. Twisted and untwisted nematic regions in a cell were created using bifunctional alignment layers, pairing carboranethiol SAMs with alkanethiol monolayers known to induce planar LC alignment in orthogonal directions.[47] The untwisted nematic regions within the cells enable determination of the easy axes of both the top and bottom alignment layers, which coincide with the director orientation. In the twisted nematic regions, however, the director deviates from the surfaces' easy axes due to an elastic restoring torque acting on the mesogens as a result of the twist deformation through the bulk of the cell. The angle (φ) by which the director deviates from the easy axes, and thus partially untwists itself, is related to the azimuthal anchoring energy (W_{az}):

$$W_{az} = \frac{2K_{22}\Psi}{d\sin(2\varphi)},$$

where K_{22} is the twist elastic constant of the mesogen and Ψ is the overall twist of the nematic director through a cell with thickness d (**Figure A.11**). In wedge cells, *d* varies continuously along their longitudinal axes and, as such, must be determined at each measurement location. Wedge thicknesses may be inferred from their apparent (transmitted) colors. When illuminated with white light and viewed between polarizers crossed at ±45° from the optical axis of an untwisted nematic with known birefringence, the color of transmitted light is related to a cell's thickness using a Michel–Levý interference color chart.[80] However, this chart provides only a qualitative measure since it is based on a subjective judgment of color and is prone to misinterpretation. Monochromatic transmission fringes visible within a cell, like those seen in **Figure A.6**, provided a quantitative means of estimating the wedge

thickness using known values of Δn and λ in eq 1. In this way, we determined the **5CB** azimuthal anchoring energies summarized in **Table A.1**.

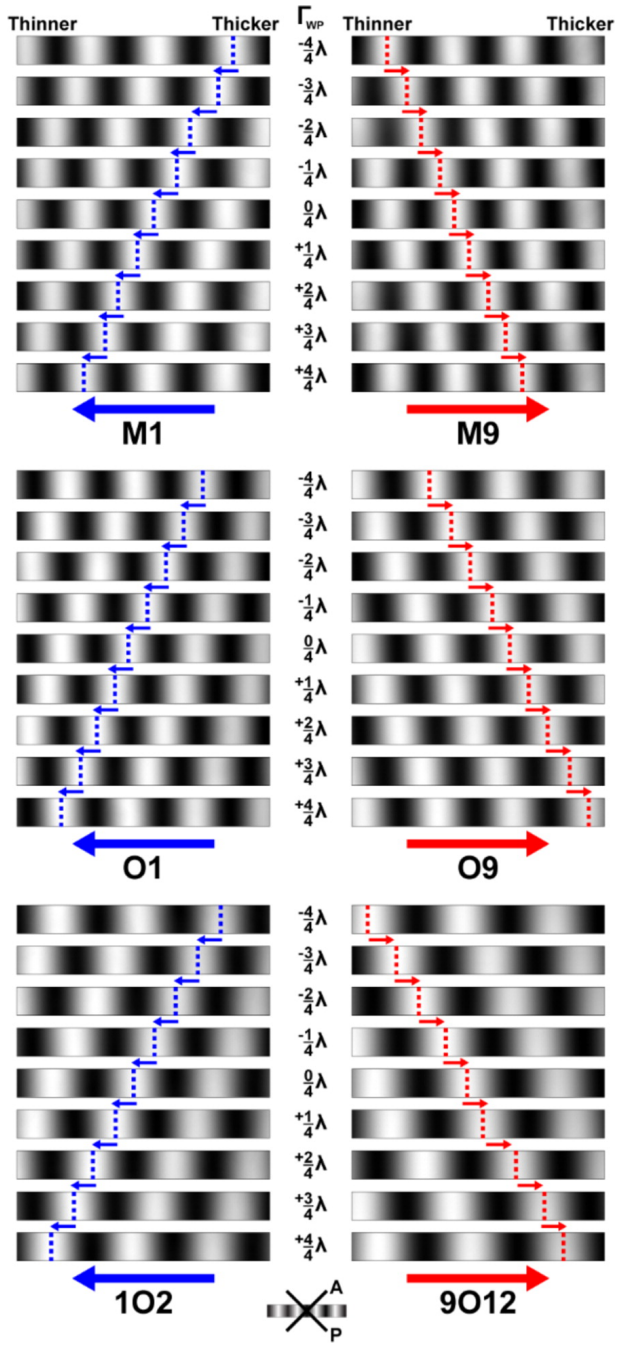

Figure A.6. Transmission fringes observed in liquid crystal (LC) wedge cells viewed between crossed polarizers while illuminated with monochromatic light (wavelength $\lambda = 531$ nm). Alignment layers prepared with matching self-assembled monolayers of *m*-1-carboranethiol (M1), *m*-9-carboranethiol (M9), *o*-1-carboranethiol (O1),

o-9-carboranethiol (O9), *o*-1,2-carboranedithiol (1O2), and *o*-9,12-carboranedithiol (9O12), as indicated, induced uniaxial planar alignment of 4-cyano-4′-pentylbiphenyl (5CB) LCs. Wave plates inserted between the polarizers modified the optical retardation of light transmitted through the cells by fixed amounts (ΓWP). Here, positive (negative) values of ΓWP signify that a wave plate's optically slow axis was aligned parallel (perpendicular) to a cell's gold deposition direction ($\overrightarrow{\text{Au}}$). Arrows and dashed lines track transmittance maxima of constant order within 4.8 mm × 0.5 mm fields of view. Fringes in cells containing M1, O1, and 1O2 monolayers were observed to shift toward the thinner ends of the wedges with increasing ΓWP (blue), indicating that their nematic directors were oriented parallel to $\overrightarrow{\text{Au}}$. By contrast, fringes shifted toward the thicker ends of cells containing M9, O9, and 9O12 monolayers (red), indicating director alignment perpendicular to $\overrightarrow{\text{Au}}$.

Anchoring SAM[a]	$\mathbf{p}_\perp$[b]	W_{az} (μJ·m^{-2})	Sample Size, *n*
O9[c]		7.5 ± 0.1	28
	↑		
9O12[d]		6.7 ± 0.1	29
M1[e]		14.3 ± 0.4	36
	↓		
O1[f]		14.3 ± 0.4	37

Table A.1. Anchoring energy (W_{az}) of 5CB liquid crystals in cells prepared with various carboranethiol self-assembled monolayers (SAMs). [a]Carboranethiol or -dithiol isomer used to align 4-cyano-4′-pentylbiphenyl (5CB). [b]Normal dipole ($\mathbf{p}_\perp$) orientation toward (↓) or away from (↑) the gold surface. [c]*o*-9-carboranethiol. [d]*o*-9,12-carboranedithiol. [e]*m*-1-carboranethiol. [f]*o*-1-carboranethiol.

If LC alignment is modulated by the monolayer's constituent dipole moments, we expect to observe differences in the anchoring strengths of alignment layers treated with different carboranethiol and -dithiol isomers. We found a nearly bimodal distribution of anchoring energies from the four carboranethiol SAMs tested here, with the stronger (weaker) anchoring surfaces corresponding to those with normal dipoles oriented toward (away from) the substrate. Anisotropic gold surfaces functionalized with either O9 or 9O12 aligned 5CB with approximately half the strength, perpendicular to $\overrightarrow{\text{Au}}$, as monolayers of M1 or O1, which induced alignment parallel to $\overrightarrow{\text{Au}}$. Although each of these molecules possesses

distinct dipole magnitudes and orientations, the anchoring strengths of M1 and O1 (both monothiol species) SAMs did not differ appreciably. By contrast, the anchoring energy measured on 9O12 (dithiol) SAMs was found to be ~10% less than the value measured on O9 (monothiol) SAMs. However, that decrease in anchoring energy coincides with a matching reduction in the areal density of 9O12 molecules within close-packed SAMs, compared with O9 monolayers, due to the larger nearest-neighbor spacing of carboranedithiol adsorbates.[15,61,65] These findings suggest that the polarity of the normal dipole moment, toward or away from the surface, and the molecular packing density are the dominant factors affecting LC anchoring in these systems. We note that the measured anchoring energies of 5CB LCs on carboranethiol monolayers (~7 $\mu J \cdot m^{-2}$ and ~14 $\mu J \cdot m^{-2}$) exceed the values reported for oligo(ethylene glycol)-containing SAMs (<6 $\mu J \cdot m^{-2}$),[79,81] and are comparable to those on unfunctionalized surfaces.[38,82,83] These values, however, are almost two orders of magnitude weaker than the anchoring strengths of rubbed polyamide films.[84,85]

Uncertainty in the local gold deposition angle is expected to be a major contributor to variations in the measured azimuthal anchoring energies.[39,81,86,87] All of the gold films used in these studies were deposited at the same angle, nominally 50° away from the surface normal. However, due to the finite sizes of the glass substrates and their positions relative to the evaporating metal source, departures of up to 6° from the intended angle are possible (see Appendix). Variations in the average grain size and surface roughness affect the substrate's contribution to LC alignment, resulting in stronger anchoring on gold films deposited at higher, more oblique angles.[86] Additionally, uncertainty in the anchoring energy typically increases with deposition angle due, in part, to its sensitivity to uncertainties in the

nematic director's twist and deviation from the easy axes.[81] This sensitivity becomes more pronounced with increasing anchoring strength (higher deposition angles). The anchoring energies reported here reflect averages of measurements performed on multiple cells, inversely weighted by their estimated variances. Such averaging, however, biases the reported values in favor of lower anchoring energies that possess correspondingly smaller uncertainties. The complete data sets, as well as a discussion of the statistical methods used in our analysis, are provided in the Appendix.

As noted above, we observe a trend in the alignment of LCs by carboranethiol monolayers prepared on anisotropic gold surfaces that follows the polarity of the adsorbate's normal dipole moment. The constituent molecules of a SAM, in general, possess dipoles with components oriented parallel and normal to the functionalized surface. The cumulative effects of the in-plane molecular dipoles are diminished by their varying or disordered azimuthal orientations expected at room temperature.[15] Molecules may adsorb to the surface with random in-plane dipole orientations and, in the cases of M9, M1, O9, and O1, which possess only a single attachment to the substrate, rotate about their Au−S bonds. If long-range orientational order is present, the formation of differently polarized domains (including closure domains) would compensate for a net in-plane dipole over macroscopic scales. Additionally, image dipoles, formed through the redistribution of charge on the underlying gold substrate, would further attenuate the effects of in-plane molecular dipoles. Normal dipole moments, however, are not subject to these mitigating factors. Each carboranethiol in a single-species SAM adsorbs to the surface with the same polar orientation and, as such, enhances the net dipole moment normal to the surface. Carboranedithiol isomers (9O12 and 1O2) were included in these experiments due to their

expected dipole orientations normal to the surface as a result of their bilateral molecular symmetry. Since these isomers bind to the substrate *via* two Au–S bonds, they are not free to rotate azimuthally. In principle, these isomers could tilt about the axis connecting their two adsorbed thiolate moieties, out of the plane normal to the gold substrate, resulting in a portion of their dipole moments orienting parallel to the surface. Nevertheless, we observe the same trend in 5CB alignment induced by carboranedithiol isomers as in the cases of monothiol isomers, dependent upon the polarity of the normal dipole. As such, we conclude that the net in-plane dipole of a SAM is either compensated through one or more of the mechanisms mentioned above, or is a less significant contributor than the normal dipole when determining LC alignment.

In addition to the factors discussed above, other surface anisotropies may contribute to the existence of an easy alignment axis. One such contribution originates from an anisotropic electric susceptibility of the alignment surface. Obliquely deposited films are expected to have an anisotropic response to electric stimuli (*e.g.*, from mesogen dipoles) due to their dune-like or columnar surface textures.[88,89] Molecular monolayers can modify this anisotropy, dependent on the adsorbate polarizabilities and orientations on the surface. To examine this effect, molecular polarizability tensors (α) were calculated using density functional theory for each of the six carboranethiol and -dithiol isomers considered here (see Supporting Information). To facilitate comparison, Cartesian coordinate bases were chosen for each molecule such that the bond(s) connecting the sulfur atom(s) to the carborane cage moiety coincided with (or symmetrically straddled) the z-axis. Additionally, one or both of the carbon atoms within the isomers were designated to lie along the x-axis, in the cases of M1, O9, O1, 9O12, and 1O2, and symmetrically about the x-axis in the case of M9. These

coordinate bases closely coincided with the molecules' principal polarizability axes, such that the off-diagonal polarizability tensor elements ($\alpha_{ij}, i \neq j$) were negligible (<1%) by comparison to the diagonal elements (αii). Considering upright adsorption, we found that the molecular polarizabilities of carboranethiols were nearly symmetric in the plane of the substrate ($\alpha_{xx} \approx \alpha_{yy}$), with variations of <2%. Larger in-plane variations in molecular polarizability were found for 9O12 and 1O2 (~10%), in part due to the lower (two-fold) rotational symmetry of carboranedithiols compared that of with monothiol isomers (five-fold). Symmetric adsorbate polarizabilities reduce the likelihood of anisotropic in-plane polarizations of a SAM inducing LC alignment on flat, isotropic surfaces. On textured surfaces, however, the local (microscopic) surface normal generally deviates from that of the average (macroscopic) plane of the substrate, effectively varying the orientations of molecules within the assembly. As a result, the in-plane electric susceptibility of a SAM depends, in part, on the polarizability of carboranethiols along their z-axes (α_{zz}), which is ~20% greater than their polarizability along orthogonal directions. Therefore, geometric surface anisotropies present in obliquely deposited films, generate additional anisotropies in a monolayer without requiring, a priori, long-range azimuthal alignment of carboranethiols. However, we do not find any consistent correlation between the observed LC alignment and all six of the carboranethiol molecular polarizabilities considered here.

Comparing the alignments of mesogens with oppositely signed dielectric anisotropies provides insight into the role of the dipolar field on LC anchoring by functionalized surfaces. Assuming direct coupling between the mesogens and the field, 5CB and MBBA LCs were expected to align along orthogonal directions, relative to each other, at the SAM-LC interface. Instead, both mesogens adopted the same planar orientation, dependent on the polarity of

the monolayer's constituent molecular dipoles normal to the surface, as detailed previously. However, in the case of MBBA alignment, M9 and 1O2 carboranethiol monolayers were found to be exceptions to this trend. Alignment layers functionalized with M9 induced alignment of MBBA parallel to $\overrightarrow{\text{Au}}$, whereas 1O2 monolayers resulted in more heterogeneous and less reproducible anchoring of MBBA than observed on surfaces treated with other isomers under the same conditions. To understand these anomalies, we reemphasize that the monolayer's constituent dipoles are not the sole factor affecting LC alignment, despite being the focus of these studies. Other influences, including surface topography, molecular geometry, tilt, and order, are still present (albeit consistent) in each cell, while the contribution from carboranethiol dipoles varies between isomers. Out of the three isomers with dipoles directed away from the underlying gold surface tested here, M9 possesses the weakest moment and is the only one to induce LC alignment counter to the prevailing trend (and only with MBBA). Previously, we noted that the anchoring strength of 5CB on carborane-functionalized surfaces did not depend on the magnitude of the molecular dipoles of a SAM. This unexpected alignment of MBBA may indicate a minimum threshold strength of molecular dipoles required to orient LCs along a particular direction on these surfaces. Alternatively, we propose that the properties of MBBA itself may instead be responsible. Relative to 5CB, MBBA has a weaker internal dipole moment and smaller dielectric anisotropy (see Appendix). As a result, the coupling strength of MBBA to external electric fields is weaker than that of 5CB, with which no alignment anomalies were observed. Future experiments using a LC with a more negative dielectric anisotropy could test this hypothesis and distinguish whether or not the observed alignment is indicative of the carboranethiol monolayer or a property of the mesogen itself. In the case of the heterogeneous alignment of

MBBA on 1O2 monolayers, we note the potential for dithiol isomers to chemisorb to the gold surface in either singly or doubly bound states. Here, we used ethanolic solutions of each of the carboranedithiols with added base (sodium hydroxide) to promote dual binding *via* both thiol moieties on each molecule. However, even under these circumstances, not every adsorbed molecule binds to the gold with both thiol moieties. We have observed elsewhere[65] that the 1O2 isomer is more likely to adsorb in mixed states (both singly and doubly bound) compared to the 9O12 isomer under alkaline conditions, resulting in a less uniform SAM. This molecular-scale heterogeneity may, in turn, produce more heterogeneous LC arrangements than those observed on alignment layers treated with other carboranethiol isomers.

A.C. Conclusions and Prospects

Here, LCs serve as advantageous probes of the nanoscale intermolecular forces between SAMs and their environment. These combinations of forces result from several factors, including surface topography, molecular orientation, and chemical functionality, which modulate the properties of the underlying substrate and mediate the assembly of adsorbates. We report on the uniaxial, planar alignment of 5CB and MBBA LCs on obliquely deposited gold films functionalized with carboranethiol and -dithiol SAMs. Carboranethiol monolayers enable direct comparisons of LC alignment modulated by differences in the magnitudes and orientations of assembled molecular dipoles on a surface. Carboranethiol monolayers hold constant other factors that influence LC alignment, such as molecular geometry, tilt, and order, which have confounded previous studies. Furthermore, comparing LC alignment on monolayers composed of monothiol isomers (M9, M1, O9, and O1) to those composed of carboranedithiols (9O12 and 1O2) enabled inference of the roles of the normal

and lateral surface dipoles. We observed that the in-plane, azimuthal orientation of mesogens on anisotropic gold films was modulated predominantly by the carboranethiol dipole component normal to the surface. Monolayers composed of carboranethiols with dipoles oriented toward (away from) the underlying gold surface induced planar alignment of 5CB parallel (perpendicular) to the gold deposition direction. A similar trend was observed in the case of alignment of MBBA, which possesses an oppositely signed dielectric anisotropy. Since LCs with dielectric anisotropies of opposite signs align similarly, dependent on the monolayer's normal dipole polarity, we conclude that it is not a direct result of dipolar field coupling between SAMs and mesogens. We attribute the observed alignment to more complex mechanisms involving intermolecular dispersion forces. To quantify SAM-LC interaction strength, we measured the azimuthal anchoring energies of 5CB on alignment layers treated with M1, O9, O1, and 9O12 monolayers. A nearly bimodal distribution of anchoring energies was measured, dependent on the polarity of the carboranethiol isomer dipole moment component normal to the surface. Monolayers composed of carboranethiol isomers with dipoles oriented away from (O9 and 9O12) and toward (M1 and O1) the substrate were measured to anchor 5CB with strengths of ~7 and ~14 $\mu J \cdot m^{-2}$, respectively. Additionally, comparing the anchoring energies of pairs of isomers with the same polarity normal to the surface, we found no difference in anchoring strengths between monothiol species (M1 and O1). However, we observed that the anchoring energies measured on surfaces treated with 9O12 (dithiol) were about 10% lower than those measured on surfaces treated of O9 (monothiol), coinciding with the decrease in areal density of carboranethiols within the close-packed monolayers. This result indicates that not only the polarities of the molecular dipoles affect LC anchoring, but also their densities on

the surfaces. We also considered other sources of surface anisotropy arising from the molecular polarizabilities of the carboranethiols used in this work that may affect LC anchoring direction and strength. We do not expect that long-range molecular alignment of carboranethiol adsorbates within SAMs at room temperature is likely.[15] However, others have previously observed azimuthal ordering of exposed methyl moieties in alkanethiol monolayers prepared on anisotropic gold films.[42] Complementary techniques, such as sum-frequency generation spectroscopy, may be used in future studies to test this possibility in the case of carboranethiol SAMs.[90] The mechanism involved remain unresolved, but this work isolates elements of the alignment of LCs on functionalized, anisotropic surfaces in order to elucidate the role of molecular dipole moments of the monolayers on the subsequent adsorption and assembly of other molecular species. Extending this knowledge to other molecular systems will enhance the predictive capabilities of nanoscale engineering and enable rational design of structures extended to macroscopic scales on complex surfaces.

A.D. Materials and Methods

A.D.1. Materials

Positional isomers of dicarba-closo-dodecaboranethiol and -dithiol O1, O9, 1O2, and 9O12 were synthesized using previously reported methods;[91–93] M1 and M9 isomers were purchased from Sigma-Aldrich (St. Louis, MO). Mesogens 5CB and MBBA, as well as sodium hydroxide, and alkanethiols 1-undecanethiol (C11) and 1-octadecanethiol (C18) were also obtained from Sigma- Aldrich. Ethanol (200 proof) was purchased from Goldshield Chemical Company (Hayward, CA), while potassium hydroxide and hydrogen peroxide (30%) were acquired from Fisher Scientific (Pittsburgh, PA). Sulfuric acid (98%) was purchased from

EMD Chemicals (Gibbstown, NJ). All commercial chemicals were used as received. Deionized (DI) water (18.2 MΩ·cm) was dispensed from a Milli-Q water purifier (EMD Millipore, Billerica, MA).

A.D.2. Polymeric Stamp Preparation

Polymeric stamps were produced using a Sylgard 184 silicone elastomer kit (Dow Corning, Midland, MI) following a previously reported procedure.[94] Flat, featureless stamps were obtained and cut into strips approximately 8 mm wide, 76 mm long, and 4 mm thick.

A.D.3. Polarizing Microscopy and Image Analysis

An Olympus BX51-P polarizing microscope and CCD camera (Center Valley, PA) were used throughout this work to record the transmittances and optical textures of LC cells as 8-bit grayscale images. The transmittance of a LC cell was computed using the average intensity of all pixels within an image (1600 × 1200 pixels). Variations in the transmittance within the microscope field of view were quantified using the standard deviation of pixel intensities. Reported transmittance values reflect aggregated analyses of multiple cells and multiple locations within each cell. Automated routines facilitated image processing.

A.D.4. Alignment Layer Preparation

Eagle XG glass (Corning Display Technologies, Corning, NY), 1.1 mm thick, was used throughout this work. Glass used in anchoring energy measurements had lateral dimensions of 76 mm × 25 mm, while pieces intended for transmittance measurements were cut to approximately 19 mm × 25 mm.

A.D.4.a. Substrate Cleaning

Glass substrates were cleaned through sequential rinsing and ultrasonication steps

(>20 min) in ethanol, DI water, and concentrated potassium hydroxide solution. Afterward, the glass was rinsed in DI water and then immersed in piranha solution (3:1 H_2SO_4/H_2O_2) for ~1 h before a final rinse in DI water and being blown dry with nitrogen gas.

A.D.4.b. Oblique Metal Deposition

Cleaned glass substrates were loaded into the vacuum chamber of an electron beam metal evaporator (Kurt J. Lesker Company, Jefferson Hills, PA) immediately after drying and held at a base pressure of $\sim 1 \times 10^{-7}$ Torr. The substrates were mounted with fixed positions and orientations within the chamber such that their surface normal was inclined at an angle of 50° away from the metal source. Semitransparent gold films (10 nm) were deposited on top of chromium adhesion layers (2 nm) at rates of ~0.5 Å/s. Nominal film thicknesses were measured using a quartz crystal microbalance orientated toward the metal source, thus overestimating the amount of metal adsorbed on the glass by a factor of sec (50°) ≈ 1.6. Due to the finite sizes of the glass substrates and their positions relative to the metal source, a deviation of <6° from the intended deposition angle is expected for gold films deposited in the same batch.

A.D.4.c. Self-Assembled Monolayer Preparation

Self-assembled monolayers were formed on obliquely deposited Au/glass substrates from 1 mM ethanolic solutions of the desired adsorbate: O1, O9, M1, M9, 1O2, 9O12, C11, or C18. In the cases of 1O2 and 9O12, 1:2 carboranedithiol/NaOH equivalent solutions in ethanol were used to promote divalent adsorption on the gold surface.[65] Immediately prior to SAM deposition, Au/glass substrates were exposed to an oxygen plasma (Harrick Plasma, Ithaca, NY) for 40 s in order to remove adventitious organic adsorbates. Substrates intended

for use in transmittance measurements were immersed in solutions of the desired carboranethiol or -dithiol isomer for 12–18 h. Afterward, the uniformly functionalized surfaces were rinsed in copious amounts of ethanol and then blown dry with nitrogen gas. By contrast, soft lithography was employed to create two adjacent, spatially separated, SAMs on substrates used in anchoring energy measurements. A polymeric stamp was soaked in a solution of either C11 or C18 "ink" for at least 20 min, then rinsed with ethanol and blown dry with nitrogen gas. The inked stamp was placed into conformal contact with a clean Au/glass surface for 10 min. This stamping resulted in the formation of an alkanethiol SAM over about one-third of the alignment surface (conformal contact area). The surface was then immersed into a solution of the carboranethiol or -dithiol under investigation for 60 min in order to functionalize the remaining bare surface. Finally, the surface was rinsed with ethanol and blown dry with nitrogen gas. Observing the distinct wetting behavior of ethanol over the two SAM regions, possessing either nonpolar (aliphatic) or polar (carborane) moieties, confirmed the bifunctional character of the surface.

A.D.5. Liquid Crystal Cell Assembly

All LC cells were assembled (*vide infra*) immediately following alignment layer preparation and their cavities filled with either 5CB or MBBA *via* capillary action. To prevent flow-induced LC alignment, the alignment layers and mesogens were heated to 5–10 °C above the mesogen's clearing temperature during filling. Afterward, the cells were allowed to cool to room temperature (~20 °C) and permanently sealed using cyanoacrylate adhesive (Henkel, Westlake, OH).

A.D.5.a. Transmittance Cells

Transmittance cells were assembled using plastic spacers (30 μm thick) to separate the matching functionalized gold surfaces of two alignment layers. Alignment layers were paired such that their gold deposition axes were either parallel or crossed at angles of ~90°, producing cells with untwisted or twisted nematic structures, respectively. Copper wires were affixed to the outermost edges of both gold surfaces using conductive carbon glue (Ted Pella, Redding, CA), enabling manipulation of LC orientations by applied electric fields (potentials).

A.D.5.b. Anchoring Orientation Cells

The alignment layers of cells used to determine the in-plane LC anchoring orientations were prepared identically to those used in transmittance measurements. However, in contrast to transmittance cells, anchoring orientation cells were constructed as wedges with a spacer separating the alignment layers at only one end. In this configuration, the thickness of the cavity between the alignment layers varied linearly along the cell's longitudinal axis, independent of the transverse position. Only untwisted nematic cells, with parallel anisotropy axes, were used to determine anchoring orientations.

A.D.5.c. Anchoring Energy Cells

Adopting the design described by Abbott and co-workers,[78,79] anchoring energy cells were constructed with the wedge cell geometry described previously and engineered to contain three nematic regions. Alignment layers were arranged with crossed gold deposition axes, oriented along the longitudinal and transverse cell axes, and with matched and mismatched overlapping SAM regions, as illustrated in **Figure A.2D**. As such, the azimuthal

director orientation was induced to twist by ~90° in the central region, whereas the regions on either side exhibited untwisted, uniaxial LC alignment (90° apart) through the bulk of the cell. To prevent flexing of the alignment layers during assembly, custom-built jigs were used to ensure uniform compression. Flexing was not observed to pose a problem when constructing other, comparatively shorter, types of LC cells.

A.D.6. Transmittance Measurements

Transmittance cells were examined between the crossed polarizers of a polarizing optical microscope while illuminated with white light. The optical axes of the cells were aligned initially with either of the microscope's polarizing axes, thus minimizing (maximizing) the relative intensity of light transmitted through cells constructed with no twist (90° twist) in their nematic directors. The transmittance was measured at 5° intervals over one complete rotation of a cell. This process was repeated three times, in different regions (1.2 mm × 0.9 mm field of view), for each cell measured. Afterward, the orientation of the cell was fixed and its transmittance measured as a sinusoidally varying voltage was applied between the alignment layers (3.0 mm × 2.2 mm field of view).

A.D.7. Anchoring Orientation Determination

Anchoring orientation cells were illuminated with monochromatic light polarized 45° from their optical axes. When viewed through an analyzer crossed 90° from the polarization of the incoming light, a series of bright and dark fringes were observed, as illustrated in **Figure A.5**. These fringes were a consequence of differences in the optical retardation of light transmitted through the birefringent, LC, wedges. Wave plates (RealD, Beverly Hills, CA, and Edmund Optics, Barrington, NJ) were inserted between the polarizers, in series with the cells, to alter this retardation by fixed amounts. Changes in the fringe positions due to the

wave plates were tracked within viewing areas of about 6.0 mm × 4.5 mm.

A.D.8. Anchoring Energy Measurements

Azimuthal anchoring energies were measured using a similar procedure to that reported by Abbott and co-workers.[79] The LC alignment directions and twist angles were determined using automated routines to fit the observed rotation–transmittance spectra in each of the cells' three nematic regions (590 μm × 440 μm field of view) to their expected trigonometric responses. Estimates of local wedge cavity thicknesses were made by comparing the observed color of cells illuminated with white light to a Michel–Lévy interference color chart.[80] These estimates were refined using the positions of the transmission fringes made visible by illuminating the cells with monochromatic light. Transmittance minima and maxima bands acted as internal graduations corresponding to known cavity thicknesses. Reported anchoring energies represent an average of all measurements weighted by their respective measurement uncertainties (see Supporting Information).

A.D.9. Density Functional Theory Calculations

The six carboranethiol isomers used in this work were analyzed using density functional theory. Optimized molecular structures, dipole moments, and polarizabilities were computed at the M062X level of theory using the 6-311G** basis set with the Gaussian 09 software package (Gaussian, Wallingford, CT).[95,96]

A.E. Appendix

A.E.1. Physical Properties of Liquid Crystals

Relevant physical properties of the liquid crystals (LCs) used in this work, 5CB and MBBA, are summarized in **Table A.2**.

Property[c]	**Liquid Crystals**	
	5CB[d]	MBBA[e]
Δn[f]	0.1873	0.184
Δε[g]	+11.5	-0.5
K_{22} (pN)[h]	4.22	4.0
T_{NI} (°C)[i]	35	47
μ (D)[j]	5.1	2.2

Table A.2. Physical properties of 5CB[a] and MBBA[b] liquid crystals. [a]4-cyano-4′-pentylbiphenyl (**5CB**). [b]N-(4-methoxybenzylidene)-4-butylaniline (MBBA). [c]The values of these properties depend on the specific measurement conditions (*e.g.*, temperature, optical wavelength, and chemical purity). Here, we report values applicable to this work. [d]See Refs. [79,97–99]. [e]See Refs. [56,77,100]. [f]Birefringence (Δn), calculated as the difference in the indices of refraction of light polarized along the mesogen's extraordinary and ordinary axes. [g]Dielectric anisotropy (Δε), calculated as the difference in the mesogen's dielectric constant parallel and perpendicular to the director. [h]Mesogen twist elastic constant (K_{22}). [i]Transition temperature (T_{NI}) between the nematic and isotropic phases. [j]Permanent molecular dipole moment (μ) of the mesogen. The dipole moment of 5CB lies along its molecular axis, whereas the dipole moment of MBBA is directed primarily perpendicular to its long axis.

A.E.2. MBBA Cell Rotation–Transmittance Spectra

Figure A.7 shows the modulation in the intensity of the light transmitted through MBBA cells as they were rotated between crossed polarizers (**Figure A.2B**). Alignment layers treated with M9, M1, O9, O1, and 9O12 SAMs induced uniaxial planar alignment in MBBA cells, as indicated by the four-fold symmetry of their transmittance spectra. Cells constructed without a twist in their nematic directors vary from nearly extinguishing all transmitted light to transmitting ~50%. By contrast, cells that possess a 90° twist in their

directors have transmittances varying from ~50% to nearly 100%, due to the rotation of the polarization of the transmitted light as it traverses the cell.

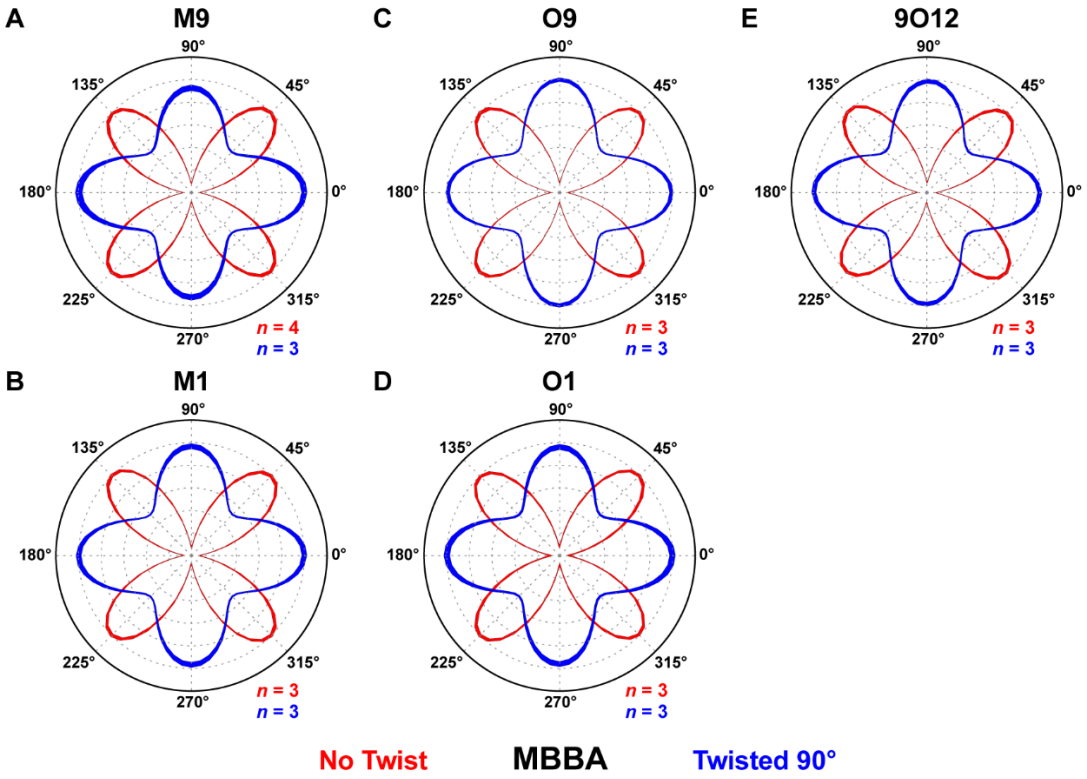

Figure A.7. Optical transmittances (indicated by the radial distance from the origin, in arbitrary units) of liquid crystal (LC) cells rotated between crossed polarizers. Alignment layers were prepared with matching self-assembled monolayers of *m*-9-carboranethiol (M9), *m*-1-carboranethiol (M1), *o*-9-carboranethiol (O9), *o*-1-carboranethiol (O1), and *o*-9,12-carboranedithiol (9O12), as indicated. At these surfaces, uniaxial, planar alignment was manifest in *N*-(4-methoxybenzylidene)-4-butylaniline (MBBA) LCs, as evidenced by the variations in optical transmittance possessing four-fold rotational symmetry. Cells were constructed with 0° or 90° angles between their alignment layers' gold deposition axes, producing untwisted (red) or twisted (blue) nematic structures, respectively. Initially, one or both of a cell's gold deposition axes were aligned with the polarizer axis, defined to be at 0°. Rotation angles were measured with respect to this reference orientation, incremented in 5° steps. Reported spectra are averages of analyses performed on separate LC cells, each consisting of three measured regions, where the radial line widths indicate the data's standard deviation. Spectra are scaled such that their respective transmittance maxima are equal; in actuality, the maximum transmittance of an untwisted nematic cell nearly equals the minimum transmittance of a cell with a 90° twist in its director.

A.E.3. MBBA Cell Voltage–Transmittance Spectra

Applying a potential difference between the alignment layers generates an electric field that can distort the LC alignment. Mesogens with negative Δε adopt an orientation perpendicular to the applied field. In the case of MBBA, such fields would induce (or reinforce) planar alignment, parallel to the surface. Any reorientation of the mesogens upon the application of an electric potential ($V_{AC} \leq 7$ V) would alter the transmittances of LC cells viewed between crossed polarizers. As seen in **Figure A.8**, transmittance of cells containing MBBA remain constant, indicating prior planar alignment of the mesogens and no subsequent reorientation.

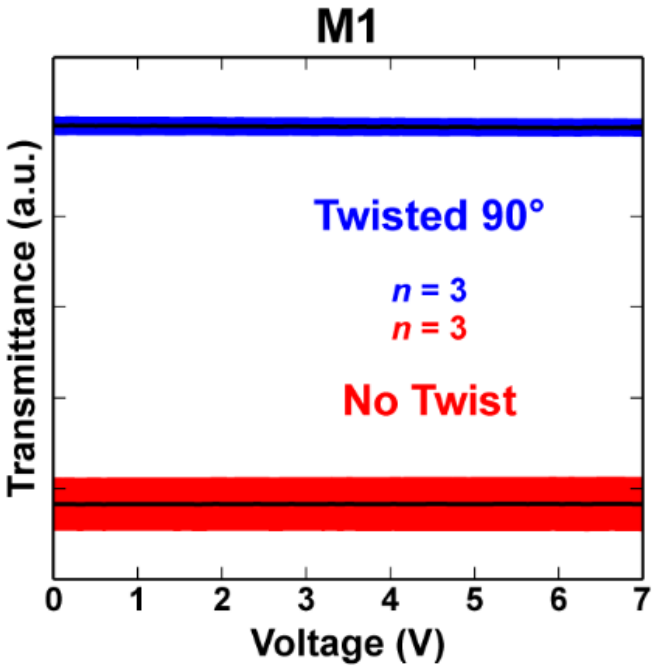

Figure A.8. Normalized optical transmittances of electrically modulated liquid crystal (LC) cells viewed between crossed polarizers. Alignment layers were prepared with matching self- assembled monolayers of *m*-1-carboranethiol (M1), which induced uniaxial planar alignment in *N*-(4-methoxybenzylidene)-4-butylaniline (MBBA) LCs. Cells were constructed with 0° or 90° angles between their alignment layers' gold deposition axes, producing untwisted (red) or twisted (blue) nematic structures, respectively. Cells were positioned between crossed polarizers such that their zero-voltage optical transmittance was maximized (minimized) for twisted (untwisted) nematic structures. Subsequently, a

sinusoidally varying (1 kHz) voltage was applied between the alignment layers. Root-mean-square voltages, varied in 0.1 V steps, are indicated along the horizontal axes. Reported spectra are averages (black lines) of analyses performed on = 3 separate LC cells, of each type, where the vertical widths of the surrounding blue outlines indicate the data's standard deviation. No changes in the transmittance spectra were observed with increasing voltage, indicating that the MBBA mesogens did not reorient as a result of the applied electric field.

A.E.4. MBBA Anchoring Orientation Cells

Anchoring orientation wedge cells were used to determine the in-plane orientation of MBBA LCs relative to $\overrightarrow{\text{Au}}$: parallel or perpendicular. As shown in **Figure A.9**, the fringes observed in cells made using M1, M9, and O1 shift toward the thinner ends of the wedges with increased optical retardation along the gold deposition axis, indicating that the MBBA nematic director is aligned parallel to $\overrightarrow{\text{Au}}$. By contrast, cells made with O9 and 9O12 exhibited planar alignment of MBBA perpendicular to $\overrightarrow{\text{Au}}$, as evident from the observed fringe shifts toward the thicker ends of the wedges. As such, the orientations of the MBBA director match those of 5CB on alignment layers treated with M1, O1, O9, and 9O12 SAMs. However, in the case of M9 SAMs, 5CB and MBBA LCs were observed to align along opposite directions, planar alignment perpendicular and parallel to $\overrightarrow{\text{Au}}$, respectively. We attribute this discrepancy to relatively weak interactions of the M9 molecular dipole moment with MBBA mesogens, in comparison to those of other carboranethiol isomers, and other factors contributing to LC alignment that are always present in each cell, though presumed consistent.

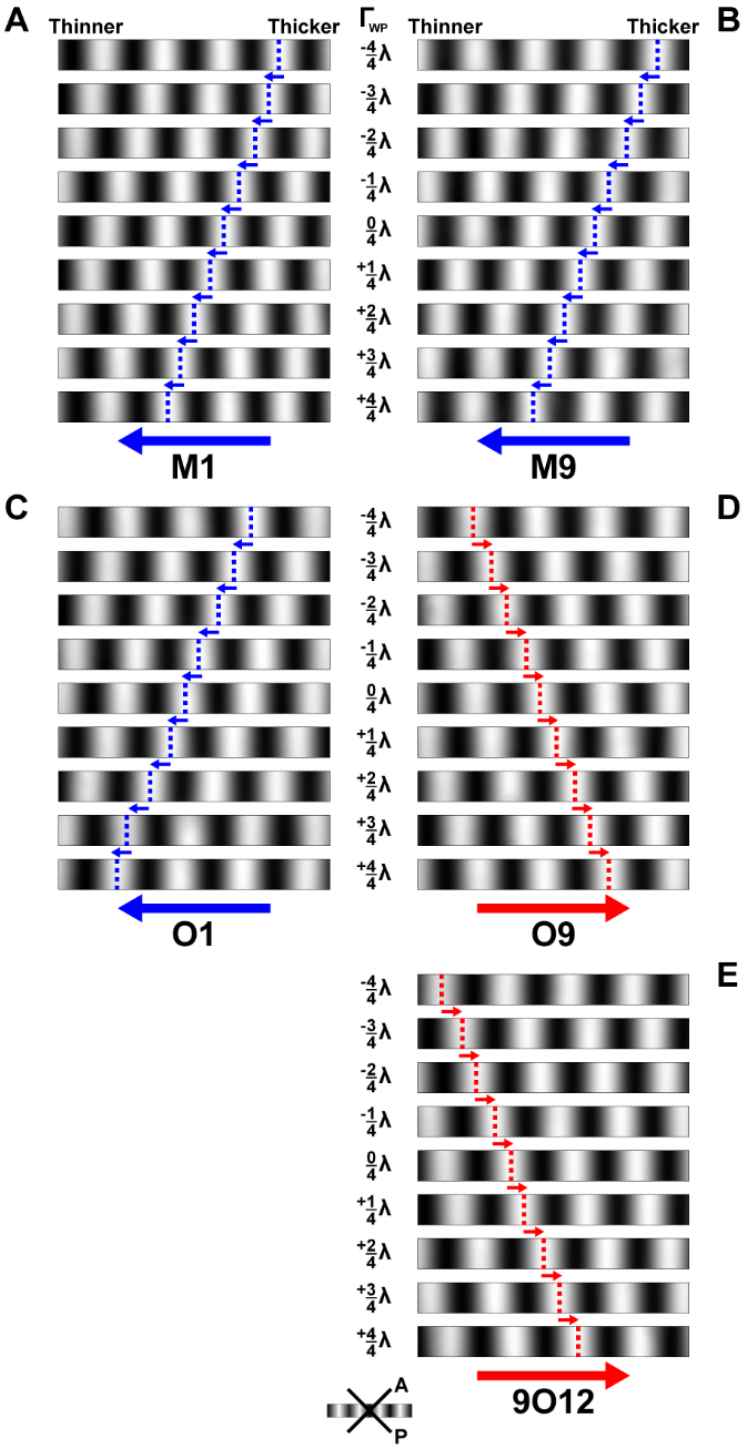

Figure A.9. Transmission fringes observed in liquid crystal (LC) wedge cells viewed between crossed polarizers while illuminated with monochromatic light (wavelength λ = 531 nm). Alignment layers prepared with matching self-assembled monolayers of *m*-1-carboranethiol (M1), *m*-9-carboranethiol (M9), *o*-1-carboranethiol (O1), *o*-9-carboranethiol (O9), and *o*-9,12-carboranedithiol (9O12), as indicated, induced uniaxial planar alignment of *N*-(4-methoxybenzylidene)-4-butylaniline (MBBA) LCs. Wave plates

inserted between the polarizers modified the optical retardation of light transmitted through the cells by fixed amounts (Γ_{WP}). Here, positive (negative) values of Γ_{WP} signify that a wave plate's optically slow axis was aligned parallel (perpendicular) to a cell's gold evaporation direction ($\overrightarrow{Au}$). Arrows and dashed lines track transmittance maxima of constant order within 4.8 mm x 0.5 μm field of view. Fringes in cells containing M1, M9, and O1 monolayers were observed to shift toward the thinner ends of the wedges with increasing Γ_{WP} (blue), indicating that their nematic directors were oriented parallel to $\overrightarrow{Au}$. By contrast, fringes shifted toward the thicker ends of wedges containing O9 and 9O12 monolayers (red), indicating director alignment perpendicular to $\overrightarrow{Au}$.

A.E.5. 5CB Cell Voltage–Transmittance Spectra

Figure A.10 depicts the normalized optical transmittances of untwisted 5CB cells modulated by an electric field. The scaling applied to these spectra exaggerates the apparent variations in the measured transmittances. Comparing absolute transmittances, the change observed in untwisted 5CB cells is only about 10% of that seen in 5CB cells with 90° twists in their directors (**Figure A.4**). The observed transmittance variations in these cells is similar to those expected from untwisted 5CB cells using other LC alignment techniques (*e.g.*, rubbed polyimide).

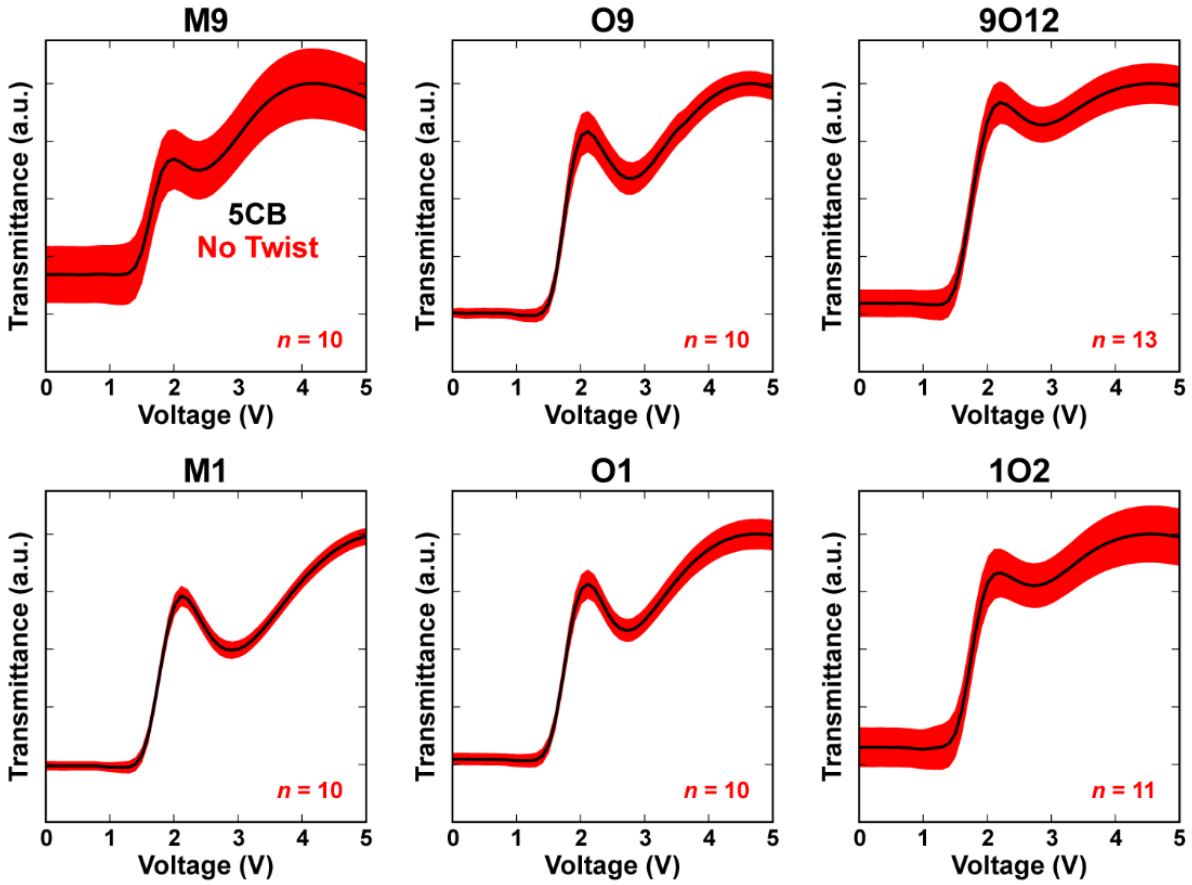

Figure A.10. Normalized optical transmittances of electrically modulated liquid crystal (LC) cells viewed between crossed polarizers. Alignment layers were prepared with matching self- assembled monolayers of *m*-9-carboranethiol (M9), *m*-1-carboranethiol (M1), *o*-9-carboranethiol (O9), *o*-1-carboranethiol (O1), *o*-9,12-carboranedithiol (9O12), and *o*-1,2-carboranedithiol (1O2), as indicated. These surfaces induced uniaxial planar alignment in 4-cyano-4′-pentylbiphenyl (5CB) LCs. Cells were constructed with parallel gold deposition axes, producing untwisted nematic structures, and were positioned between crossed polarizers such that their zero-voltage optical transmittance was minimized. Subsequently, a sinusoidally varying (1 kHz) voltage was applied between the alignment layers in order to distort the LC director away from the surface. Root-mean-square voltages, varied in 0.1 V steps, are indicated along the horizontal axes. Reported spectra are averages (black lines) of analyses performed on *n* separate LC cells, where the vertical widths of the surrounding red outlines indicate the data's standard deviation.

A.E.6. Azimuthal Anchoring Energy

Azimuthal anchoring energies of 5CB aligned by SAMs composed of M1, O9, O1, and 9O12 isomers were measured using the torque balanced method described by Abbott and

coworkers.[79] Here, we summarize the methods used to determine the parameters d, φ, and Ψ in Eq. 2. All measurements were made on anchoring energy wedge cells (**Figure A.2D**) viewed between crossed polarizers. Wedge thicknesses (d) were estimated by comparing the observed (transmitted) color of the cells, illuminated with white light polarized ±45° from their optical axes, to a Michel-Lévy interference color chart,[80] and then refined using Eq. 1 and the positions of the transmission fringes made visible using monochromatic light (λ = 531 nm).

We calculated φ and Ψ using the values of δ and γ (**Figure A.11**), which were determined by monitoring the transmission of light through each of the three nematic regions within an anchoring energy cell. The easy alignment axis of the bottom carboranethiol alignment layer (η_0-bottom) was found by rotating the cell with respect to crossed polarizers while examining an untwisted nematic region. There, transmission minima occur when η_0-bottom coincides with either of the polarizer or analyzer axes. After aligning η_0-bottom with the polarizer, the easy axis of the top carboranethiol alignment layer (η_0-top) was identified by rotating the analyzer with respect the fixed cell until the intensity of light transmitted through the second untwisted nematic region was minimized. In doing so, the analyzer was aligned perpendicular to η_0-top. The relative angle formed between the polarizer and analyzer axes equaled δ. Finally, the optical transmittance in the central, twisted nematic, region was minimized by, again, rotating the analyzer while keeping the cell orientation fixed. In this configuration, the analyzer was orthogonal to the equilibrium orientation of the director anchored by the top alignment layer (η_d-top), and the angle formed between the analyzer and polarizer axes equaled γ.

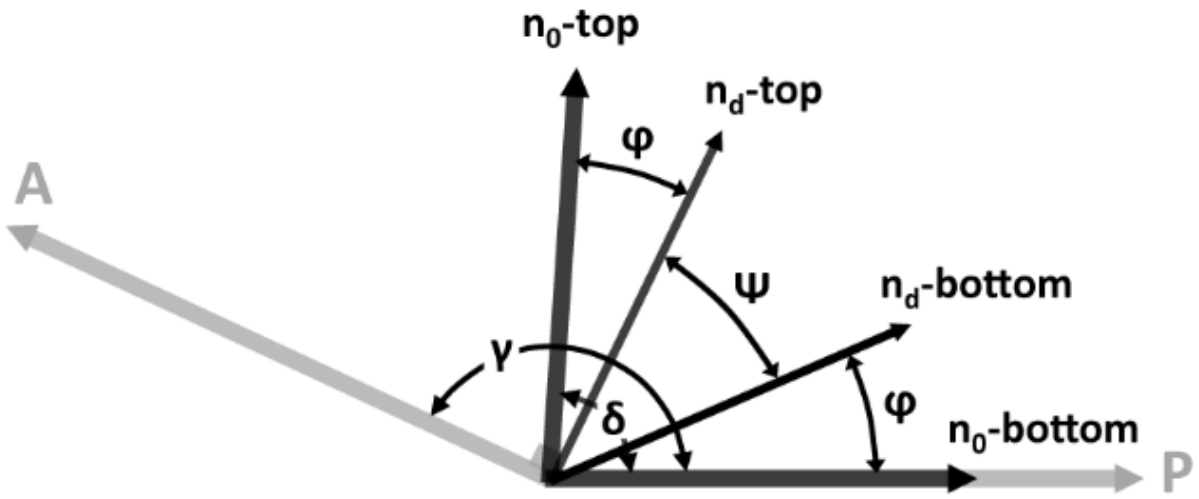

Figure A.11. Schematic illustrating the angles used to compute the azimuthal anchoring energy. Orientations of the polarizer and analyzer are denoted by P and A, respectively. Easy alignment axes are indicated for the top (η_0-top) and bottom (η_0-bottom) alignment layers, while η_d-top and η_d-bottom indicate the equilibrium director orientations at the top and bottom alignment surfaces, respectively, as a result the opposing torques acting on the twisted nematic. The angle by which the azimuthal orientation of the director deviates from the easy axes is denoted by φ, whereas Ψ is the twist in the LC director between the top and bottom alignment surfaces. Figure adapted with permission from Ref. [79]. Copyright 2006 American Chemical Society.

Once δ and γ were determined, the angle (φ) by which the azimuthal orientation of the director departs from the easy alignment axes and the angular twist (Ψ) of the director through the cell's thickness were found using the equations:

$$\varphi = \delta - (\gamma - 90°)$$

$$\Psi = 2\gamma - 90° - \delta$$

The anchoring energies reported in **Table 1** represent a weighted average of measurements made on multiple cells (at least four of a given isomer) σ and multiple areas within each cell (up to 10). We computed the uncertainties (σ) of *d*, φ, and Ψ using the following equations:

$$\sigma_d = \frac{\sigma_\Gamma}{\Delta n}$$

$$\sigma_\varphi = \sqrt{\sigma_\delta^2 + \sigma_\gamma^2}$$

$$\sigma_\Psi = \sqrt{\sigma_\delta^2 + (2\sigma_\gamma)^2}$$

The partial derivatives of W_{az} were found with respect to φ, Ψ, and d, as shown below:

$$\partial W_{az}/_{\partial \Psi} = {2K_{22}}/_{dsin(2\varphi)}$$

$$\partial W_{az}/_{\partial \varphi} = {-4K_{22}\Psi}/_{dtan(2\varphi)sin(2\varphi)}$$

$$\partial W_{az}/_{\partial d} = {-2K_{22}\Psi}\Big/_{d^2 sin(2\varphi)}$$

These quantities evaluated using the parameters of each measurement, were then used to compute the compute the uncertainty in W_{az} ($\sigma_{w\,az}$):

$$\sigma_{W_{az}} = \sqrt{\left(\partial W_{az}/_{\partial \Psi}\ \mathrm{x}\ \sigma_\Psi\right)^2 + \left(\partial W_{az}/_{\partial \varphi}\ \mathrm{x}\ \sigma_\varphi\right)^2 + \left(\partial W_{az}/_{\partial \mathrm{d}}\ \mathrm{x}\ \sigma_\mathrm{d}\right)^2}$$

The weighted average of W_{az} and $\sigma_{W_{az}}$ were calculated for i independent measurements using:

$$\text{Weighted Average } W_{az} = \left.\sum_i \frac{W_{az_i}}{\sigma^2_{W_{az_i}}}\right/ \sum_i \frac{1}{\sigma^2_{W_{az_i}}}$$

$$\text{Weighted Average } \sigma_{W_{az}} = 1\Big/\sqrt{\sum_i \frac{1}{\sigma^2_{W_{az_i}}}}$$

Table A.3. Azimuthal anchoring energy (W_{az}) of 4-cyano-4′-pentylbiphenyl (5CB) liquid crystals in cells prepared with *m*-1-carboranethiol (M1) SAMs.

M1		Γ (nm)[a]	δ (°)[b]	γ (°)[c]	$\boldsymbol{W_{az}}$ (μJ·m^{-2})
Sample 1	Spot 1	1590	86.1	1.6	24 ± 3
	Spot 2	2120	86.2	0.8	21 ± 3
Sample 2	Spot 1	800	89.2	1.7	160 ± 30
	Spot 2	1060	89.0	1.2	90 ± 30
	Spot 3	1330	81.8	5.5	11 ± 1
	Spot 4	1590	88.6	1.3	49 ± 13
	Spot 5	1860	88.4	1.4	37 ± 9
	Spot 6	2120	88.5	0.9	41 ± 12
Sample 3	Spot 1	1860	88.0	1.3	35 ± 8
	Spot 2	2120	87.7	2.8	19 ± 3
Sample 4	Spot 1	800	89.1	1.5	110 ± 30
	Spot 2	1060	89.4	1.3	110 ± 40
	Spot 3	1330	89.6	1.0	120 ± 60
	Spot 4	1590	89.8	1.1	110 ± 60
	Spot 5	1860	89.8	0.6	150 ± 140
	Spot 6	2120	89.7	0.9	85 ± 51
	Spot 7	2390	89.9	0.4	180 ± 270
Sample 5	Spot 1	800	86.3	2.0	46 ± 6
	Spot 2	1060	85.0	3.3	24 ± 2
	Spot 3	1330	86.0	2.7	24 ± 3
	Spot 4	1590	85.6	2.9	18 ± 2
	Spot 5	1860	85.5	2.3	16 ± 2
	Spot 6	2120	85.5	3.0	13 ± 1
	Spot 7	2390	86.2	2.2	15 ± 2
	Spot 8	2660	85.7	2.6	11 ± 1
	Spot 9	2920	85.9	2.3	11 ± 1
	Spot 10	3190	86.3	1.9	12 ± 2

Sample 6	Spot 1	1330	88.9	0.8	85 ± 32
	Spot 2	1590	88.6	0.9	58 ± 18
	Spot 3	1860	88.6	0.4	65 ± 26
	Spot 4	2120	88.0	0.0	49 ± 17
	Spot 5	2390	88.0	0.7	32 ± 9
	Spot 6	2660	88.2	0.1	43 ± 17
	Spot 7	2920	88.5	0.1	45 ± 20
Sample 7	Spot 1	1330	86.7	2.7	26 ± 3
	Spot 2	1590	85.8	3.4	17 ± 2
Weighted Average (n = 36)					14.3 ± 0.4

[a]Retardation (Γ) between ordinary and extraordinary waves traversing the cell. All retardation values are assumed to have a measurement uncertainty of $\sigma_\Gamma = 50$ nm. [b]The angle (δ) formed between the alignment layers' easy axes. [c]The relative angle (γ) between the polarizer and analyzer. The measurement uncertainty in the measured angles (δ and γ) are $\sigma_\delta = \sigma_\gamma = 0.5^\circ$.

Table A.4. Azimuthal anchoring energy (W_{az}) of 4-cyano-4′-pentylbiphenyl (5CB) liquid crystals in cells prepared with *o*-1-carboranethiol (O1) SAMs.

O1		Γ (nm)[a]	δ (°)[b]	γ (°)[c]	$\boldsymbol{W_{az}}$ (μJ·m^{-2})
Sample 1	Spot 1	1060	84.7	3.5	22 ± 2
	Spot 2	1330	83.1	4.3	14 ± 1
	Spot 3	1590	84.8	2.9	16 ± 2
	Spot 4	1860	85.3	2.5	16 ± 2
	Spot 5	2120	85.4	2.2	14 ± 2
Sample 2	Spot 1	800	87.0	2.1	51 ± 8
	Spot 2	1060	86.7	3.4	29 ± 3
	Spot 3	1330	86.9	3.2	25 ± 3
	Spot 4	1590	86.9	2.5	24 ± 3
	Spot 5	1860	87.5	1.6	27 ± 5
	Spot 6	2120	87.2	0.1	35 ± 9

Sample 3	Spot 1	1330	88.3	3.5	30 ± 4
	Spot 2	1590	88.1	1.1	45 ± 11
	Spot 3	1860	88.7	2.4	30 ± 6
	Spot 4	2120	88.6	2.7	24 ± 4
	Spot 5	2390	89.4	2.3	30 ± 7
	Spot 6	2660	89.0	2.0	27 ± 6
Sample 4	Spot 1	2920	88.2	1.7	20 ± 4
	Spot 2	3190	88.0	1.4	19 ± 4
	Spot 3	3450	87.4	1.1	17 ± 3
Sample 5	Spot 1	530	81.9	0.5	46 ± 6
	Spot 2	800	85.3	4.8	27 ± 2
	Spot 3	1330	85.4	4.3	17 ± 2
	Spot 4	1590	85.4	2.3	19 ± 2
	Spot 5	1860	86.3	2.5	18 ± 2
	Spot 6	2120	85.7	3.7	12 ± 1
	Spot 7	2390	86.6	3.0	14 ± 2
	Spot 8	2660	86.8	2.6	13 ± 2
Sample 6	Spot 1	1060	85.7	3.7	24 ± 2
	Spot 2	1330	86.0	3.5	21 ± 2
	Spot 3	1590	86.0	2.8	19 ± 2
	Spot 4	1860	86.6	1.9	21 ± 3
	Spot 5	2120	86.4	2.9	15 ± 2
	Spot 6	2390	86.6	2.4	15 ± 2
	Spot 7	2660	86.6	2.4	14 ± 2
	Spot 8	2920	87.0	2.4	13 ± 2
	Spot 9	3190	87.2	1.9	14 ± 2
Weighted Average (n = 37)					14.3 ± 0.4

[a]Retardation (Γ) between ordinary and extraordinary waves traversing the cell. All retardation values are assumed to have a measurement uncertainty of $\sigma_\Gamma = 50$ nm. [b]The angle (δ) formed between the alignment layers' easy axes. [c]The relative angle (γ) between the polarizer and analyzer. The measurement uncertainty in the measured angles (δ and γ) are $\sigma_\delta = \sigma_\gamma = 0.5^\circ$.

Table A.5. Azimuthal anchoring energy (W_{az}) of 4-cyano-4′-pentylbiphenyl (5CB) liquid crystals in cells prepared with *o*-9-carboranethiol (O9) SAMs.

O9		Γ (nm)[a]	δ (°)[b]	γ (°)[c]	W_{az} (μJ·m^{-2})
Sample 1	Spot 1	1060	87.4	2.4	40 ± 6
	Spot 2	1590	87.5	2.3	27 ± 4
	Spot 3	3190	88.6	0.7	32 ± 11
Sample 2	Spot 1	1060	90.3	2.0	110 ± 50
	Spot 2	1330	90.0	1.6	96 ± 41
	Spot 3	1590	89.9	2.4	54 ± 16
	Spot 4	1860	89.4	0.8	83 ± 43
Sample 3	Spot 1	800	85.4	5.5	26 ± 2
	Spot 2	1060	83.4	7.6	14 ± 1
	Spot 3	1330	84.8	5.6	14 ± 1
	Spot 4	1590	84.9	7.0	11 ± 1
	Spot 5	1860	85.3	5.1	11 ± 1
	Spot 6	2120	84.3	6.5	7.9 ± 0.5
Sample 4	Spot 1	1060	84.4	4.3	20 ± 2
	Spot 2	1330	84.6	3.8	17 ± 1
	Spot 3	1590	84.7	4.0	14 ± 1
	Spot 4	1860	85.2	3.0	14 ± 1
	Spot 5	2120	85.7	3.3	13 ± 1
	Spot 6	2390	85.2	3.4	11 ± 1
Sample 5	Spot 1	1060	81.5	9.9	11 ± 1
	Spot 2	1330	83.4	7.4	11 ± 1
	Spot 3	1590	83.1	7.7	8.9 ± 0.5
	Spot 4	1860	83.5	6.7	8.4 ± 0.5

	Spot 5	2120	83.2	7.4	6.8 ± 0.4
	Spot 6	2390	83.7	6.4	6.8 ± 0.4
	Spot 7	2660	83.3	7.0	5.6 ± 0.3
	Spot 8	2920	83.7	6.5	5.5 ± 0.3
	Spot 9	3190	83.7	6.1	5.2 ± 0.3
Weighted Average (n = 28)					7.5 ± 0.1

[a]Retardation (Γ) between ordinary and extraordinary waves traversing the cell. All retardation values are assumed to have a measurement uncertainty of $\sigma_\Gamma = 50$ nm. [b]The angle (δ) formed between the alignment layers' easy axes. [c]The relative angle (γ) between the polarizer and analyzer. The measurement uncertainty in the measured angles (δ and γ) are $\sigma_\delta = \sigma_\gamma = 0.5^\circ$.

Table A.6. Azimuthal anchoring energy (W_{az}) of 4-cyano-4′-pentylbiphenyl (5CB) liquid crystals in cells prepared with *o*-9,12-carboranedithiol (9O12) SAMs.

9O12		Γ (nm)[a]	δ (°)[b]	γ (°)[c]	W_{az} (μJ·m^{-2})
Sample 1	Spot 1	800	86.2	4.6	31 ± 3
	Spot 2	1060	83.5	3.1	20 ± 2
	Spot 3	1330	84.7	0.3	28 ± 4
	Spot 4	1590	84.2	0.7	20 ± 2
	Spot 5	1860	85.5	2.0	17 ± 2
	Spot 6	2120	84.2	0.6	15 ± 2
	Spot 7	2390	85.9	0.8	18 ± 3
Sample 2	Spot 1	1590	89.9	3.4	38 ± 8
	Spot 2	1860	89.9	2.4	46 ± 13
	Spot 3	2120	88.7	2.2	29 ± 6
	Spot 4	2390	89.1	1.7	34 ± 9
	Spot 5	2660	89.9	2.4	32 ± 9
	Spot 6	2920	88.8	3.3	16 ± 3
Sample 3	Spot 1	1330	81.6	7.0	10 ± 1
	Spot 2	1590	80.9	7.5	7.8 ± 0.4
	Spot 3	1860	82.6	5.7	8.5 ± 0.5
	Spot 4	2120	81.9	6.5	6.6 ± 0.3

	Spot 5	2390	82.8	5.4	6.8 ± 0.4
	Spot 6	2660	81.8	5.8	5.6 ± 0.3
	Spot 7	2920	83.5	5.2	6.0 ± 0.4
	Spot 8	3190	81.5	6.4	4.3 ± 0.2
Sample 4	Spot 1	1330	85.8	5.8	16 ± 1
	Spot 2	1590	86.0	5.7	13 ± 1
	Spot 3	1860	85.8	3.8	14 ± 1
	Spot 4	2120	85.7	4.4	11 ± 1
	Spot 5	2390	86.0	2.9	13 ± 1
	Spot 6	2660	86.1	2.7	12 ± 1
	Spot 7	2920	85.9	2.4	11 ± 1
	Spot 8	3190	84.9	3.0	8.0 ± 0.7
Weighted Average (n = 29)					6.7 ± 0.1

[a]Retardation (Γ) between ordinary and extraordinary waves traversing the cell. All retardation values are assumed to have a measurement uncertainty of $\sigma_\Gamma = 50$ nm. [b]The angle (δ) formed between the alignment layers' easy axes. [c]The relative angle (γ) between the polarizer and analyzer. The measurement uncertainty in the measured angles (δ and γ) are $\sigma_\delta = \sigma_\gamma = 0.5^\circ$.

A.E.7. Oblique Gold Deposition

Gold was deposited at an oblique angle (50° away from the normal) onto glass substrates, as shown in **Figure A.12**. This angle describes the incidence angle of metal deposited in the center of the tilted substrate, located directly above the metal source. However, for extended substrates, this angle depends on the surface's distance away from the central deposition axis. Here, this deviation is no more than 6° from the intended deposition angle.

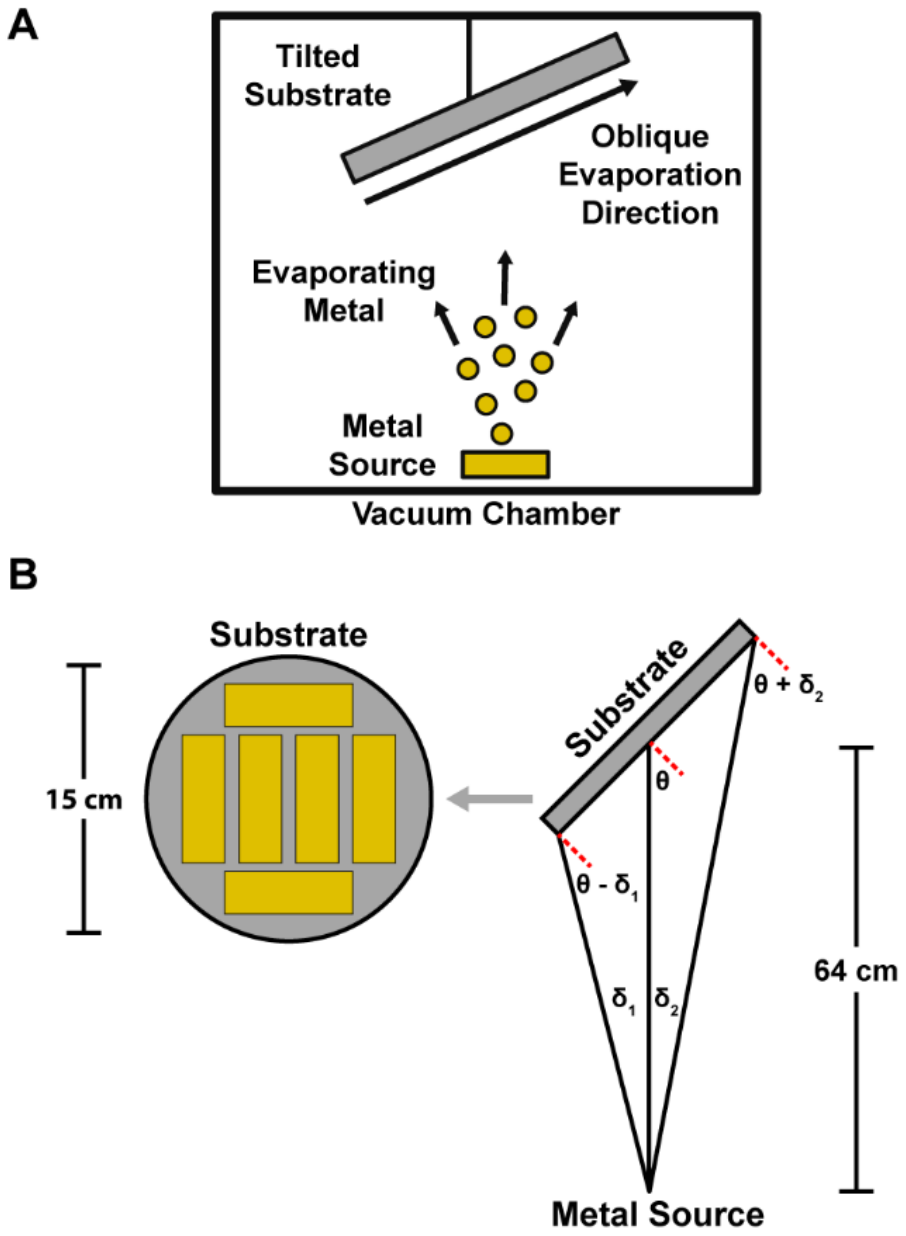

Figure A.12. Schematic of oblique gold deposition. (A) Inside a vacuum chamber, gold is heated by an electron beam (not shown), causing it to evaporate from a source and deposit onto a tiled substrate located above. (B) Due to the non-zero widths and arrangement of glass, the deposition angle varies across the surface and between slides. Deviations from the intended angle ($\theta = 50°$) are expected to be, at most, $ß_1 = ß_2 = 6°$ for the dimensions and configuration used in this work.

A.E.8. Gaussian Calculations

A.E.8.a. Molecular Dipole Moments

Table A.8 summarizes the molecular dipole moments of M9, M1, O9, O1, 9O12, and 1O2 calculated using density functional theory and the Gaussian 09 software package at the M062X level with the 6-311G** basis set. Dipole component vectors ($p_{\parallel}$ and $p_{\perp}$) assume upright adsorption of the carboranethiol species on a gold surface.

Isomer	Molecular Dipole Moment (D) Magnitude	$\boldsymbol{p}_{\parallel}$[a]	$\boldsymbol{p}_{\perp}$[b]
M9[c]	3.94	1.38	3.70
M1[d]	2.20	2.13	-0.558
O9[e]	5.46	2.18	5.01
O1[f]	3.59	1.90	-3.05
9O12[g]	6.78	0.00	6.78
1O2[h]	3.20	0.00	-3.20

Table A.7. Molecular dipole moments (p) of carboranethiol and -dithiol isomers. [a]In-plane dipole moment, parallel to the surface. [b]Out-of-plane dipole moment, normal to the surface. [c]*m*-9-carboranethiol (M9). [d]*m*-1-carboranethiol (M1). [e]*o*-9-carboranethiol (O9). [f]*o*-1-carboranethiol (O1). [g]*o*-9,12-carboranedithiol (9O12). [h]*o*-1,2-carboranedithiol (1O2).

A.E.8.b. Molecular Polarizability Tensor

The molecular polarizability tensor (α) of all six carboranethiols studied here were computed with the Gaussian 09 software package:

$$\alpha = \begin{bmatrix} \alpha_{xx} & \alpha_{xy} & \alpha_{xz} \\ \alpha_{xy} & \alpha_{yy} & \alpha_{yz} \\ \alpha_{xz} & \alpha_{yz} & \alpha_{zz} \end{bmatrix}$$

As described in the main text, Cartesian coordinate bases were chosen for each isomer based on its molecular symmetry and assumed upright adsorption onto underlying gold substrates. We found the polarizability tensors of each isomer to be *nearly* diagonalized in the chosen coordinate basis. As such, we consider only the carboranethiol polarizabilities along each of

the coordinate axes (α_{xx}, α_{yy}, and α_{zz}), as summarized in **Table A.8**.

Isomer	Principal Polarizabilities (Å^3)		
	$\boldsymbol{\alpha_{xx}}$	$\boldsymbol{\alpha_{yy}}$	$\boldsymbol{\alpha_{zz}}$
M9[a]	19.4	19.2	24.3
M1[b]	19.4	19.6	23.6
O9[c]	19.5	19.8	24.0
O1[d]	19.4	19.7	23.7
9O12[e]	24.0	21.3	26.3
1O2[f]	23.4	21.3	26.4

Table A.8. Molecular polarizabilities (α) of carboranethiol and -dithiol isomers. [a]*m*-9-carboranethiol (M9). [b]*m*-1-carboranethiol (M1). [c]*o*-9-carboranethiol (O9). [d]*o*-1-carboranethiol (O1). [e]*o*-9,12-carboranedithiol (9O12). [f]*o*-1,2-carboranedithiol (1O2).

A.E.8.c. Optimized Molecular Geometries and Dipoles

Computed values of the molecular dipole vectors and polarizability tensors depend on the optimized orientation of the thiol moiety (S–H bond) in each carboranethiol isomer. However, the hydrogen on the molecule's thiol functionality is lost during chemisoption onto the gold surface (becoming -thiol*ate*). As such, the dipoles and polarizabilities computed for these structures do not accurately reflect those of the actual *adsorbed* molecule. To account for this change in molecular structure upon chemisorption, we computed the molecular dipoles and polarizabilities of each isomer as the average of those values from multiple (nearly degenerate) conformations of each isomer. Each molecular conformation was distinguished by the initial value of the carborane–sulfur–hydrogen dihedral angle in the unoptimized structure, reflecting the rotational symmetry of the thiol moieties in each isomer (five-fold and two-fold symmetries in the cases of mono- and dithiol species, respectively). Averaging effectively eliminates the thiol contributions to the in-plane molecular dipole and polarizability. **Table A.9** present the atomic coordinates of each

structure after optimization, labeled with the initial thiol dihedral angles. During optimization, atoms in each structure were allowed to relax into their lowest energy positions with the exceptions of dihedral angles denoted by "F." In these "frozen" structures, the value of the thiol dihedral angle was not optimized in order to maintain the desired molecular symmetry. These molecular conformations do not represent energetically optimized structures. If optimized without restrictions, an unfavorable interaction between the electron deficient carbon atoms in the carborane cage and the polar S–H bond would cause the thiol dihedral angle to deviate significantly from its initial value and disrupt the symmetry of the model. As such, these structures were used with only partial structural optimization. We reiterate, however, that the adsorbed molecule does not possess the carborane–sulfur–hydrogen dihedral angle left unoptimized here. In the cases of carboranedithiol isomers, the two conformations are distinguished by an "M" (or its absence) in the table heading. These conformations are mirror-symmetric versions of the fully optimized structures, reflecting the bilateral symmetry of the dithiol species.

Table A.9. Optimized molecular geometries and dipoles of each carboranethiol and –dithiol isomer.

M9 (0°) Energy: -730.121306 Eh

Atom	Position Coordinates (Å)		
	X	Y	Z
B	0.112328	-0.4994	-1.422584
B	-1.393971	-1.240065	-0.862785
B	0.131359	1.192437	-0.906861
B	1.065263	-0.016128	-0.000362
B	0.115184	-1.520253	0.025303
B	-1.360695	1.500783	-0.024783
B	0.132472	1.22187	0.865364
B	0.113277	-0.451841	1.437922
B	-1.393854	-1.210304	0.904755
C	-1.319917	0.443261	1.287942
H	0.545346	-0.778257	-2.48149
H	0.633748	-2.580157	0.042517
H	0.562947	2.034117	-1.609023
H	-1.965234	2.508414	-0.040872
H	0.54684	-0.695522	2.505253
H	0.564102	2.086491	1.539219
H	-1.978863	-1.950561	1.609212
H	-1.979496	-2.003201	-1.541961
B	-2.308671	-0.005531	0.000636
C	-1.321212	0.400457	-1.301621
H	-1.816124	0.69738	-2.21541
H	-3.478525	0.103897	-0.00055
H	-1.813884	0.770472	2.191888
S	2.927707	-0.084822	-0.000618
H	3.119158	1.243927	0.010164

M9 (72°, F) Energy: -730.121033 Eh

Atom	Position Coordinates (Å)		
	X	Y	Z
B	-0.107117	1.489342	-0.232513
B	1.407478	1.341038	0.681516
B	-0.124049	0.23107	-1.485054
B	-1.064653	0.023934	0.015641
B	-0.099851	0.71243	1.358978
B	1.361379	-0.70142	-1.331054
B	-0.144687	-1.331282	-0.667711
B	-0.12732	-1.032239	1.085953
B	1.396634	-0.222552	1.496113
C	1.298797	-1.351164	0.224497
H	-0.52408	2.559672	-0.494616
H	-0.619224	1.205486	2.295336
H	-0.556541	0.456686	-2.556171
H	1.961981	-1.17588	-2.222646
H	-0.567869	-1.855249	1.805434
H	-0.587619	-2.333491	-1.100653
H	1.982563	-0.502995	2.478173
H	2.004867	2.297188	1.021268
B	2.308309	-0.015211	0.004933
C	1.326391	0.944199	-0.974342
H	1.825069	1.607339	-1.666786
H	3.477842	-0.077383	-0.089676
H	1.778651	-2.3084	0.37096
S	-2.928377	0.083104	-0.008285
H	-3.103354	-1.236404	0.156996

M9 (144°) Energy: -730.121494 Eh

Atom	Position Coordinates (Å)		
	X	Y	Z
B	0.115038	-0.247782	1.486599
B	-1.389949	0.678357	1.355552
B	0.123054	-1.48438	0.211914
B	1.064465	0.002157	0.005351
B	0.124923	1.340214	0.714753
B	-1.376141	-1.318956	-0.701775
B	0.11839	-0.660627	-1.352864
B	0.124748	1.079833	-1.040262
B	-1.378709	1.50418	-0.204677
C	-1.321241	0.238252	-1.340791
H	0.547625	-0.521716	2.54693
H	0.654528	2.273163	1.206619
H	0.543676	-2.564026	0.422844
H	-1.989435	-2.205945	-1.168597
H	0.560845	1.805697	-1.859864
H	0.546522	-1.092243	-2.360608
H	-1.95537	2.496756	-0.466906
H	-1.972793	1.023154	2.318847
B	-2.308361	0.019761	0.005842
C	-1.322341	-0.970733	0.950342
H	-1.818246	-1.668702	1.609747
H	-3.479332	-0.064677	-0.041078
H	-1.815604	0.39646	-2.288699
S	2.927231	-0.080245	0.011026
H	3.116097	1.237102	-0.155119

M9 (216°) Energy: -730.121477 Eh

Atom	Position Coordinates (Å)		
	X	Y	Z
B	-0.124597	1.086609	-1.033387
B	1.379	1.505224	-0.195074
B	-0.118495	-0.651983	-1.35705
B	-1.06448	0.002546	0.005272
B	-0.124588	1.335919	0.723338
B	1.37587	-1.314633	-0.71017
B	-0.123365	-1.485513	0.202565
B	-0.115139	-0.256927	1.48488
B	1.390147	0.669584	1.359842
C	1.322024	-0.976836	0.944141
H	-0.560253	1.817911	-1.848367
H	-0.653903	2.265837	1.221148
H	-0.546574	-1.077265	-2.367499
H	1.988938	-2.198763	-1.182581
H	-0.548029	-0.537573	2.543311
H	-0.544392	-2.566275	0.40671
H	1.973231	1.007945	2.325235
H	1.955856	2.499308	-0.451081
B	2.308375	0.019311	0.005949
C	1.321141	0.246531	-1.339235
H	1.815492	0.410709	-2.286122
H	3.479296	-0.064984	-0.041786
H	1.817685	-1.679032	1.599219
S	-2.927112	-0.080227	0.011179
H	-3.116187	1.236947	-0.157323

M9 (288°, F) Energy: -730.121018 Eh

Atom	Position Coordinates (Å)		
	X	Y	Z
B	0.127109	-1.028763	1.089338
B	-1.396597	-0.217475	1.496728
B	0.144485	-1.33351	-0.663294
B	1.064659	0.023668	0.015675
B	0.099985	0.716784	1.356662
B	-1.361459	-0.705701	-1.328731
B	0.124055	0.226207	-1.485686
B	0.10728	1.488266	-0.237305
B	-1.407242	1.34333	0.677033
C	-1.326282	0.941081	-0.977404
H	0.567346	-1.849514	1.81159
H	0.619366	1.212841	2.291423
H	0.587356	-2.337148	-1.092998
H	-1.961899	-1.18308	-2.21888
H	0.524468	2.557678	-0.502845
H	0.556726	0.44801	-2.557526
H	-2.004556	2.300618	1.013718
H	-1.982526	-0.494497	2.479764
B	-2.308381	-0.014963	0.00492
C	-1.298953	-1.350281	0.228872
H	-1.778958	-2.306977	0.378352
H	-3.477942	-0.077368	-0.089287
H	-1.824922	1.602042	-1.671963
S	2.928368	0.083084	-0.008571
H	3.103583	-1.235965	0.160289

M1 (0°) Energy: -730.087128 Eh

Atom	Position Coordinates (Å)		
	X	Y	Z
B	-0.006375	-2.29319	0
B	-0.459726	-1.363726	1.437534
B	-0.459726	-1.363726	-1.437534
B	1.223728	-1.384639	-0.891013
B	1.223728	-1.384639	0.891013
B	-1.182181	0.149111	-0.892629
B	0.48693	0.123759	-1.444556
B	1.518888	0.119307	0
B	0.48693	0.123759	1.444556
B	0.024159	0.931496	0
S	0.083814	2.73539	0
H	-0.167801	-3.459906	0
H	2.067258	-1.914586	1.522554
H	2.067258	-1.914586	-1.522554
H	-0.921438	-1.89197	-2.383428
H	-2.065369	0.721566	-1.41736
H	-1.248119	2.907203	0
H	2.505108	0.764927	0
H	0.772391	0.773359	-2.38313
H	0.772391	0.773359	2.38313
H	-0.921438	-1.89197	2.383428
B	-1.182181	0.149111	0.892629
C	-1.363978	-1.267222	0
H	-2.347043	-1.716478	0
H	-2.065369	0.721566	1.41736

M1 (72°) Energy: -730.086719 Eh

Atom	Position Coordinates (Å)		
	X	Y	Z
B	-2.292922	0.008104	0.001202
B	-1.351529	1.477475	-0.319174
B	-1.366046	-1.382705	-0.59101
B	-1.384156	-0.997583	1.139364
B	-1.379755	0.774135	1.307899
B	0.135976	-0.774191	-1.272138
B	0.130363	-1.474634	0.347126
B	0.113794	-0.145286	1.521828
B	0.140591	1.378588	0.620809
C	0.931724	-0.00727	0.019786
S	2.734587	-0.082457	0.004335
H	-3.460917	0.028378	-0.149555
H	-1.904398	1.332514	2.204708
H	-1.913163	-1.710976	1.915695
H	-1.899745	-2.282461	-1.131451
H	0.704107	-1.213897	-2.20145
H	2.914123	1.246972	-0.047249
H	0.765394	-0.243144	2.497542
H	0.774677	-2.442482	0.538475
H	0.790995	2.289757	0.99037
H	-1.872732	2.469755	-0.681038
B	0.147192	0.989834	-1.103327
C	-1.281687	0.132558	-1.354182
H	-1.738415	0.228793	-2.329122
H	0.71892	1.595678	-1.932806

M1 (144°) Energy: -730.087017 Eh

Atom	Position Coordinates (Å)		
	X	Y	Z
B	-2.293109	0.017216	0.001486
B	-1.360217	0.669061	-1.354707
B	-1.373176	-1.313809	0.72623
B	-1.380499	0.282112	1.492663
B	-1.361946	1.51154	0.203894
B	0.134621	-1.474987	-0.174985
B	0.12058	-0.64859	1.381965
B	0.132345	1.09069	1.051876
B	0.143705	1.333847	-0.710188
C	0.932064	0.001243	0.013466
S	2.734744	-0.080646	-0.013276
H	-3.462148	-0.082814	-0.103683
H	-1.873994	2.567262	0.326204
H	-1.906431	0.46288	2.532934
H	-1.911767	-2.294378	1.094128
H	0.69376	-2.483458	-0.404766
H	2.912093	1.23049	0.212904
H	0.787364	1.799228	1.729461
H	0.766035	-1.098792	2.256971
H	0.799147	2.184055	-1.196109
H	-1.887121	0.999917	-2.354646
B	0.135456	-0.251719	-1.468886
C	-1.285171	-0.976151	-0.939641
H	-1.745808	-1.684442	-1.613714
H	0.7028	-0.536976	-2.456955

M1 (216°) Energy: -730.087017 Eh

Atom	Position Coordinates (Å)		
	X	Y	Z
B	2.293109	0.017216	0.001486
B	1.373176	-1.313809	0.72623
B	1.360217	0.669061	-1.354707
B	1.361946	1.51154	0.203894
B	1.380499	0.282112	1.492663
B	-0.135456	-0.251719	-1.468886
B	-0.143705	1.333847	-0.710188
B	-0.132345	1.09069	1.051876
B	-0.12058	-0.64859	1.381965
C	-0.932064	0.001243	0.013466
S	-2.734744	-0.080646	-0.013276
H	3.462148	-0.082814	-0.103683
H	1.906431	0.46288	2.532934
H	1.873994	2.567262	0.326204
H	1.887121	0.999917	-2.354646
H	-0.7028	-0.536976	-2.456955
H	-2.912093	1.23049	0.212904
H	-0.787364	1.799228	1.729461
H	-0.799147	2.184055	-1.196109
H	-0.766035	-1.098792	2.256971
H	1.911767	-2.294378	1.094128
B	-0.134621	-1.474987	-0.174985
C	1.285171	-0.976151	-0.939641
H	1.745808	-1.684442	-1.613714
H	-0.69376	-2.483458	-0.404766

M1 (288°) Energy: -730.086719 Eh

Atom	Position Coordinates (Å)		
	X	Y	Z
B	2.292922	0.008104	0.001202
B	1.366046	-1.382705	-0.59101
B	1.351529	1.477475	-0.319174
B	1.379755	0.774135	1.307899
B	1.384156	-0.997583	1.139364
B	-0.147192	0.989834	-1.103327
B	-0.140591	1.378588	0.620809
B	-0.113794	-0.145286	1.521828
B	-0.130363	-1.474634	0.347126
C	-0.931724	-0.00727	0.019786
S	-2.734587	-0.082457	0.004335
H	3.460917	0.028378	-0.149555
H	1.913163	-1.710976	1.915695
H	1.904398	1.332514	2.204708
H	1.872732	2.469755	-0.681038
H	-0.71892	1.595678	-1.932806
H	-2.914123	1.246972	-0.047249
H	-0.765394	-0.243144	2.497542
H	-0.790995	2.289757	0.99037
H	-0.774677	-2.442482	0.538475
H	1.899745	-2.282461	-1.131451
B	-0.135976	-0.774191	-1.272138
C	1.281687	0.132558	-1.354182
H	1.738415	0.228793	-2.329123
H	-0.704107	-1.213897	-2.20145

O9 (0°) Energy: -730.094599 Eh

Atom	Position Coordinates (Å)		
	X	Y	Z
B	0.542841	0.916284	0
B	1.083677	-0.516861	0.891108
B	1.083677	-0.516861	-0.891108
B	-0.350068	0.357946	-1.448694
B	-1.227917	0.912141	0
B	-0.350068	0.357946	1.448694
B	-0.350068	-1.400445	-1.44712
B	-1.778961	-0.51853	-0.88931
B	-1.778961	-0.51853	0.88931
B	-0.350068	-1.400445	1.44712
C	0.464261	-1.805781	0
C	-1.152496	-1.811643	0
H	-0.338989	0.957717	2.463669
H	-1.861642	1.90792	0
H	-0.338989	0.957717	-2.463669
H	2.096703	-0.672771	-1.472741
H	-0.344929	-2.189553	-2.319443
H	-2.788995	-0.685343	1.471825
H	-2.788995	-0.685343	-1.471825
H	-0.344929	-2.189553	2.319443
H	2.096703	-0.672771	1.472741
H	0.945015	-2.77296	0
H	-1.627003	-2.78164	0
S	1.505326	2.513933	0
H	2.719823	1.944986	0

O9 (72°) Energy: -730.0948 Eh

Atom	Position Coordinates (Å)		
	X	Y	Z
B	1.064565	-0.007598	0.027938
B	0.134338	-0.810727	-1.258873
B	0.143316	0.956589	-1.144262
B	0.12899	1.404468	0.576582
B	0.107352	-0.099379	1.526885
B	0.118428	-1.470079	0.38939
B	-1.357907	1.47662	-0.363681
B	-1.387357	0.81101	1.280286
B	-1.393438	-0.959102	1.166661
B	-1.371079	-1.41017	-0.549248
C	-1.287983	0.089642	-1.355432
C	-2.1468	0.007	0.006049
H	0.620355	-2.509586	0.634328
H	0.616099	-0.1701	2.588755
H	0.640394	2.4016	0.948246
H	0.552876	1.598589	-2.043203
H	-2.01611	2.381335	-0.726398
H	-2.075255	-1.594078	1.887139
H	-2.064889	1.354372	2.07603
H	-2.038895	-2.255197	-1.021612
H	0.540415	-1.333767	-2.232292
H	-1.853578	0.151736	-2.27357
H	-3.220411	0.019033	-0.108353
S	2.928301	-0.082815	0.011069
H	3.11884	1.243098	-0.068264

O9 (144°) Energy: -730.094923 Eh

Atom	Position Coordinates (Å)		
	X	Y	Z
B	1.065074	0.002122	0.023183
B	0.131243	-1.41369	-0.487481
B	0.136771	0.050894	-1.495056
B	0.133297	1.456604	-0.419792
B	0.121093	0.852553	1.261458
B	0.109025	-0.925264	1.219941
B	-1.363324	0.942262	-1.193502
B	-1.374003	1.431907	0.509057
B	-1.393051	-0.034717	1.511838
B	-1.37787	-1.444914	0.443129
C	-1.288402	-0.758845	-1.122134
C	-2.145982	0.016273	0.004706
H	0.614246	-1.594332	2.048968
H	0.631342	1.453155	2.140577
H	0.649726	2.46875	-0.739337
H	0.546208	-0.002402	-2.597481
H	-2.024455	1.432524	-2.033672
H	-2.075201	-0.078673	2.471003
H	-2.04357	2.353589	0.807858
H	-2.050969	-2.399175	0.583474
H	0.529885	-2.428919	-0.932385
H	-1.855808	-1.278364	-1.880146
H	-3.220111	-0.040784	-0.090707
S	2.927638	-0.075125	-0.021175
H	3.121548	1.183284	0.401344

O9 (216°) Energy: -730.094923 Eh

Atom	Position Coordinates (Å)		
	X	Y	Z
B	-1.065074	0.002122	0.023183
B	-0.136771	0.050906	-1.495056
B	-0.131243	-1.413686	-0.487492
B	-0.109025	-0.925274	1.219934
B	-0.121093	0.852544	1.261465
B	-0.133297	1.456607	-0.41978
B	1.37787	-1.444918	0.443117
B	1.393051	-0.034729	1.511837
B	1.374003	1.431903	0.509069
B	1.363324	0.942272	-1.193494
C	1.288402	-0.758837	-1.12214
C	2.145982	0.016273	0.004706
H	-0.649726	2.468756	-0.739317
H	-0.631342	1.453138	2.140589
H	-0.614246	-1.594348	2.048955
H	-0.529884	-2.428912	-0.932404
H	2.050969	-2.39918	0.583455
H	2.04357	2.353583	0.807876
H	2.075201	-0.078692	2.471003
H	2.024455	1.43254	-2.033661
H	-0.546207	-0.002381	-2.597482
H	1.855808	-1.278349	-1.880156
H	3.220111	-0.040784	-0.090707
S	-2.927638	-0.075125	-0.021175
H	-3.121547	1.183287	0.401335

O9 (288°) Energy: -730.094802 Eh

Atom	Position Coordinates (Å)		
	X	Y	Z
B	-1.064536	-0.007643	0.027622
B	-0.143157	0.954654	-1.145996
B	-0.134092	-0.812797	-1.257729
B	-0.11843	-1.469495	0.391623
B	-0.107604	-0.096901	1.526948
B	-0.129094	1.405411	0.574124
B	1.3712	-1.410938	-0.546798
B	1.393238	-0.957141	1.168435
B	1.387126	0.813125	1.279144
B	1.357892	1.475956	-0.36596
C	1.288246	0.087446	-1.355482
C	2.146739	0.007061	0.006297
H	-0.640899	2.402939	0.944164
H	-0.616934	-0.165838	2.588657
H	-0.620565	-2.508485	0.63831
H	-0.539891	-1.337663	-2.230285
H	2.039156	-2.25677	-1.017509
H	2.064568	1.358071	2.07388
H	2.075001	-1.591204	1.889772
H	2.016151	2.380114	-0.729966
H	-0.552612	1.595351	-2.045913
H	1.85402	0.148077	-2.273603
H	3.220378	0.018915	-0.107836
S	-2.928263	-0.082801	0.01103
H	-3.118797	1.243109	-0.068106

O1 (36°, F) Energy: -730.060377 Eh

Atom	Position Coordinates (Å)		
	X	Y	Z
B	-2.30685	0.033849	-0.027383
B	-1.328504	1.451868	-0.443923
B	-1.348304	0.036824	-1.512923
B	-1.395652	-1.419808	-0.50585
B	-1.421482	-0.895385	1.195554
B	-1.385301	0.882307	1.234811
B	0.121861	-0.902669	-1.218768
B	0.092666	-1.464022	0.464238
B	0.088928	-0.049452	1.542483
B	0.14777	1.401038	0.53479
C	0.094886	0.79469	-1.064737
C	0.919258	-0.049581	0.053283
S	2.718972	-0.073822	0.019126
H	-3.485049	0.078135	-0.074749
H	-1.884132	1.531127	2.084568
H	-1.955341	-1.531757	2.03398
H	-1.904568	-2.414726	-0.884153
H	-1.701203	0.148253	-2.631379
H	0.80432	-1.367142	-2.054957
H	2.852449	1.198599	-0.389503
H	0.749676	-0.06051	2.516726
H	0.743071	-2.408403	0.737016
H	0.836606	2.332059	0.745296
H	-1.669078	2.503683	-0.850972
H	0.699184	1.32844	-1.784302

O1 (108°) Energy: -730.064318 Eh

Atom	Position Coordinates (Å)		
	X	Y	Z
B	-2.306267	0.00202	-0.040636
B	-1.339281	0.75951	-1.314289
B	-1.341434	-1.003303	-1.132273
B	-1.38994	-1.384791	0.599931
B	-1.423673	0.156642	1.487431
B	-1.3781	1.484951	0.304025
B	0.139879	-1.475167	-0.273575
B	0.084712	-0.75728	1.347705
B	0.097254	1.006965	1.163099
B	0.143612	1.386444	-0.572655
C	0.086061	-0.135484	-1.328059
C	0.921732	0.001967	0.076731
S	2.710186	-0.082665	-0.015151
H	-3.48456	0.000161	-0.102136
H	-1.873222	2.53962	0.490543
H	-1.958579	0.268377	2.533586
H	-1.896601	-2.376141	0.990377
H	-1.693514	-1.691212	-2.021323
H	0.821799	-2.385723	-0.575103
H	2.902823	1.240347	0.102007
H	0.752809	1.668739	1.885281
H	0.738169	-1.2607	2.187737
H	0.829823	2.215287	-1.049843
H	-1.687246	1.253901	-2.325501
H	0.704755	-0.228859	-2.20906

O1 (180°) Energy: -730.060695 E_h

Atom	Position Coordinates (Å)		
	X	Y	Z
B	-0.027166	-2.3076	0
B	-1.220813	-1.348573	0.888096
B	-1.220813	-1.348573	-0.888096
B	0.460222	-1.389453	-1.442525
B	1.500646	-1.406745	0
B	0.460222	-1.389453	1.442525
B	-0.427438	0.12721	-1.45233
B	1.249234	0.101204	-0.890081
B	1.249234	0.101204	0.890081
B	-0.427438	0.12721	1.45233
C	-1.329101	0.090015	0
C	0.059761	0.918474	0
S	-0.089639	2.717101	0
H	-0.081066	-3.486251	0
H	0.759699	-1.890494	2.467891
H	2.560175	-1.927466	0
H	0.759699	-1.890494	-2.467891
H	-2.178727	-1.703393	-1.474799
H	-0.821022	0.810995	-2.323021
H	1.238015	2.913728	0
H	2.03239	0.761416	1.473893
H	2.03239	0.761416	-1.473893
H	-0.821022	0.810995	2.323021
H	-2.178727	-1.703393	1.474799
H	-2.230976	0.686226	0

O1 (252°) Energy: -730.064318 E_h

Atom	Position Coordinates (Å)		
	X	Y	Z
B	2.306267	0.00202	-0.040636
B	1.341434	-1.003303	-1.132273
B	1.339281	0.75951	-1.314289
B	1.3781	1.484951	0.304025
B	1.423673	0.156642	1.487431
B	1.38994	-1.384791	0.599931
B	-0.143612	1.386444	-0.572655
B	-0.097254	1.006965	1.163099
B	-0.084712	-0.75728	1.347705
B	-0.139879	-1.475167	-0.273575
C	-0.086061	-0.135484	-1.328059
C	-0.921732	0.001967	0.076731
S	-2.710186	-0.082665	-0.015151
H	3.48456	0.000161	-0.102136
H	1.896601	-2.376141	0.990377
H	1.958579	0.268377	2.533586
H	1.873222	2.53962	0.490543
H	1.687246	1.253901	-2.325501
H	-0.829823	2.215287	-1.049843
H	-2.902823	1.240347	0.102007
H	-0.738169	-1.2607	2.187737
H	-0.752809	1.668739	1.885281
H	-0.821799	-2.385723	-0.575103
H	1.693514	-1.691212	-2.021323
H	-0.704755	-0.228859	-2.20906

O1 (324°, F) Energy: -730.060377 E_h

Atom	Position Coordinates (Å)		
	X	Y	Z
B	2.30685	0.033849	-0.027383
B	1.348304	0.036824	-1.512923
B	1.328504	1.451868	-0.443923
B	1.385301	0.882307	1.234811
B	1.421482	-0.895385	1.195553
B	1.395652	-1.419808	-0.505851
B	-0.14777	1.401038	0.53479
B	-0.088928	-0.049452	1.542483
B	-0.092666	-1.464022	0.464238
B	-0.121862	-0.902669	-1.218768
C	-0.094886	0.79469	-1.064737
C	-0.919258	-0.049581	0.053283
S	-2.718972	-0.073822	0.019126
H	3.485049	0.078135	-0.074749
H	1.904568	-2.414726	-0.884153
H	1.955341	-1.531757	2.03398
H	1.884132	1.531127	2.084568
H	1.669078	2.503683	-0.850972
H	-0.836606	2.332059	0.745296
H	-2.852449	1.198599	-0.389503
H	-0.743071	-2.408403	0.737016
H	-0.749675	-0.060511	2.516726
H	-0.80432	-1.367142	-2.054957
H	1.701203	0.148253	-2.631379
H	-0.699184	1.32844	-1.784302

9O12 (±45°) Energy: -1128.303216 E_h

Atom	Position Coordinates (Å)		
	X	Y	Z
B	0.535882	0.897152	0.003172
B	-0.902604	1.433649	-0.889713
B	-0.902743	1.435681	0.882307
B	-0.015434	0.000035	1.441041
B	0.535975	-0.897034	0.003185
B	-0.014025	0.000031	-1.437214
B	-1.77226	-0.000068	1.446071
B	-0.902593	-1.435704	0.882248
B	-0.90249	-1.433668	-0.889672
B	-1.779833	-0.000048	-1.445936
C	-2.193546	0.806423	-0.003676
C	-2.193468	-0.806438	-0.003681
H	0.590193	0.000054	-2.450789
H	0.586889	0.000075	2.456094
H	-1.059389	2.445061	1.469722
H	-2.555257	-0.000124	2.323534
H	-1.054603	-2.441755	-1.477865
H	-1.059401	-2.444977	1.469814
H	-2.558908	-0.000119	-2.326608
H	-1.054576	2.441888	-1.477674
H	-3.16217	1.284042	0.000373
H	-3.161933	-1.284378	0.000376
S	2.111133	-1.884974	-0.066359
S	2.111078	1.885012	-0.066373
H	1.928085	-2.521092	1.101578
H	1.928399	2.520681	1.101867

9O12 (±45°, M) Energy: -1128.303216 E_h

Atom	Position Coordinates (Å)		
	X	Y	Z
B	-0.535882	0.897152	0.003172
B	0.902743	1.435681	0.882307
B	0.902604	1.433649	-0.889713
B	0.014025	0.000031	-1.437214
B	-0.535975	-0.897034	0.003185
B	0.015434	0.000035	1.441041
B	1.779833	-0.000048	-1.445936
B	0.90249	-1.433668	-0.889672
B	0.902593	-1.435704	0.882248
B	1.77226	-0.000068	1.446071
C	2.193546	0.806423	-0.003676
C	2.193468	-0.806438	-0.003682
H	-0.586889	0.000075	2.456094
H	-0.590193	0.000054	-2.450789
H	1.054576	2.441888	-1.477674
H	2.558908	-0.000119	-2.326608
H	1.059401	-2.444977	1.469814
H	1.054603	-2.441755	-1.477865
H	2.555257	-0.000124	2.323534
H	1.059389	2.445061	1.469722
H	3.16217	1.284042	0.000373
H	3.161933	-1.284378	0.000376
S	-2.111133	-1.884974	-0.066359
S	-2.111078	1.885012	-0.066373
H	-1.928085	-2.521092	1.101578
H	-1.928399	2.520681	1.101867

1O2 (±45°) Energy: -1128.239475 E_h

Atom	Position Coordinates (Å)		
	X	Y	Z
B	2.335055	0.883042	0.006139
B	0.913764	1.438384	-0.885606
B	0.904109	1.440401	0.884974
B	1.765084	-0.000011	1.443479
B	2.335052	-0.883037	0.006125
B	1.77926	0.000017	-1.434374
B	0.000667	0.000003	1.415744
B	0.904088	-1.440395	0.884941
B	0.91377	-1.438375	-0.885644
B	0.006779	0.00001	-1.418041
C	-0.409429	0.860743	-0.002616
C	-0.409434	-0.860747	-0.00264
H	2.354583	0.000047	-2.464216
H	2.330562	-0.000056	2.479187
H	0.734061	2.43911	1.487298
H	-0.78023	-0.000066	2.298465
H	0.746364	-2.436059	-1.487646
H	0.7341	-2.439103	1.487277
H	-0.771712	0.000081	-2.302012
H	0.746422	2.436074	-1.487613
H	3.322752	1.528521	0.012549
H	3.322727	-1.528551	0.012538
S	-1.969506	1.717671	-0.080274
S	-1.969479	-1.717719	-0.080256
H	-2.045457	-1.962396	1.23783
H	-2.045378	1.962987	1.237691

1O2 (±45°, M) Energy: -1128.239475 E_h

Atom	Position Coordinates (Å)		
	X	Y	Z
B	-2.335055	0.883042	0.006139
B	-0.904109	1.440401	0.884974
B	-0.913764	1.438384	-0.885606
B	-1.77926	0.000017	-1.434374
B	-2.335052	-0.883037	0.006125
B	-1.765084	-0.000011	1.443479
B	-0.006779	0.00001	-1.418041
B	-0.91377	-1.438375	-0.885644
B	-0.904088	-1.440395	0.884941
B	-0.000667	0.000003	1.415744
C	0.409429	0.860743	-0.002616
C	0.409434	-0.860747	-0.00264
H	-2.330562	-0.000056	2.479187
H	-2.354583	0.000047	-2.464216
H	-0.746422	2.436074	-1.487613
H	0.771712	0.000081	-2.302012
H	-0.7341	-2.439103	1.487277
H	-0.746364	-2.436059	-1.487646
H	0.78023	-0.000066	2.298465
H	-0.734061	2.43911	1.487298
H	-3.322752	1.528521	0.012549
H	-3.322727	-1.528551	0.012538
S	1.969506	1.717672	-0.080274
S	1.969479	-1.717719	-0.080256
H	2.045457	-1.962396	1.23783
H	2.045377	1.962988	1.237691

A.F. References

(1) Schwartz, J. J.; Mendoza, A. M.; Wattanatorn, N.; Zhao, Y.; Nguyen, V. T.; Spokoyny, A. M.; Mirkin, C. A.; Baše, T.; Weiss, P. S. Surface Dipole Control of Liquid Crystal Alignment. *JACS*. **2016**, *138*, 5957–5967.

(2) Whitesides, G. M.; Grzybowski, B. Self-Assembly at All Scales. *Science* **2002**, *295*, 2418–2421.

(3) Smith, R. K.; Lewis, P. A.; Weiss, P. S. Patterning Self-Assembled Monolayers. *Prog. Surf. Sci.* **2004**, *75*, 1–68.

(4) Love, J. C.; Estroff, L. A.; Kriebel, J. K.; Nuzzo, R. G.; Whitesides, G. M. Self-Assembled Monolayers of Thiolates on Metals as a Form of Nanotechnology. *Chem. Rev.* **2005**, *105*, 1103–1170.

(5) Claridge, S. A.; Liao, W.-S.; Thomas, J. C.; Zhao, Y.; Cao, H. H.; Cheunkar, S.; Serino, A. C.; Andrews, A. M.; Weiss, P. S. From the Bottom up: Dimensional Control and Characterization in Molecular Monolayers. *Chem. Soc. Rev.* **2013**, *42*, 2725–2745.

(6) Fersht, A. R.; Matouschek, A.; Serrano, L. The Folding of an Enzyme: I. Theory of Protein Engineering Analysis of Stability and Pathway of Protein Folding. *J. Mol. Biol.* **1992**, *224*, 771–782.

(7) Kudernac, T.; Lei, S.; Elemans, J. A. A. W.; Feyter, S. D. Two-Dimensional Supramolecular Self-Assembly: Nanoporous Networks on Surfaces. *Chem. Soc. Rev.* **2009**, *38*, 402–421.

(8) Grzelczak, M.; Vermant, J.; Furst, E. M.; Liz-Marzán, L. M. Directed Self-Assembly of Nanoparticles. *ACS Nano* **2010**, *4*, 3591–3605.

(9) Israelachvili, J. N. *Intermolecular and Surface Forces*, 3rd Edition.; Israelachvili, J. N., Ed.; Academic Press: San Diego, 2011.

(10) Lee, H. J.; Jamison, A. C.; Lee, T. R. Surface Dipoles: A Growing Body of Evidence Supports Their Impact and Importance. *Acc. Chem. Res.* **2015**, *48*, 3007–3015.

(11) Paniagua, S. A.; Hotchkiss, P. J.; Jones, S. C.; Marder, S. R.; Mudalige, A.; Marrikar, F. S.; Pemberton, J. E.; Armstrong, N. R. Phosphonic Acid Modification of Indium−Tin Oxide Electrodes: Combined XPS/UPS/Contact Angle Studies. *J. Phys. Chem. C* **2008**, *112*, 7809–7817.

(12) Bishop, K. J. M.; Wilmer, C. E.; Soh, S.; Grzybowski, B. A. Nanoscale Forces and Their Uses in Self-Assembly. *Small* **2009**, *5*, 1600–1630.

(13) Liang, H.; Sun, W.; Jin, X.; Li, H.; Li, J.; Hu, X.; Teo, B. K.; Wu, K. Two-Dimensional Molecular Porous Networks Formed by Trimesic Acid and 4,4′-Bis(4-Pyridyl)Biphenyl on Au(111) through Hierarchical Hydrogen Bonds: Structural Systematics and Control of Nanopore Size and Shape. *Angew. Chem. Int. Ed.* **2011**, *50*, 7562–7566.

(14) Kim, J.; Rim, Y. S.; Liu, Y.; Serino, A. C.; Thomas, J. C.; Chen, H.; Yang, Y.; Weiss, P. S. Interface Control in Organic Electronics Using Mixed Monolayers of Carboranethiol Isomers. *Nano Lett.* **2014**, *14*, 2946–2951.

(15) Thomas, J. C.; Schwartz, J. J.; Hohman, J. N.; Claridge, S. A.; Auluck, H. S.; Serino, A. C.; Spokoyny, A. M.; Tran, G.; Kelly, K. F.; Mirkin, C. A.; et al. Defect-Tolerant Aligned Dipoles within Two-Dimensional Plastic Lattices. *ACS Nano* **2015**, *9*, 4734–4742.

(16) Kulkarni, C.; Bejagam, K. K.; Senanayak, S. P.; Narayan, K. S.; Balasubramanian, S.; George, S. J. Dipole-Moment-Driven Cooperative Supramolecular Polymerization. *JACS.* **2015**, *137*, 3924–3932.

(17) Lewis, P. A.; Smith, R. K.; Kelly, K. F.; Bumm, L. A.; Reed, S. M.; Clegg, R. S.; Gunderson, J. D.; Hutchison, J. E.; Weiss, P. S. The Role of Buried Hydrogen Bonds in Self-Assembled Mixed Composition Thiols on Au{111}. *J. Phys. Chem. B* **2001**, *105*, 10630–10636.

(18) Zhang, S. Fabrication of Novel Biomaterials through Molecular Self-Assembly. *Nat. Biotechnol.* **2003**, *21*, 1171–1178.

(19) Dameron, A. A.; Charles, L. F.; Weiss, P. S. Structures and Displacement of 1-Adamantanethiol Self-Assembled Monolayers on Au{111}. *JACS.* **2005**, *127*, 8697-8704.

(20) Barth, J. V.; Costantini, G.; Kern, K. Engineering Atomic and Molecular Nanostructures at Surfaces. *Nature* **2005**, *437*, 671–679.

(21) Aizenberg, J.; Black, A. J.; Whitesides, G. M. Oriented Growth of Calcite Controlled by Self-Assembled Monolayers of Functionalized Alkanethiols Supported on Gold and Silver. *JACS.* **1999**, *121*, 4500–4509.

(22) Chen, S.; Liu, L.; Zhou, J.; Jiang, S. Controlling Antibody Orientation on Charged Self-Assembled Monolayers. *Langmuir* **2003**, *19*, 2859–2864.

(23) Briseno, A. L.; Aizenberg, J.; Han, Y.-Jin.; Penkala, R. A.; Moon, H.; Lovinger, A. J.; Kloc, C.; Bao, Z. Patterned Growth of Large Oriented Organic Semiconductor Single Crystals on Self-Assembled Monolayer Templates. *JACS.* **2005**, *127*, 12164–12165.

(24) Hermes, S.; Schröder, F.; Chelmowski, R.; Wöll, C.; Fischer, R. A. Selective Nucleation and Growth of Metal–Organic Open Framework Thin Films on Patterned COOH/CF_3-Terminated Self-Assembled Monolayers on Au(111). *JACS.* **2005**, *127*, 13744–13745.

(25) Lee, C.-Y.; Gong, P.; Harbers, G. M.; Grainger, D. W.; Castner, D. G.; Gamble, L. J. Surface Coverage and Structure of Mixed DNA/Alkylthiol Monolayers on Gold: Characterization by XPS, NEXAFS, and Fluorescence Intensity Measurements. *Anal. Chem.* **2006**, *78*, 3316–3325.

(26) Scherb, C.; Schödel, A.; Bein, T. Directing the Structure of Metal–Organic Frameworks by Oriented Surface Growth on an Organic Monolayer. *Angew. Chem.* **2008**, *120*, 5861–5863.

(27) Yao, Y.; Dong, H.; Hu, W. Ordering of Conjugated Polymer Molecules: Recent Advances and Perspectives. *Polym. Chem.* **2013**, *4*, 5197–5205.

(28) Palma, C.-A.; Cecchini, M.; Samorì, P. Predicting Self-Assembly: From Empirism to Determinism. *Chem. Soc. Rev.* **2012**, *41*, 3713–3730.

(29) Roussel, T. J.; Barrena, E.; Ocal, C.; Faraudo, J. Predicting Supramolecular Self-Assembly on Reconstructed Metal Surfaces. *Nanoscale* **2014**, *6*, 7991–8001.

(30) Meier, G.; Sackmann, E.; Grabmaier, J. G. *Applications of Liquid Crystals*; Springer-Verlag: Berlin, 1975.

(31) Gelbart, W. M. Molecular Theory of Nematic Liquid Crystals. *J. Phys. Chem.* **1982**, *86*, 4298–4307.

(32) Jerome, B. Surface Effects and Anchoring in Liquid Crystals. *Rep. Prog. Phys.* **1991**, *54*, 391.

(33) Lee, K.-W.; Paek, S.-H.; Lien, A.; Durning, C.; Fukuro, H. Microscopic Molecular Reorientation of Alignment Layer Polymer Surfaces Induced by Rubbing and Its Effects on LC Pretilt Angles. *Macromolecules* **1996**, *29*, 8894–8899.

(34) Stöhr, J.; Samant, M. G. Liquid Crystal Alignment by Rubbed Polymer Surfaces: A Microscopic Bond Orientation Model. *J. Electron Spectrosc. Relat. Phenom.* **1999**, *98-99*, 189–207.

(35) Janning, J. L. Thin Film Surface Orientation for Liquid Crystals. *Appl. Phys. Lett.* **1972**, *21*, 173–174.

(36) Ichimura, K. Photoalignment of Liquid-Crystal Systems. *Chem. Rev.* **2000**, *100*, 1847-1874.

(37) O'Neill, M.; Kelly, S. M. Photoinduced Surface Alignment for Liquid Crystal Displays. *J. Phys. Appl. Phys.* **2000**, *33*, R67.

(38) Skaife, J. J.; Abbott, N. L. Quantitative Characterization of Obliquely Deposited Substrates of Gold by Atomic Force Microscopy: Influence of Substrate Topography on Anchoring of Liquid Crystals. *Chem. Mater.* **1999**, *11*, 612–623.

(39) Wilderbeek, H. T. A.; van der Meer, F. J. A.; Feldman, K.; Broer, D. J.; Bastiaansen, C. W. M. Alignment of Liquid Crystals on Self-Assembled Monolayers Using Ultra-Thin Gold Films. *Adv. Mater.* **2002**, *14*, 655–658.

(40) Berreman, D. W. Solid Surface Shape and the Alignment of an Adjacent Nematic Liquid Crystal. *Phys. Rev. Lett.* **1972**, *28*, 1683–1686.

(41) Abelmann, L.; Lodder, C. Oblique Evaporation and Surface Diffusion. *Thin Solid Films* **1997**, *305*, 1–21.

(42) Follonier, S.; Miller, W. J. W.; Abbott, N. L.; Knoesen, A. Characterization of the Molecular Orientation of Self-Assembled Monolayers of Alkanethiols on Obliquely Deposited Gold Films by Using Infrared–Visible Sum-Frequency Spectroscopy. *Langmuir* **2003**, *19*, 10501–10509.

(43) Hoogboom, J.; Rasing, T.; Rowan, A. E.; Nolte, R. J. M. LCD Alignment Layers. Controlling Nematic Domain Properties. *J. Mater. Chem.* **2006**, *16*, 1305–1314.

(44) Drawhorn, R. A.; Abbott, N. L. Anchoring of Nematic Liquid Crystals on Self-Assembled Monolayers Formed from Alkanethiols on Semitransparent Films of Gold. *J. Phys. Chem.* **1995**, *99*, 16511–16515.

(45) Evans, S. D.; Allinson, H.; Boden, N.; Henderson, J. R. Surface-Field Induced Organisation at Solid/Fluid Interfaces. *Faraday Discuss.* **1996**, *104*, 37–48.

(46) Gupta, V. K.; Abbott, N. L. Uniform Anchoring of Nematic Liquid Crystals on Self-Assembled Monolayers Formed from Alkanethiols on Obliquely Deposited Films of Gold. *Langmuir* **1996**, *12*, 2587–2593.

(47) Gupta, V. K.; Abbott, N. L. Azimuthal Anchoring Transition on Nematic Liquid Crystals on Self-Assembled Monolayers Formed from Odd and Even Alkanethiols. *Phys. Rev. E* **1996**, *54*, R4540–R4543.

(48) Gupta, V. K.; Abbott, N. L. Design of Surfaces for Patterned Alignment of Liquid Crystals on Planar and Curved Substrates. *Science* **1997**, *276*, 1533–1536.

(49) Alkhairalla, B.; Allinson, H.; Boden, N.; Evans, S. D.; Henderson, J. R. Anchoring and Orientational Wetting of Nematic Liquid Crystals on Self-Assembled Monolayer Substrates: An Evanescent Wave Ellipsometric Study. *Phys. Rev. E* **1999**, *59*, 3033-3039.

(50) Carlton, R. J.; Hunter, J. T.; Miller, D. S.; Abbasi, R.; Mushenheim, P. C.; Tan, L. N.; Abbott, N. L. Chemical and Biological Sensing Using Liquid Crystals. *Liq. Cryst. Rev.* **2013**, *1*, 29–51.

(51) Bramble, J. P.; Evans, S. D.; Henderson, J. R.; Anquetil, C.; Cleaver, D. J.; Smith, N. J. Nematic Liquid Crystal Alignment on Chemical Patterns. *Liq. Cryst.* **2007**, *34*, 1059-1069.

(52) Critchley, K.; Cheadle, E. M.; Zhang, H.-L.; Baldwin, K. J.; Liu, Q.; Cheng, Y.; Fukushima, H.; Tamaki, T.; Batchelder, D. N.; Bushby, R. J.; et al. Surface Plasmon Raman Scattering Studies of Liquid Crystal Anchoring on Liquid-Crystal-Based Self-Assembled Monolayers. *J. Phys. Chem. B* **2009**, *113*, 15550–15557.

(53) Yoon, H.; Kang, S.-W.; Lehmann, M.; Park, J. O.; Srinivasarao, M.; Kumar, S. Homogeneous and Homeotropic Alignment of Bent-Core Uniaxial and Biaxial Nematic Liquid Crystals. *Soft Matter* **2011**, *7*, 8770–8775.

(54) Crawford, G. P.; Ondris-Crawford, R. J.; Doane, J. W.; Zumer, S. Systematic Study of Orientational Wetting and Anchoring at a Liquid-Crystal-Surfactant Interface. *Phys. Rev. E* **1996**, *53*, 3647–3661.

(55) Tao, F.; Bernasek, S. L. Understanding Odd−Even Effects in Organic Self-Assembled Monolayers. *Chem. Rev.* **2007**, *107*, 1408–1453.

(56) Nakata, M.; Zanchetta, G.; Buscaglia, M.; Bellini, T.; Clark, N. A. Liquid Crystal Alignment on a Chiral Surface: Interfacial Interaction with Sheared DNA Films. *Langmuir* **2008**, *24*, 10390–10394.

(57) Bai, Y.; Abbott, N. L. Enantiomeric Interactions between Liquid Crystals and Organized Monolayers of Tyrosine-Containing Dipeptides. *JACS.* **2012**, *134*, 548-558.

(58) Bai, Y.; Abbasi, R.; Wang, C.; Abbott, N. L. Liquid Crystals Anchored on Mixed Monolayers of Chiral versus Achiral Molecules: Continuous Change in Orientation as a Function of Enantiomeric Excess. *Angew. Chem. Int. Ed.* **2014**, *53*, 8079–8083.

(59) Grimes, R. N. *Carboranes*, 2nd Edition.; Academic Press: Oxford, 2011.

(60) Kaszynski, P.; G. Douglass, A. Organic Derivatives of Closo-Boranes: A New Class of Liquid Crystal Materials. *J. Organomet. Chem.* **1999**, *581*, 28–38.

(61) Hohman, J. N.; Zhang, P.; Morin, E. I.; Han, P.; Kim, M.; Kurland, A. R.; McClanahan, P. D.; Balema, V. P.; Weiss, P. S. Self-Assembly of Carboranethiol Isomers on Au{111}: Intermolecular Interactions Determined by Molecular Dipole Orientations. *ACS Nano* **2009**, *3*, 527–536.

(62) Hohman, J. N.; Claridge, S. A.; Kim, M.; Weiss, P. S. Cage Molecules for Self-Assembly. *Mater. Sci. Eng. R* **2010**, *70*, 188–208.

(63) Cioran, A. M.; Musteti, A. D.; Teixidor, F.; Krpetić, Ž.; Prior, I. A.; He, Q.; Kiely, C. J.; Brust, M.; Viñas, C. Mercaptocarborane-Capped Gold Nanoparticles: Electron Pools and Ion Traps with Switchable Hydrophilicity. *JACS.* **2012**, *134*, 212–221.

(64) Kabytaev, K. Z.; Everett, T. A.; Safronov, A. V.; Sevryugina, Y. V.; Jalisatgi, S. S.; Hawthorne, M. F. B-Mercaptocarboranes: A New Synthetic Route. *Eur. J. Inorg. Chem.* **2013**, *2013*, 2488–2491.

(65) Thomas, J. C.; Goronzy, D. P.; Serino, A. C.; Auluck, H. S.; Irving, O. R.; Jimenez-Izal, E.; Deirmenjian, J. M.; Macháček, J.; Sautet, P.; Alexandrova, A. N.; et al. Acid-Base Control of Valency within Carboranedithiol Self-Assembled Monolayers: Molecules Do the Can-Can. *ACS Nano* **2018**, *12*, 2211–2221.

(66) Kristiansen, K.; Stock, P.; Baimpos, T.; Raman, S.; Harada, J. K.; Israelachvili, J. N.; Valtiner, M. Influence of Molecular Dipole Orientations on Long-Range Exponential Interaction Forces at Hydrophobic Contacts in Aqueous Solutions. *ACS Nano* **2014**, *8*, 10870–10877.

(67) Dey, S.; Pal, A. J. Layer-by-Layer Electrostatic Assembly with a Control over Orientation of Molecules: Anisotropy of Electrical Conductivity and Dielectric Properties. *Langmuir* **2011**, *27*, 8687–8693.

(68) Brennan, T. P.; Tanskanen, J. T.; Bakke, J. R.; Nguyen, W. H.; Nordlund, D.; Toney, M. F.; McGehee, M. D.; Sellinger, A.; Bent, S. F. Dynamical Orientation of Large Molecules on Oxide Surfaces and Its Implications for Dye-Sensitized Solar Cells. *Chem. Mater.* **2013**, *25*, 4354–4363.

(69) Breuer, T.; Witte, G. Controlling Nanostructures by Templated Templates: Inheriting Molecular Orientation in Binary Heterostructures. *ACS Appl. Mater. Interfaces* **2015**, *7*, 20485–20492.

(70) Pang, S. H.; Medlin, J. W. Controlling Catalytic Selectivity *via* Adsorbate Orientation on the Surface: From Furfural Deoxygenation to Reactions of Epoxides. *J. Phys. Chem. Lett.* **2015**, *6*, 1348–1356.

(71) Arrows Illustrating Dipole Moments Point from Regions of Relative Negative to Positive Charge within the Molecule.

(72) Baše, T.; Bastl, Z.; Šlouf, M.; Klementová, M.; Šubrt, J.; Vetushka, A.; Ledinský, M.; Fejfar, A.; Macháček, J.; Carr, M. J.; et al. Gold Micrometer Crystals Modified with Carboranethiol Derivatives. *J. Phys. Chem. C* **2008**, *112*, 14446–14455.

(73) Lübben, J. F.; Baše, T.; Rupper, P.; Künniger, T.; Macháček, J.; Guimond, S. Tuning the Surface Potential of Ag Surfaces by Chemisorption of Oppositely-Oriented Thiolated Carborane Dipoles. *J. Colloid Interface Sci.* **2011**, *354*, 168–174.

(74) Kunkel, D. A.; Hooper, J.; Simpson, S.; Miller, D. P.; Routaboul, L.; Braunstein, P.; Doudin, B.; Beniwal, S.; Dowben, P.; Skomski, R.; et al. Self-Assembly of Strongly Dipolar Molecules on Metal Surfaces. *J. Chem. Phys.* **2015**, *142*, 101921.

(75) Mauguin, C. Sur Les Cristaux Liquides de Lehman. *Bull Soc Fr Min.* **1911**, *34*, 71–117.

(76) Fréedericksz, V.; Zolina, V. Forces Causing the Orientation of an Anisotropic Liquid. *Trans. Faraday Soc.* **1933**, *29*, 919–930.

(77) De Jeu, W. H. *Physical Properties of Liquid Crystalline Materials*; Gordon and Breach: New York, **1980**.

(78) Fonseca, J. G.; Galerne, Y. Simple Method for Measuring the Azimuthal Anchoring Strength of Nematic Liquid Crystals. *Appl. Phys. Lett.* **2001**, *79*, 2910–2912.

(79) Clare, B. H.; Guzmán, O.; de Pablo, J. J.; Abbott, N. L. Measurement of the Azimuthal Anchoring Energy of Liquid Crystals in Contact with Oligo(Ethylene Glycol)-Terminated Self-Assembled Monolayers Supported on Obliquely Deposited Gold Films. *Langmuir* **2006**, *22*, 4654–4659.

(80) Sørensen, B. E. A Revised Michel-Lévy Interference Colour Chart Based on First-Principles Calculations. *Eur. J. Mineral.* **2013**, *25*, 5–10.

(81) Lowe, A. M.; Ozer, B. H.; Bai, Y.; Bertics, P. J.; Abbott, N. L. Design of Surfaces for Liquid Crystal-Based Bioanalytical Assays. *ACS Appl. Mater. Interfaces* **2010**, *2*, 722–731.

(82) Fukuda, J.; Yoneya, M.; Yokoyama, H. Consistent Numerical Evaluation of the Anchoring Energy of a Grooved Surface. *Phys. Rev. E* **2009**, *79*, 011705.

(83) Choi, Y.; Yokoyama, H.; Gwag, J. S. Determination of Surface Nematic Liquid Crystal Anchoring Strength Using Nano-Scale Surface Grooves. *Opt. Express* **2013**, *21*, 12135–12144.

(84) Faetti, S.; Marianelli, P. Strong Azimuthal Anchoring Energy at a Nematic-Polyimide Interface. *Phys. Rev. E* **2005**, *72*, 051708.

(85) Anchoring Energies Depend on a Variety of Factors. When Comparing Values from Such Dissimilar Surfaces, One Should Acknowledge the Significant Influence of Textural and Chemical Differences in Determining Anchoring Strengths.

(86) Skaife, J. J.; Brake, J. M.; Abbott, N. L. Influence of Nanometer-Scale Topography of Surfaces on the Orientational Response of Liquid Crystals to Proteins Specifically Bound to Surface-Immobilized Receptors. *Langmuir* **2001**, *17*, 5448–5457.

(87) Clare, B. H.; Guzmán, O.; de Pablo, J.; Abbott, N. L. Anchoring Energies of Liquid Crystals Measured on Surfaces Presenting Oligopeptides. *Langmuir* **2006**, *22*, 7776-7782.

(88) Otiti, T.; Niklasson, G. A.; Svedlindh, P.; Granqvist, C. G. Anisotropic Optical, Magnetic, and Electrical Properties of Obliquely Evaporated Ni Films. *Thin Solid Films* **1997**, *307*, 245–249.

(89) Everitt, D. L.; Miller, W. J. W.; Abbott, N. L.; Zhu, X. D. Evolution of a Preferred Orientation of Polycrystalline Grains in Obliquely Deposited Gold Films on an Amorphous Substrate. *Phys. Rev. B* **2000**, *62*, R4833–R4836.

(90) Jang, J. H.; Jacob, J.; Santos, G.; Lee, T. R.; Baldelli, S. Image Contrast in Sum Frequency Generation Microscopy Based on Monolayer Order and Coverage. *J. Phys. Chem. C* **2013**, *117*, 15192–15202.

(91) Smith, H. D.; Obenland, C. O.; Papetti, S. A New Series of Organoboranes. IX. The Preparation and Some Reactions of Sulfur-Carborane Derivatives. *Inorg. Chem.* **1966**, *5*, 1013–1015.

(92) Plešek, J.; Janoušek, Z.; Heřmánek, S. Synthesis and Properties of Some Icosahedral Carborane B,B'-Dithiols. *Collect. Czechoslov. Chem. Commun.* **1980**, *45*, 1775–1779.

(93) Spokoyny, A. M.; Machan, C. W.; Clingerman, D. J.; Rosen, M. S.; Wiester, M. J.; Kennedy, R. D.; Stern, C. L.; Sarjeant, A. A.; Mirkin, C. A. A Coordination Chemistry Dichotomy for Icosahedral Carborane-Based Ligands. *Nat. Chem.* **2011**, *3*, 590–596.

(94) Schwartz, J. J.; Hohman, J. N.; Morin, E. I.; Weiss, P. S. Molecular Flux Dependence of Chemical Patterning by Microcontact Printing. *ACS Appl. Mater. Interfaces* **2013**, *5*, 10310–10316.

(95) Goerigk, L.; Grimme, S. A Thorough Benchmark of Density Functional Methods for General Main Group Thermochemistry, Kinetics, and Noncovalent Interactions. *Phys. Chem. Chem. Phys.* **2011**, *13*, 6670–6688.

(96) Hickey, A. L.; Rowley, C. N. Benchmarking Quantum Chemical Methods for the Calculation of Molecular Dipole Moments and Polarizabilities. *J. Phys. Chem. A* **2014**, *118*, 3678–3687.

(97) Toyooka, T.; Chen, G.; Takezoe, H.; Fukuda, A. Determination of Twist Elastic Constant K22 in 5CB by Four Independent Light-Scattering Techniques. *Jpn. J. Appl. Phys.* **1987**, *26*, 1959.

(98) Belyaev, B. A.; Drokin, N. A.; Shabanov, V. F.; Shepov, V. N. Dielectric Anisotropy of 5CB Liquid Crystal in a Decimeter Wavelength Range. *Phys. Solid State* **2000**, *42*, 577–579.

(99) Li, J.; Wen, C.-H.; Gauza, S.; Lu, R.; Wu, S.-T. Refractive Indices of Liquid Crystals for Display Applications. *J. Disp. Technol.* **2005**, *1*, 51–61.

(100) Maurel, P.; Price, A. H. Dipole Moment of N-(p-Methoxybenzylidene)-p-Butylaniline. *J Chem Soc Faraday Trans 2* **1973**, *69*, 1486–1490.

Appendix B

Photoinduced Charge Transfer in

Single-Molecule *p*–*n* Junctions

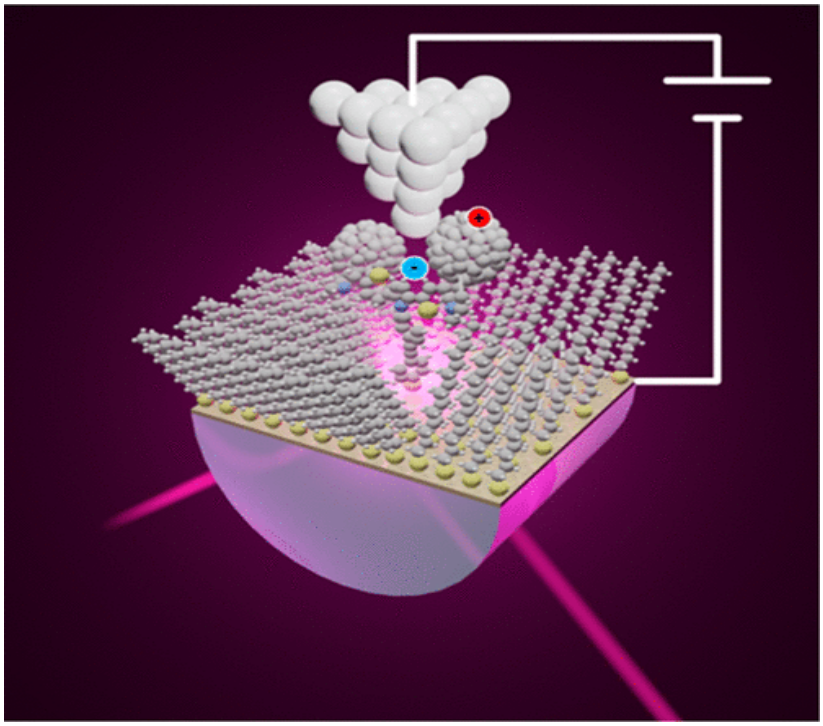

The information in this chapter was published in
J. Phys. Chem. Lett. **2019**,*10,* 2175-2181
and has been reproduced here with permission.[1]

Authors: Shenkai Wang, Natcha Wattanatorn, Naihao Chiang, Yuxi Zhao, Moonhee Kim, Hong Ma, Alex K.-Y. Jen, and Paul S. Weiss

B.A. Introduction

The photoconversion of sunlight to electricity is a key ingredient in meeting future energy needs.[2–4] Organic photovoltaic devices consisting of small-molecule donor–acceptor heterojunctions show great promise for photoconversion due to their ease of manufacture, their synthetic variability, and their cost effectiveness.[5–7] Understanding electron transfer at the molecular level is critical for the rational design and optimization of organic optoelectronics and photovoltaics.[8] Considerable effort has been directed toward the study of electron transport at the single-molecule/assembly scale. A variety of experimental techniques have been developed to study charge transport in single-molecule junctions including tip-enhanced Raman spectroscopy,[9–14] break-junction measurements,[15-18] inelastic electron tunneling spectroscopy,[19] ultrafast optical excitation,[20–22] photon emission from local excitation,[23,24] and microwave polarizability mapping.[25,26] However, most of the available approaches require ultrahigh vacuum and/or low temperature, which make these techniques time-consuming, complicated, and of limited relevance to real systems.

Fullerenes and their derivatives are promising components of photovoltaics due to their high degree of π-electron delocalization.[27–29] A number of molecular dyads, triads, and tetrads of fullerenes covalently linked to electron donors, such as porphyrins, phthalocyanines, tetrathiafulvalenes, ferrocenes, and other moieties, have been synthesized and intensively studied.[30–33] These fullerene donor-linked compounds exhibit excellent photovoltaic efficiencies upon illumination.[34–36] Furthermore, enhancements of nonlinear optical responses were observed for fullerene dyads compared to those of pristine fullerenes.[32,33] A C_{60}-tethered 2,5-dithienylpyrrole triad (C_{60}triad, **Figure B.1A**) has

C_{60} groups attached to both ends of an electron-rich chromophore, and a rigid backbone provides a stable and conducting tether.[35] This donor–acceptor triad structure makes light harvesting more efficient, resulting in large photocurrents, as observed in photoelectrochemical cells.

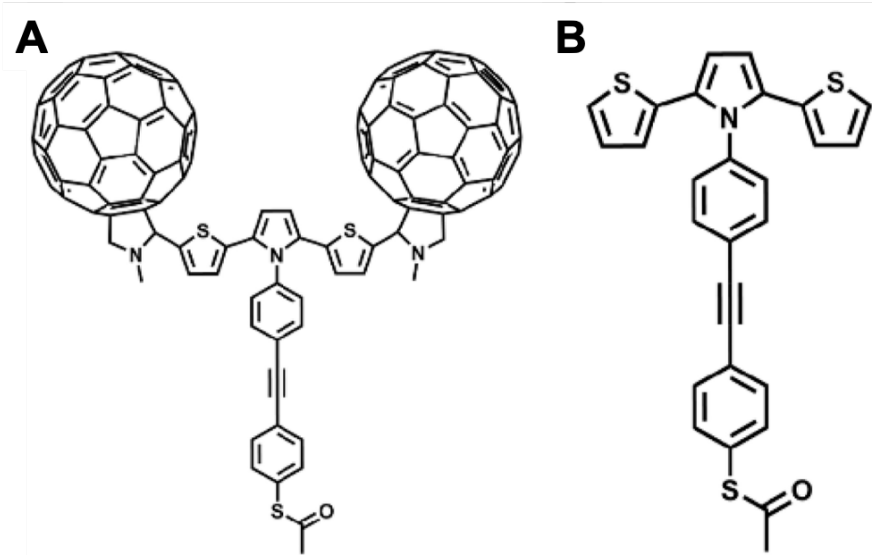

Figure B.1. Chemical structure of (A) C_{60}-tethered 2,5-dithienylpyrrole triad and (B) the control that has no C_{60} attached (DTP).

B.B. Results and Discussion

Scanning tunneling microscopy (STM) and associated spectroscopic imaging methods, with atomic resolution, have been widely used to investigate electron transfer through single molecules and assemblies in metal–molecule–metal junctions.[9,25,37-43] Incorporating laser irradiation into the tunneling junction further extends the ability of STM and enables us to probe photoinduced carrier dynamics at the nanoscale.[22,44–60] Here, we used our custom-built laser-assisted STM (photon STM)[55] to measure photoinduced charge generation and separation in single-molecule triads under ambient conditions. A laser (wavelength 405 ± 5 nm) modulated by a chopper wheel at

4.8 kHz was introduced into the tunneling junction via total internal reflection.[50] The chopper wheel creates a reference frequency input to a lock-in amplifier (LIA) for phase-sensitive detection, so that light-triggered changes in the tunneling current can be recorded. The expected laser-induced tunneling current changes reflect the fast surface dynamics and are only a small contribution to the total tunneling current. Rapid amplitude modulation of the illumination with a mechanical chopper, combined with photosensitive detection, enables photoresponse spatial registration in simultaneously acquired multimodal images. Likewise, built-in control experiments test that the observed signals are due to photoconductance. These controls include measuring the photoconductance of the (nonabsorbing) matrix and "dummy" inserted chromophores with similar chemical structures but no significant absorption spectra at the excitation wavelength. In this way, we consistently test for the effects of sample and STM tip heating (without changing samples[55]), either or both of which could affect the tunneling current and spectra.

The incident light illuminates the back of the sample, undergoing total internal reflection at the half-cylindrical sapphire prism surface, and evanescently propagates through the gold film and gold-supported organic monolayer, exciting the adsorbed chromophores without significant probe tip absorption.[55] The metal thickness and illumination geometry are optimized to couple light evanescently to adsorbates and to minimize transmission that could illuminate the probe tip (which would lead to heating, expansion, and thus image artifacts–we test explicitly for such signals). The STM probe tip is positioned over the illumination spot and is used to image the local environment, and to probe the optical response of photoactive molecules (and the nonabsorbing control molecules and matrix). With the submolecular resolution of STM, we can detect local spectral

changes rather than integrating over large areas. Thus, we are able to elucidate the effects of the local environment and ultimately target optimized supramolecular assemblies that maximize photon absorption and energy conversion efficiency.

We used vapor-deposited *n*-dodecanethiolate (C12) self-assembled monolayers (SAMs) on sapphire-prism-supported Au{111} as the two-dimensional matrix, and inserted photoactive molecules into the defects in C12 SAMs so that they can be studied at the single molecular level.[61,62] The C_{60}-tethered 2,5-dithienylpyrrole triads (C_{60} triads, **Figure B.1A**) and the control molecules without the C_{60} moieties (DTP, **Figure B.1B**) were synthesized following previously reported procedures[35] and were inserted into the defects in C12 SAMs through solution deposition.[63,64]

Consecutively obtained topographic images of the same region and simultaneously acquired spectroscopic images are shown in **Figure B.2**. The chopper wheel was turned on throughout the data collection process to ensure that all phase-sensitive signals were acquired with the same reference frequency of 4.8 kHz. The laser illumination was blocked for **Figure B.2A,B** and was on for **Figure B.2C-F**. The lattice structures in **Figure B.2A,C,E** reflect the C12 matrix molecules, and the protrusions represent C_{60} moieties in C_{60} triad molecules. Each C_{60} triad molecule has two C_{60} groups, but they are not symmetrically arranged because of the conformations of the molecules (even though the molecules are *topologically* symmetric), so that, in each molecule, one C_{60} feature appears less protruding or does not even appear in the topographic images. This difference is the result of STM images being convolutions of geometric and electronic structure.[38,57,65,66]

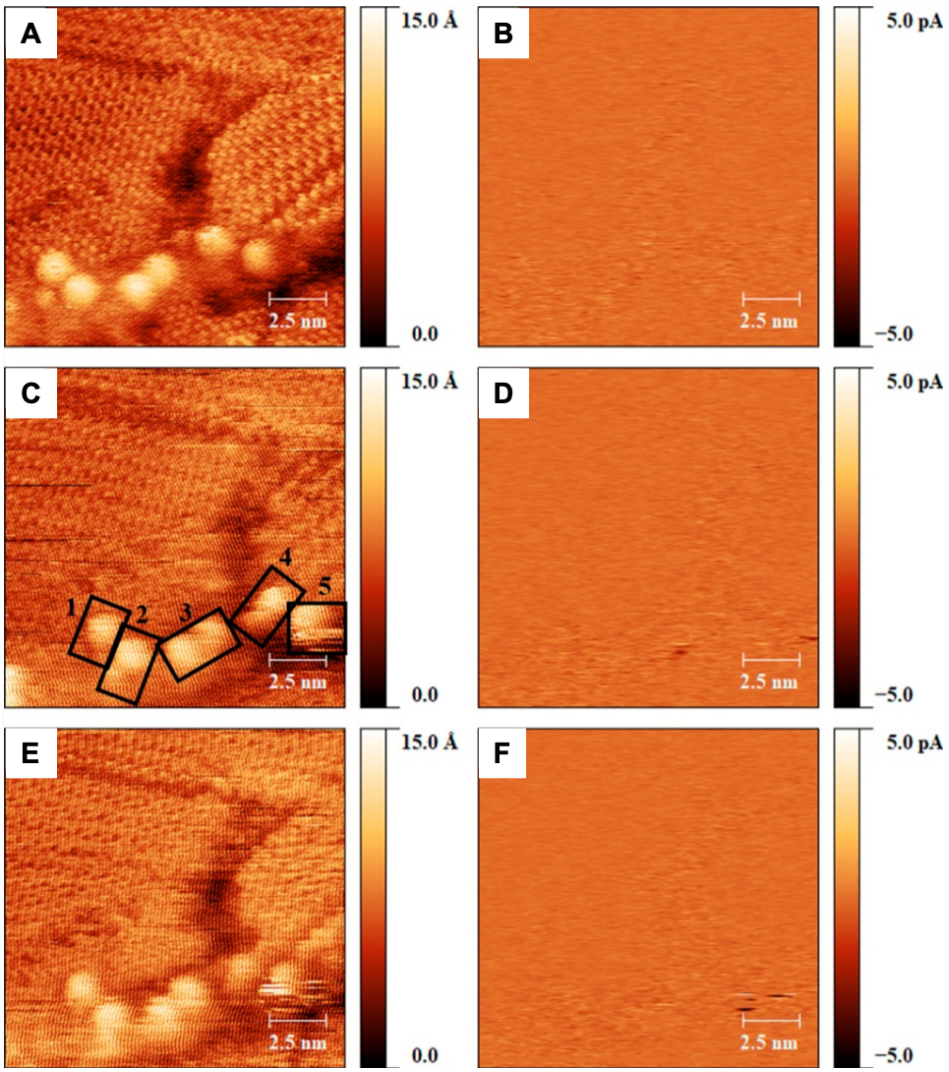

Figure B.2. Consecutively collected scanning tunneling microscopy images showing C_{60} triad molecules inserted in dodecanethiolate monolayer matrix on Au{111}. (A) Topographic and (B) spectroscopic (see text) images were simultaneously obtained when the laser was not illuminating the sample. (C) Topographic and (D) spectroscopic images were simultaneously obtained when the laser illuminated the sample evanescently. (E) Topographic and (F) spectroscopic images were simultaneously obtained immediately after (C) and (D). All images were collected at a sample bias of −1.00 V and a tunneling current of 12.0 pA. All spectroscopic images were collected phase sensitively with a reference frequency of 4.8 kHz created by a chopper wheel that was used to modulate the evanescent sample illumination.

For example, in the area shown in **Figure B.2A,C,E**, we observe five C_{60} triad molecules, as labeled in **Figure B.2C**. The lattice structures of C12 SAMs in **Figure B.2A,C,E** are not observed in the spectroscopic images under these conditions. This result is

consistent with C12 not absorbing incident photons at this energy, leading to no detectable photocurrent corresponding to the excitation. By comparing **Figure B.2B,D,F**, we can see that there are large positive and negative signals in the lower regions of **Figure B.2D,F** (illuminated) that were *not* observed in **Figure B.2B** (no illumination). Such positive and negative signals are much larger than the background and *only* present under illumination.

Schemes showing the experimental setup are shown in **Figure B.3A,B**. We use phase-sensitive detection with mechanical chopping of the laser illumination to record the photoinduced tunneling current change (**Figure B.2B,D,F** and **B3C**). In **Figure B.3C**, while under illumination, the average values of the in-phase signals calculated from **Figure B.2D,F** (and other consecutively collected spectroscopic images not shown here) are more negative than those without illumination. The number *n* in **Figure B.3C** represents the number of spectroscopic images we used to calculate the average values. The average values of **Figure B.2D,F** and other spectroscopic images collected under illumination were calculated from the regions corresponding to dodecanethiol molecules only (highlighted in **Figure B.S2**). The error bars represent the deviation of average values between different images. When we change the sample bias from −1 V to +1 V, we observe that, under illumination, the average in-phase signal is more positive than that without illumination. That is, the phase shift for the photoinduced signal changes 180° when we change the polarity of the bias. We attribute the negative shift of the *average* in-phase signal under illumination in **Figure B.3C** to tunneling of photoinduced hot electrons from the surface to the tip. Since photoinduced electrons generated in C_{60} triad molecules should have the same phase shift as hot electrons, in **Figure B.2**, we conclude that local positive signals in the spectroscopic images indicate that the position has higher densities of photoinduced holes

and negative signals in the spectroscopic images indicate that the position has higher densities of photogenerated electrons.[53,58–60] Our results in **Figure B.2** and related data enable us to characterize the distribution of photoinduced charges *within* C_{60} triad molecules.

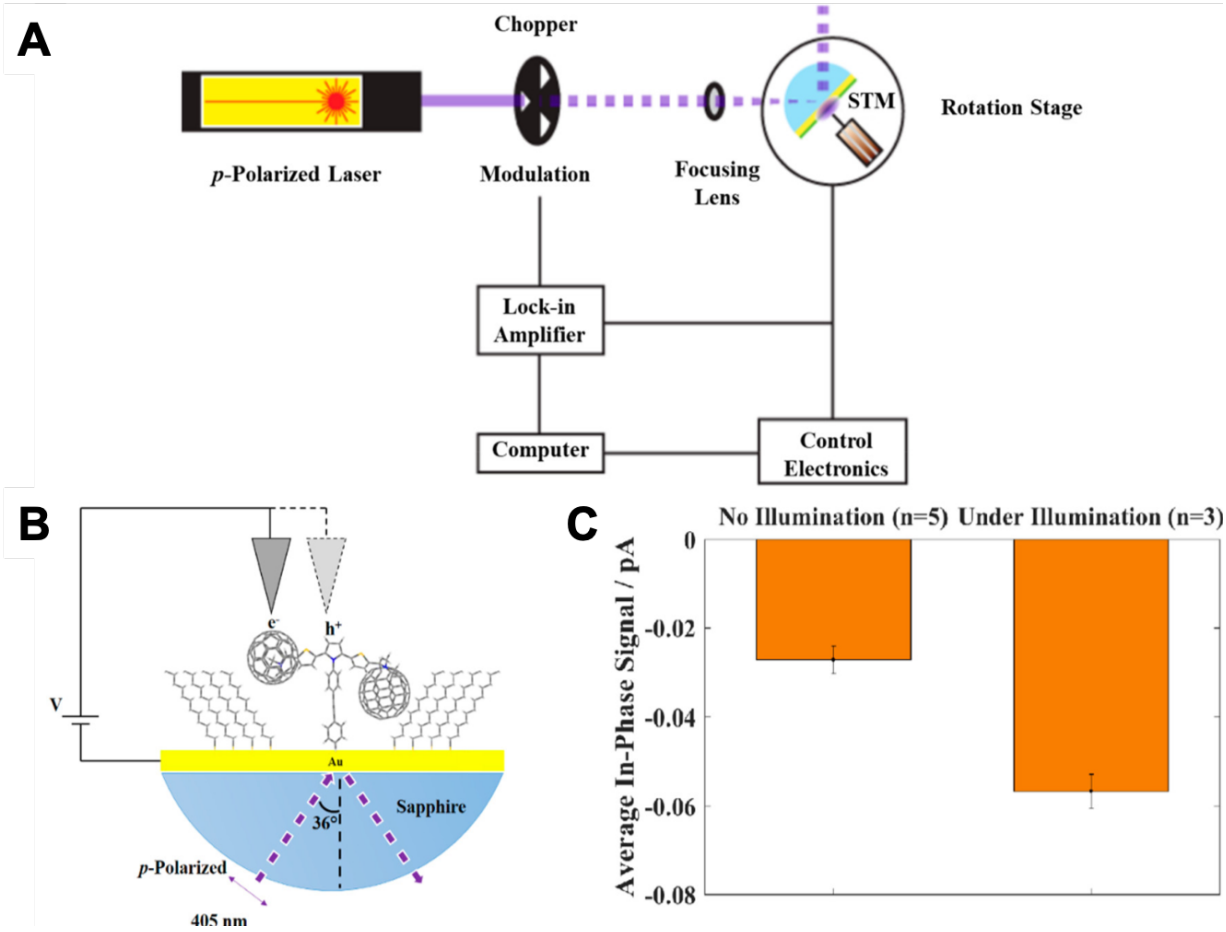

Figure B.3. (A) Schematic illustration of the experimental setup for laser-assisted scanning tunneling microscopy. (B) Scheme of evanescent illumination and photogeneration of charge separation, measured in submolecular resolution spectroscopic images. (C) Average of the in-phase signals calculated from spectroscopic images in Figure B.2 and consecutively collected data.

Photoinduced signals in **Figure B.2D,F** were further extracted from background through a simple height thresholding method (see Supporting Information). Data for the matrix molecules in the upper areas in **Figure B.2D,F** were used as background, and their intensity ranges were used as threshold references. Only data points with higher absolute intensity than background were used to determine the photoinduced signals. Extracted photoinduced signals from **Figure B.2D,F** are shown in **Figure B.4B,E** separately, and corresponding topographic images **Figure B.2C,E** are shown as **Figure B.4A,D** for analysis. In the data in **Figure B.4B**, we find that the three regions of signals highlighted by black, green, and red boxes correspond to the C_{60} triad molecules labeled 2, 3, and 5, respectively, in **Figure B.4A**. While in **Figure B.4E**, the two regions of signals highlighted by green and red boxes correspond to the C_{60} triad molecules labeled 3, 4, and 5, respectively, in **Figure B.4D**. The relative intensities of the photoinduced signals can also be seen in **Figure B.4C,F**, which are displays of **Figure B.4B,E** in the yz plane. The signals corresponding to the molecule labeled 2 (black box) in **Figure B.4C** disappear in **Figure B.4F**, and the signal corresponding to the molecule labeled 3 (green box) in **Figure B.4C** only has positive signal left in **Figure B.4F** and the intensity has greatly decreased. However, the signal corresponding to the molecule labeled 5 (red box) in **Figure B.4C** greatly increased in **Figure B.4F**. We tentatively attribute the differences in the intensities of photoinduced signals and the observations that photoinduced signals were not observed for all C_{60} triad molecules as likely due to (dynamic) differences in conformations of C_{60} triad molecules.

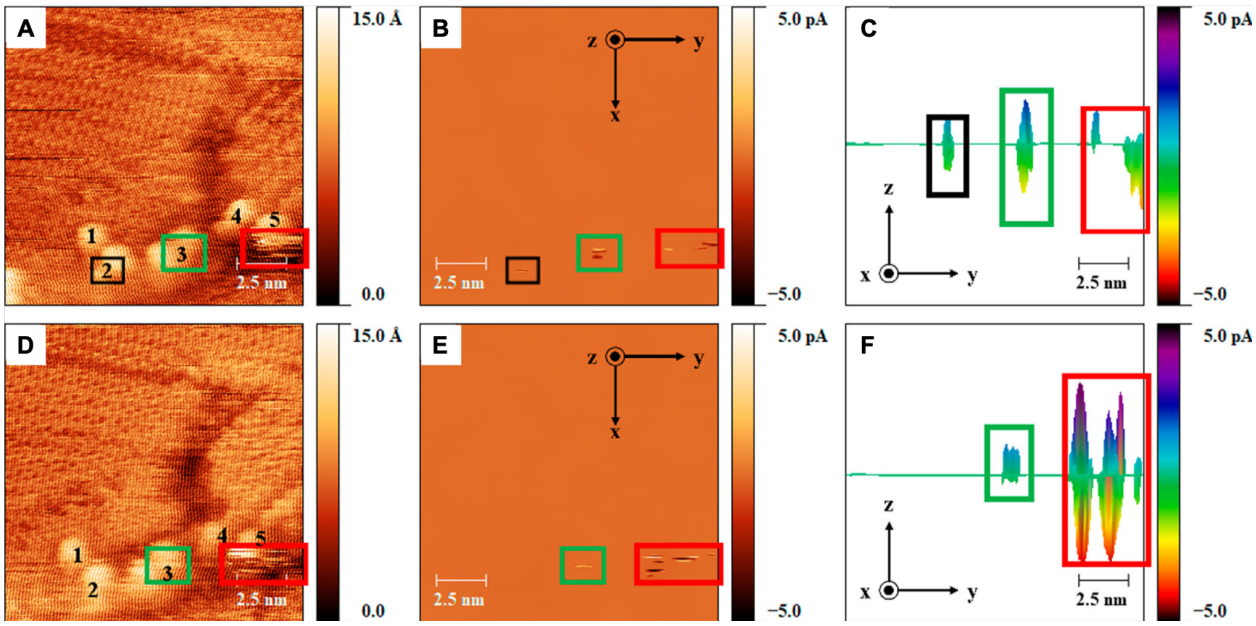

Figure B.4. Consecutively collected scanning tunneling microscopy images under evanescent laser illumination, showing C_{60} triad molecules inserted in a dodecanethiolate monolayer matrix on Au{111}. (A) Topographic image reproduced from Figure B.2C. (B) Photoinduced charge separation extracted from Figure B.2D. (C) Projection of image (B) on the yz plane. (D) Topographic image reproduced from Figure B.2E. (E) Photoinduced charge separation extracted from Figure B.2F. (F) Projection of image (E) in the yz plane. All images were collected at a sample bias of −1.00 V and a tunneling current of 12.0 pA. All spectroscopic images were collected phase sensitively with a reference frequency of 4.8 kHz created by a chopper wheel that was used to modulate the sample illumination.

In order to test whether we have detected photoinduced charge separation in C_{60} triad molecules using scanning tunneling microscopy, we performed control experiments in which molecules *without* C_{60} groups (DTP, **Figure B.1B**) were inserted into the defects in C12 SAMs and the surface was characterized by laser-assisted STM. **Figure B.5A,B** show simultaneously obtained topographic and spectroscopic images without illumination. **Figure B.5C,D** show simultaneously obtained topographic and spectroscopic images with evanescent laser illumination. We attribute the protrusions in **Figure B.5A,C** highlighted by the circles as DTP molecules. The DTP molecules cannot be characterized as clearly as C_{60} triad molecules even though the lattice of C12 matrix molecules is still observed. We

attribute this difference to DTP molecules being substantially smaller than C_{60} triad molecules, which makes them more mobile under ambient conditions and room temperature.(66)When the laser was blocked to stop illumination, some signals near the background level were observed in **Figure B.5B** at the same position as the DTP molecule in **Figure B.5A**. After illumination, the signal corresponding to the DTP molecule (highlighted by the circle) in the spectroscopic image **Figure B.5D** did *not* increase significantly beyond the background (matrix) level. These and similar results on DTP and other molecules indicate that the charge separation observed in **Figure B.2D,F** is only observed in molecular *p*–*n* junctions when both electron donors and electron acceptors are present.

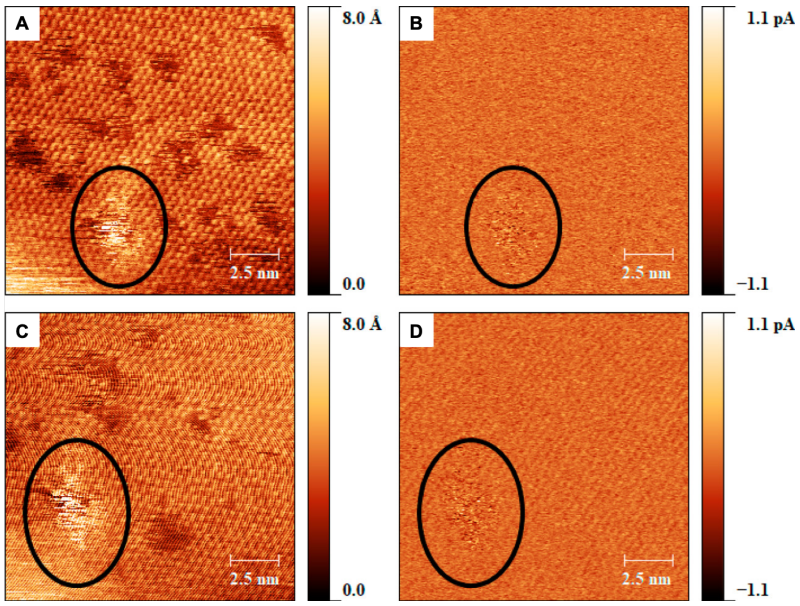

Figure B.5. Scanning tunneling microscopy images showing 2,5-dithienylpyrrole control molecules inserted in a dodecanethiolate self-assembled monolayer matrix on Au{111}. (A,B) Simultaneously obtained topographic and spectroscopic images without illumination. (C,D) Simultaneously obtained topographic and spectroscopic images with evanescent illumination. All images were collected at a sample bias of −1.00 V and a tunneling current of 12.0 pA. All spectroscopic images were collected phase sensitively with a reference frequency of 4.8 kHz created by a chopper wheel that was used to modulate the evanescent sample illumination.

B.C. Conclusions and Prospects

In summary, we have successfully detected photoinduced charge separation in single molecular *p*–*n* junctions with laser-assisted STM. This method can serve as a diagnostic tool to measure the intrinsic photovoltaic efficiency of single molecules and assemblies for solar cell applications. By investigating candidate molecules and assemblies with laser-assisted STM, our method has the potential to compare the photovoltaic efficiency quantitatively with submolecular resolution and to provide direct figures of merit for energy conversion. We can use these measurements to optimize photoabsorption, charge separation, and connections of the molecules or assemblies to the contact. The critical details of the orientations and contacts can be extracted in a way inaccessible to ensemble measurements of photovoltaics. We anticipate that this approach will elucidate important design principles and feedback for synthetic chemists, materials scientists, and engineers and will help to determine key molecular and materials components and conformations for efficient light conversion. Further experiments will focus on extending our method to other photoactive molecules and assemblies with different functionality and electron donors and acceptors.

B.D. Materials and Methods

B.D.1. Preparation of Au{111} Substrates.

Thin (45 nm), flat (roughness 0.3-1 nm) epitaxial Au {111} films are deposited on c-cut sapphire cylindrical prisms. Half-cylindrical sapphire prisms (1 cm × 1 cm, 1 cm diameter) with epi-polished c-cut planes, Al_2O_3 (0001) were purchased from Meller Optics (Providence, RI). These substrates were annealed in air at 1100 ^{o}C and 1400 ^{o}C for 24 h and 18 h, respectively, in consecutive cycles. Thin Au{111} films were grown on c-cut plane

sapphire prisms with a Nb seed layer.[67] The annealed sapphire substrates were introduced to the ultrahigh vacuum evaporator chamber with a base pressure in the 10^{-10} mbar range, and were outgassed for 1 h at 150 °C to remove adsorbed water. A 2-nm-thick Nb seed layer was evaporated at a rate of 0.15 Å/s at room temperature.[68] The pressure increased to $\sim 5 \times 10^{-9}$ mbar during evaporation. Room temperature deposition favors the Nb{110} orientation over Nb{111}, while elevated temperatures (over 800 °C) yield Nb{111}.[69] The orientation of Au {111} is parallel to Nb{110} with the epitaxial relationship as follows:[68,70,71] $Au(111)[011]||Nb\{111\}[001]||Al2O3/0001/[1010]$. Thin Au films (45 nm) were then deposited at a substrate temperature of 300 °C and an evaporation rate of 0.50 Å/s. The surface temperature should not exceed 300 °C, to avoid inter-diffusion and intermetallic compounds (primarily $AuNb_3$ and Au_2Nb_3) that occur above 325 °C.[72]

B.D.2. Preparation of n-Dodecanethiolate Self-Assembled Monolayer Matrices.

Freshly flame- annealed Au{111}/Al_2O_3(0001) substrates were placed in the airspace in a vial over gravimetrically prepared 1 mM n-dodecanethiol (Sigma Aldrich, St. Louis, MO) ethanolic solution for 3 h at 78 °C. Substrates were then rinsed thoroughly with ethanol and were blown dry using nitrogen.

B.D.3. Insertion of C_{60}-Tethered 2,5-Dithienylpxyrrole Triads (C_{60} Triads) and the Control Molecules without C_{60} (DTP) into n-Dodecanethiolate Self-Assembled Monolayer Matrices.

With ultrasonication to speed up the dissolution, the solution of 2,5-dithienylpyrrole with conjugated tether (DTP, 0.05 mM, 10 mL) in toluene (HPLC purity) was prepared and purged with dry nitrogen. Ammonium hydroxide (28.0-30.0% NH_3, 5 μL) was added to 1 mL of the solution. The aqueous ammonia hydrolyzed the thioacetyl protecting group, generating the thiolate in situ. After 2 min ultrasonication to mix ammonium hydroxide with toluene solution, the mixture was let stand for 30 min for deprotection before use. Monolayers with DTP inserted were prepared by submerging the gold substrate with vapor-deposited dodecanethiol SAM matrix into solution of deprotected DTP molecules overnight at room temperature. The solution of C_{60} triad (0.05 mM, 10 mL) in toluene (HPLC purity) was ultrasonicated and bubbled with dry nitrogen. The partial solution (2 mL) were transferred into a vial and diluted with 0.25 mL of ethanol to ease the dissolution of ammonium hydroxide. Two doses of ammonium hydroxide (28.0-30.0% NH_3, 25 μL) were added with 3 min sonication in between. After the solution was stirred for 0.5 h, the Au substrates were immersed into the solution for 24 h, followed by rinsing with toluene and ethanol, and drying with a nitrogen stream. The color of the solution turning to light brown indicates that the acetate protecting group has been removed.

B.D.4. Scanning Tunneling Microscopy.

All scanning tunneling microscopy (STM) measurements were conducted using a custom-built laser-assisted STM.[50] All topographic images were collected in atmospheric air

and at room temperature with constant tunneling current mode. The Pt/Ir 80:20 tip wire was supplied by Alfa Aesar (Ward Hill, MA) and were freshly cut before use. The gain of the piezoelectric scanners was calibrated by comparison of a dodecanethiol monolayer on Au{111} to its known lattice constant of 4.99 Å and Au{111} monoatomic step height of 2.34 Å. All STM images were collected at a resolution of 256 pixels times 256 pixels and the scanning rate for all images was set as 1 ms per pixel. The laser beam (p-polarized, 405 ± 5 nm, Coherent Inc. CUBE diode laser) is modulated by a chopper wheel to create reference frequency input to the lock-in amplifier (Stanford Research Systems Inc., Model SR850), so that light-triggered change in the tunneling current can be recorded phase sensitively. The tunneling current was amplified through a gain of 10^{10} mV/pA and the sensitivity of lock-in amplifier was set to 50 mV, which correspond to 5 pA. The time constant of the lock-in amplifier was set to 3 ms for all measurements. The incident field is transmitted through a broadband window on the wall of the acoustic enclosure and focused onto the Au/air interface by a converging lens (focal length = 75 mm). The alignment of the focusing lens is accomplished by stepper motor actuator (Newport Corporation, TRA25PPD). We have installed a motorized continuous rotation stage (Thorlabs, Inc., CR1Z7) to align the lens focal plane perpendicular to the propagation direction of the incident beam. The light incident angle at Au/sapphire interface can be varied by revolving the scanner and prism holder with the rotating stage (Newport Corporation, RV160PE-F) underneath. We analyze the light reflected off the interface at discrete incident angles via a CCD camera beam profiler (Thorlabs Inc., BC106-VIS) that orbits above the tip/sample junction. Phase sensitive images were collected as the laser beam illuminated the tunneling junction from the rear sapphire at an incident angle of 37°. The electric field intensity distributions at sapphire/Au/Air

interfaces were simulated with the finite-difference time-domain method for different incident angles and are shown in **Figure B.S1A**. At an incident angle of 37° relative to the surface normal, the electric field intensity is plotted as a function of position x in **Figure B.S1B**. The depth of penetration, defined by the 1/e attenuation, is approximately 160 nm. At this wavelength, the incident electromagnetic field excites an interband transition in the gold, instead of surface plasmons.[73] The frequency of the chopper wheel was maintained at 4.8 kHz and was used as the reference frequency of the lock-in amplifier. Hence, the laser on/off switching rate is faster than the response time (approximately 1 ms) of the tip height control loop.

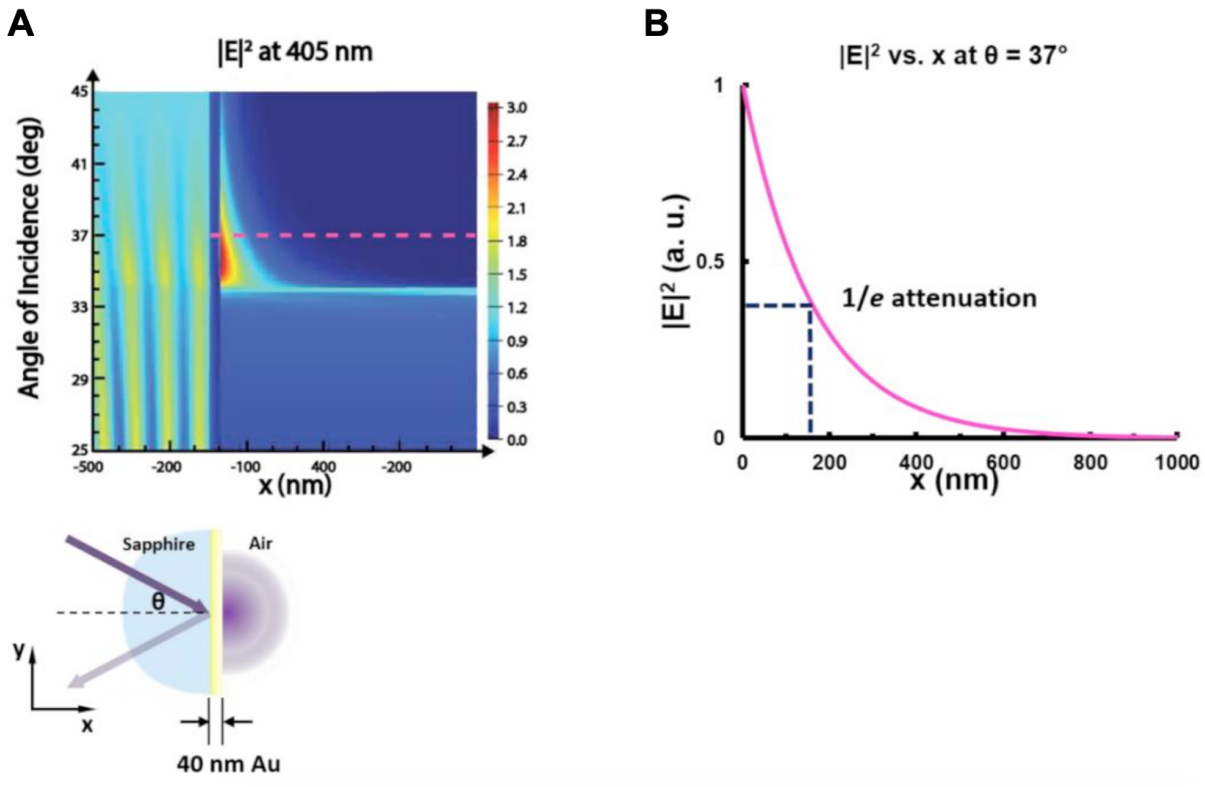

Figure B.S1. (A) Electric field intensity distribution at sapphire/Au/Air interface for different incident angles. (B) Electric field intensity distribution above sapphire surface at 37° incident angle relative to the surface normal.

B.D.5. Image Processing.

All STM images were processed by Gwyddion.[S9] Photoinduced signals in the phase-sensitive spectroscopic images in **Figure B.2D,F** were extracted from the background through a height thresholding method. Height thresholds were determined based on the data intensity range of the area corresponding to n-dodecanethiol matrix molecules in phase-sensitive spectroscopic images, as highlighted in **Figure B.S2**. **Figure B.S2A,B** is reproduced from **Figure B.2D,F**. For **Figure B.2D**, data points with value smaller than -1.286 pA and larger than 0.941 pA and their adjacent areas with slope larger than 20% of the whole image and curvature larger than 60% of the whole image were conserved. The rest of the data points in **Figure B.2D** were replaced by the mean value of the whole image. The processed image is shown as **Figure B.4B** in the paper. For **Figure B.2F**, data points with values smaller than -0.933 pA and larger than 0.848 pA and their adjacent areas with slope larger than 20% of the whole image and curvature larger than 60% of the whole image were conserved. The rest of the data points in **Figure B.2F**were replaced by the mean value of the entire image. The processed image is shown as **Figure B.4E** in the main text.

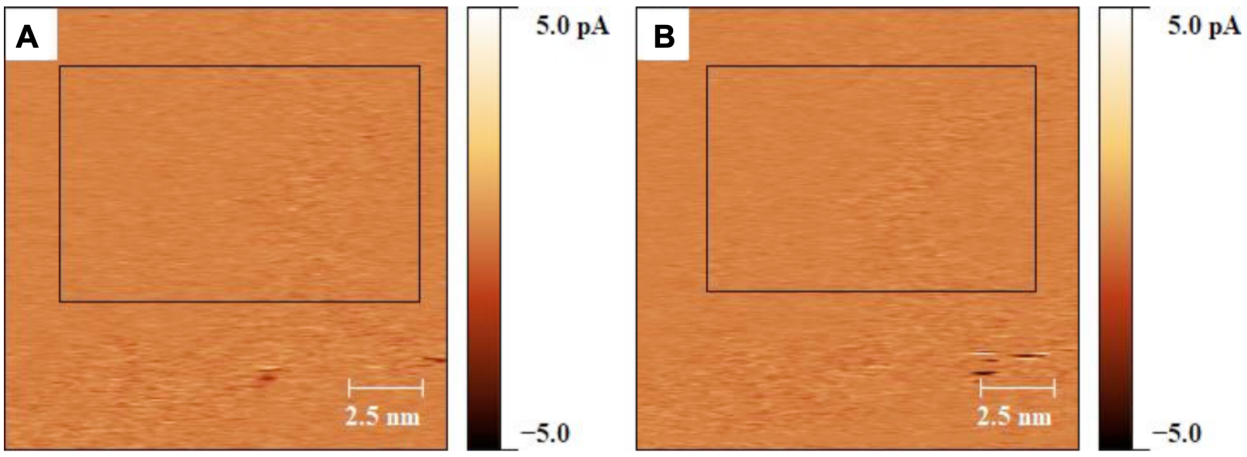

Figure B.S2. (A) Phase-sensitive spectroscopic image reproduced from Figure B.2D. (B) Phase-sensitive spectroscopic image reproduced from Figure B.2F.

B.D.6. Supplemental Data.

We observed that in **Figures B.2,4**, the regions with large phase-sensitive signals in the spectroscopic images correspond to the regions with strips with significant signal fluctuations in the topographic images. The strips in the topographic images were caused by the conformational changes and motion of C_{60} triad molecules during scanning. In order to test whether the phase sensitive signals we observed were related to motion of the molecules, we collected another set of images of the same region when the surface was not under illumination, shown in **Figures B.S3**. In **Figures B.S3A**, we observe signal fluctuations near one of the C_{60} triad molecules, which we interpret as conformational changes and motion of the C_{60} triad molecules not being caused (exclusively) by illumination. In the corresponding spectroscopic image, **Figures B.S3B**, we do not observe significant phase-sensitive signals in the region corresponding to the fluctuations, indicating that the movement of the C_{60} triad molecules will not generate "mechanical" noise in the spectroscopic images as recorded (which would have to be phase sensitive to be observed).

Such results suggest that the phase-sensitive signals we observed in **Figures B.2,4** were caused by the photo-induced charges.

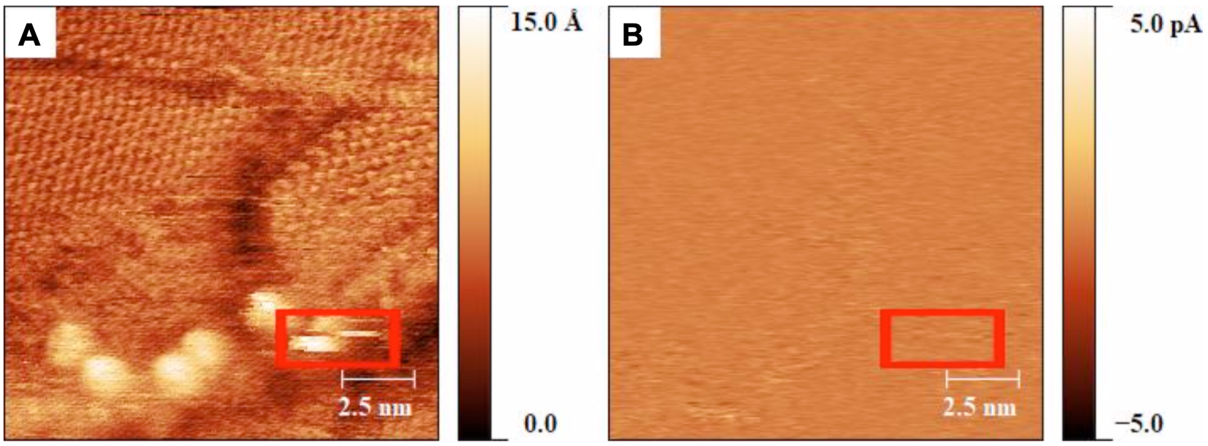

Figure B.S3. (A) Topographic and (B) spectroscopic images showing C_{60} triad molecules inserted in dodecanethiolate monolayer matrix on Au{111}. Images were collected without any illumination of the surface. All images were collected at a sample bias of -1.00 V and a tunneling current of 12.0 pA.

In order to test whether we can detect the distribution of photo-induced charges on different C_{60} triad molecules, we also collected topographic and spectroscopic images for different regions on different samples. Two typical sets of data are shown in **Figures B.S4,5**. **Figures B.S4A,B** was collected without any illumination and **Figures B.S4C,D** was collected when the surface was illuminated by a 405 nm laser. In **Figures B.S4D**, we observe positive and negative in-phase signals (highlighted by the black box) corresponding to the position of a C_{60} triad molecule in **Figures B.S4C**. Such signals were not observed in **Figure B.S4B**. All images in **Figures B.5** were collected with a +1.00 V sample bias, which is different from all the other STM images shown in the main text and the supporting information. **Figures B.S5A,B** was collected without any illumination and **Figures B.S5C,D** was collected when the surface was illuminated by a 405 nm laser. Photo-induced signals were observed

in **Figure B.S5D** (highlighted by the black box) and their positions correlate to the positions of C_{60} triad molecules in **Figure B.S5C**.

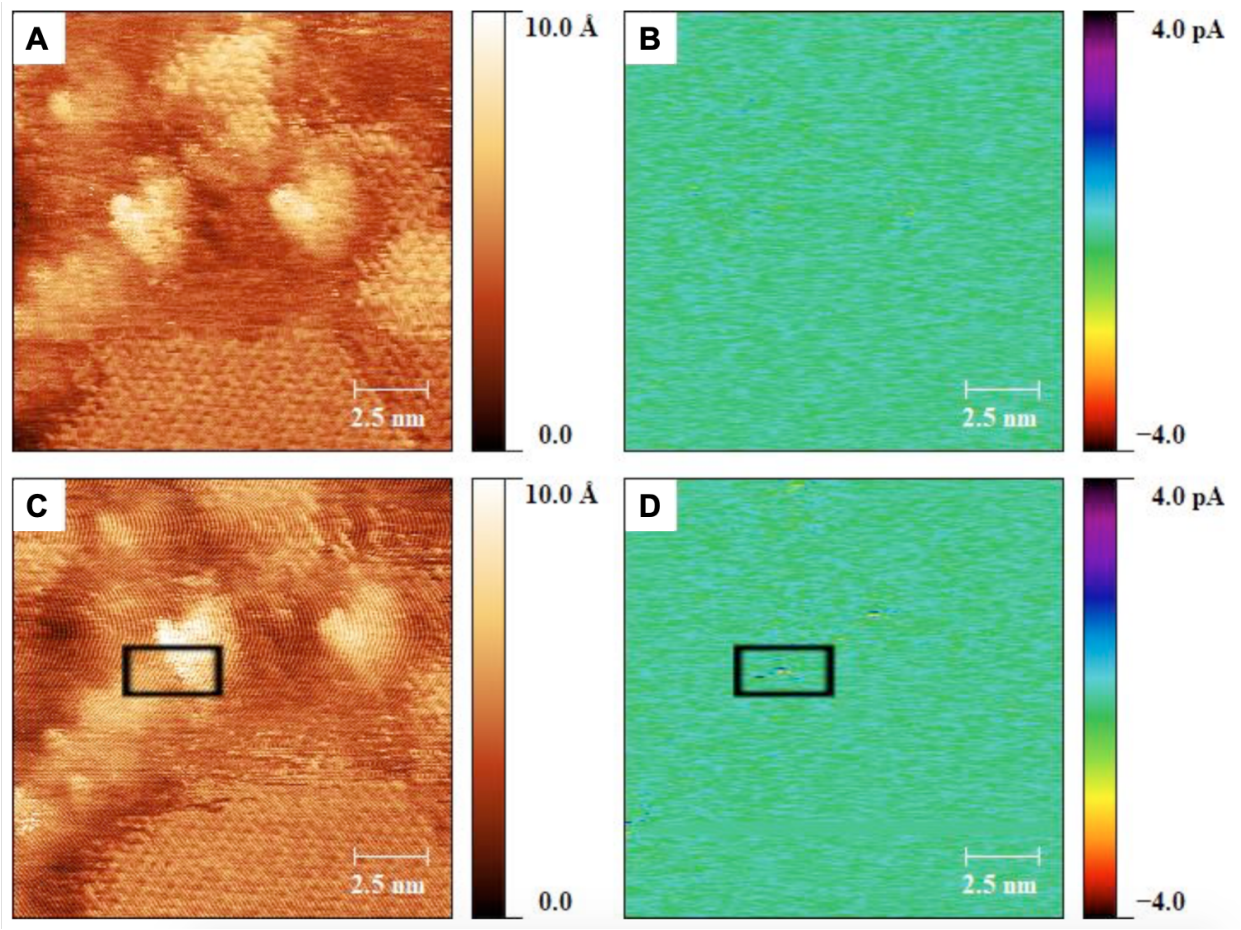

Figure B.S4. Scanning tunneling microscopy images showing C_{60} triad molecules inserted in a dodecanethiolate monolayer matrix on Au{111}. (A) Topographic and (B) spectroscopic images were simultaneously obtained when the laser was not illuminating the sample. (C) Topographic and (D) spectroscopic images were simultaneously obtained when the laser (405 nm) illuminated the sample evanescently. All images were collected at a sample bias of -1.00 V and a tunneling current of 12.0 pA. All spectroscopic images were collected phase sensitively with a reference frequency of 4.8 kHz created by a chopper wheel that was used to modulate the evanescent sample illumination.

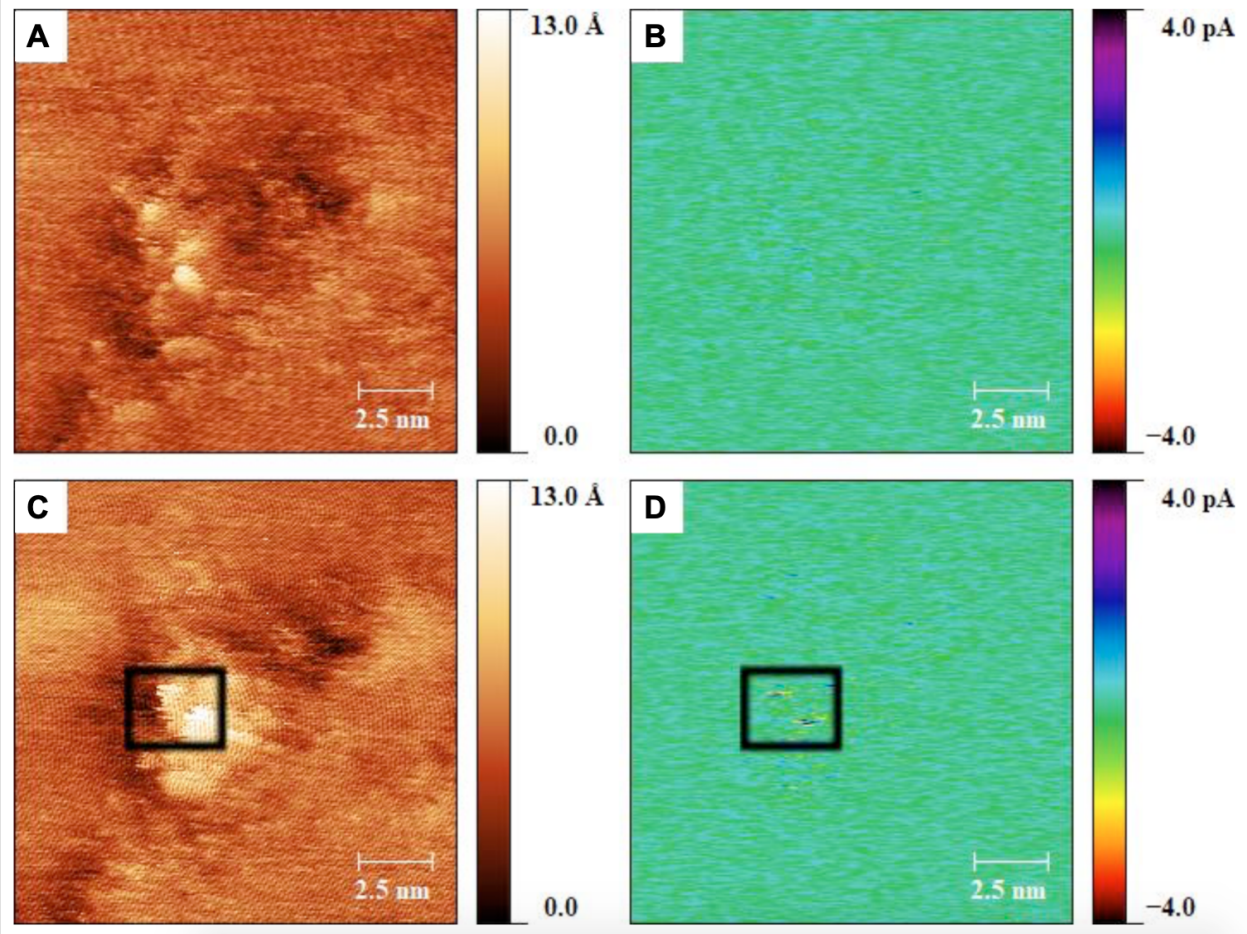

Figure B.S5. Scanning tunneling microscopy images showing C_{60} triad molecules inserted in a dodecanethiolate monolayer matrix on Au{111}. (A) Topographic and (B) spectroscopic images were simultaneously obtained when the laser was not illuminating the sample. (C) Topographic and (D) spectroscopic images were simultaneously obtained when the laser (405 nm) illuminated the sample evanescently. All images were collected at a sample bias of +1.00 V and a tunneling current of 12.0 pA. All spectroscopic images were collected phase sensitively with a reference frequency of 4.8 kHz created by a chopper wheel that was used to modulate the evanescent sample illumination.

We also collected the 90° phase offset images for **Figure B.2C,E**, shown as **Figure B.S6C,F**, separately. **Figure B.2C-F** is reproduced as **Figure B.S6A-E** for comparison. In **Figure B.S6C,F**, we observe positive and negative phase-sensitive signals at the same positions as **Figure B.S6B,E**. The phase shift of the phase-sensitive signal only depends on the electronic delays of the system and is constant as long as the settings of the chopper encoder and lock-in amplifier are kept the same. It can vary within a small range due

electronic noise and small uncertainties of the instruments (vibrations etc.) resulting in small signals in the 90° phase offset images. The purpose of this work is to test if we can map the distributions of photo-induced charges at the sub-molecular level. We have the potential to obtain more valuable information after further engineering of the instrument and the systems.

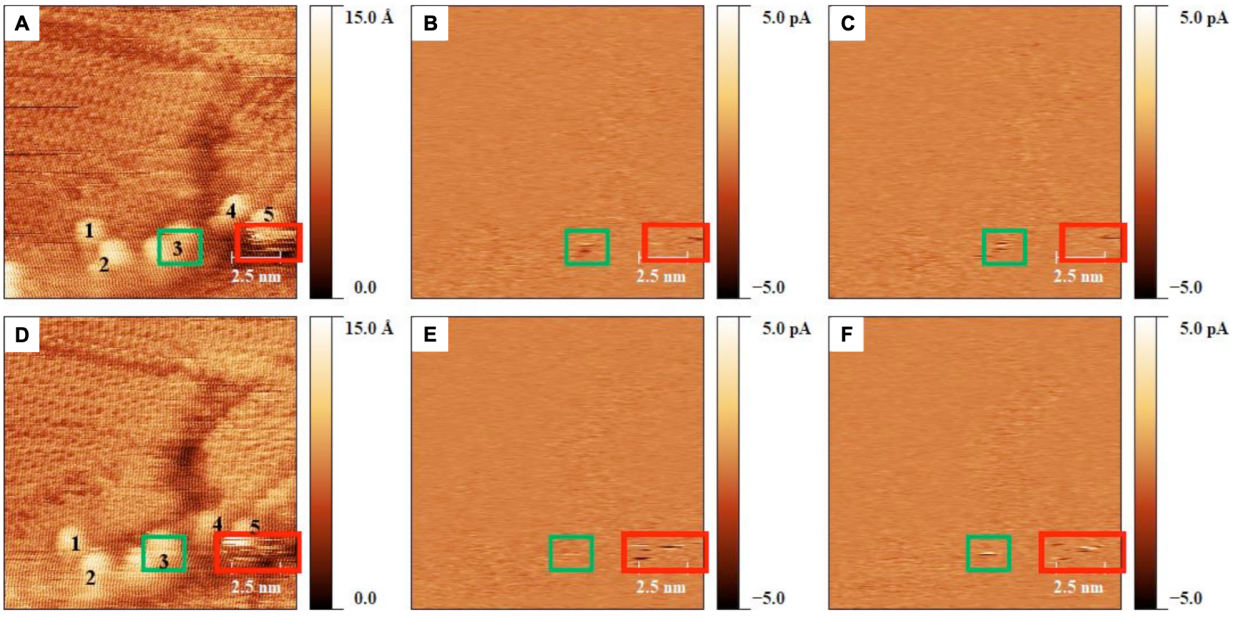

Figure B.S6. Consecutively collected scanning tunneling microscopy images under evanescent laser illumination, showing C_{60} triad molecules inserted in a dodecanethiolate monolayer matrix on Au{111}. (A) Topographic image reproduced from Figure B.2C. (B) Spectroscopic image reproduced from Figure 2d. (C) 90° phase offset image collected simultaneously with (A) and (B). (D) Topographic image reproduced from Figure B.2E. (E) Spectroscopic image reproduced from Figure 2f. (F) 90° phase offset image collected simultaneously with (D) and (E). All images were collected at a sample bias of -1.00 V and a tunneling current of 12.0 pA. All spectroscopic images were collected phase sensitively with a reference frequency of 4.8 kHz created by a chopper wheel that was used to modulate the sample illumination.

The projection of **Figure B.5B,D** is shown in **Figure B.S7** for comparison. The vertical scale of **Figure B.S7** has been adjusted to be the same as **Figure B.4C,F** so that the relative magnitude of the signals can be compared. When the laser was blocked to stop illumination, some signals near the background level were observed in **Figure B.S7A**. After illumination, the signal corresponding to the DTP molecule in the spectroscopic image **Figure B.5D** did not increase significantly beyond the background (matrix) level and the signal is close to noise, compared to **Figure B.4C,F**.

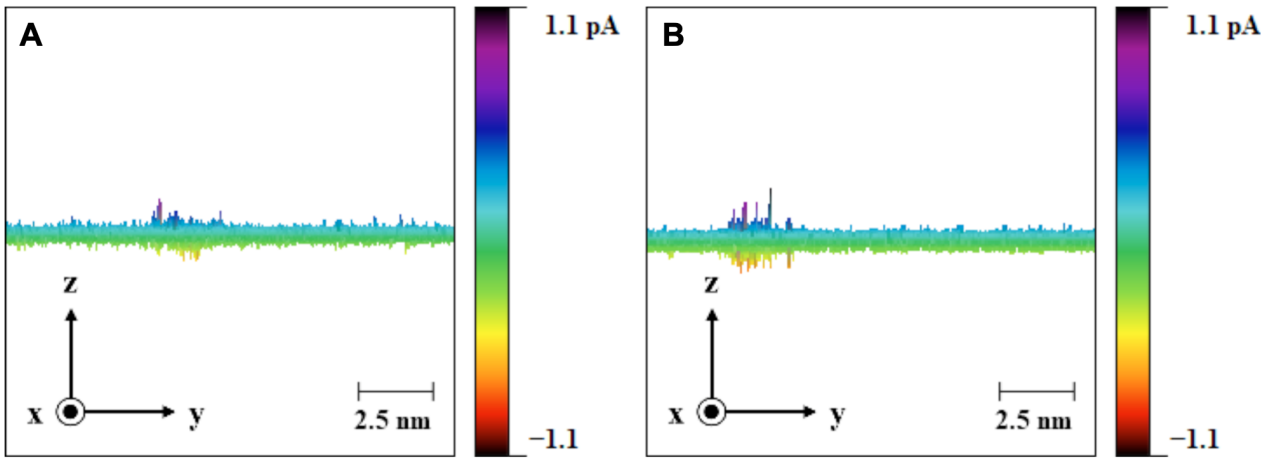

Figure B.S7. (A) Projection of Figure B.5B in the yz plane. (B) Projection of Figure B.5D in the yz plane.

We have extracted five line profiles across the signals in **Figure B.2D,F** and reproduced as **Figure B.S8A,B** and the five lines are shown and numbered. The corresponding line profiles are shown in **Figure B.S9**.

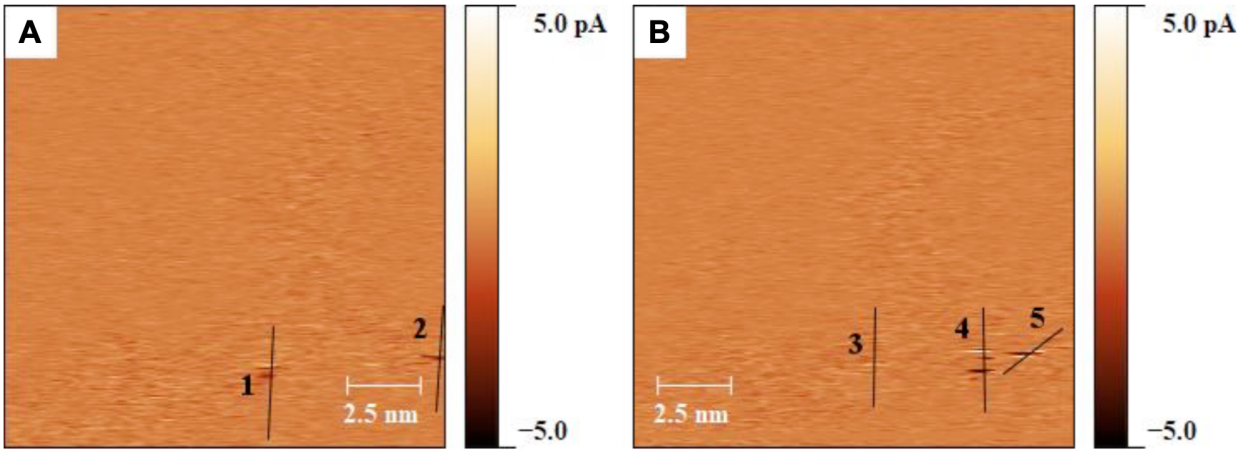

Figure B.S8. (A) Spectroscopic image reproduced from Figure B.2D. (B) Spectroscopic image reproduced from Figure B.2F.

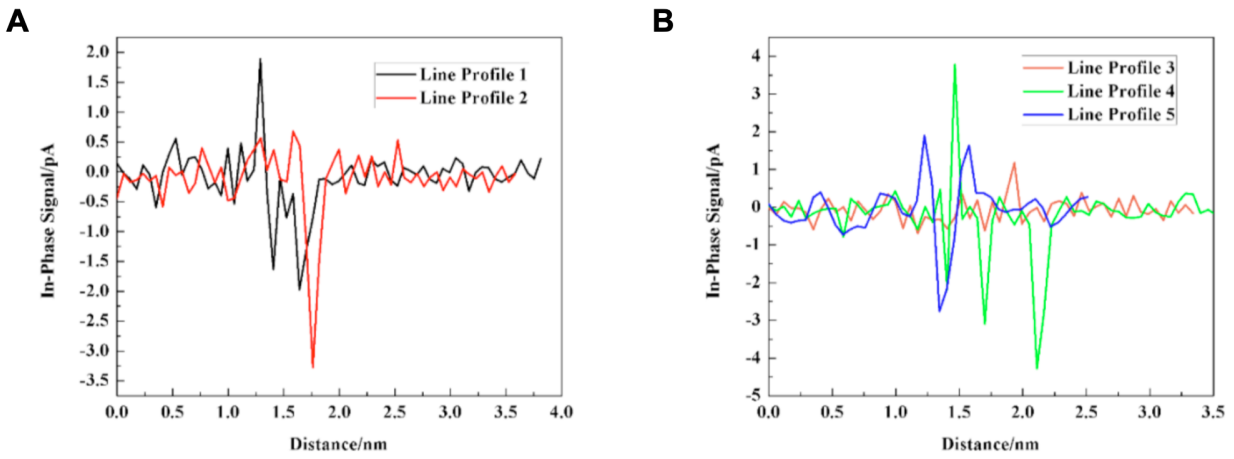

Figure B.S9. (A) Line profiles corresponding to the lines in Figure B.S8A. (B) Line profiles corresponding to the lines in Figure B.S8B.

B.E. References

(1) Wang, S.; Wattanatorn, N.; Chiang, N.; Zhao, Y.; Kim, M.; Ma, H.; Jen, A. K.-Y.; Weiss, P. S. Photoinduced Charge Transfer in Single-Molecule *p–n* Junctions. *J. Phys. Chem. Lett.* **2019**, *10*, 2175–2181.

(2) Kamat, P. V. Meeting the Clean Energy Demand: Nanostructure Architectures for Solar Energy Conversion. *J. Phys. Chem. C* **2007**, *111*, 2834–2860.

(3) Graetzel, M. Recent Advances in Sensitized Mesoscopic Solar Cells. *Acc. Chem. Res.* **2009**, *42*, 1788–1798.

(4) Odobel, F.; Le Pleux, L.; Pellegrin, Y.; Blart, E. New Photovoltaic Devices Based on the Sensitization of P-Type Semiconductors: Challenges and Opportunities. *Acc. Chem. Res.* **2010**, *43*, 1063–1071.

(5) Dennler, G.; Scharber, M. C.; Brabec, C. J. Polymer-Fullerene Bulk-Heterojunction Solar Cells. *Adv. Mater.* **2009**, *21*, 1323–1338.

(6) Mishra, A.; Baeuerle, P. Small Molecule Organic Semiconductors on the Move: Promises for Future Solar Energy Technology. *Angew. Chem.-Int. Ed.* **2012**, *51*, 2020–2067.

(7) Lin, Y.; Li, Y.; Zhan, X. Small Molecule Semiconductors for High-Efficiency Organic Photovoltaics. *Chem. Soc. Rev.* **2012**, *41*, 4245.

(8) Bredas, J.-L.; Norton, J. E.; Cornil, J.; Coropceanu, V. Molecular Understanding of Organic Solar Cells: The Challenges. *Acc. Chem. Res.* **2009**, *42*, 1691–1699.

(9) Bumm, L. A.; Arnold, J. J.; Dunbar, T. D.; Allara, D. L.; Weiss, P. S. Electron Transfer through Organic Molecules. *J. Phys. Chem. B* **1999**, *103*, 8122–8127.

(10) Wassel, R. A.; Credo, G. M.; Fuierer, R. R.; Feldheim, D. L.; Gorman, C. B. Attenuating Negative Differential Resistance in an Electroactive Self-Assembled Monolayer-Based Junction. *JACS.* **2004**, *126*, 295–300.

(11) Monnell, J. D.; Stapleton, J. J.; Dirk, S. M.; Reinerth, W. A.; Tour, J. M.; Allara, D. L.; Weiss, P. S. Relative Conductances of Alkaneselenolate and Alkanethiolate Monolayers on Au{111}. *J. Phys. Chem. B* **2005**, *109*, 20343–20349.

(12) Tao, N. J. Electron Transport in Molecular Junctions. *Nat. Nanotechnol.* **2006**, *1*, 173-181.

(13) Schmid, T.; Opilik, L.; Blum, C.; Zenobi, R. Nanoscale Chemical Imaging Using Tip-Enhanced Raman Spectroscopy: A Critical Review. *Angew. Chem. Int. Ed.* **2013**, *52*, 5940–5954.

(14) Sonntag, M. D.; Pozzi, E. A.; Jiang, N.; Hersam, M. C.; Van Duyne, R. P. Recent Advances in Tip-Enhanced Raman Spectroscopy. *J. Phys. Chem. Lett.* **2014**, *5*, 3125–3130.

(15) Battacharyya, S.; Kibel, A.; Kodis, G.; Liddell, P. A.; Gervaldo, M.; Gust, D.; Lindsay, S. Optical Modulation of Molecular Conductance. *Nano Lett.* **2011**, *11*, 2709–2714.

(16) Aradhya, S. V.; Venkataraman, L. Single-Molecule Junctions beyond Electronic Transport. *Nat. Nanotechnol.* **2013**, *8*, 399–410.

(17) Aram, T. N.; Ernzerhof, M.; Asgari, A.; Mayou, D. The Impact of Long-Range Electron-Hole Interaction on the Charge Separation Yield of Molecular Photocells. *J. Chem. Phys.* **2017**, *146*, 034103.

(18) Zhou, J.; Wang, K.; Xu, B.; Dubi, Y. Photoconductance from Exciton Binding in Molecular Junctions. *JACS.* **2018**, *140*, 70–73.

(19) Moore, A. M.; Weiss, P. S. Functional and Spectroscopic Measurements with Scanning Tunneling Microscopy. *Annu. Rev. Anal. Chem.* **2008**, *1*, 857–882.

(20) Gerstner, V.; Knoll, A.; Pfeiffer, W.; Thon, A.; Gerber, G. Femtosecond Laser Assisted Scanning Tunneling Microscopy. *J. Appl. Phys.* **2000**, *88*, 4851.

(21) Gaffney, K. J.; Miller, A. D.; Liu, S. H.; Harris, C. B. Femtosecond Dynamics of Electrons Photoinjected into Organic Semiconductors at Aromatic-Metal Interfaces. *J. Phys. Chem. B* **2001**, *105*, 9031–9039.

(22) Wu, S. W.; Ho, W. Two-Photon-Induced Hot-Electron Transfer to a Single Molecule in a Scanning Tunneling Microscope. *Phys. Rev. B* **2010**, *82*.

(23) Berndt, R.; Gimzewski, J. K. Photon Emission in Scanning Tunneling Microscopy: Interpretation of Photon Maps of Metallic Systems. *Phys. Rev. B* **1993**, *48*, 4746–4754.

(24) McCarty, G. S.; Weiss, P. S. Scanning Probe Studies of Single Nanostructures. *Chem. Rev.* **1999**, *99*, 1983–1990.

(25) Bumm, L. A.; Arnold, J. J.; Cygan, M. T.; Dunbar, T. D.; Burgin, T. P.; Jones, L.; Allara, D. L.; Tour, J. M.; Weiss, P. S. Are Single Molecular Wires Conducting? *Science* **1996**, *271*, 1705–1707.

(26) Moore, A. M.; Yeganeh, S.; Yao, Y.; Claridge, S. A.; Tour, J. M.; Ratner, M. A.; Weiss, P. S. Polarizabilities of Adsorbed and Assembled Molecules: Measuring the Conductance through Buried Contacts. *ACS Nano* **2010**, *4*, 7630–7636.

(27) Guldi, D. M. Fullerenes: Three Dimensional Electron Acceptor Materials. *Chem. Commun.* **2000**, No. 5, 321–327.

(28) D'Souza, F.; Ito, O. Supramolecular Donor-Acceptor Hybrids of Porphyrins /Phthalocyanines with Fullerenes/Carbon Nanotubes: Electron Transfer, Sensing, Switching, and Catalytic Applications. *Chem. Commun.* **2009**, No. 33, 4913-4928.

(29) Gayathri, S. S.; Wielopolski, M.; Pérez, E. M.; Fernández, G.; Sánchez, L.; Viruela, R.; Ortí, E.; Guldi, D. M.; Martín, N. Discrete Supramolecular Donor-Acceptor Complexes. *Angew. Chem. Int. Ed.* **2009**, *48*, 815–819.

(30) Hirayama, D.; Yamashiro, T.; Takimiya, K.; Aso, Y.; Otsubo, T.; Norieda, H.; Imahori, H.; Sakata, Y. Preparation and Photoelectrochemical Properties of Gold Electrodes Modified with [60]Fullerene-Linked Oligothiophenes. *Chem. Lett.* **2000**, *29*, 570–571.

(31) Imahori, H.; Tamaki, K.; Guldi, D. M.; Luo, C.; Fujitsuka, M.; Ito, O.; Sakata, Y.; Fukuzumi, S. Modulating Charge Separation and Charge Recombination Dynamics in Porphyrin–Fullerene Linked Dyads and Triads: Marcus-Normal versus Inverted Region. *JACS.* **2001**, *123*, 2607–2617.

(32) Tsuboya, N.; Hamasaki, R.; Ito, M.; Mitsuishi, M.; Miyashita, T.; Yamamoto, Y. Nonlinear Optical Properties of Novel Fullerene–Ferrocene Hybrid Molecules. *J. Mater. Chem.* **2003**, *13*, 511–513.

(33) Xenogiannopoulou, E.; Medved, M.; Iliopoulos, K.; Couris, S.; Papadopoulos, M. G.; Bonifazi, D.; Sooambar, C.; Mateo-Alonso, A.; Prato, M. Nonlinear Optical Properties of Ferrocene- and Porphyrin–[60]Fullerene Dyads. *ChemPhysChem* **2007**, *8*, 1056–1064.

(34) Yamada, H.; Imahori, H.; Nishimura, Y.; Yamazaki, I.; Ahn, T. K.; Kim, S. K.; Kim, D.; Fukuzumi, S. Photovoltaic Properties of Self-Assembled Monolayers of Porphyrins and Porphyrin−Fullerene Dyads on ITO and Gold Surfaces. *JACS.* **2003**, *125*, 9129–9139.

(35) Kim, K.-S.; Kang, M.-S.; Ma, H.; Jen, A. K.-Y. Highly Efficient Photocurrent Generation from a Self-Assembled Monolayer Film of a Novel C_{60} -Tethered 2,5-Dithienylpyrrole Triad. *Chem. Mater.* **2004**, *16*, 5058–5062.

(36) Roncali, J. Linear π-Conjugated Systems Derivatized with C_{60}-Fullerene as Molecular Heterojunctions for Organic Photovoltaics. *Chem. Soc. Rev.* **2005**, *34*, 483.

(37) Feenstra, R. M.; Stroscio, J. A.; Fein, A. P. Tunneling Spectroscopy of the Si(111)2 × 1 Surface. *Surf. Sci.* **1987**, *181*, 295–306.

(38) Feenstra, R. M.; Stroscio, J. A.; Tersoff, J.; Fein, A. P. Atom-Selective Imaging of the GaAs(110) Surface. *Phys. Rev. Lett.* **1987**, *58*, 1192–1195.

(39) Hamers, R. J.; Hovis, J. S.; Lee, S.; Liu, H.; Shan, J. Formation of Ordered, Anisotropic Organic Monolayers on the Si(001) Surface. *J. Phys. Chem. B* **1997**, *101*, 1489–1492.

(40) Hamers, R. J.; Coulter, S. K.; Ellison, M. D.; Hovis, J. S.; Padowitz, D. F.; Schwartz, M. P.; Greenlief, C. M.; Russell, J. N. Cycloaddition Chemistry of Organic Molecules with Semiconductor Surfaces. *Acc. Chem. Res.* **2000**, *33*, 617–624.

(41) Strother, T.; Cai, W.; Zhao, X.; Hamers, R. J.; Smith, L. M. Synthesis and Characterization of DNA-Modified Silicon (111) Surfaces. *JACS.* **2000**, *122*, 1205–1209.

(42) Donhauser, Z. J. Conductance Switching in Single Molecules Through Conformational Changes. *Science* **2001**, *292*, 2303–2307.

(43) Yang, W.; Auciello, O.; Butler, J. E.; Cai, W.; Carlisle, J. A.; Gerbi, J. E.; Gruen, D. M.; Knickerbocker, T.; Lasseter, T. L.; Russell, J. N.; et al. DNA-Modified Nanocrystalline Diamond Thin-Films as Stable, Biologically Active Substrates. *Nat. Mater.* **2002**, *1*, 253–257.

(44) Reddick, R.; Warmack, R.; Ferrell, T. New Form Of Scanning Optical Microscopy. *Phys. Rev. B* **1989**, *39*, 767–770.

(45) Vigoureux, J.; Girard, C.; Courjon, D. General-Principles Of Scanning Tunneling Optical Microscopy. *Opt. Lett.* **1989**, *14*, 1039–1041.

(46) Reddick, R. C.; Warmack, R. J.; Chilcott, D. W.; Sharp, S. L.; Ferrell, T. L. Photon Scanning Tunneling Microscopy. *Rev. Sci. Instrum.* **1990**, *61*, 3669–3677.

(47) Jiang, S.; Tomita, N.; Ohsawa, H.; Ohtsu, M. A Photon Scanning Tunneling Microscope Using an AlGaAs Laser. *Jpn. J. Appl. Phys.* **1991**, *30*, 2107–2111.

(48) Dawson, P.; Defornel, F.; Goudonnet, J. Imaging Of Surface-Plasmon Propagation And Edge Interaction Using A Photon Scanning Tunneling Microscope. *Phys. Rev. Lett.* **1994**, *72*, 2927–2930.

(49) Meixner, A.; Bopp, M.; Tarrach, G. Direct Measurement Of Standing Evanescent Waves With A Photon-Scanning Tunneling Microscope. *Appl. Opt.* **1994**, *33*, 7995–8000.

(50) Feldstein, M. J.; Vöhringer, P.; Wang, W.; Scherer, N. F. Femtosecond Optical Spectroscopy and Scanning Probe Microscopy. *J. Phys. Chem.* **1996**, *100*, 4739–4748.

(51) Takahashi, S.; Fujimoto, T.; Kato, K.; Kojima, I. High Resolution Photon Scanning Tunneling Microscope. *Nanotechnology* **1997**, *8*, A54–A57.

(52) Kim, H.; Lee, J.; Kahng, S.-J.; Son, Y.-W.; Lee, S. B.; Lee, C.-K.; Ihm, J.; Kuk, Y. Direct Observation of Localized Defect States in Semiconductor Nanotube Junctions. *Phys. Rev. Lett.* **2003**, *90*.

(53) Ballard, J. B.; Carmichael, E. S.; Shi, D. X.; Lyding, J. W.; Gruebele, M. Laser Absorption Scanning Tunneling Microscopy of Carbon Nanotubes. *Nano Lett.* **2006**, *6*, 45–49.

(54) Shigekawa, H.; Yoshida, S.; Takeuchi, O.; Aoyama, M.; Terada, Y.; Kondo, H.; Oigawa, H. Nanoscale Dynamics Probed by Laser-Combined Scanning Tunneling Microscopy. *Thin Solid Films* **2008**, *516*, 2348–2357.

(55) Kim, M.; Hohman, J. N.; Cao, Y.; Houk, K. N.; Ma, H.; Jen, A. K.-Y.; Weiss, P. S. Creating Favorable Geometries for Directing Organic Photoreactions in Alkanethiolate Monolayers. *Science* **2011**, *331*, 1312–1315.

(56) Atkin, J. M.; Berweger, S.; Jones, A. C.; Raschke, M. B. Nano-Optical Imaging and Spectroscopy of Order, Phases, and Domains in Complex Solids. *Adv. Phys.* **2012**, *61*, 745–842.

(57) Bonnell, D. A.; Basov, D. N.; Bode, M.; Diebold, U.; Kalinin, S. V.; Madhavan, V.; Novotny, L.; Salmeron, M.; Schwarz, U. D.; Weiss, P. S. Imaging Physical Phenomena with Local Probes: From Electrons to Photons. *Rev. Mod. Phys.* **2012**, *84*, 1343–1381.

(58) Nienhaus, L.; Wieghold, S.; Nguyen, D.; Lyding, J. W.; Scott, G. E.; Gruebele, M. Optoelectronic Switching of a Carbon Nanotube Chiral Junction Imaged with Nanometer Spatial Resolution. *Acs Nano* **2015**, *9*, 10563–10570.

(59) Cocker, T. L.; Peller, D.; Yu, P.; Repp, J.; Huber, R. Tracking the Ultrafast Motion of a Single Molecule by Femtosecond Orbital Imaging. *Nature* **2016**, *539*, 263–267.

(60) Nguyen, D.; Nguyen, H. A.; Lyding, J. W.; Gruebele, M. Imaging and Manipulating Energy Transfer Among Quantum Dots at Individual Dot Resolution. *ACS Nano* **2017**, *11*, 6328–6335.

(61) Bumm, L. A.; Arnold, J. J.; Charles, L. F.; Dunbar, T. D.; Allara, D. L.; Weiss, P. S. Directed Self-Assembly to Create Molecular Terraces with Molecularly Sharp Boundaries in Organic Monolayers. *JACS.* **1999**, *121*, 8017–8021.

(62) Donhauser, Z. J.; Price, D. W.; Tour, J. M.; Weiss, P. S. Control of Alkanethiolate Monolayer Structure Using Vapor-Phase Annealing. *JACS.* **2003**, *125*, 11462–11463.

(63) Cygan, M. T.; Dunbar, T. D.; Arnold, J. J.; Bumm, L. A.; Shedlock, N. F.; Burgin, T. P.; Jones, L.; Allara, D. L.; Tour, J. M.; Weiss, P. S. Insertion, Conductivity, and Structures of Conjugated Organic Oligomers in Self-Assembled Alkanethiol Monolayers on Au{111}. *JACS.* **1998**, *120*, 2721–2732.

(64) Claridge, S. A.; Liao, W.-S.; Thomas, J. C.; Zhao, Y.; Cao, H. H.; Cheunkar, S.; Serino, A. C.; Andrews, A. M.; Weiss, P. S. From the Bottom up: Dimensional Control and Characterization in Molecular Monolayers. *Chem. Soc. Rev.* **2013**, *42*, 2725–2745.

(65) Eigler, D. M.; Weiss, P. S.; Schweizer, E. K.; Lang, N. D. Imaging Xe with a Low-Temperature Scanning Tunneling Microscope. *Phys. Rev. Lett.* **1991**, *66*, 1189–1192.

(66) Pascual, J. I.; Jackiw, J. J.; Song, Z.; Weiss, P. S.; Conrad, H.; Rust, H.-P. Adsorbate-Substrate Vibrational Modes of Benzene on Ag(110) Resolved with Scanning Tunneling Spectroscopy. *Phys. Rev. Lett.* **2001**, *86*, 1050–1053.

(67) Kästle, G.; Boyen, H.-G.; Koslowski, B.; Plettl, A.; Weigl, F.; Ziemann, P. Growth of Thin, Flat, Epitaxial () Oriented Gold Films on c-Cut Sapphire. *Surf. Sci.* **2002**, *498*, 168–174.

(68) Wildes, A. R.; Mayer, J.; Theis-Bröhl, K. The Growth and Structure of Epitaxial Niobium on Sapphire. *Thin Solid Films* **2001**, *401*, 7–34.

(69) Wagner, T. High Temperature Epitaxial Growth and Structure of Nb Films on α-Al_2O_3 (0001). *J. Mater. Res.* **1998**, *13*, 693–702.

(70) Gutekunst, G.; Mayer, J.; Rühle, M. Atomic Structure of Epitaxial Nb-Al_2O_3 Interfaces I. Coherent Regions. *Philos. Mag. A* **1997**, *75*, 1329–1355.

(71) Wildes, A. R.; Cowley, R. A.; Ward, R. C. C.; Wells, M. R.; Jansen, C.; Wireen, L.; Hill, J. P. The Structure of Epitaxially Grown Thin Films: A Study of Niobium on Sapphire. *J. Phys. Condens. Matter* **1998**, *10*, L631–L637.

(72) Kitada, M. Reactions in Au/Nb Bilayer Thin Films. *Thin Solid Films* **1994**, *250*, 111–114.

(73) Zhao, Y. Interface Properties of Functional Molecules on Au{111}: From Photoinduced Charge Transfer to Exchange Reactions. Ph.D. Dissertation, University of California, Los Angeles, CA, **2014**.